4D SEISMIC ANALYSIS OF THE HIBERNIA OIL FIELD, GRAND BANKS, CANADA

RICHARD JAMES WRIGHT

4D SEISMIC ANALYSIS OF THE

HIBERNIA OIL FIELD, GRAND BANKS, CANADA

by

© Richard James Wright

A thesis submitted to the

School of Graduate Studies

in partial fulfillment of the

requirements for the degree of

Doctor of Philosophy

Department of Earth Sciences (Geophysics)

Memorial University of Newfoundland

June 2004

St. John's

Newfoundland

Table of contents

iv

Abstract

The seismic reflection method, traditionally a geologic structural imaging tool, is increasingly being utilized for petroleum reservoir monitoring purposes. Time-lapse, or four dimensional (4D) seismic reservoir monitoring is the process by which repeated 3D seismic surveys are acquired over a common area during the production of a petroleum reservoir in an effort to spatially image production related changes. While if successful, this seismic method can have a significant impact on an oil field's development plan, the sometimes subtle nature of the 4D seismic signals restricts the universal application of 4D seismic methods in all reservoirs and operating environments. To examine the potential use of 4D seismic on Canada's Grand Banks, this thesis conducts a 4D seismic analysis of the Hibernia oil field – the first example of 4D seismic technology on the Grand Banks.

Due to a challenging environment (seismic and reservoir) at Hibernia for 4D seismic success, rock physics modeling predicts a subtle 4D seismic response for areas of both water and gas injection. To equalize the 4D seismic datasets, specialized poststack cross equalization including a volume event warping process is applied to two 3D post stack seismic datasets from the Hibernia oil field, a pre-production "legacy" survey acquired in 1991, and a 2001 survey. The cross equalization processing improves the repeatability of non-reservoir events fieldwide and enhances reservoir anomalies in some areas of the field. While the data contains a fair degree of noise, 4D seismic anomalies above the noise level can be imaged in areas of both water and gas injection. Through

interpretation, some of these anomalies are shown to be consistent with modeled responses to water and gas injection. In addition, there is evidence that some of the seismic anomalies may be due to pore pressure changes in the reservoir. The results of the Hibernia 4D seismic analysis are then used as background for a feasibility analysis for the application of 4D seismic in other fields on the Grand Banks, which compared to Hibernia, prove to have similar 4D seismic potential. In accomplishing these objectives, this thesis makes new contributions in the areas of rock physics modeling, 4D seismic in marginal environments, methods for 4D seismic pressure/saturation inversion, and 4D seismic interpretation.

As Hibernia is the first producing field in the region, this thesis provides an important benchmark for the evaluation of the potential role of 4D seismic analysis on development decisions for other Grand Banks fields currently in early production (Terra Nova), or under development (White Rose, Hebron).

Disclaimer

The thesis was supported financially and logistically by the Hibernia Management and Development Company Ltd. (COMPANY). However, the results and conclusions reached in this thesis should not be construed in any way as those of the COMPANY. The opinions expressed in this thesis are solely those of the AUTHOR, Richard Wright, based on the analysis detailed in this thesis. The COMPANY is performing their own prestack time-lapse seismic analysis which is scheduled for completion in mid-2004.

List of tables

List of figures

Chapter 3

Chapter 4

Chapter 5

Chapter 6

Acknowledgements

Chapter 1

Introduction

1.1 Thesis overview

The seismic reflection method, traditionally a geologic structural imaging tool, is increasingly being utilized for petroleum reservoir monitoring purposes (Lumley, 2001). Time-lapse, or four dimensional (4D) seismic reservoir monitoring is the process by which repeat 3D seismic surveys are acquired over a common area during the production of a petroleum reservoir. Assuming the time frame between surveys is sufficiently small to neglect geologic time scale effects, the change in reservoir seismic response as a function of production time can be attributed to production-related physical changes in the reservoir such as changes in pressure, temperature, or pore fluid type. These physical changes can be monitored over time to delineate reservoir continuity, sealing potential of reservoir faults, performance of existing wells, and the planning of future wells (Jack, 1998; Koster et. al, 2000; Lumley, 2001). While 4D seismic data has the potential to be used as an enhanced recovery method (Nur, 1989), the sometimes subtle nature of production-induced seismic change and the difficulty of detecting such changes seismically, restricts the application of 4D seismic methods in all reservoirs and operating environments.

In this thesis, I conduct the first 4D seismic analysis on an offshore eastern Canadian oil field - the Hibernia field, to determine the expected seismic response to production

1

related changes and assess the limitations of the technique in this specific environment. As Hibernia is the first producing field in the region, this research will provide an important benchmark for the evaluation of the potential role of 4D seismic analysis on development decisions for other Grand Banks fields currently in early production (Terra Nova), or under development (White Rose, Hebron). These fields are all in the challenging acquisition environment of the North Atlantic, an area that can have considerable ocean swell height (Evans, 2004) and high winds contributing to seismic noise. In addition, the fairly hard rocks and considerable depth to the reservoirs (up to 4 kms), tend to make the time-lapse seismic response more subtle compared to shallower, softer targets such as those in some fields that have had 4D seismic surveys in the Gulf of Mexico or West Africa (Lumley et al. 1997).

This seismic method has significant economic benefits if the surveys can be used to map in 3D the migration of fluids through the porous reservoir rocks. This can indicate to the oil field operator areas that are characterized by bypassed (remaining) oil or leaking faults, allowing for optimized targeting of infill drilling which ultimately raises the recoverable reserves from the field. As a result of this potential economic benefit, 4D seismic data is now being integrated into many oil field development plans worldwide (Lumley, 2001).

This research establishes the following: (1) through modeling, the subtle nature of the expected Hibernia 4D seismic response; (2) through specialized processing, the ability to

detect reservoir seismic changes in the Hibernia 4D data; (3) through interpretation, verification of 4D seismic anomalies by calibration with the modeled response; and (4) through a basin 4D seismic feasibility study using the Hibernia results as a reference, the potential future use of 4D seismic technology at other fields on the Grand Banks. In accomplishing these objectives, this research makes new contributions in the areas of rock physics modeling, 4D seismology in marginal environments, methods for 4D seismic pressure/saturation inversion, and 4D seismic interpretation.

1.2 Historical Perspective

One of the goals in hydrocarbon extraction is to maximize the recovery of the resource from a producing field. Starting in the 1980's there has been an effort to increase production in oil fields by drilling injection wells that can be used to control reservoir pressure and to sweep the reservoir with fluids that enhance oil recovery. The widespread introduction of three dimensional (3D) seismic data and the routine migration of seismic data in the late 1980's further enhanced recoveries as wells were situated more strategically and seismically imageable reservoir heterogeneities between wells were better understood (Jack, 1998). The challenge faced by production managers of that time was that once production started, the only measurements readily available for field appraisal were down-hole production observations in wells, such as pressure tests, fluid saturations, and production/injection rates (Nur, 1989). While these data provide information near the borehole, they provide limited understanding of reservoir conditions beyond tens of metres away from the well. More complex production problems such as

the occurrence of early water breakthrough in a production well, and the spatial delineation of pressure communication between the injection and production wells require spatial mapping of reservoir changes and this is where 4D seismic methods play a significant role. The one dimensional (vertical) nature of well measurements cannot sample the earth at a sufficient lateral resolution to provide adequate insight into these types of three dimensional problems (Nur, 1989).

Amos Nur, in a 1989 foundation paper, outlined the petrophysical case for 4D seismology. He proposed that repeated 3D seismic surveys over a production period had the potential to become a central tool in reservoir management because they allow for the possibility of remote monitoring of the migration of pore fluids over the three dimensional extent of the reservoir. Early papers on 4D seismic case studies included work on seismic monitoring of a fireflood (Greaves and Fulp, 1987) and a steam flood (Pullin et. al, 1987). In the early 1990's, work was done on monitoring gas-fluid movement in reservoirs (Lumley, 2001). A few years later, 4D seismic implementations were used to monitor oil-water interaction (Wang et al, 1991; Sonneland et al, 1997). In the late 1990's there began a great deal of discussion on permanent installations such as ocean bottom cables and down-hole instruments to improve repeatability between surveys, allow for the acquisition of shear waves, and improve the turnaround time and lower costs for repeated surveys (Ebrom, 1999; Lumley, 2001b).

Currently, there is considerable research aimed at quantitative estimation of reservoir properties and the subsequent integration into reservoir management (Christie et al., 2002). One of the key elements in quantitative reservoir property estimation is the separation of pressure change from saturation change in the time-lapse seismic data. Using seismic amplitude variation with offset principles, Tura and Lumley (1998) present the first published work on the separation of pressure from saturation effects in time-lapse seismic data. Landro (2001) presents ideas to discriminate pressure from saturation change in the Gullfaks field, North Sea. Cole et. al. (2002) and Lumley et al. (2003b) present methods that utilize rock physics data to quantitatively invert 4D seismic for pressure and saturation change. In certain 4D seismic projects, inverted 4D seismic pressure and saturation data is integrated with the reservoir flow simulation models to provide time-varying 3D earth models of reservoir pressure and pore fluid migration (Christie et al., 2002).

1.3 Physical basis

The seismic reflection method relies on subsurface acoustic impedance (I) contrasts to image the interface between different lithologic units. A reflection coefficient (RC) is generated from a contrast in acoustic impedance, and is considered proportional to seismic amplitude. For normal incidence, the reflection coefficient (RC) for a boundary between two subsurface layers is given by:

$$RC = \frac{I_2 - I_1}{I_1 + I_2} \quad (1.1),$$

5

where I_1 is the acoustic impedance of the top layer, and I_2 is the acoustic impedance of the deeper layer. Acoustic impedance is represented as the product of density (ρ) and velocity (v) in the following expression:

$$I = \rho v \quad (1.2).$$

4D seismology relies on the fact that the density and velocity of a reservoir rock unit vary as a function of fluid saturation, pore pressure, and temperature. During the production phase of an oil field, one, two, or all three of these reservoir parameters change, and depending on the magnitude of the changes and a number of other factors, one may expect an associated change in the seismic response. Figure 1.1 illustrates the effect water flooding (water flushing oil in rock pore space) may have on the 4D seismic response.

Time-lapse or 4D seismic data is obtained by acquiring multiple 3D seismic surveys over an oil field at different times in the production history (e.g. before production, 5 years into production, 10 years into production, etc.). The surveys are compared both qualitatively and quantitatively to look for changes in the seismic response resulting from physical changes in the reservoir, such as fluid migration or pore pressure change.

Definitions:

ϕ : porosity

S_w : water saturation = 1 - oil saturation (fractional percent)

RC : Reflection Coefficient
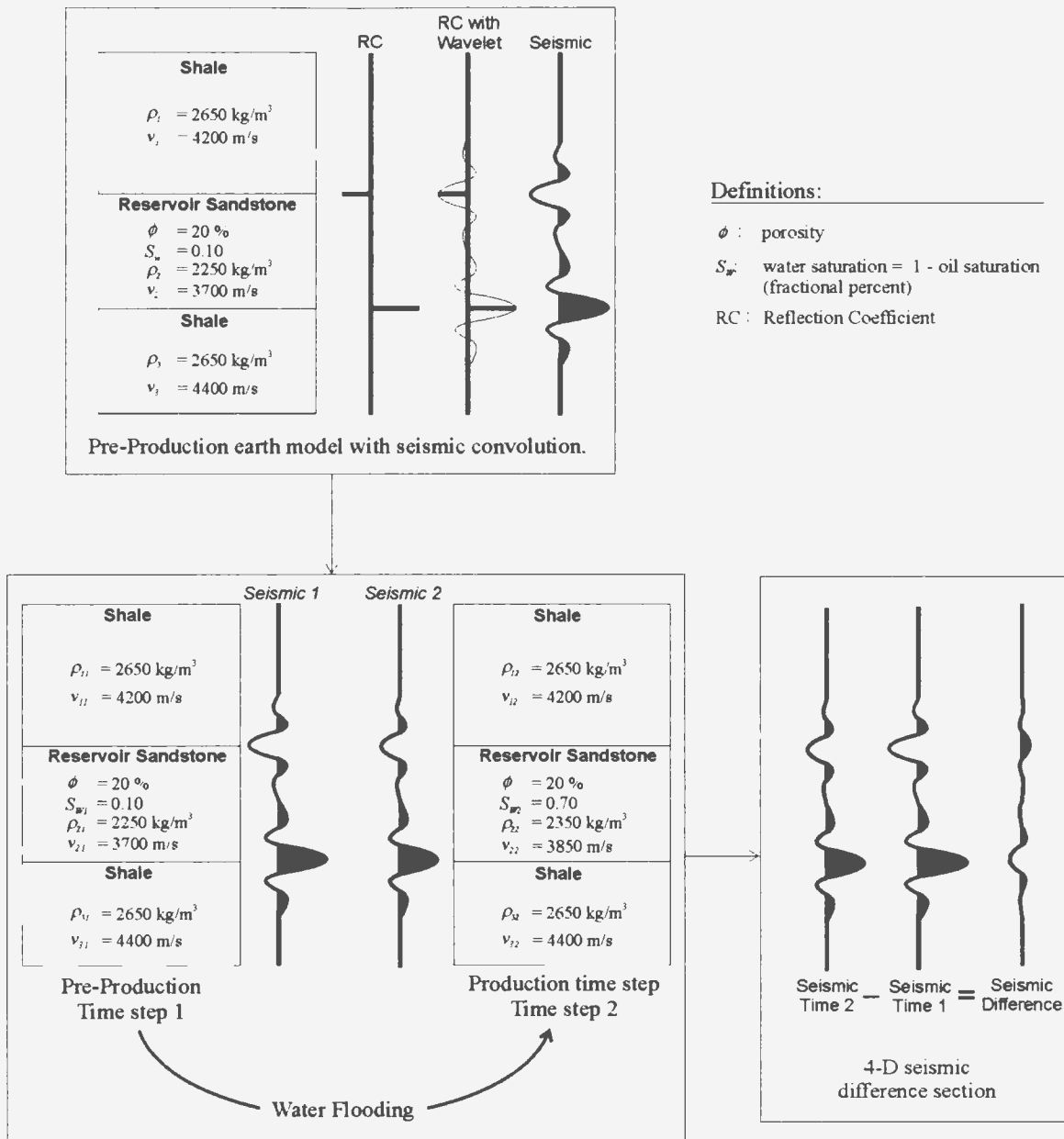
Figure 1.1. *A flowchart schematically demonstrating the seismic effect of replacing pore hydrocarbons with water (a higher density, higher velocity fluid). Because the pore space is now filled with a fluid having a higher acoustic impedance, the overall acoustic impedance of the reservoir sandstone layer increases, decreasing the impedance contrast with the surrounding shale. The 4D seismic difference trace demonstrates the seismic amplitude changes between observations. Physical properties are used for illustrative purposes only.*

1.4 Hibernia field background

The focus of this thesis research is a 4D seismic analysis of the Hibernia oil field. The Hibernia oil field is located approximately 315 km east-southeast of St. John's, Newfoundland as shown in figure 1.2. Commencing production in late 1997, it is Canada's largest offshore oil field with an estimated 865 million barrels recoverable (Canada-Newfoundland Offshore Petroleum Board, 2003) and daily production rates of nearly 200,000 barrels per day. Three different vintages of 3D seismic data have been acquired over the field; the first survey in 1981, another 3D survey in 1991, and another in 2001. The 1991 (pre-production) and 2001 (acquired 4 years into production) 3D seismic surveys are used in this research. All production and injection wells are drilled from the Hibernia gravity-based structure (GBS) located near the centre of the field which rests on the ocean floor in about 80 metres of water. (Wright, 1999)
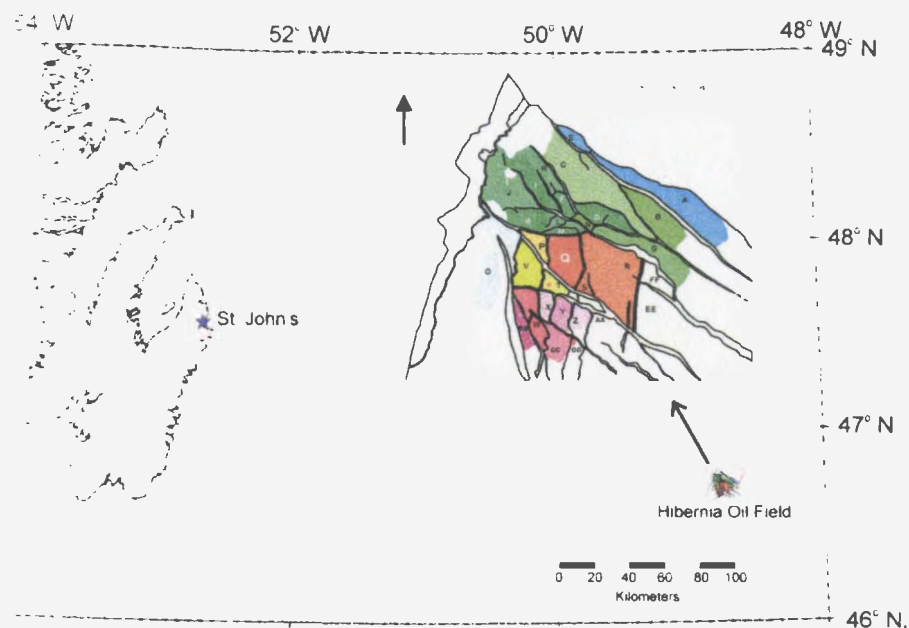
Figure 1.2. *Hibernia location map with inset showing showing the reservoir's numerous fault blocks (adapted from Wright, 1999)*

The Hibernia reservoir is at a depth of approximately 3300-3700 metres and is a rollover anticline structure associated with a listric normal fault (Geological Survey of Canada, 1992). The reservoir section is an early Cretaceous fluvial braided stream deposit bounded seismically at the top by the Hibernia Lower Zone horizon (top of layer 1) and at the bottom by the Fortune Bay shale horizon. The oil producing interval in the portion of the field shown in figure 1.3 is the lower 55 metres of Layer 3 below the gas oil contact; although the upper part of Layer 3 and Layer 2 are good porosity gas saturated sandstones. The gas-oil and oil-water contacts vary in their position in the section throughout the field as the depth of the reservoir section changes.

		P Velocity (m/s)	Vp/Vs	Density	Ave Porosity	
60m	Layer 1	4170	1.74	2550	3.8%	Layer 1
25m	Layer 2	3890	1.59	2260	18.0%	Layer 2
20m	Medial Shale	4310	1.7	2620	1.0%	Medial Shale
25m	Layer 3	4020	1.62	2350	15.0%	Layer 3
GOC 55m						
	Fortune Bay	4250	1.81	2600	1.4%	Fortune Bay
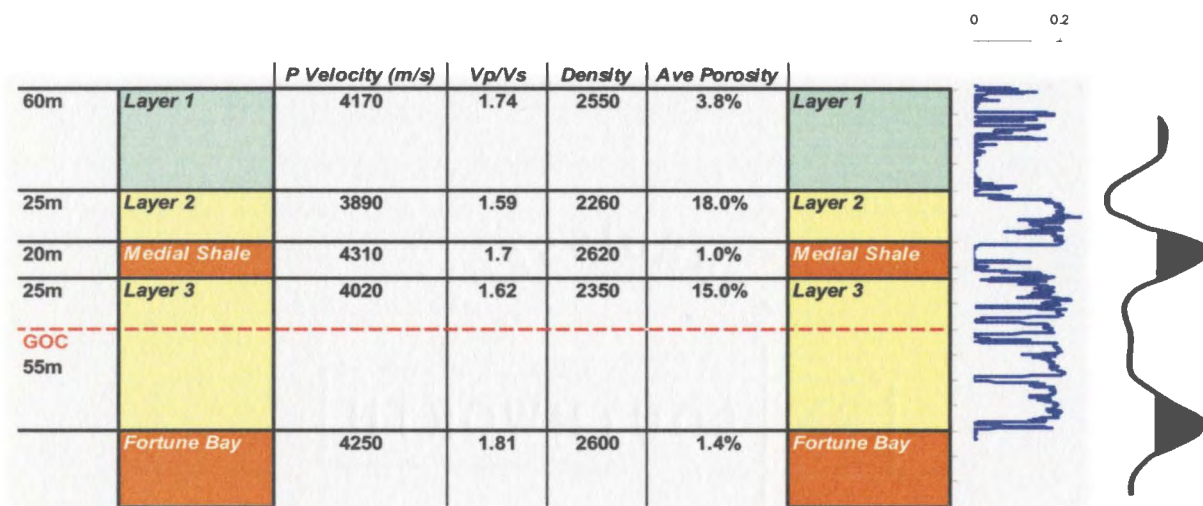
Figure 1.3 *Hibernia reservoir layers with average properties. A porosity log with scale ranging from 0 to 0.20 (fraction) is given in blue and a seismic trace (far right)*

The success of the 4D seismic method is dependent on two elements; the physical changes in the reservoir having sufficient magnitude to be imaged seismically, and the

time-lapse seismic data having adequate repeatability to detect such changes. This is well described by the 4D seismic signal to noise ratio (Lumley, 2004), which is defined as the ratio of the magnitude of the 4D seismic reservoir anomaly to the background noise after one seismic dataset has been subtracted from the other (e.g. 2001-1991). For the Hibernia field, the modeled seismic changes due to production are likely to be subtle as a result of the hard rocks, low frequencies, high pore pressures, and intermediate porosities in the reservoir unit. The two 3D seismic surveys (1991 and 2001), were acquired and processed independently, meaning that parameters such as the streamer length, airgun volume, and pre-stack processing flow were different for each survey. In addition, the environmental conditions such as water temperature, tides, and sea states on the Grand Banks varied within and between surveys. As a result of the items outlined above, there are a number of elements in addition to legitimate reservoir changes that could conceivably contribute to differences between surveys in the Hibernia 4D seismic data. In this thesis, I examine these items that make the use of 4D seismic at Hibernia challenging, and explore methods (including original methods) to enhance the potential of garnering meaningful reservoir information from the 4D seismic data.

1.5   Overview of thesis research

The principal goal of this thesis is to conduct a comprehensive 4D seismic analysis of the Hibernia oil field, Grand Banks, Canada. To meet this objective, the thesis has four principal components: (1) modeling of the 4D seismic response from first physical principles, (2) specialized processing to equalize Hibernia 4D seismic data, (3)

interpretation and validation of 4D seismic data results, and (4) feasibility analysis of 4D seismic in other Grand Banks oil fields. Chapter 2 presents methods for the determination of rock and fluid properties, including original research on the determination of pressure and facies dependent elastic moduli. Chapter 3 presents pressure and saturation based 4D seismic models of the Hibernia reservoir and includes original research on inverse methods for solving for pressure and saturation change from the 4D seismic data. Chapter 4 presents the post-stack cross equalization processing methodology used to balance the 1991 and 2001 datasets and enhance the 4D seismic signal to noise ratio. Chapter 5 presents the 4D seismic interpretation results including the first order validation of anomalies through modeling. Chapter 6 is a comparative feasibility study that presents a risk assessment of 4D seismic potential of other Grand Banks oil fields in light of the Hibernia results in this thesis. This is especially relevant given that the other fields on the Grand Banks have similar 4D seismic parameters when compared with those at Hibernia. As the first 4D seismic investigation in the basin, this research will provide an important benchmark for the evaluation of the potential role of 4D seismic analysis on development decisions for other Grand Banks fields.

Chapter 2

Modeling of Hibernia rock and fluid properties

2.1 Overview

4D seismic modeling is a process that uses fundamental and empirical rock physics relationships to create synthetic seismic data to represent different steps in a reservoir's production history. Figure 2.1 shows the relative position of 4D seismic modeling in the overall Hibernia 4D seismic analysis work flow. This chapter examines the 4D seismic related rock and fluid properties of the Hibernia reservoir, while the following chapter (3) uses the calculated rock and fluid property data to generate 4D synthetic seismograms.

The saturated rock modeling in this thesis is based on the separate calculation of dry porous rock properties and pore fluid properties which are then combined to yield a saturated rock model. The pore fluid properties of gas, oil, and brine are computed using empirical relations from Batzle and Wang (1992). The pressure-dependent dry rock properties are derived from my original thesis research based on Hibernia core rock physics analysis. These independently calculated rock and fluid properties are combined together using Gassmann's relationship (Gassmann, 1951; Berryman and Milton, 1991) to create a numerical saturated rock model from which the seismic properties of density, P-wave velocity, and S-wave velocity can be determined. In Chapter 3, these properties are used to create offset dependant synthetic 4D seismic data for different pore fluid and pressure scenarios.
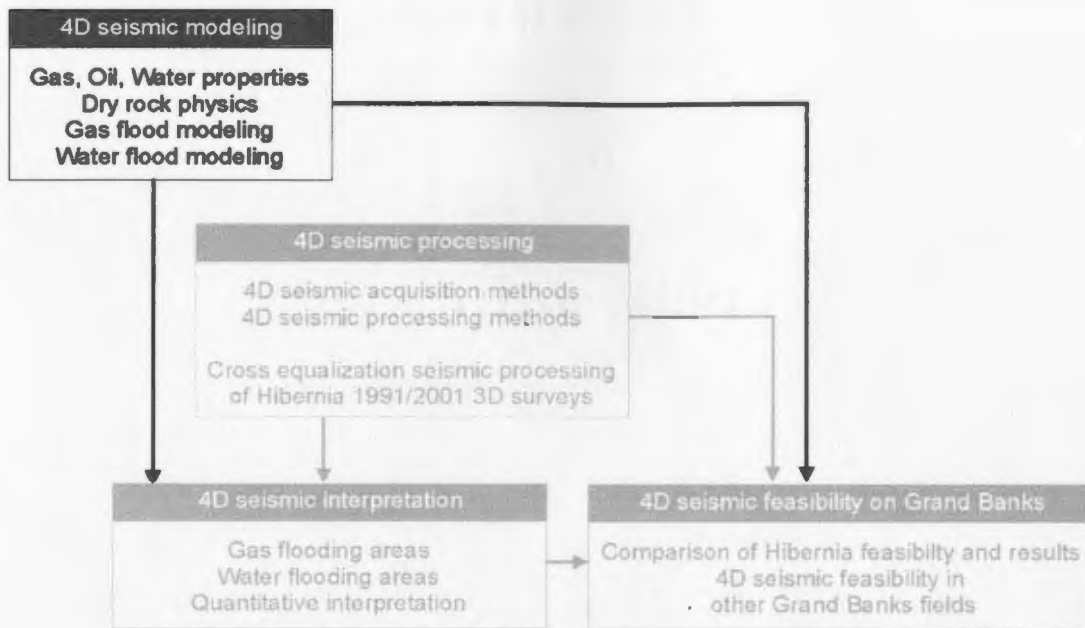
Figure 2.1. *Thesis outline flowchart. 4D seismic modeling is required to accurately understand the type of time-lapse seismic response that may be anticipated for a given reservoir change. In addition, the seismic modeling will enable the creation of a set of relationships that link seismic response to physical reservoir change. This can aid in time-lapse seismic interpretation by allowing the inversion of the observed seismic response in the reservoir to yield physical reservoir changes such as saturation or pore pressure.*

2.2 Introduction

The success of a 4D seismic effort is a function of a number of reservoir and seismic acquisition parameters (Lumley et. al., 1997). In certain fields, production effects can be clearly imaged with 4D seismic data, while in others such as Hibernia it is more difficult to extract meaningful time-lapse seismic signals, as will be discussed. By Lumley's (1997) ranking, parameters that are positive for potential 4D seismic detection at Hibernia include: a high gas-oil ratio (GOR) oil (1000+ scf/bbl) yeilding a good oil/water contrast, good sweep efficiency allowing for greater fluid substituion, and a relatively large reservoir thickness of approximately 60 m. Parameters that make detection of time-lapse seismic signals more difficult include: a depth of approximately 3500-4000m, a moderately high dry rock bulk modulus (13-18 GPa) which dominates in the bulk rock the contribution of the smaller fluid moduli, high pore and effective pressures (40 and 50 MPa respectively), low seismic frequencies (20-25 Hz), a challenging acquisition environment, and no visible seismic fluid contacts in the legacy data. These parameters combine to suggest that this is a high risk 4D seismic experiment. A summary of selected Hibernia reservoir properties is given in table 2.1.

Hibernia Reservoir Parameters	
Temperature	95 C
Pore Pressure	40 MPa
Net Pressure	50 MPa
GOR	1000+ scf/bbl
Reservoir Thickness	up to 60m
Reservoir Depth	3500-4000m
Dry Bulk Modulus	13-18 GPa
Seismic Frequencies	20-25 Hz
Porosity	20%

Table 2.1 *Hibernia reservoir parameter summary*

As each oil field has different geologic and reservoir parameters, the potential 4D seismic response can be estimated by forward modeling a computational representation of the reservoir. To build a saturated time-dependent earth model for the Hibernia reservoir, it is first necessary to determine the pore fluid and dry rock properties independently, then merge them using Gassmann's relationship (Gassmann, 1951; Berryman and Milton, 1991). This research uses a variation of a 4D seismic modeling workflow first assembled by Lumley (1995). The modeling workflow for this thesis is illustrated in figure 2.2. A slightly modified version of figure 2.2 appears throughout both the current chapter (rock and fluid properties), and the following chapter (4D seismic modeling), to allow the reader to quickly locate the discussed research topic in the proper context in the 4D seismic modeling workflow.
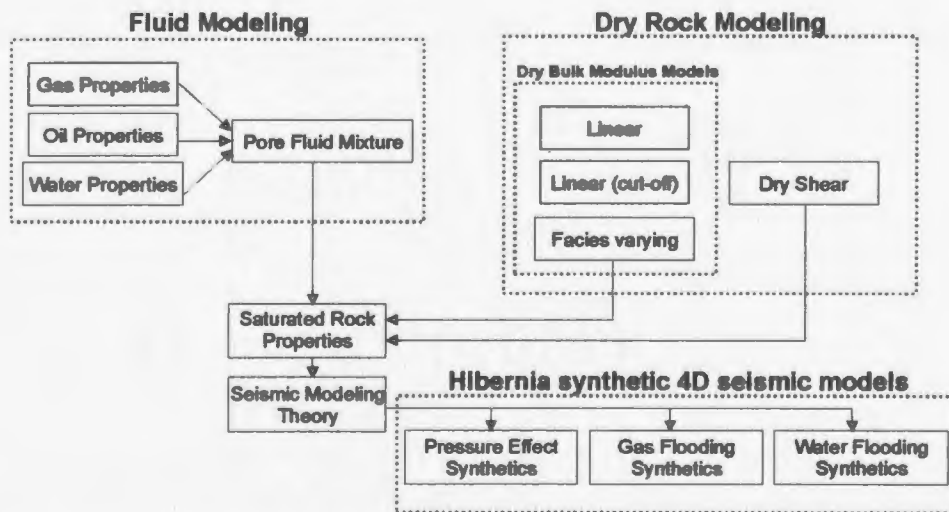
Figure 2.2. *Hibernia 4D seismic modeling workflow. The pore fluid properties and dry rock properties are computed independently, then merged using Gassmann's relationship to produce saturated rock properties. The saturated rock model is then forward modeled with different pressures and saturations to produce 4D synthetic seismic data for various production scenarios.*

2.3 Pore fluid physics modeling

The determination of the seismic properties of pore fluids is crucial when estimating the type of seismic response that may be anticipated from a 4D seismic survey. While there exist some physical relationships to calculate the properties of mixtures of gas, oil, and brine, the determination of single fluid phase properties is largely approached from an empirical perspective when not measured directly through pressure, volume, temperature (PVT) analysis. In this section, I present published relationships for calculating the individual properties of gas, oil, and brine in the Hibernia reservoir. Once the properties of the individual fluid components are determined, I will examine the physical properties of the pore fluid mixtures, which is an important consideration in 4D seismic modeling.

2.3.1 Gas modeling

Gas property modeling is the first step in the Hibernia 4D seismic modeling workflow as shown in figure 2.3. For pressure dependent 4D seismic modeling, gas properties can be calculated from the empirical relationships outlined in the widely referenced paper on the seismic properties of pore fluids by Batzle and Wang (1992).

Gas mixtures are referenced to a specific gas gravity, G, which is the ratio of gas density to air density at standard temperature and pressure. G typically ranges from 0.56 (pure methane) to 1.8 for gases with heavier carbon compounds (Batzle and Wang, 1992). The reservoir gas in the Hibernia reservoir has a specific gravity of approximately 0.7 (Wright, 1999).

16
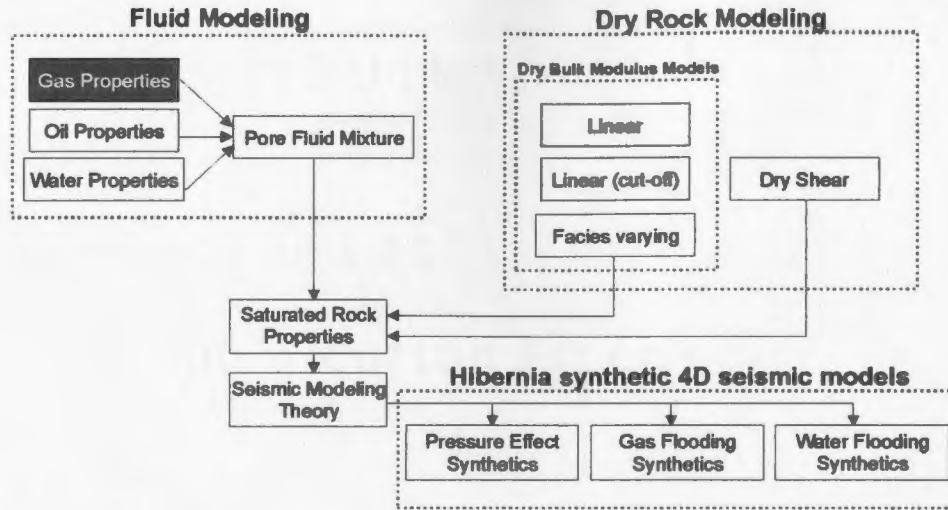
Figure 2.3. *Hibernia 4D seismic modeling workflow, with the determination of gas properties highlighted.*

Thomas et. al. (1970) found the following simple relationships linking G, pseudo-reduced temperature (T_{pr}), and pseudo-reduced pressure (P_{pr}).

$$P_{pr} = \frac{P}{4.892 - 0.4048G} \quad , \quad (2.1)$$

$$T_{pr} = \frac{T_a}{94.72 + 170.75G} \quad , \quad (2.2)$$

where P is in MPa and T_a is the absolute temperature in degrees Kelvin. Using these pseudo-reduced temperatures and pressures, a gas density can be approximated by:

$$\rho \cong \frac{28.8GP}{ZRT_a} \quad , \quad (2.3)$$

where,

$$Z = \left[0.03 + 0.00527(3.5 - T_{pr})^3\right]P_{pr} + (0.642T_{pr} - 0.007T_{pr}^4 - 0.52) + E , \quad (2.4)$$

and

$$E = 0.109(3.85 - T_{pr})^2 e^{-\left[0.45 + 8(0.56 - 1/T_{pr})^2\right]P_{pr}^{1.2}/T_{pr}} \quad , \quad (2.5)$$

where P is in MPa and R is the universal gas constant of 8.31. Figure 2.4 illustrates gas densities as a function of pressure and temperature for a light ($G = 0.6$) and heavy ($G = 1.2$) gas.
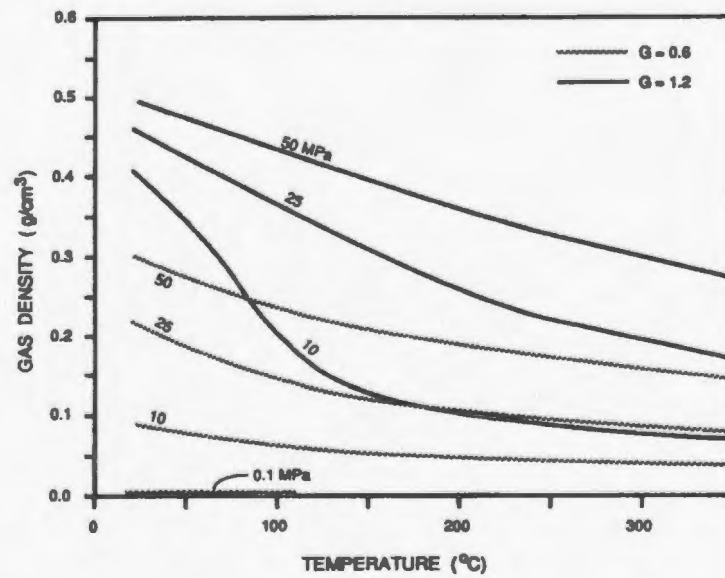
Figure 2.4. *Gas density as a function of specific gravity, pressure and temperature. From Batzle and Wang (1992).*

The adiabatic bulk modulus for gas (K_S) is approximated (Batzle and Wang, 1992) by:

$$K_S \cong \frac{P}{\left(1 - \dfrac{P_{pr}}{Z} \dfrac{\partial Z}{\partial P_{pr}}\right)_T} \gamma_0 \quad , (2.6)$$

where

$$\gamma_0 = 0.85 + \frac{5.6}{P_{pr} + 2} + \frac{27.1}{(P_{pr} + 3.5)^2} - 8.7 e^{-0.65(P_{pr} + 1)} \quad , (2.7)$$

18

and $\dfrac{\partial Z}{\partial P_{pr}}$ can be computed from equations 2.4 and 2.5. Figure 2.5 displays gas bulk

modulus as a function of pressure and temperature for a light ($G = 0.6$) and heavy ($G = 1.2$) gas.
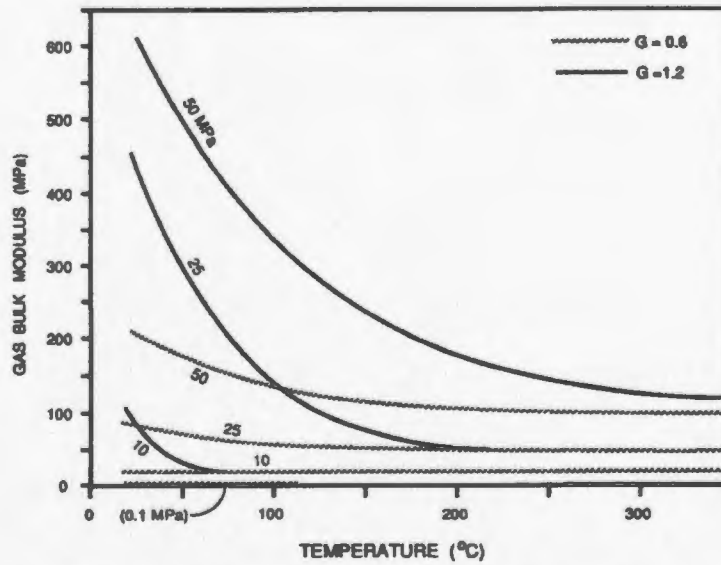
Figure 2.5. *Gas bulk modulus as a function of specific gravity, pressure and temperature. From Batzle and Wang (1992).*

Figure 2.4 and figure 2.5 show that gas density and bulk modulus increase with pressure

and decrease with temperature. The gas in the Hibernia reservoir with a specific gravity

of 0.7, a reservoir pore pressure of 40 MPa, and a temperature of approximately $100^{O}C$

has a density (ρ) of approximately 0.25 g/cm^3 and a bulk modulus of 0.11 GPa. The fluid

bulk modulus (K) relationship is given as:

$$K = \rho V^2 \quad , \quad (2.8)$$

where V is the acoustic fluid velocity. Solving for gas velocity (V), an approximate

value of 670 m/s is determined for Hibernia hydrocarbon gas.

2.3.2 Oil modeling

Now that the properties of Hibernia gas have been predicted, let us consider the oil component, highlighted in the modeling workflow in figure 2.6.
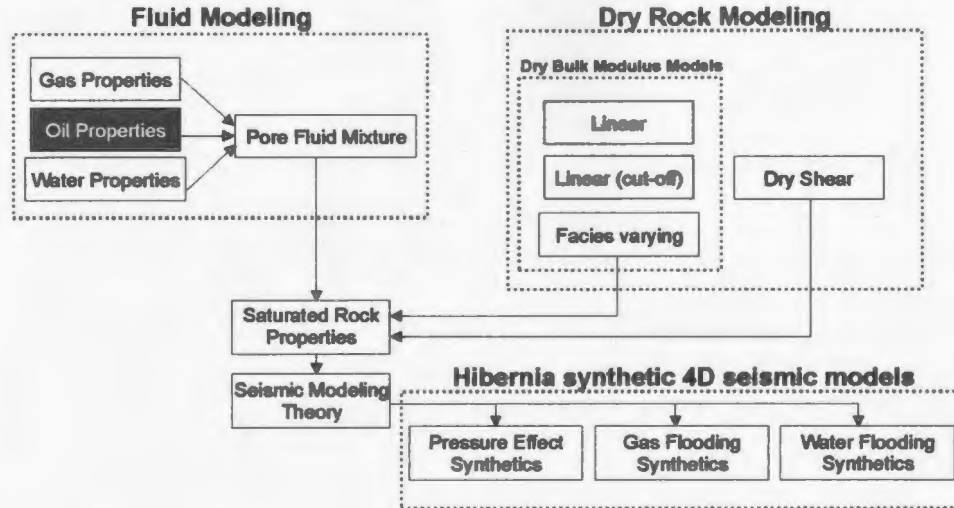
Figure 2.6. *Hibernia 4D seismic modeling workflow, with the determination of oil properties highlighted.*

The physical properties of oil can vary significantly, ranging from light oil condensates to heavy oil tars. Light oils can absorb gas into solution and can have a high gas-oil ratio (GOR) making their bulk properties gas like, while very heavy oils such as bitumen and kerogen behave basically as solids (Batzle and Wang, 1992). To help classify oils numerically, the American Petroleum Institute has developed a categorization scheme that ranks oils numerically from light to heavy depending on their reference density (ρ_0) at standard pressures and temperatures. The American Petroleum Institute oil gravity number (API) is (Clark, 1992):

$$API = \frac{141.5}{\rho_0} - 131.5 \quad (2.9)$$

Because of the inverse relationship with density, light oils such as those found at Hibernia (API = 36) have a high API while heavy oils can have oil gravity below 10. While the standard temperature/pressure reference density for Hibernia oil is 0.85 g/cm^3, the *in situ* physical properties at reservoir temperatures and pressures are of interest for seismic modeling purposes.

The density of oil as a function of pressure and temperature can be calculated using empirical relationships presented by Batzle and Wang (1992). For a dead oil with no gas dissolved into solution, the density (ρ) is given by:

$$\rho = \frac{\rho_0 + (0.0027P - 1.71 \times 10^{-7} P^3)(\rho_0 - 1.15)^2}{0.972 + 3.81 \times 10^{-4} (T + 17.78)^{1.175}} , \quad (2.10)$$

where ρ_0 is the reference density, T is temperature in degrees Celsius, and P is pressure in MPa. The acoustic velocity (V) of an oil containing no dissolved gas is given empirically as (Batzle and Wang, 1992):

$$V = 2096 \sqrt{\frac{\rho_0}{2.6 - \rho_0}} - 3.7T + 4.64P + 0.0115 \left[4.12 \sqrt{\frac{1.08}{\rho_0} - 1} - 1 \right] TP . \quad (2.11)$$

The Hibernia reservoir has an approximate reference density (ρ_0) of 0.85 g/cm^3, a temperature of 95 degrees Celsius, and a pore pressure of approximately 40 MPa (CNOPB, 1997). Inserting these values into equations 2.10 and 2.11 yields an *in situ* oil density of 0.80 g/cm^3 and acoustic velocity of 1330 m/s. The velocity and density of

21

water is roughly approximated[†] to be 1500 m/s and 1.00 g/cm^3 respectively. As a result, the seismic impedance contrast between water and dead oil is approximately 45%. Because in situ light oil often has gas dissolved into solution, it is very important to consider the seismic properties of live oil as part of 4D seismic modeling.

The ratio of dissolved gas to oil (GOR) in solution can significantly alter the seismic properties of oil, due to compressibility effects. In general, oil density and velocity decrease with increasing GOR. This is important when investigating the seismic reservoir monitoring potential of secondary oil production when either a gas or water flood is utilized. Considering a water flood, higher GOR oil increases the oil/water impedance contrast and improves the prospect that production can be monitored seismically. In a gas flooding situation, higher GOR oil reduces the impedance contrast between the gas and oil subsequently reducing the time-lapse seismic effect of fluid substitution.

The maximum amount of gas that can be dissolved into oil (R_G) is given by Batzle and Wang (1992) as a function of composition, pressure and, temperature:

$$R_G = 0.02123G \left[Pe^{\frac{4.072}{\rho_0} - 0.00377T} \right]^{1.205}, \quad (2.12)$$

where R_G is L/L (litres/litre), G is gas gravity, ρ_0 is oil reference density, P is pressure in MPa, and T is temperature in degrees Celsius. Equation 2.12 shows as the oil reference

---

[†] The seismic properties of water (brine) are approximated here for comparison purposes only and are robustly calculated in section 2.3.3.

density (ρ_0) decreases, the oil can accommodate more dissolved gas, so lighter oils can have a higher component of dissolved gas compared to heavier oils. Using the R_G calculated from equation 2.12, an expanded gas density (ρ') can be computed from (Batzle and Wang, 1992):

$$\rho' = \frac{\rho_0}{B_0}(1 + 0.001R_G)^{-1} \quad , \quad (2.13)$$

where B_0 is a volume factor from Standing (1962):

$$B_0 = 0.972 + 0.00038\left[2.4R_G\sqrt{\frac{G}{\rho_0}} + T + 17.8\right]^{1.175} \quad . \quad (2.14)$$

By substituting Hibernia's values into these equations, a volume factor (B_0) of 1.78 and an expanded gas density (ρ') of 0.38 g/cm^3 are determined. The expanded gas density can be substituted as a reference density in equation 2.11, which yields a live oil velocity of approximately 890 m/s, appreciably different from the 1330 m/s dead oil velocity determined by neglecting solution GOR.

Oil density also changes as a function of gas saturation. Batzle and Wang (1992) give an empirical relationship to determine the density of oil with dissolved gas (ρ_G).

$$\rho_G = \frac{0.0012GR_G}{B_0} \quad (2.15)$$

Substitution of parameters from the Hibernia reservoir calculated in the above equations yields an approximate live oil density (ρ_G) of 0.60 g/cm^3. Calculation of the "dead oil" density in equation 2.10 generated a value of 0.80 g/cm^3, about 30% higher than the more

realistic oil density accounting for solution gas. Because the live oil has lower velocity and density than oil with no dissolved gas, it has a much greater impedance contrast with water. Based solely on the Hibernia oil properties calculated in this section, the prospect of seismically imaging water floods is enhanced as a result of the increased water-oil impedance contrast due to the high GOR. Conversely, the high GOR oil has less of an impedance contrast with gas than a lower GOR oil reducing the probability of seismically imaging gas flooding. These general statements, in which the individual fluid components only are examined, do not reflect the potential effect of pressure changes on 4D seismic response in gas/water injection areas - a topic that will be discussed extensively in later sections.

2.3.3 Water (brine) property modeling

With Hibernia gas and oil properties calculated, consideration is now given to the water(brine) component, highlighted in the modeling workflow in figure 2.7 below.
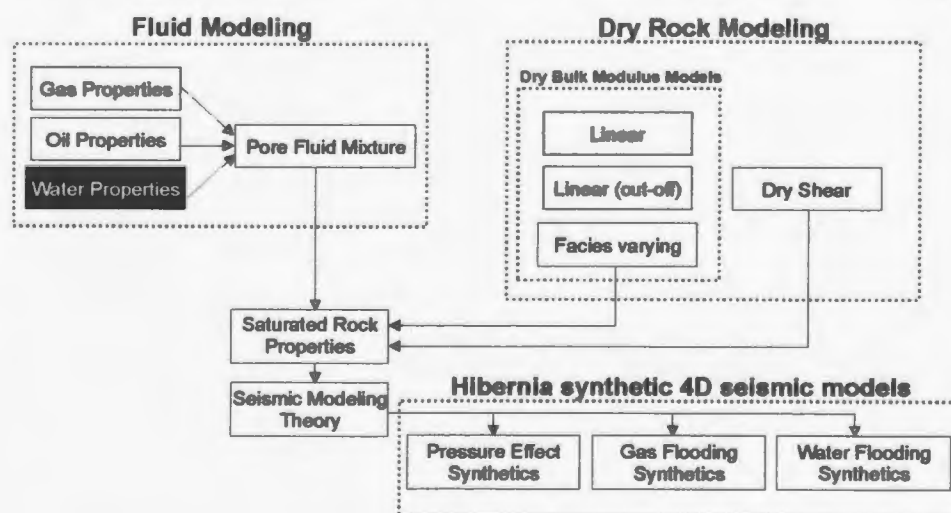
Figure 2.7. *Hibernia 4D seismic modeling workflow, with the determination of water (brine) properties highlighted.*

Brine is the most common pore fluid found in rock. Brine is the generic term for water containing varying degrees of dissolved salt. For 4D seismic modeling, it is important to consider water properties because brine is found in the pore space, and sea water is used for injection. Brine is also often present in the fraction of pore space not occupied by hydrocarbons. Batzle and Wang (1992) present empirical polynomials to calculate the density of water (ρ_W) and brine (ρ_B) as a function of temperature (T in °C), pressure (P in MPa), and salinity (S in ppm dissolved NaCl).

$$
\begin{aligned}
\rho_W = \ & 1 + 1 \times 10^{-6}(-80T - 3.3T^2 + 0.00175T^3 + 489P - 2TP \\
& + 0.016T^2P - 1.3 \times 10^{-5}T^3P - 0.333P^2 - 0.002TP^2) \ ,
\end{aligned} \qquad (2.16)
$$

and,

$$
\begin{aligned}
\rho_B = \ & \rho_W + S(0.668 + 0.44S + 1 \times 10^{-6} \ (300P - 2400PS + T(80 \\
& - 3T - 3300S - 13P + 47PS)))
\end{aligned} \qquad (2.17)
$$

The brine relationship is limited to sodium chloride solutions and can contain errors when other mineral salts are present. For the Hibernia 4D study, it is a reasonable assumption to use this relationship because the majority of water calculations involve injected seawater, which is predominately a dissolved salt solution. At an isobaric reservoir pressure of 40 MPa, figure 2.8 displays a plot of brine density as a function of temperature and salinity using the relationships in equations 2.16 and 2.17. In general brine has increasing density with salinity and decreasing density with temperature. Using values typical of Hibernia of a temperature of 95°C, a

25
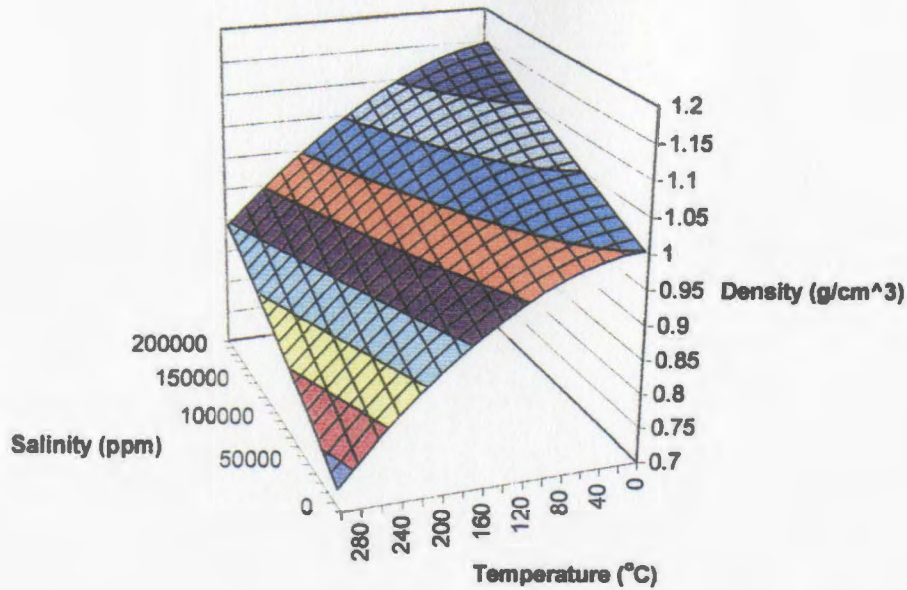
Figure 2.8. *Brine density at 40 MPa as a function of temperature and salinity. From Wright (1999).*

salinity of 50,000 ppm, and a pore pressure of 40 MPa, a brine density of 1.04 g/cm^3 is determined by these relationships. A salinity of 50,000 ppm is estimated from mixing the injected seawater which has a salinity of approximately 35,000 ppm (USGS, 2003) with the brine in the Hibernia reservoir pores which has a higher dissolved salt concentration of 108,000 ppm (Wright, 1999). Injected seawater (at between 0-15°C) will initially have a much lower temperature than the reservoir, so there will be a trend to cool the rocks slightly while increasing the temperature of the water. As the variation in seismic properties of the water is relatively small over this temperature range, the modeling in this study assumes a pore temperature of between 90 and 100 degrees Celsius, which is the more conservative case, as a decreased brine temperature increases slightly the acoustic impedance contrast between the injected brine and oil.

Relationships describing the acoustic velocity of brine are largely based on empirical

datasets. Helgeson and Kirkham (1974) assembled a sizeable amount of data to

calculate the physical properties of water over given temperature and pressure ranges.

Batzle and Wang (1992) used these calculations to solve for the acoustic velocity of pure

water (V_W) as a function of pressure and temperature as shown in figure 2.9.
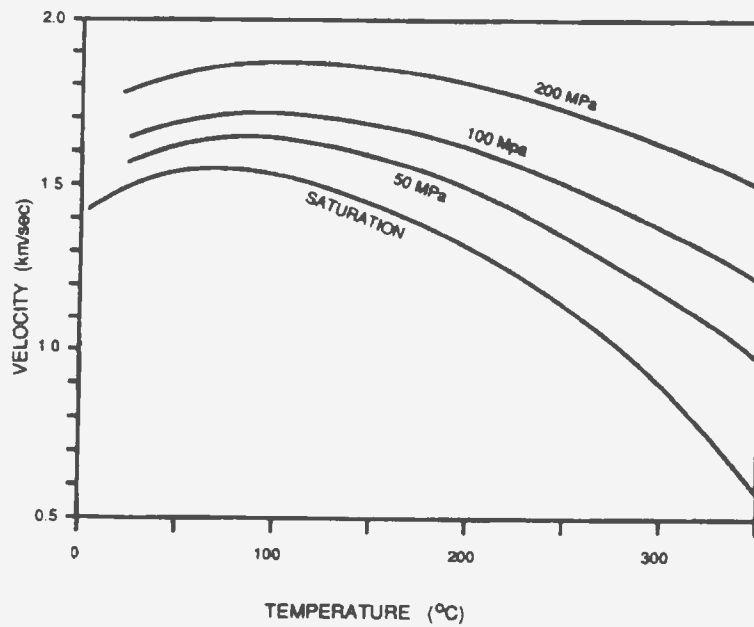
Figure 2.9. *The acoustic velocity of pure water as a function of pressure and temperature. From Batzle and Wang (1992).*

Batzle and Wang (1992) introduce a statistical velocity regression that extends the pure

water velocity (V_W) relationship (figure 2.9) to solve for the acoustic velocity of brine

(V_B).

$$V_B = V_W + S(1170 - 9.6T + 0.055T^2 - 8.5 \times 10^{-5}T^3 + 2.6P - 0.0029TP - 0.0476P^2) + S^{1.5}(780 - 10P + 0.16P^2) - 1820S^2 \qquad (2.18)$$

27

The above relationship indicates an increase in velocity for increasing salinity. Using typical Hibernia reservoir values, a pure water velocity is determined to be approximately 1600 m/s (figure 2.9), and equation 2.18 yields a brine velocity of 1690 m/s, and coupled with the density, a fluid bulk modulus of 2.97 GPa is determined (equation 2.8).

The pore fluid property determination is largely empirical, but fairly robust as the relationships summarized by Batzle and Wang (1992) are based on a voluminous amount of data. By examining the fluid properties alone, which are summarized in table 2.2, some general observations can be noted. As expected, the density, velocity, and bulk modulus increase moving from gas through oil to water. It is notable that there is greater fluid compressibility change seen in the bulk modulus ratio for a complete water flood compared to a full gas flood. This is due to the fact that the compressibility of gas and high GOR oil are very similar, since dissolved gas makes fluid very compressible, compared to water that contains no gas component.

Fluid	Density	Velocity	Bulk Mod. (K)	Impedance (AI)
	g/cm3	m/s	GPa	g/cm3*m/s
Gas	0.25	665	0.11	166.25
Oil	0.6	890	0.48	534
Brine	1.04	1690	2.97	1757.6
Ratios				
Oil/Gas	2.40	1.34	4.30	3.21
Brine/Oil	1.73	1.90	6.25	3.29

Table 2.2 *Summary fluid property data for gas, water, and brine for the Hibernia reservoir. This is pore fluid property data only, not fluids in porous reservoir rocks – which will be discussed in later sections. For a full pore fluid saturation change (ie. 100%), there is a greater change in the bulk modulus for brine replacing oil (6.25) compared to gas replacing oil (4.3). The acoustic impedance ratios of the two injecting pore fluids to oil are very similar ranging from 3.2 for gas-oil to 3.3 for brine-oil.*

28

The numbers displayed in table 2.2 are for bulk properties where one fluid makes up the entire pore fluid composition. In real oil reservoirs, initial oil and residual oil saturations are rarely if ever 100% and 0% respectively so it is important to consider the physical properties of intermediate cases where the bulk pore fluid is a mixture of the different reservoir pore fluids.

2.3.4 Pore fluid mixtures

In the previous three sections, the physical properties of gas, oil, and water in the Hibernia reservoir were calculated. This section, outlined below in the 4D seismic modeling workflow in figure 2.10, presents methods of calculating the bulk properties of various mixtures of these three pore fluids.
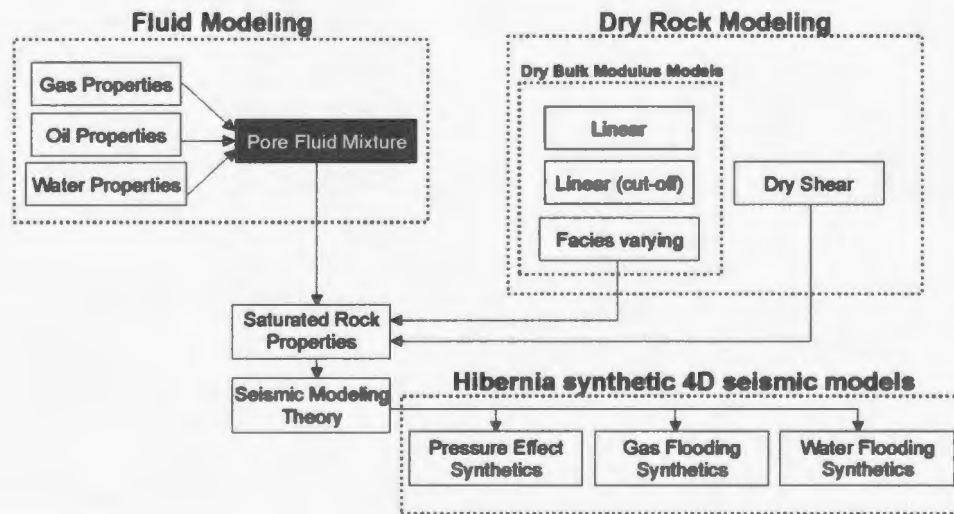
Figure 2.10. *Hibernia 4D seismic modeling workflow, with the section on pore fluid mixtures highlighted.*

The 4D seismic method is primarily utilized to monitor hydrocarbon recovery, a process which is often enhanced by gas and/or water injection. Mixtures of pore fluids can exist at the initial pre-production stage where there is some connate water in the pores (Wardlaw, 2002), during secondary oil recovery processes such as gas or water flooding, and during special reservoir situations where the pore pressure drops below bubble point and gas is exsolved from the oil solution (Batzle and Wang, 1992).

30

The density of a fluid mixture (ρ_f) is simply the volume weighted average of the constituent densities, and is represented as:

$$\rho_f = f_1\rho_1 + f_2\rho_2 \quad , \quad (2.19)$$

where f_1 and f_2 are the volume fractions of fluids 1 and 2, and ρ_1, ρ_2 are their respective densities. The total volume of the mixture ($\overline{V}_f$) is simply the sum of the component volumes $\overline{V}_1$ and $\overline{V}_2$. To calculate the modulus of the fluid mixture, one may assume that the pressures in the two phases are always equal (Batzle and Wang, 1992). In other words, the increase in pore pressure from the passage of a seismic wave must equilibrate to each constituent fluid phase (Dvorkin, 1999). The change in volume of a component of the fluid mixture is a function of the change in pressure (Batzle and Wang, 1992) as follows:

$$d\overline{V}_1 = (-\overline{V}_1\beta_1\partial P)_S = \left(\frac{\overline{V}_1}{K_1}\partial P\right)_S \quad , \quad (2.20)$$

where K_1 is the adiabatic bulk modulus and β_1 the compressibility of fluid component 1. Therefore for a fluid mixture, the iso-stress (Reuss) (Dvorkin et al., 1999) bulk modulus of the fluid (K_f) is given as (Batzle and Wang, 1992):

$$\frac{1}{K_f} = \frac{1}{\overline{V}_1 + \overline{V}_2}\frac{1}{\partial P}\left(\frac{\overline{V}_1}{K_1}\partial P + \frac{\overline{V}_2}{K_2}\partial P\right) \qquad (2.21)$$

$$= \frac{f_1}{K_1} + \frac{f_2}{K_2} \qquad (2.22)$$

31

This is also known as Wood's equation (Batzle and Wang, 1992). The relationship in equation 2.22 is often referred to as the homogenous fluid mixing equation where each pore of the "pore space" is assumed to have the same mixture and distribution of pore fluids.

While the Wood's equation is commonly used in fluid substitution modeling, a number of authors have suggested that for some reservoirs the homogeneous mixing of pore fluids is an invalid assumption. Domenico (1976) suggested calculating the heterogeneous fluid mixing modulus from the iso-strain Voigt average given as (Dvorkin, 1999):

$$K_f = f_1 K_1 + f_2 K_2 \qquad (2.23)$$

The relationship in equation 2.23 is often used when describing fluid mixtures that have so-called "patchy" saturations (Mavko and Mukerji, 1998). The iso-strain Voigt average (equation 2.23) and the iso-stress Reuss average (equation 2.22) are considered to be the upper and lower bounds of the fluid mixing moduli relationships.

In the preceding paragraphs, I have outlined two models for the determination of pore fluid mixtures: (1) a homogeneous (Reuss) fluid mixing model (equation 2.22); (2) and a "patchy" (Voigt) fluid mixing model (equation 2.23). I use the method presented by Dvorkin et al. (1999) to determine the optimal model to use for Hibernia pore fluid mixing modeling. This method is a first principles application of assuming one model (uniform or patchy) to forward model the well log data to get seismic properties

(velocity, density) and comparing those calculated properties with the measured well logs. The assumed model that best fits the well log data, likely reflects the distribution of pore fluids in the interval studied (Dvorkin et al., 1999). This method is tested on a couple of Hibernia wells for which P-velocity, S-velocity, and density logs are available. Due to the high bulk modulus of the dry rock frame compared to the pore fluid component in the Hibernia reservoir, there was not any appreciable difference in the data-model comparison between the homogeneous and patchy mixing models. This is not to say conclusively that there is not a difference in these models or that the Hibernia data reflects an intermediate solution. It does however indicate that the noise levels in the well log data and the relatively small differences in patchy/homogeneous velocity precludes this type of quantitative determination.

With a quantitative solution to the optimal fluid mixing model not possible given the data quality, an attempt is made to intuitively determine the appropriate model. The iso-stress Reuss model is appropriate if the pore fluids are uniformly mixed so that the pore pressure in each phase has time to diffuse and equilibrate during a seismic period. The scale at which such an assumption is appropriate is a function of the permeability/porosity, fluid bulk modulus, and seismic frequencies (Dvorkin et al., 1999) The high average permeability of 640 mD (CNOPB, 1997), the relatively good porosity (15-25%), and the fairly low (20-25 Hz) seismic frequencies indicate that the wave-induced increments of pore pressure in each fluid phase are more likely than not to

33

equilibrate during a seismic period, and as such, the homogeneous model (Reuss/Woods) will be used for pore fluid mixing in this research.

The numerical results for single phase pore fluids in the Hibernia reservoir were discussed in sections 2.3.1-2.3.3. Figure 2.11 illustrates the Hibernia modeled variation in fluid mixture bulk modulus as a function of oil-gas and oil-water saturation for both the Voigt and Reuss (Wood's) models. As mentioned above, the Reuss model (Wood's equation) is chosen for this study. In the oil-water fluid mixture bulk modulus plot (figure 2.11 – right), it is interesting to note that using the homogenous mixing model of Reuss, a small amount of oil in the system (10%) reduces the fluid modulus from 3 to 2 GPa or by approximately 33%. This is due largely to the high GOR found in Hibernia crude, so only a small amount of gassy (live) oil is required to significantly reduce the bulk modulus of the water saturated system. In the gas-oil curve, as the oil already has a high amount of dissolved gas (high GOR), the addition of a small amount of gas in the system fails to reduce the modulus on the same scale as does the introduction of gassy oil into the brine dominated system. This effect can also be seen in the velocity curves for the fluid mixtures seen in figure 2.12. The shape of the upper and lower bounds have different character than the bulk modulus curves due to the contribution of fluid mixture densities (equation 2.8, 2.19) which are linear. Through modeling that appears in later sections, when the bulk rock is considered (dry rock and fluid component combined), the velocity difference for various saturations between the Reuss and Voight model is demonstrated to be a maximum of approximately 1%, a relatively small quantity.
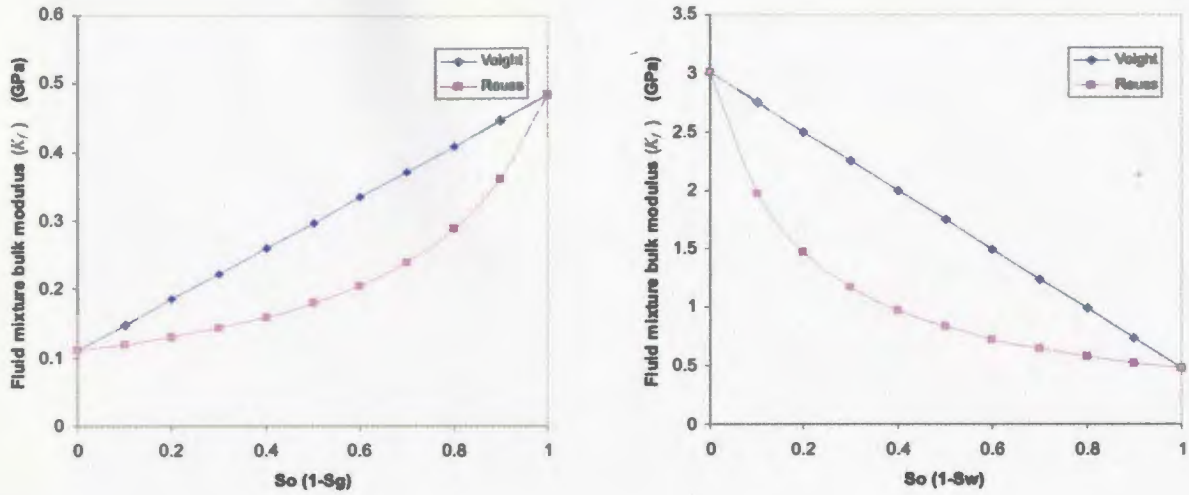
Figure 2.11. *Pore fluid mixing model showing fluid bulk modulus as a function of oil saturation in an oil-gas mixture left, and oil saturation in a oil-water mixure right. The upper bounds indicated by the patchy saturation model of Voigt, is indicated in the blue, while the lower bounding homogeneous mixing model of Reuss is indicated in pink. The Reuss homogeneous mixing model is chosen for the Hibernia 4D modeling study.*
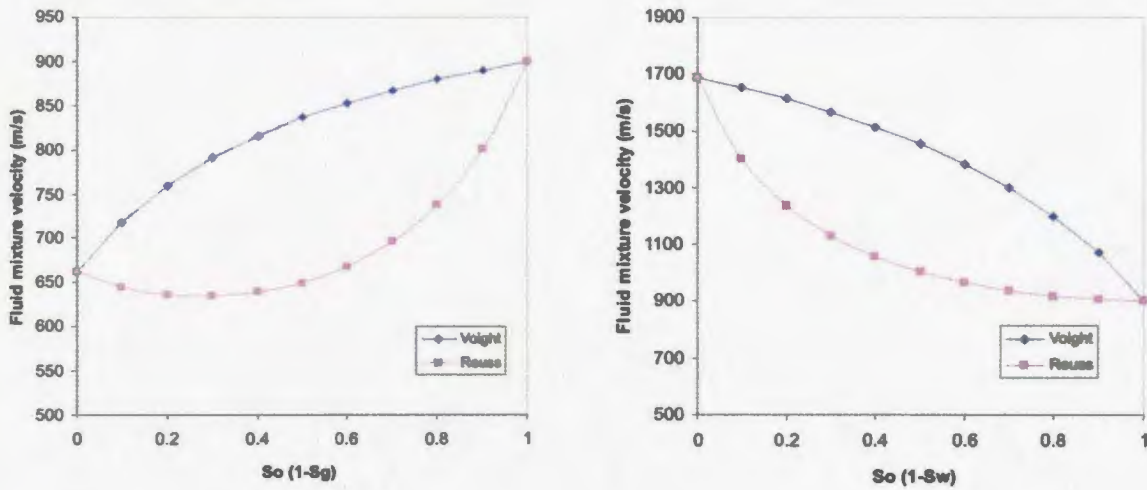
Figure 2.12. *Pore fluid mixing model showing fluid mixture velocity as a function of oil saturation in an oil-gas mixture left, and oil saturation in a oil-water mixure right. The upper bounds indicated by the patchy saturation model of Voigt, is indicated in the blue, while the lower bounding homogeneous mixing model of Reuss is indicated in pink. The Reuss homogeneous mixing model is chosen for the Hibernia 4D modeling study.*

35

The velocity of the gas-oil fluid mixture (Reuss) gives the counter intuitive result that from full gas saturation to 70% gas saturation-30% oil saturation the velocity of the fluid mixture decreases. This can be attributed to the effect of the volume weighted fluid mixture density in the denominator of equation 2.8 when solving for velocity.

The pore fluid physics discussed in this section has been independent of any rock properties. The next section presents the results of the Hibernia dry rock physics modeling. I examine a number of elements of dry rock physics, particularly how the properties of the rock matrix (bulk modulus, shear modulus, density) may vary with porosity, facies, and pore pressure. The pore fluid physics model calculated in this section is then added to the dry rock model to produce a saturated rock model from which synthetic 4D seismic data can be generated.

2.4 Dry rock physics modeling

With the pore fluid properties for Hibernia determined, the independent dry rock properties are needed to create a saturated rock model that can be used for 4D seismic modeling (figure 2.13).
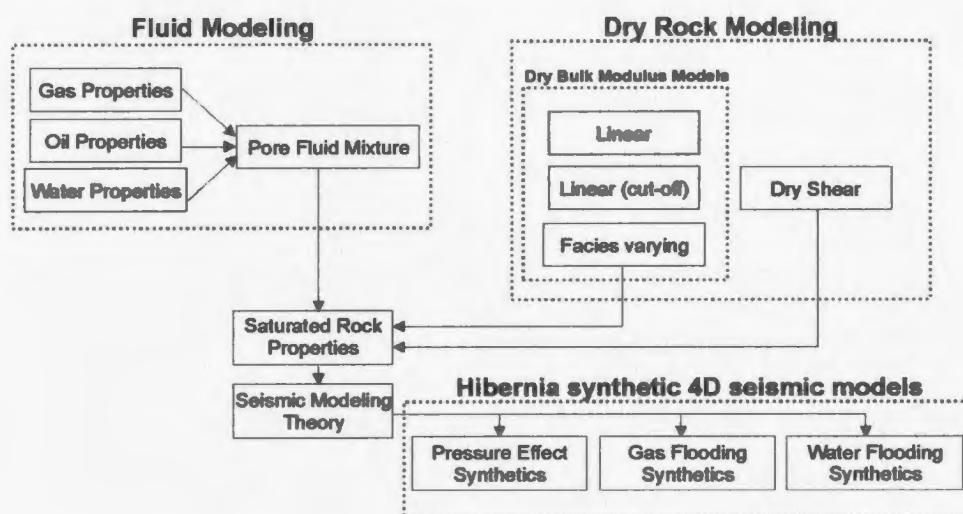
Figure 2.13. *Hibernia 4D seismic modeling workflow.*

The accurate determination of the dry bulk (K_{dry}) and shear (G_{dry}) moduli is a key element in the 4D seismic modeling and inversion process. In the rock physics literature, a number of different relationships have been presented that attempt to describe the variation of K_{dry} and G_{dry} with parameters such as porosity and pressure. Many of these relationships are based on data originating from core rock physics measurements and well log analysis (Wang et al, 1989).

Using available Hibernia data, I present an original method for fitting bulk and shear modulus data for the case where there are two primary rock types, sand and shale, with distinctive elastic moduli. Using this method, I attempt to fit all of the porosity and pressure data simultaneously with a single equation that accounts for the different grain moduli of sand and shale. This method is appropriate for the Hibernia reservoir example because there are two primary rock types (sand and shale) that have a continuous, gradational relationship with respect to grain size and porosity.

2.4.1 Background

The dry bulk/shear moduli as a function of effective pressure are commonly determined by fitting core/log data with a logarithmic or polynomial model as shown in figure 2.14 (Wang et al., 1989; Lumley, 1995; Meadows et al, 2002). In this method, individual cores are usually given a single porosity value, and their dry moduli as a function of pressure fit (polynomial or logarithmic) is input into the rock physics modeling process.

Lab Measured Dry Bulk Modulus
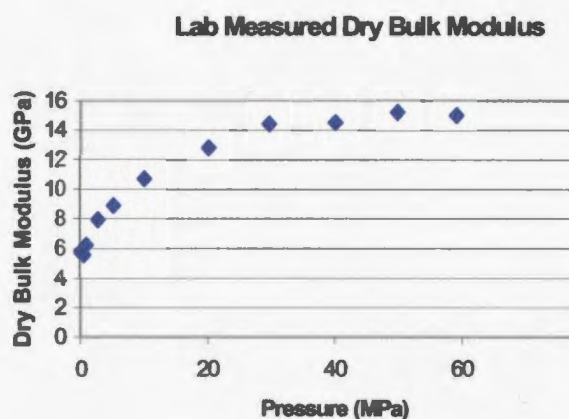
Figure 2.14. *The logarithmic relationship between effective pressure (Overburden Pressure – Pore Pressure) and dry bulk modulus for a given Hibernia rock sample (Hibernia, 2000).*

Once a dry modulus vs. pressure relationship is defined, consideration can be given to the variation of the dry moduli with porosity or facies. By collecting an array of measurements from a variety of cores with different facies/porosity values, one can establish a number of individual moduli-pressure relationships to be used for clusters of similar facies/porosity rocks (Lumley, 1995; Meadows et al., 2002). This can be done a number of ways including averaging the individual moduli/pressure fits based on facies, or assuming that the dry modulus varies as a function of porosity. Similar to the iso-strain Voigt relationships, these moduli-porosity relationships at a constant pressure can be in a linear form, like (Nolen-Hoeksema, 2000):

$$K_{dry}(\phi) = K_{gr} - a\phi \quad (2.24)$$

$$G_{dry}(\phi) = G_{gr} - b\phi \quad (2.25)$$

where K_{dry} and G_{dry} are the bulk and shear dry moduli respectively, K_{gr} and G_{gr} are the bulk and shear grain moduli respectively, ϕ the porosity, and a and b determined empirical parameters.

In this thesis, I am proposing a facies dependent moduli-pressure method (section 2.4.5) that attempts to fit pressure, porosity and dry modulus for sandstone and shale facies simultaneously in one relationship. This single dry modulus equation approach is designed to be integrated into a 4D seismic modeling workflow (Lumley, 1995; Meadows et al., 2002), including a reservoir model with time varying pressures and

39

saturations. As this method concentrates on the dry rock properties, I will discuss them at length in this section.

The method assumes:

- the relationship between dry modulus and pressure is logarithmic as seen in a number of studies including: Wyllie et. al (1958); Landro (2001); and Meadows et al. (2002).

- there are two facies (i.e. sand and shale) that have a continuous function between them (e.g. Vshale which is the fractional volume of shale and is usually calibrated from a gamma ray log on a scale from 0 to 1 with 1 being 100% shale content). This is demonstrated for the Hibernia reservoir in figure 2.13 and 2.14.

- the relationship between dry modulus and porosity is linear for a given facies end member. Presented as the Voigt model in Nolen-Hoeksema (2000).

2.4.2 Sand-shale facies relationship

To lay the foundation for this formulation, I first examine the characteristics of the individual rocks. Figure 2.15 shows four thin section photos of Hibernia reservoir core data, ranging from low porosity (primarily shale with very fine grained sandstone and siltstone) to higher porosity medium grained sandstone. The lower porosity rocks have smaller grain size, less quartz (white material on thin section), and more grain boundaries. The higher porosity rocks have larger grain size, are almost exclusively quartz, and have a far lower number of grain boundaries per unit volume. As is discussed in the following sections, these physical characteristics partially determine how the dry moduli of these rocks vary with porosity and pressure.

$\phi = 2\%$ $\phi = 8\%$

$\phi = 17\%$ $\phi = 23\%$
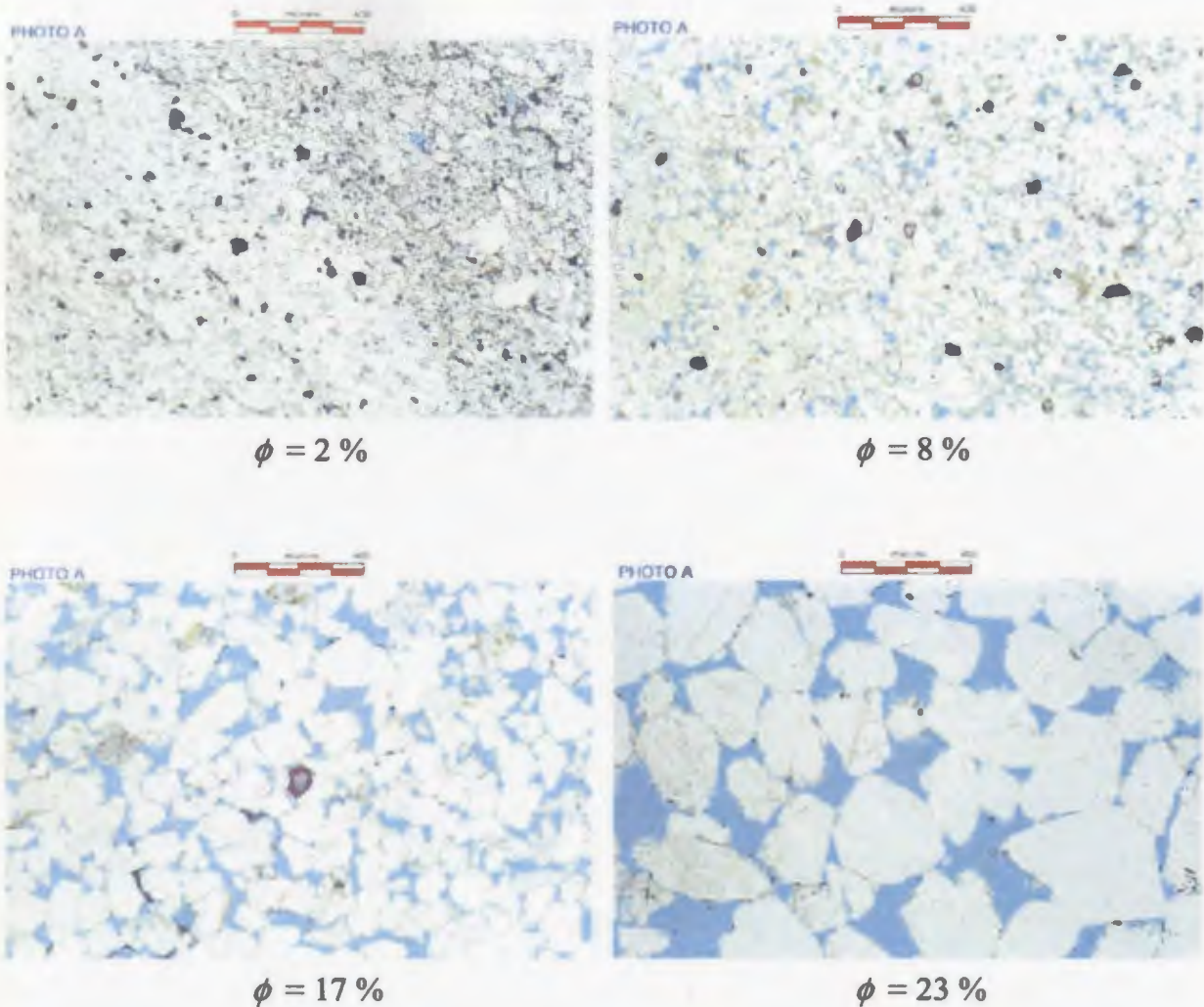
Figure 2.15. *Thin sections from the Hibernia reservoir at different porosity values (ϕ) ranging from 2% to 23%. All images are scaled the same, the bar at the top of each image is from 0 to 400 microns. The different sections clearly show the increasing grain size and decreasing number of grain boundaries with increasing porosity.*

As seen in figure 2.15, the porosity value which is seen in many reservoir models can also act in some way as a facies discriminator. A generalization could be lower porosity rocks are more shaly and the higher porosity samples are composed primarily of quartz

41

rich sand grains. Figure 2.16 is generated by plotting a Vshale (volume of fraction of shale) well log against porosity in a number of Hibernia wells at the reservoir level.
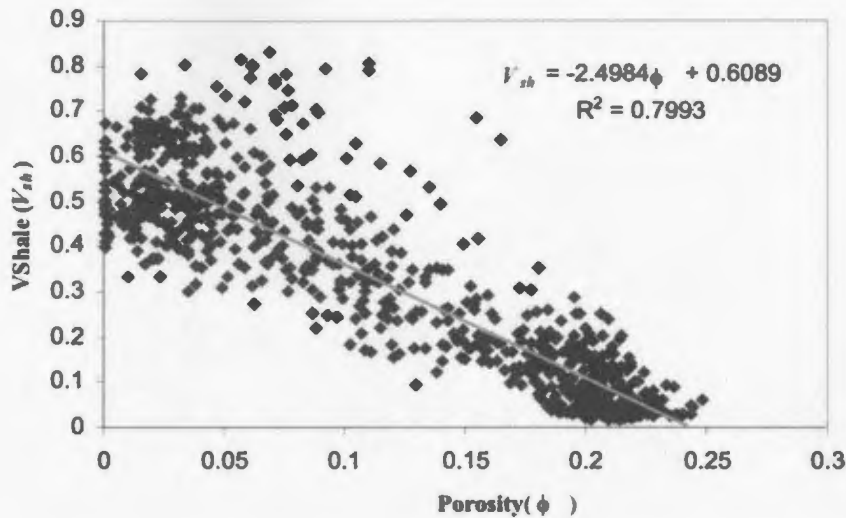
Figure 2.16. *Vshale as a function of porosity showing increasing shale content with decreasing porosity, a result that is consistent with the thin section images in figure 2.15.*

The relationship between porosity and Vshale shown in figure 2.16 is consistent with the trend that is demonstrated in the thin sections (figure 2.15). Near zero porosity, there is a breakdown of approximately 60% shale, 40% sandstone grains (quartz). In the higher porosities, the matrix is almost exclusively quartz rich, sand-sized grains. In the Hibernia reservoir, sandstone has a higher grain modulus (both bulk and shear) than the shale.

Using these conceptual ideas from the Hibernia geology as background, I present three possible models for the determination of Hibernia dry bulk modulus as a function of pressure and porosity. These models are compared against dry rock data from Hibernia

rock physics core analysis (Hibernia, 2000) and well log data for which the dry bulk modulus has been approximated. The rock physics data, which were acquired over a pressure range of 5-60 MPa, are available for a number of higher porosity samples. For the lower porosity samples, well log data including P-sonic, S-sonic, and density logs were calibrated and used to approximate a dry bulk modulus in three Hibernia wells. For each of the models presented a graph giving a description of the model and a plot evaluating the quality of the fit on the core and well log data is given.

2.4.3. Dry rock model #1: Linear, single facies

The first dry bulk modulus model I discuss varies linearly with porosity and logarithmically with pressure and is highlighted in the 4D seismic workflow chart in figure 2.17.
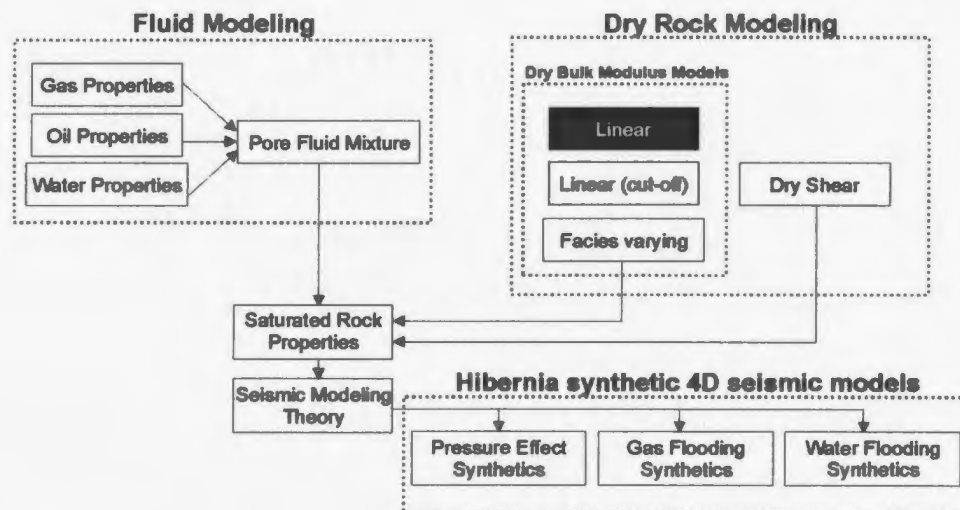
Figure 2.17. *Hibernia 4D seismic modeling workflow, with the first dry bulk modulus model (Linear in porosity) highlighted.*

Because dry bulk modulus increases logarithmically with pressure (figure 2.14), and decreases with porosity, the two variables pressure and porosity can be combined to create a single two variable function (original to this thesis) to fit dry bulk modulus. This relatively simple model ignores the relationship between facies and porosity established in the previous section, and assumes that low porosity rocks are low-porosity quartz sandstones and not shales. Figure 2.18 demonstrates such a function, which is fit using only Hibernia core rock physics data. The well data is not used in this model because this model assumes a single facies across all porosities (in this case sandstone); therefore only sandstone measurements are utilized, and extrapolated from the regression
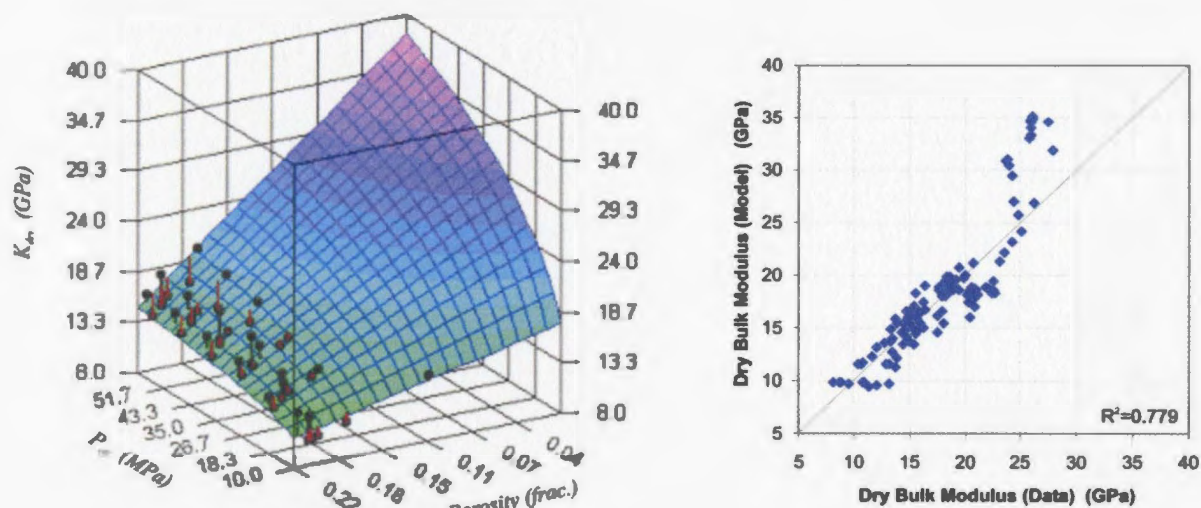
Figure 2.18. *Hibernia reservoir rock physics data dry bulk modulus as a function of effective pressure (logarithmic) and porosity (linear). While only the sandstone core data points were used in the fitting of the function, all of the data is used to determine how well the model predicts dry bulk modulus (right). The data prediction graph (right) demonstrates that the model over-predicts dry bulk modulus in lower porosities or regions of high dry bulk modulus.*

to lower porosities. The model is represented in the form:

$$K_{dry} = A(\phi)\ln\big[B(P_{eff})\big] + C(\phi) \quad , (2.26)$$

which is linear in porosity (ϕ) and logarithmic in pressure (P_{eff}) with A, B, and C being determined parameters.

As shown in figure 2.18, the data points are from good quality reservoir sandstones in the porosity range of 16-23%. Due to software limitations, it is not possible to plot the well log data points if they are not used in the fitting, but all of the data (core and well) points are displayed in the fitting graph (right) in figure 2.18. The linear fit in porosity is extrapolated back to zero percent porosity over a range of effective pressures. At 50 MPa effective pressure, the approximate Hibernia reservoir value, the K_{dry} zero porosity intercept is about 37 GPa. This value is close to the estimated grain modulus of the quartz grains of 40 GPa (Mavko et. al, 1998). The large deviation in K_{dry} with pressure at low porosities may possibly be attributed to the higher number of softer grain boundaries at lower porosities due to the absence of pore space and decreasing grain size, but it is difficult to characterize due to the lack of data at low porosities. Because the dry bulk modulus dependence on porosity is linear, the model assumes that lower porosity rocks are the same composition (~95% quartz) as the higher porosity reservoir rocks. However, from the thin sections (figure 2.15), and the VShale-porosity relationship seen in figure 2.16 lower porosity facies clearly have higher shale content. Because the model erroneously assumes a quartz rich composition at lower porosities, it over predicts the

45

bulk modulus in lower porosity, high bulk modulus samples that in the Hibernia reservoir are shale rich.

2.4.4 Dry rock model #2: Linear, shale cut-off

The second model I discuss attempts to address the over-prediction of bulk modulus in the lower porosities by introducing a shale cut-off porosity value below which the rocks are treated as a different facies. This second dry bulk modulus model is highlighted in the 4D seismic modeling workflow chart in figure 2.19.
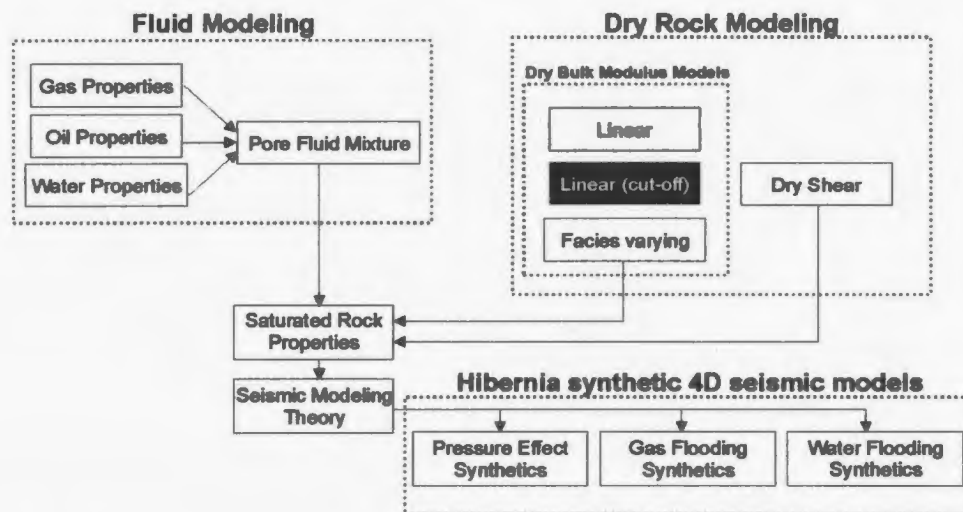
Figure 2.19. *Hibernia 4D seismic modeling workflow, with the second dry bulk modulus model (Linear in porosity with a shale cut-off) highlighted.*

Figure 2.20 demonstrates this idea using the linear relationship in porosity for a given effective pressure level. Moduli values below the porosity shale cut-off value (in this case 5%) are set at a fixed shale value, while dry rock moduli above this cut-off value

46

follow the linear trend in porosity, logarithmic in pressure as per model #1. While this method addresses the end members adequately, in the Hibernia case there is the possibility of a discontinuity in the dry rock modulus function. If in the case shown in figure 2.20, the shale cut-off porosity value chosen doesn't equal the porosity at which the shale cut-off modulus and sandstone modulus lines intersect, a discontinuity in the function will occur. As a result, rocks that have very similar porosities that fall on either side of the cut-off will be assigned appreciably different dry bulk moduli. While the fit of the data is better than the linear model, the discontinuity of the shale cut-off function can lead to "spiky" behavior in the modeled velocities as is demonstrated in section 2.4.6.
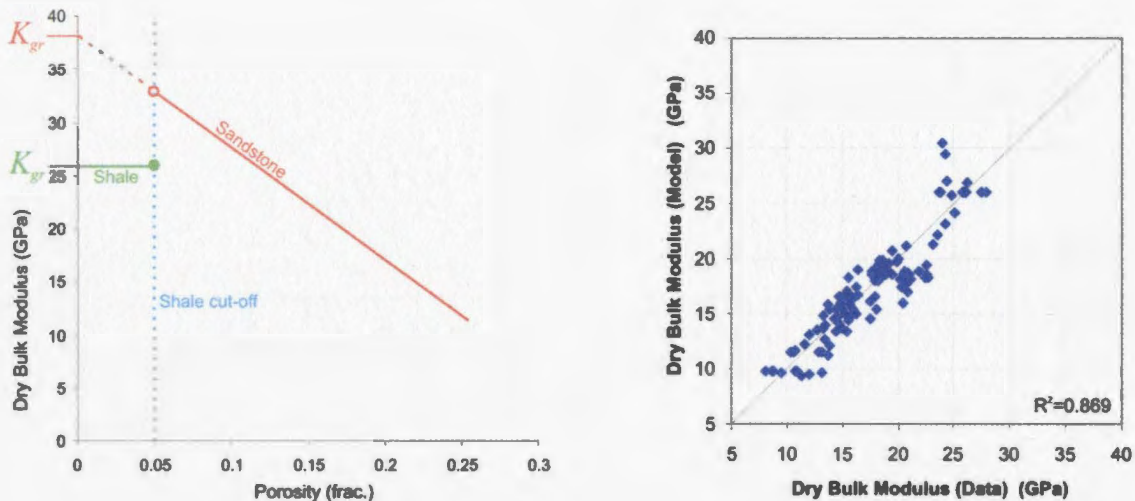
Figure 2.20. *Shale cut-off dry rock modulus model for a constant effective pressure (50 MPa) . The shale cut-off in this case is 5% porosity, under which the rock is assumed to have a constant shale or non-reservoir value. While the fit of the data is better than the linear model, this cut-off can lead to "spiky" behavior in the modeled velocities.*

2.4.5 Dry rock model #3: Facies-varying model

Given the variation of facies in the Hibernia reservoir with changing porosity, a dry rock moduli model which accounts for this change is desired. This section presents an original model that given pressure and porosity inputs, yields both a dry rock bulk modulus (K_{dry}) and facies dependent grain modulus (K_{gr}). The location of this model in the 4D seismic modeling flow is given below in figure 2.21.
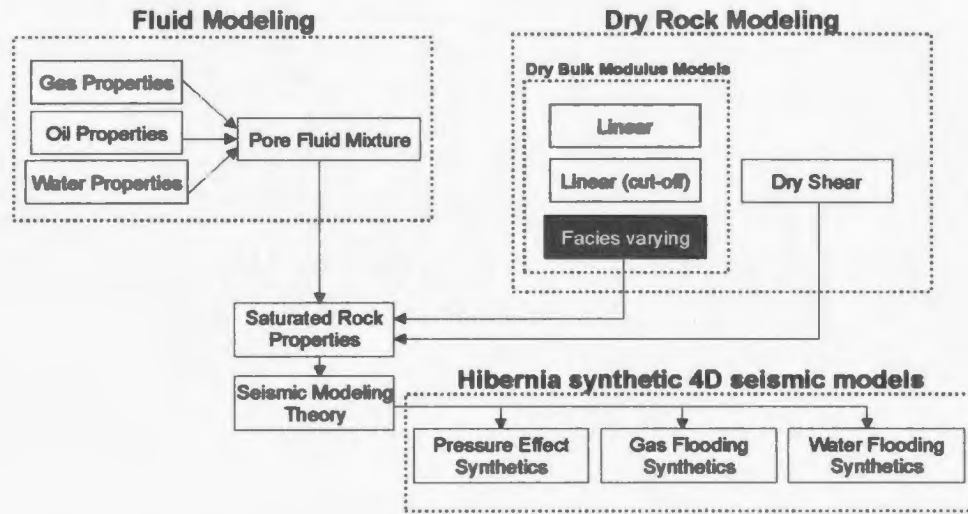
Figure 2.21. *Hibernia 4D seismic modeling workflow, with the third and final dry bulk modulus model (facies-varying) highlighted.*

For this method, the dry modulus - effective pressure relationship varies logarithmically as before. However, dry modulus - porosity now changes as a second order polynomial or parabolically. The proposed model has an equation in the form of:

$$K_{dry}(P_{eff},\phi) = aP_{eff}{}^{b}\phi^{2} + c\ln(dP_{eff}) + e \quad , \quad (2.27)$$

48

where *a, b, c, d*, and *e* are extracted parameters from a fitting of the dry rock moduli data as a function of effective pressure (P_{eff}) and porosity (ϕ).   The relationship is written so that the partial derivative with respect to porosity is linear in porosity:

$$\frac{\partial K_{dry}}{\partial \phi} = 2aP_{eff}^{\ b}\phi \quad . \ (2.28)$$

Evaluated at zero porosity, the dry rock modulus function is horizontal in porosity as shown by:

$$\frac{\partial K_{dry}}{\partial \phi}(0) = 0 \quad . \ (2.29)$$

The grain modulus is determined from equations 2.27 and 2.28 by finding the intercept of the partial derivative of the dry rock modulus function at zero porosity as:

$$K_{gr}(\phi) = K_{dry} - \frac{\partial K_{dry}}{\partial \phi}\phi \quad . \ (2.30)$$

Graphically, the relationship between dry rock and inverted grain modulus for this model is shown in figure 2.22.

The rationale behind this polynomial variation in porosity has its basis in the variation in rock composition (sand-shale) with changes in porosity. This model with its equation shown in equation 2.28 has a partial derivative that is linear in porosity.   This yields a number of linear porosity-dry moduli relationships for different rock compositions in the form of equation 2.24 as shown in figure 2.22 as the tangents to sample points R1, R2,

49
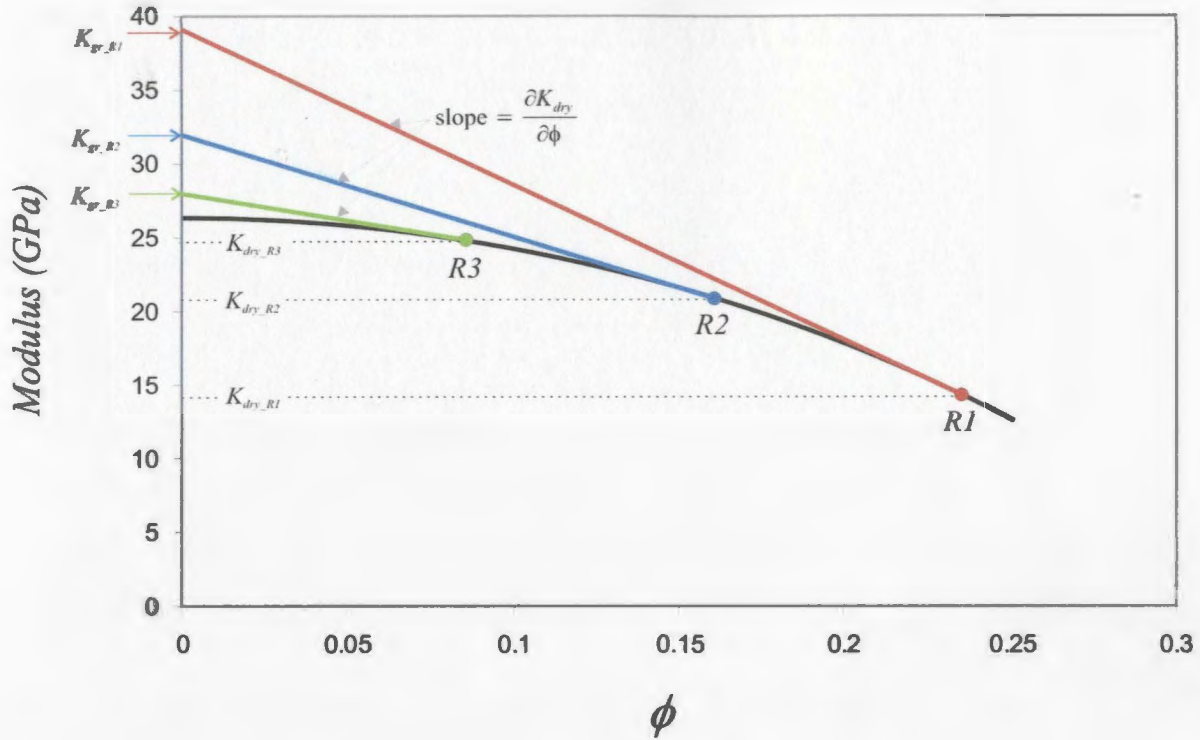
Figure 2.22. *The facies-varying dry bulk modulus – porosity model at a constant pressure (50 MPa). The black parabolic curve is the dry bulk modulus. The red, blue, and green lines are tangents to this curve taken at the sample points R1, R2, and R3. The zero porosity intercept of these lines are used as the grain modulus, such as K_{gr_R1}. As shown the dry rock modulus decreases smoothly with increasing porosity, while the inverted grain modulus increases representing the shift from shale to quartz sandstone.*

and R3. For example, R1 is a sandstone end member composed primarily of quartz grains (see figures 2.15 and 2.16). As such, its inverted grain modulus (K_{gr_R1}) is fairly high. The intermediate R2 (~ 16% porosity) is still primarily sandstone, but has a higher shale content (figure 2.16) and a resulting lower grain modulus (K_{gr_R2}).

These models can now be used to fit existing Hibernia rock physics and well log data. In figure 2.23 the facies-varying model (equation 2.27) is used to fit the Hibernia rock physics data which are primarily the points from 5-60 MPa and varying from 15 to 25%

porosity. In addition, well logs are now used to acquire data for the more shaly portions of the reservoir, which can be accommodated in the facies-varying model. The line of data points at 50 MPa effective pressure running from 0 to 20% porosity are estimated values of K_{dry} calculated from multi-well log measurements in the Hibernia reservoir.
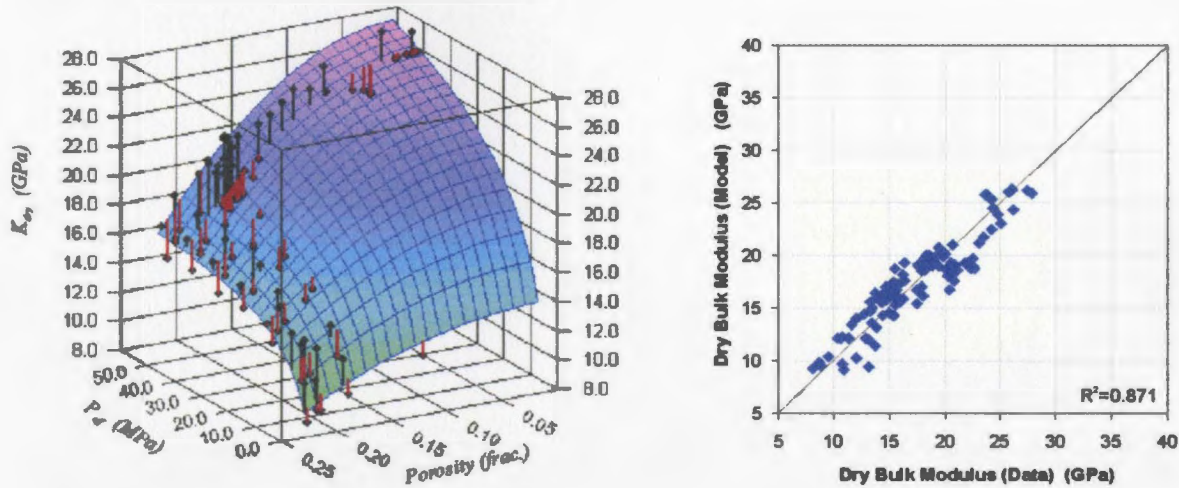
Figure 2.23 *Facies-varying dry bulk modulus model derived from effective pressure and porosity. Hibernia rock physics data which are primarily the points from 5-60 MPa and varying from 15 to 25% porosity. The line of data points at 50 MPa from 0 to 20% porosity are values of K_{dry} inverted from multi-well log measurements in the Hibernia reservoir. The model has a fairly good correlation with the data points for regions where data is available.*

2.4.6 Dry bulk modulus model validation

The best way to examine the validity of a model is to test its accuracy against real measurements. In this section, the three dry bulk moduli models outlined in the previous sections: linear, shale-cutoff and facies-varying, are tested against velocity well logs from 2 different Hibernia wells. This is accomplished by using actual well logs to saturate the

51

numerical dry rock model. The well logs used include temperature, pore pressure, fluid saturation, porosity, and density. The calculated P-wave velocity can then be compared to the P-wave sonic log measured in the well to check the accuracy of the dry bulk modulus model. As the dry rock modulus is much larger than the oil modulus, errors in oil modulus computation are relatively small.

The Gassmann equation (Gassmann, 1951; Berryman, 1999; Dvorkin et al., 1999) provides a means for computing approximate reservoir rock velocities. The isotropic, no fluid viscosity, and low frequency assumptions of the Gassmann equation are considered to be reasonable for this case. For my purposes this is a three step process, first solving for saturated bulk modulus (K_{Sat}):

$$K_{sat} = K_{gr} \frac{\phi K_{dry} - (1+\phi)K_f K_{dry}/K_{gr} + K_f}{(1-\phi)K_f + \phi K_{gr} - K_f K_{dry}/K_{gr}} \quad , (2.31)$$

where:

K_{dry} is the dry bulk modulus. K_{dry} is determined as described for each model.

K_{gr} is the grain modulus. For the linear and shale cut-off cases, K_{gr} is the zero porosity model intercept at 50 MPa, from figure 2.18, this would be approximately 37 GPa. For the facies-varying model, this is determined by equation (2.27) as a function of K_{dry} and porosity given again below:

$$K_{gr}(\phi) = K_{dry} - \frac{\partial K_{dry}}{\partial \phi}\phi \quad (2.32)$$

ϕ is the porosity.

K_f is the fluid bulk modulus

The saturated rock density (ρ_{sat}) can be computed as a volume weighted average of the grain density (ρ_{gr}) assumed to be a constant 2.65 g/cm^3 as determined by core and well log analysis, and the pore fluid density (ρ_f) as follows (Landro, 2001):

$$\rho_{sat} = \rho_f \phi + \rho_{gr}(1 - \phi) \quad . \quad (2.33)$$

With K_{Sat} and density determined, the velocities can be computed. First the dry shear wave modulus can be solved using the approximation $G_{Dry} \approx G_{Sat}$ as the shear modulus is relatively unaffected by pore fluid content (Dvorkin et. al, 1999):

$$G_{dry} \approx G_{sat} = \rho_{sat} V_S^2 \quad , \quad (2.34)$$

where ρ_{Sat} is the density, and V_S the shear velocity. The same shear modulus function is used for each of the three models to test the validity of the bulk modulus in looking at model variations in P-velocity output. V_p is solved by (Dvorkin et al., 1999):

$$V_P = \sqrt{(K_{sat} + \frac{4}{3} G_{dry})/\rho_{sat}} \quad . (2.35)$$

Figure 2.24 and figure 2.25 (following pages) show the P-velocity output from these three models compared to the actual P-velocity logs in two Hibernia reservoir wells.
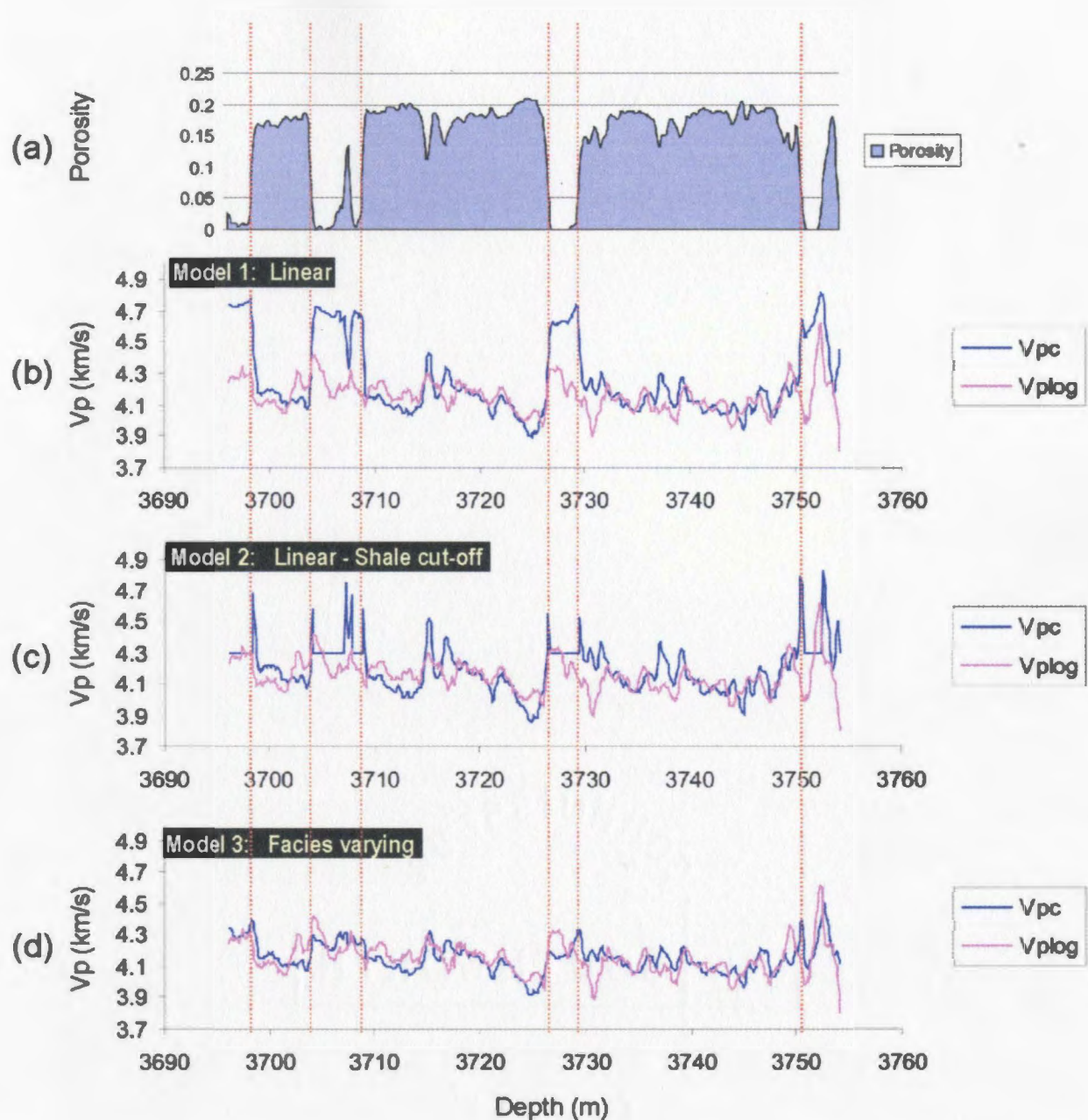
Figure 2.24. *Comparison of Vp from dry bulk modulus modeling and actual Hibernia layer 3 well logs from B-16-6. (a) The porosity log varying with depth. (b) Calculated P-velocity log (Vpc) derived from the linear in porosity dry modulus model (figure 2.16) and the actual P-velocity well log (Vplog). (c) Linear model with a 5% porosity shale cut-off with constant Vp=4.3 km/s in the shale seen as seen in figure 2.20. (d) Calculated P-velocity (Vpc) based on the facies-varying dry modulus model seen in figures 2.22 and 2.23 compared again to the actual well log.*

54
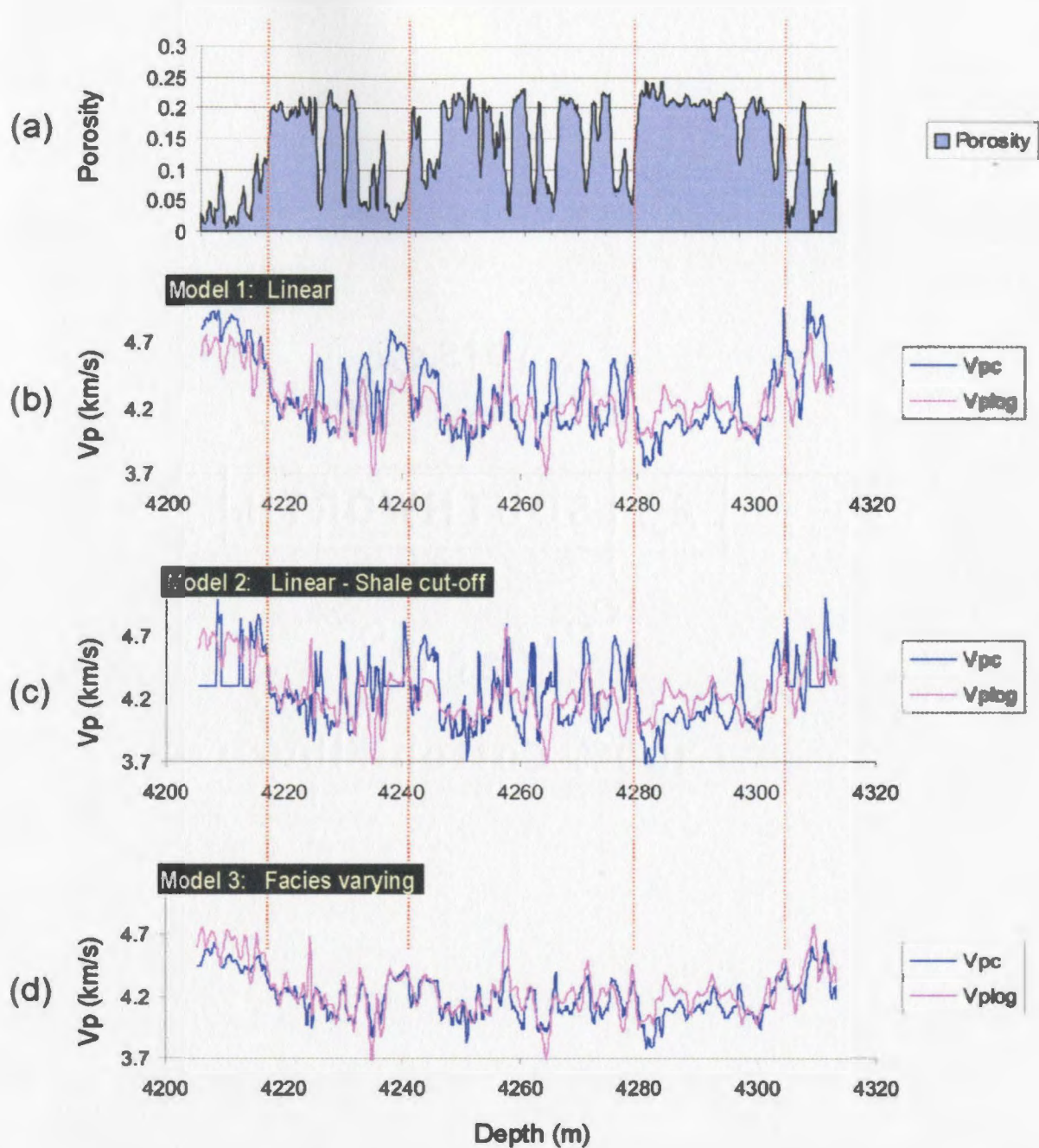
Figure 2.25. *Comparison of Vp from dry bulk modulus modeling and actual Hibernia layer 3 well logs from B-16-21. (a) The porosity log varying with depth. (b) Calculated P-velocity log (Vpc) derived from the linear in porosity dry modulus model (figure 2.16) and the actual P-velocity well log (Vplog). (c) Linear model with a 5% porosity shale cut-off with constant Vp=4.3 km/s in the shale seen as seen in figure 2.20. (d) Calculated P-velocity (Vpc) based on the facies-varying dry modulus model seen in figures 2.22 and 2.23 compared again to the actual well log.*

Comments applicable to all 3 models

The linear, shale cut-off, and facies-varying bulk modulus models are all fit as function of pressure and porosity. Rather than fitting pressure-modulus and porosity-modulus relationships independently, the multivariable nature of the fits allows for a robust over-determined dataset solved for 5 parameters from 120 datapoints. By comparison, fitting an individual pressure core, as seen in figure 2.14, results in solving for at least 2 parameters with only 10 data points. As a result, if the rock physics data can be described by an approximate porosity/facies-modulus relationship, solving for moduli as a function of pressure and porosity/facies can yield a more robust solution. In addition, by fitting the data as a function of pressure and porosity simultaneously, small decreases in porosity with pressure in the same core sample can be modeled instead of picking an average porosity value for the entire core. The following sub-sections examine the unique elements of each model.

Linear Model

The linear in porosity model adequately models the Hibernia P-velocities in good quality sandstones of about 15% porosity and higher. However, due to the linear variation with porosity, the sandstone trend is extrapolated back to the very low porosities. For these lower porosities, this model tends to over predict the velocity because the model assumes that 0% porosity is high-velocity quartz with no pore space. As seen in both the thin sections (figure 2.15) and the Vshale-porosity line (figure 2.16), it is apparent that an increase in shale content and decrease in quartz rich sandstone occurs as porosity

decreases. Consequently, in the well logs in figures 2.24 and 2.25, this model accurately predicts velocities for higher porosity sections, but in lower porosity intervals the velocity predicted can be 15-20% higher than the velocity measured in the Hibernia well logs.

Shale cut-off model

The shale cut-off model attempts to address the problems of the linear model at lower porosities. By assigning a constant shale bulk modulus to samples below 5% porosity, the problem of unrealistically high velocity shale is overcome. However, the log becomes far more "spiky" as the porosity moves from either side of the cut-off value clearly shown in the sand-shale transition areas in figure 2.24. This can be detrimental to seismic modeling and inversion as the modeled seismic trace will have artificially heightened reflectivity due to the discontinuous velocity function seen in figure 2.20.

Facies-varying Model

Of the three models examined, the facies-varying model most accurately matches the Hibernia well log results. The model appears to be as accurate in the higher porosities as in the lower porosity shaly rocks. This model assumes increasing shale content (lower grain modulus) with decreasing porosity, so the model under-predicts the velocities for lower porosity sandstones that have low shale content. While this is an issue to consider, the vast majority of the Hibernia reservoirs lower porosity rocks are primarily composed of shale.

Pressure Dependency

For the facies-varying model, the dry bulk modulus varies logarithmically with effective pressure in a manner related to the porosity. In Hibernia reservoir rocks with higher porosity, the dry bulk modulus varies less with pressure than it does in rocks with lower porosities (lower amount of hard quartz, smaller grain size, more grain boundaries). A possible explanation is that the lower porosity higher clay rocks have smaller, softer grains and more grain boundaries, allowing changes in pressure to have greater influence on the large number of grain boundaries and the softer material. The higher porosity rocks have less clay content and may be less susceptible to pressure effects as seen in figures 2.18 and 2.23, but the data coverage is too sparse to draw any definitive conclusions. It is possible that the larger, harder grains as well as a much smaller number of grain boundaries make the rock less subject to changes in modulus resulting from changes in pressure. Dry modulus data exists for only limited pressure and porosity regions in this study. As such, some of the model is extrapolated beyond known data values. While this is a concern, the greater effect of pressure in lower porosity over higher porosity rocks has been seen in other reservoirs (Meadows et. al., 2002). It is important to note that over typical reservoir production pressures of 40 to 60 MPa effective pressure, the facies-varying model is fairly well constrained by Hibernia core and well data points.

2.4.7 Dry bulk modulus summary

This research has examined the effects that pressure, porosity and facies have on the accurate determination of dry bulk modulus as part of the larger 4D seismic modeling workflow. Due to the changing facies-porosity relationship in the Hibernia reservoir, the development of a new facies-varying dry rock modulus model provides the most accurate estimation of reservoir velocities. This model integrates well into a modeling flow as it requires pressure and porosity data which is readily available from reservoir simulation models and well logs. From the input pressure and porosity, a value for dry moduli (equation 2.27) and grain moduli (equation 2.30) are predicted, allowing computation of velocities once the fluid modulus data (K_f) is added. After densities and velocities are determined, a reflectivity series can be constructed and convolved with a wavelet to generate a synthetic seismic trace. As more log and core data become available, especially in shale zones, it is possible that these models can be refined and improved.

2.4.8 Dry shear modulus

In contrast to the dry bulk modulus determination, the dry shear modulus determination is approached in this thesis from a strictly empirical standpoint due to the relatively high noise level in both shear logs and core measurements. As shown in figure 2.26, the determination of dry shear modulus is final step in the 4D seismic workflow before the calculation of a saturated rock model. The underlying assumption in this modeling is that the dry shear modulus and saturated shear modulus are approximately equal
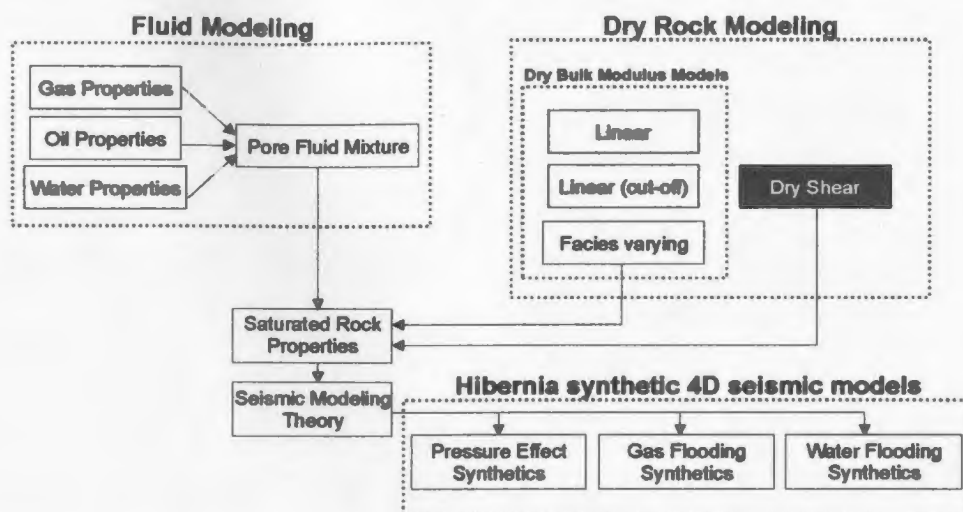
Figure 2.26. *Hibernia 4D seismic modeling workflow, with the section on the determination of dry shear modulus highlighted.*

(Lumley, 1995; Dvorkin et. al, 1999) because of the insensitivity of shear wave transmission to pore fluid content. For the Hibernia reservoir, there are both core and well log data available to use in the determination of bulk shear modulus. Figure 2.27 displays the variation of dry shear modulus (G_{dry}) with effective pressure in six different Hibernia reservoir samples. As with the dry bulk modulus, the trend is logarithmic in character, with lower effective pressures having a higher slope (G_{dry}/P_{eff}).
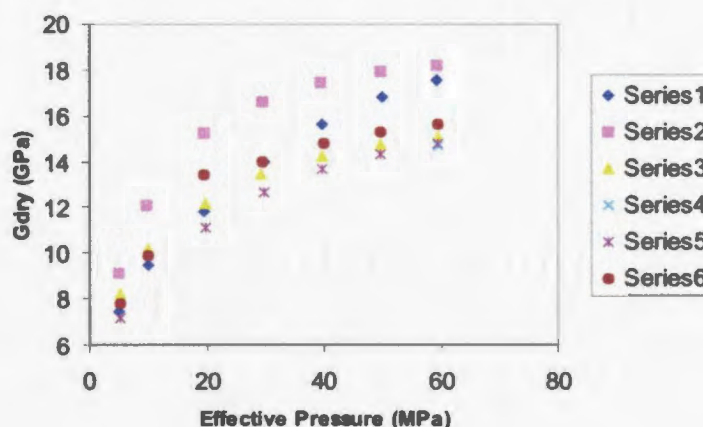
Figure 2.27. *Dry shear modulus as a function of effective pressure for six Hibernia sandstone core samples. (Hibernia, 2000)*

60

Shear sonic logs are available for some Hibernia wells. For the purpose of examining the effect of porosity on the shear velocity - and by equation 2.34 – on dry shear modulus, the same three wells used in the determination of dry bulk modulus are again utilized. The shear sonic data is fairly noisy and has a lower correlation with porosity than does the compressional velocity. Figure 2.28 displays calculated (equation 2.34) dry shear modulus as a function of porosity in these three wells. While the data contain a large degree of noise, a general trend can be determined. The shear modulus is fairly constant in the 0 to 10% porosity range, but above 10% porosity it decreases with a greater slope. This is consistent with lower shear rock rigidity with increasing pore volume.
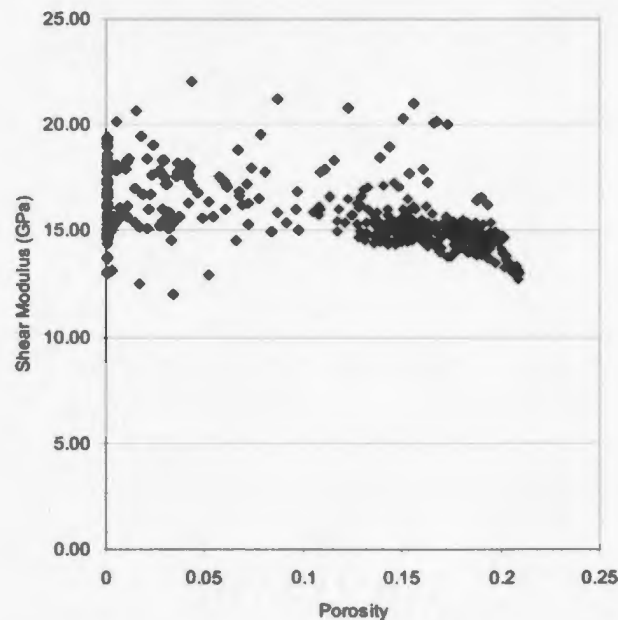
Figure 2.28. *Shear modulus derived from shear sonic and density well logs plotted against porosity (fractional). This is well log data with an effective pressure of 50 MPa.*

61

Due to the noise in the shear wave log data, a strictly statistical fit to the data is calculated using the data points and general relationships in figure 2.27 and figure 2.28. The resulting dry shear modulus as a function of porosity and effective pressure is shown in figure 2.29. This surface is a polynomial regression with no physical meaning, but it is consistent with the general trends seen in figures 2.27 and figure 2.28. Prediction of shear modulus at pressure/porosity combinations outside of the data control areas is less certain. The majority of reservoir effective pressures occur between 40-60 MPa, so a clear understanding of shear modulus at a pressure/porosity far from data control is less important, and the general trends should suffice for typical reservoir sections.
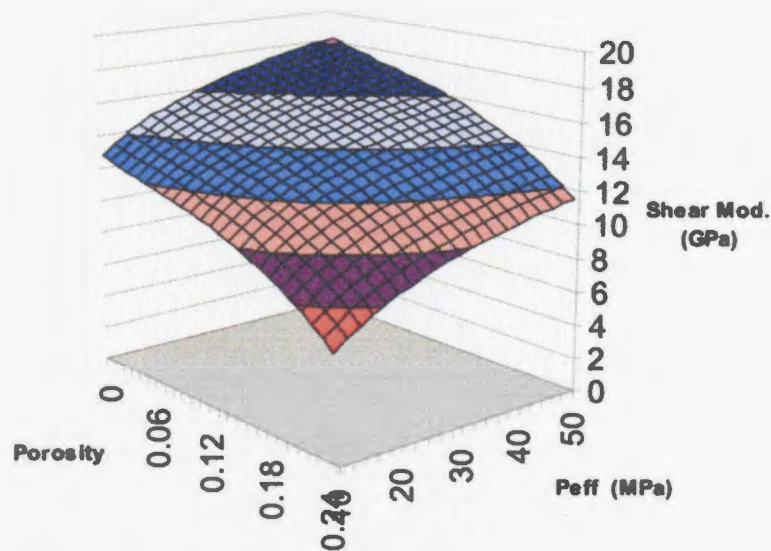
$$G_{dry} = 3.306\ln(P_{eff}) - 422.6\phi^3 + 72.35\phi^2 + 21.27\phi + 5.328 \quad (2.36)$$

Figure 2.29. *Surface plot displaying statistically determined dry shear modulus as a function of porosity and effective pressure and associated equation.*

2.5 Saturated rock modeling

With the pore fluid and dry rock properties independently estimated, it is possible using the Gassmann equation (Gassmann, 1951; Berryman, 1999; Dvorkin et al., 1999) to calculate saturated rock properties (figure 2.30).
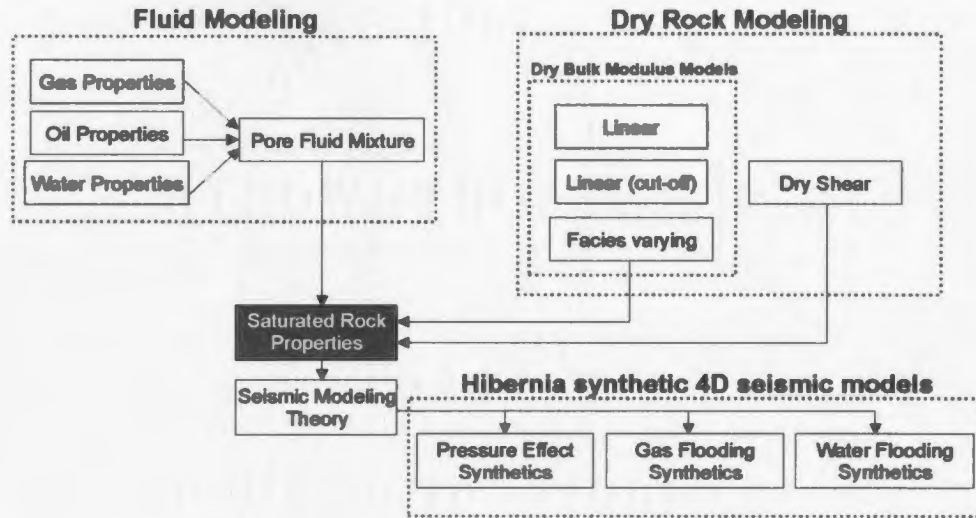
Figure 2.30. *Hibernia 4D seismic modeling workflow, showing the saturated rock property calculation requiring inputs from the pore fluid mixture models, facies-varying dry bulk modulus model, and the dry shear modulus model.*

The Gassmann equation is given by (Dvorkin et al., 1999):

$$K_{sat} = K_{gr} \frac{\phi K_{dry} - (1+\phi)K_f K_{dry}/K_{gr} + K_f}{(1-\phi)K_f + \phi K_{gr} - K_f K_{dry}/K_{gr}} \quad , \quad (2.37)$$

where K_{sat} is the saturated bulk modulus, K_{gr} the grain bulk modulus, K_{dry} the dry rock bulk modulus, K_f the bulk modulus of the pore fluid mixture, and ϕ the porosity. From

the work in section 2.4, the facies-varying dry rock modulus (K_{dry}), and derived grain

modulus (K_{gr}) are determined to be:

$$K_{dry} = aP_{eff}^{b}\phi^2 + c\ln(dP_{eff}) + e \quad (2.38)$$

$$K_{gr} = K_{dry} - \frac{\partial K_{dry}}{\partial \phi}\phi = K_{dry} - 2aP_{eff}^{b}\phi^2 \quad (2.39)$$

where for the Hibernia dataset the parameters are: a =-47.79, b =0.4036, c =5.638,

d=1.251, and e =2.906. The shear modulus is determined statistically and is given in

equation 2.36. The saturated rock density (ρ_{sat}) can be computed as a volume weighted

average of the grain density (ρ_{gr}) and the pore fluid density (ρ_f) as follows (Landro,

2001):

$$\rho_{sat} = \rho_f\phi + \rho_{gr}(1-\phi) \quad (2.40)$$

Using the elastic equations, P-wave velocity (V_p) requires the determination of shear

modulus (G_{dry}) and can be calculated as (Dvorkin et al., 1999):

$$V_p = \sqrt{(K_{sat} + \frac{4}{3}G_{dry})/\rho_{sat}} \quad (2.41)$$

The shear velocity (V_s) is solved from the shear modulus ($G_{dry} \approx G_{sat}$) and density (ρ_{sat})

(Dvorkin et al., 1999):

$$V_s = \sqrt{\frac{G_{sat}}{\rho_{sat}}} \quad . \quad (2.42)$$

64

2.6 Conclusions

In this chapter, I have calculated the saturated rock properties by examining in detail the individual components: pore fluid properties, and dry rock moduli. The pore fluid properties are determined, giving the interesting result that due to the high GOR oil at Hibernia, gas and oil have more similar physical properties than do water and oil. I then present new and original models for the determination of dry bulk modulus. The final model discussed, the facies-varying model, is directly applicable to the Hibernia reservoir geology, and significantly improves the accuracy of predicted reservoir velocities. The pore fluid physics and dry rock properties are then merged using Gassmann's relationship to produce a saturated rock model from which synthetic 4D seismic data can be generated.

Chapter 3

4D seismic modeling and inversion methods

3.1 Overview

4D seismic modeling is a process that uses a saturated reservoir model to generate synthetic 4D seismic data that represents different steps in a reservoir's production history (gas flooding/water flooding). This step is located in the thesis flowchart in figure 3.1 under modeling. In this chapter, through modeling, I predict relative changes in amplitude and the reservoir traveltime that can be attributed to production related pressure effects, gas saturation increases, and water saturation increases. I use the quantitative analysis of the modeled 4D seismic data to produce new and original inversion methods that use the stacked seismic data to solve for time-lapse reservoir pressure and saturation change. In the interpretation chapter, Chapter 5, I apply these inversion methods to the Hibernia 4D seismic data.

3.2 Introduction

In the previous sections, a number of empirical and fundamental relationships have been presented that model the physical properties of Hibernia reservoir rock for varying fluid saturation and pressure conditions. The seismic monitoring of fluid flow through porous media is based on the principle that subsurface migration of pore fluids and pressure fronts alter the physical properties of the reservoir. Under favorable circumstances, these changes in physical properties can be detected seismically (Lumley, 1995; Jack, 1998). In
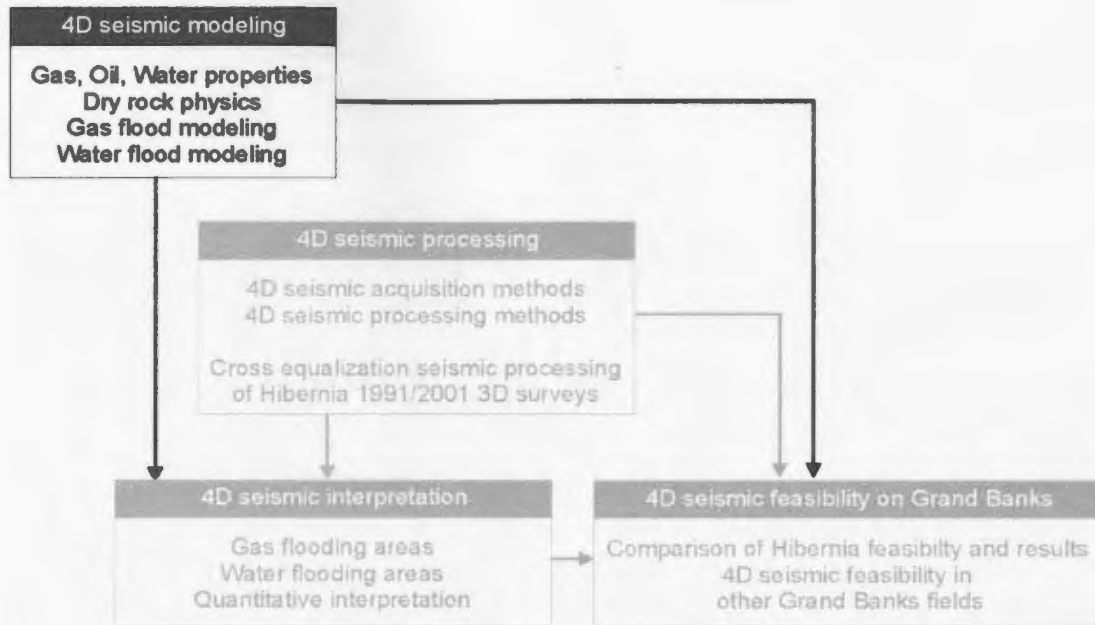
Figure 3.1. *Thesis outline flowchart. 4D seismic modeling is required to accurately understand the type of 4D seismic response that may be anticipated for a given reservoir change. In addition, the seismic modeling will enable the creation of a set of relationships that link seismic response to physical reservoir change. This can aid in 4D seismic interpretation by allowing the inversion of the observed seismic response in the reservoir to yield physical reservoir changes such as saturation or pore pressure.*

this chapter, I use the saturated reservoir model to generate synthetic 4D seismic data for different production scenarios including pressure change, gas flooding, and water flooding.

4D seismic modeling is often limited to fluid substitution analysis due to the unavailability of local rock physics data. Such modeling does not account for production related pressure changes that occur in many oil fields including Hibernia. However, for this research, rock physics data for selected Hibernia cores are available allowing the

saturated rock modeling to incorporate both pore fluid change and effective pressure changes in the reservoir. The unique seismic properties of the various pore fluids coupled with the seismic effect of pressure change produces varying seismic responses for different fluid saturation and pressure combinations. In this section, I model the 4D seismic response from saturated rock models for characteristic reservoir conditions expected in the Hibernia reservoir. This modeling work helps to both determine the optimal reservoir zones for observing 4D seismic anomalies and to create inverse relationships between 4D seismic response and changes in the causative rock and fluid properties. These inverse relationships have the potential to aid 4D seismic interpretation by isolating the physical causes of potential anomalies.

3.3 Seismic modeling theory

In this section, highlighted in the modeling workflow in figure 3.2, I review the seismic modeling theory that is used to generate 4D seismic models for this thesis.
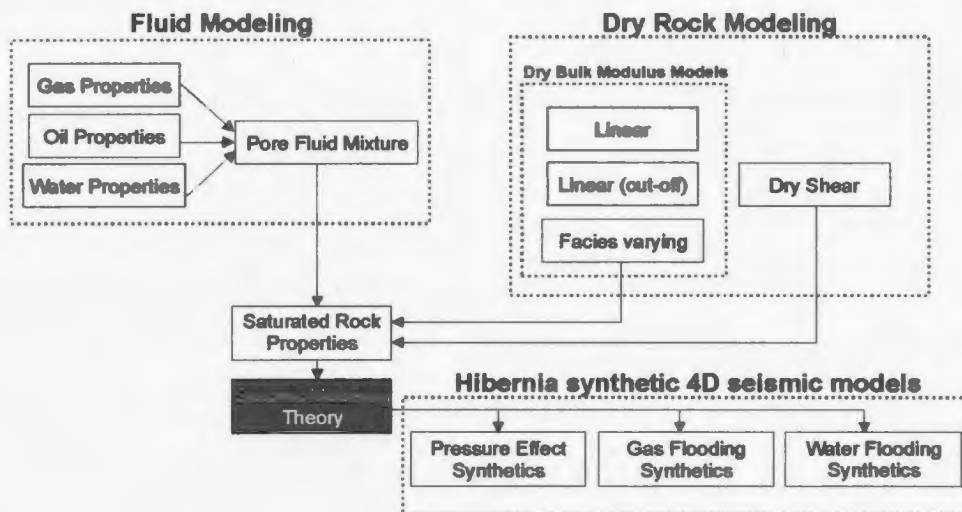
Figure 3.2. *Hibernia 4D seismic modeling workflow, with the section on seismic modeling theory highlighted.*

The seismic reflection method relies on a subsurface acoustic impedance (I) contrast to reflect energy back to the surface. It is possible that exchanging the pore fluid and altering the reservoir pressure in a reservoir unit can create sufficient change in acoustic impedance that the amplitude, timing, and character of the seismic reflection will vary between repeated surveys. Acoustic impedance is the product of density and velocity which are calculated by methods presented in the preceding section:

$$I = \rho_{sat} V_p \quad . \quad (3.1)$$

For a zero offset reflection, the normal incidence reflection coefficient (R_{ni}) between two layers can be given as:

$$R_{ni} = \frac{I_2 - I_1}{I_2 + I_1} \quad , \quad (3.2)$$

where I_1 and I_2 are the acoustic impedances of the upper and lower layer respectively. The reflection coefficient can be thought of conceptually as being proportional to the seismic amplitude of a reflector. As the reservoir is bounded above or below by a non-reservoir unit, the impedance of non-reservoir layers remains constant while the reservoir layer changes, allowing differences in reflection amplitude to be attributed to changes in reservoir acoustic impedance.

Because the 4D seismic data acquired at Hibernia has certain non-zero offset ranges, it is important to consider the reflection coefficient in the case of non-normal incidence. The 4D seismic modeling in this chapter uses the offset ranges of the real Hibernia seismic data to create synthetic stacked seismic data. To calculate the offset dependent

reflectivity, I use a generalized linear approximation of the Zoeppritz equations by Aki and Richards (1980) given below:

$$R_\theta = \frac{1}{2}\left(1 - \frac{4V_s^2}{V_p^2}\sin^2\theta\right)\frac{\Delta\rho}{\rho_{avg}} + \frac{1}{2\cos^2\theta}\frac{\Delta V_p}{V_{pavg}} - \frac{4V_s^2}{V_p^2}\frac{\Delta V_s}{V_{savg}}\sin^2\theta \quad , (3.3)$$

where,

$$\Delta V_p = V_{p2} - V_{p1} \quad \text{and} \quad V_{pavg} = (V_{p1} + V_{p2})/2 \quad , (3.4)$$

$$\Delta V_s = V_{s2} - V_{s1} \quad \text{and} \quad V_{savg} = (V_{s1} + V_{s2})/2 \quad , (3.5)$$

$$\Delta\rho = \rho_2 - \rho_1 \quad \text{and} \quad \rho_{avg} = (\rho_1 + \rho_2)/2 \quad , (3.6)$$

and, θ is the angle of incidence, and subscripts 1 and 2 indicate the upper and lower layers respectively. The angle of incidence at a reflected boundary is dependent on the velocity gradient in the subsurface, the depth, and the horizontal offset (Aki and Richards, 1980; Graul, 2003). Snell's law (Sheriff and Geldart, 1982) which governs the incident and transmitted angles for a given reflecting interface, is given as:

$$\frac{\sin\theta_1}{V_1} = \frac{\sin\theta_2}{V_2} \quad , (3.7)$$

where θ_1 and θ_2 are the incident and transmitted angles respectively, and V_1 and V_2 are the velocities of the upper and lower layer respectively. As a result, as a seismic wave propagates into a higher velocity medium, the angle of transmission increases. Conversely, if the velocity of the layers is constant, there will be no change in the angle of the ray path.

When calculating the angle to use for amplitude variation with offset (AVO) reflection amplitude modeling, it is important to determine whether a straight ray model which assumes constant velocity in the overburden is appropriate or if bending or curved rays are more suitable. Figure 3.3 displays conceptual ray path diagrams for both straight and bent rays. In the diagram, the velocity increases with depth, so in keeping with Snell's law a bending ray model that results in a higher incident angle at the reflected interface is most appropriate. Figure 3.4 displays a Hibernia velocity-depth relationship and also the incident angle versus offset for both straight and curved ray assumptions. For the AVO modeling research conducted in this thesis, a curved ray assumption is used as there is 5-8 degree difference in angle compared to straight rays at the far offset distances which are 3000 and 4500 metres for the 1991 and 2001 surveys respectively.
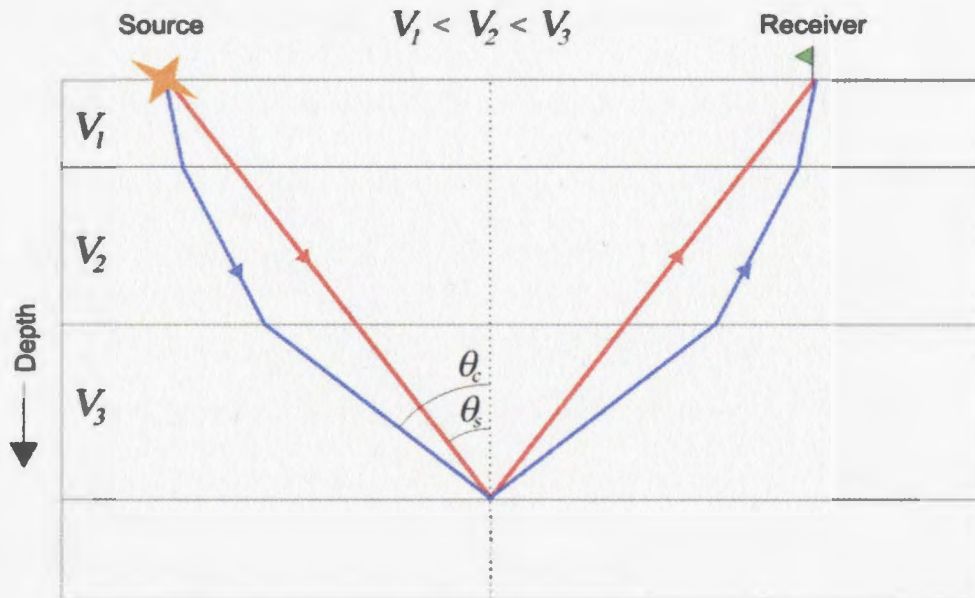
Figure 3.3. *Plot showing ray paths for a straight ray (red) and bending ray (blue) assumptions. In geologic models with increasing velocity with depth, the angle of incidence for the bent ray (θ_c) will be greater than the angle of incidence for the straight ray (θ_s).*
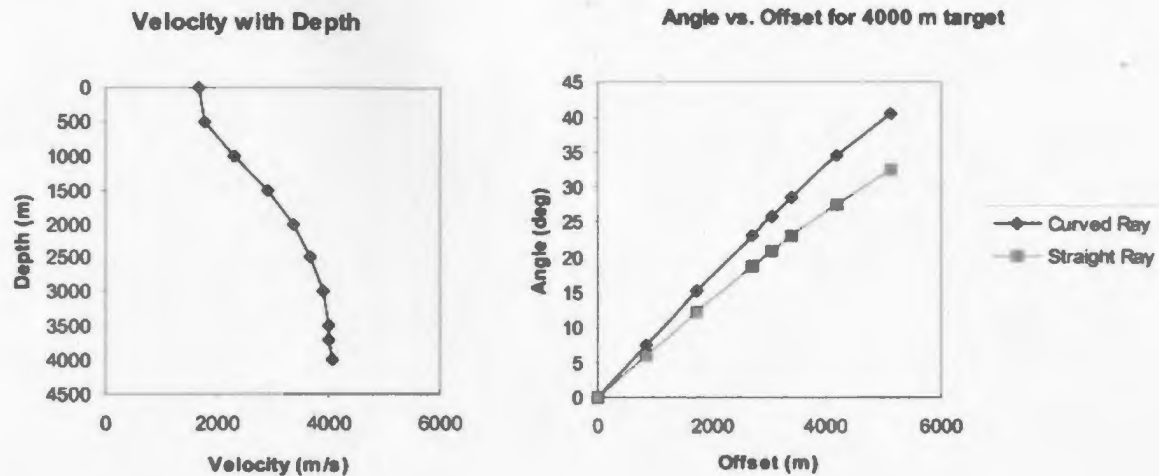
Figure 3.4 *Velocity with depth profile (left) derived from well sonic logs and angle versus offset (right) for 4000 m target (reservoir approximate) for both curved and straight ray assumptions. The curved rays have increasingly greater angles with offset.*

Offset range synthetic calculations

For each of the 4D seismic modeling sections in this chapter, synthetic seismic amplitudes are calculated for two different amplitude variation with offset (AVO) cases. Firstly, a normal incidence model is computed that assumes zero offset seismic for both the 1st survey (pre-production) and 2nd survey configuration. Secondly, I consider a stacked case over the offset range of with the 1991 offsets of 230-3205 m which is approximated to be 2-28 degrees (figure 3.4) used for both seismic datasets. This modeling attempt endeavors to match the results expected from co-processing of the seismic datasets which will involve using offset ranges common to both surveys. The 2001 3D seismic dataset has an offset range of 300-4800 m, and in later sections through

processing I attempt to balance the 2001 to the 1991 AVO response through a first order correction.

3.4 Seismic modeling process and calibration

This section focuses on the specific Hibernia reservoir parameters that are used for 4D seismic modeling as well as calibration of the modeling results with real data. To examine the effect that hydrocarbon production may have on seismic response, it is imperative that a consistent modeling approach be applied to each production scenario that is modeled. To establish a standard set of time constant reservoir parameters such as porosity distribution, a single well in a representative reservoir section is chosen. The bulk lithologies and physical properties of this well shown are shown in figure 3.5.

		P Velocity (m/s)	Vp/Vs	Density	Ave Porosity	
60m	Layer 1	4170	1.74	2550	3.8%	Layer 1
25m	Layer 2	3890	1.59	2260	18.0%	Layer 2
20m	Medial Shale	4310	1.7	2620	1.0%	Medial Shale
25m	Layer 3	4020	1.62	2350	15.0%	Layer 3
GOC 55m						
	Fortune Bay	4250	1.81	2600	1.4%	Fortune Bay
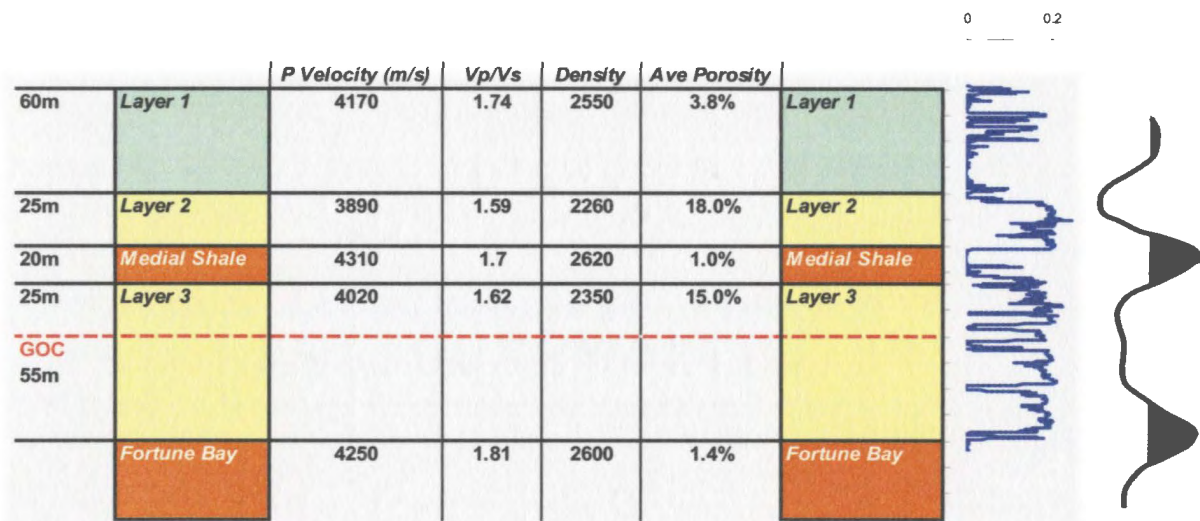
Figure 3.5. *Average layer properties extracted from the well on which modeling will be performed with a porosity log (0 – 0.2 frac) and modeled seismic trace to the right. The reservoir interval is layer 3 with the Fortune Bay shale marker immediately below it.*

For 4D seismic modeling it is important that the modeled properties are comparable to those observed in well logs. The primary inputs for well log modeling are porosity, pore

pressure, and fluid saturation. From these inputs, a P and S wave velocity log and a density log can be derived, allowing the generation of synthetic seismic data. Figure 3.6 shows a display of a Hibernia well log and 1991 3D seismic data compared to the modeled impedance log and generated normal incidence synthetic seismic data. The modeled impedance log is generated with the modeling code outlined in the previous sections. The modeling inputs are values representative of the pre-production conditions that existed during the 1991 seismic acquisition and include: well log porosity, 40 MPa pore pressure (50 MPa effective pressure), 95 degrees Celsius temperature, and 0.95 oil saturation (0.05 water saturation).
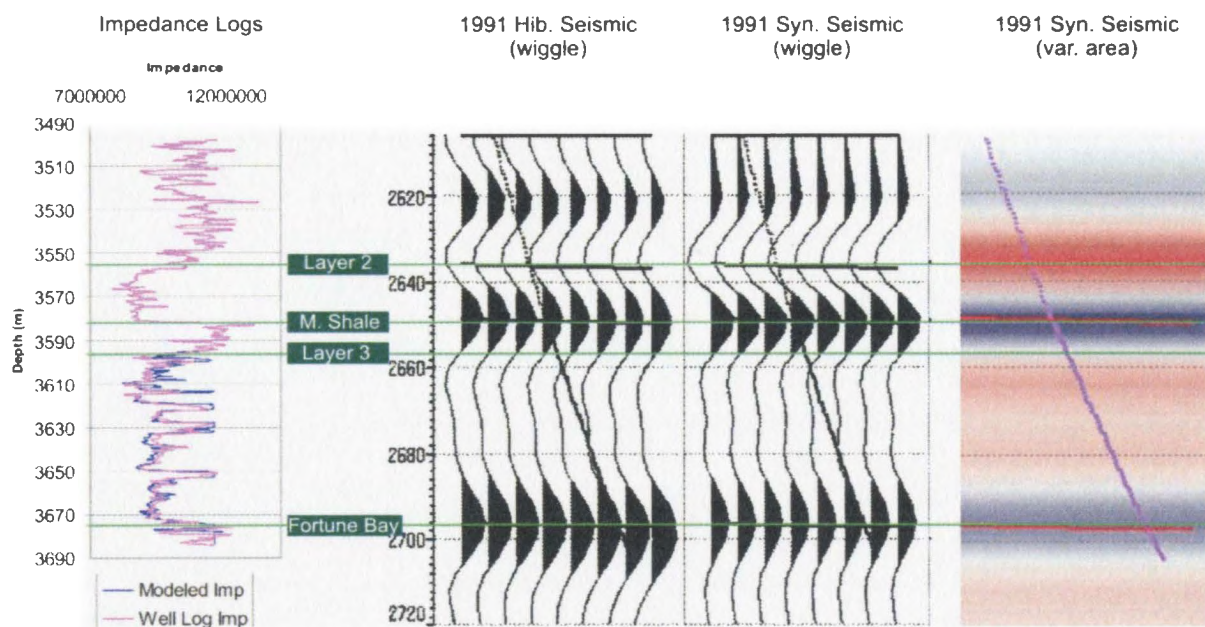
Figure 3.6. *A four panel display showing from left to right: well impedance log (purple) and calculated saturated impedance log (blue) from modeling with an oil saturation at 0.95 and a pore pressure of 40 MPa (initial conditions). Also displayed is actual 1991 Hibernia 3D seismic data for the well track, synthetic normal incidence seismic data generated from modeled impedance log (wiggle trace), and the same synthetic shown in variable area.*

The modeled and actual impedance logs are very similar over the reservoir interval. This is due in part to the quality of the new facies-varying dry rock moduli model (figure 2.25). The seismic to synthetic tie shows similar location and character of reflection events, but the relative amplitude of events varies slightly from seismic to synthetic. The ability of the modeling code to produce impedance values that are similar to the pre-production well logs and synthetic seismic data that are comparable to pre-production 1991 seismic data signifies that the modeling algorithms and input values are likely appropriate for saturated rock seismic modeling in the Hibernia reservoir. In the modeling scenarios to follow, I examine the modeled seismic response of this reservoir section to various pore fluid saturations and pore pressures.

3.5 Seismic attribute extraction

To quantitatively measure the 4D seismic response, I employ the use of seismic attributes. Measurements directly derived from seismic data are called seismic attributes (Sheriff and Geldart, 1982), and include measures such as instantaneous phase, instantaneous frequency, and maximum peak amplitude. The extraction of seismic attributes has been a subject that has gained increasing importance over the past couple of decades with the advent of reservoir seismic analysis. Traditionally used solely for structural imaging, seismic data is now also being utilized for quantitative reservoir property estimation (e.g., Hilterman, 2001). A lot of this work is done through the extraction of numerical attributes from digital seismic data. As one cannot directly measure seismic properties such as impedance in the actual seismic data, seismic

attributes are calibrated during modeling to track their variation with physical changes in the reservoir. These relationships can then be inverted and applied to real time-lapse seismic data to estimate the change in underlying physical properties. For the seismic modeling analysis in this study, the Fortune Bay shale marker at the base of the reservoir is the reflection chosen for attribute extraction. The Fortune Bay is chosen because it is the boundary of a reservoir and non-reservoir unit, so relative changes in the seismic response should be correlated solely with physical reservoir changes, and not changes in the static non-reservoir unit. The two attributes selected for this research are maximum peak amplitude and instantaneous phase. The maximum peak amplitude is chosen because it returns the peak amplitude of a reflector, which is proportional to reflection coefficient (equation 3.2, 3.3), allowing for indirect measure of time-lapse impedance change. The instantaneous phase attribute indirectly measures pull-up and lag of a reflector, and as such is used to measure time-lapse changes in reservoir velocity.

Maximum Peak Amplitude Attribute

The maximum peak amplitude is the peak amplitude over a given reservoir window. In the example in figure 3.7, the maximum peak amplitude extraction is shown for an extraction window +/-10 ms of the Fortune Bay horizon. The three largest amplitude samples in the extraction window are fitted in the software with a parabolic function that is interpolated to find the maximum peak amplitude (Landmark, 1999).
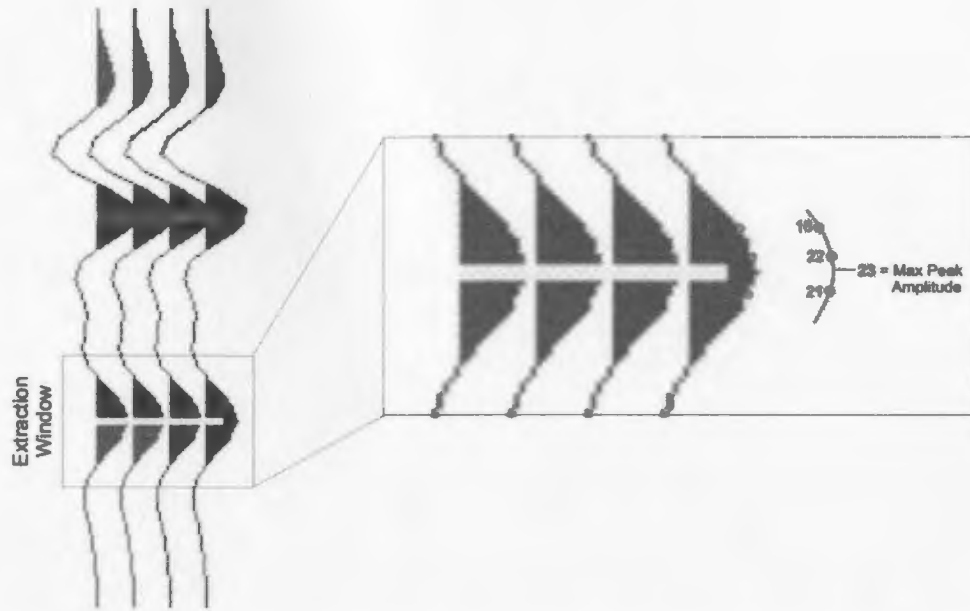
Figure 3.7. *Maximum peak amplitude extraction method. The algorithm searches for the 3 highest samples in a given window and fits a parabolic function to the three points to determine the interpolated maximum peak amplitude.*

Instantaneous Phase Attribute

Instantaneous phase is a seismic attribute that depicts the angle between the phasor and the real axis as a function of time (Landmark, 1999). As it is a rotating vector, it always forms an angle between -180° and +180°. At 180°, there is a discontinuity in the instantaneous phase plot as it passes to -180°, a feature clearly shown in figure 3.8 which displays the modeled reservoir seismic trace and the derived instantaneous phase function. This discontinuity at the maximum trough amplitude is called phase wrapping. At a positive peak, the instantaneous phase is zero, meaning the angle between the phasor and the real axis is zero. By extracting the instantaneous phase around a given horizon, one can measure how close the peak of the seismic data is to the reference horizon. For time-lapse purposes, the relative movement of the base reservoir peak, due to production

Seismic Trace   Instantaneous Phase
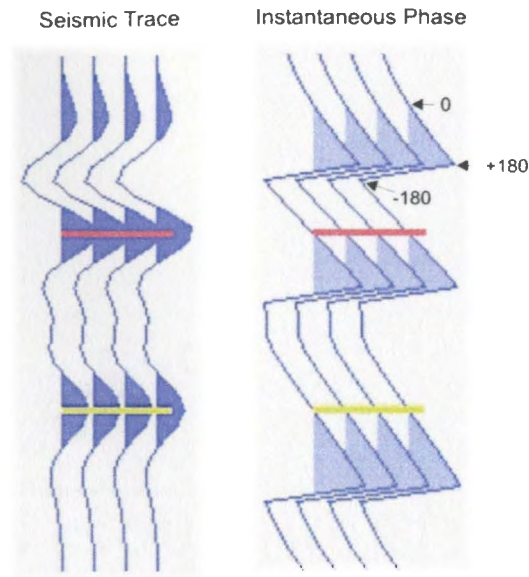
Figure 3.8. *Seismic trace(left) and derived instantaneous phase (right). Instantaneous phase is zero at maximum peaks and +/- 180° at trough locations. Phase wrapping, a sharp discontinuity at the maximum trough is clearly seen, although instantaneous phase extraction from a 20 ms window around the Fortune Bay horizon (yellow) prevents phase wrapping effects to be averaged into the attribute determination.*

related traveltime differences, will manifest in increasing instantaneous phase for a traveltime decrease (increase in velocity) and decreasing instantaneous phase for traveltime increase (decrease in velocity).

By experimentation, it is determined for this dataset that instantaneous phase provides a more precise measure of traveltime differences compared to re-picking the seismic peak as it shifts. This is possibly due to the relatively large 360° dynamic range of the instantaneous phase calculation, the 4 ms seismic sample rate making it difficult to precisely pick sub sample time differences from peak amplitude shifts directly, and the ability to extract the instantaneous phase over a window. For the purposes of this

78

modeling study, I extract the average instantaneous phase for a 20 ms window centered on the Fortune Bay reflection. As this reflection is a peak and therefore a zero crossing of instantaneous phase, extraction of the attribute over this small window prevents the inclusion of phase wrapping effects in the extracted attribute value.

By varying the reservoir traveltime and measuring the instantaneous phase attribute, a relationship between traveltime change and change in instantaneous phase is determined and shown in figure 3.9. If the reservoir thickness is generally known, the determination of traveltime change can be used to solve for reservoir velocity change.
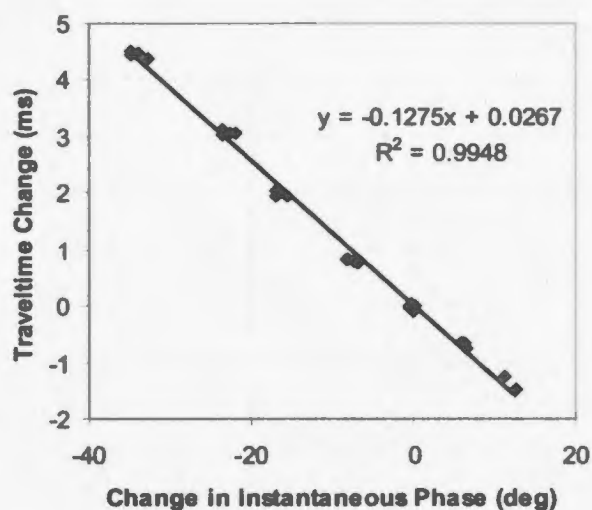
Figure 3.9. *Relationship between instantaneous phase and traveltime change for the base reservoir Fortune Bay reflector.*

3.6 Effect of pressure change

A key result of this modeling research is to examine the effect that pore pressure change has on the 4D seismic response at Hibernia, as shown in the thesis modeling workflow in figure 3.10. Due to a lack of available rock physics measurements, 4D seismic modeling is often based solely on pore fluid substitution. Pressure change can have as great an influence as pore fluid substitution on the 4D seismic response depending on the lithology, overburden pressure, pore pressure range, and the net effective pressure range of the reservoir. For this research, calculation of the Hibernia synthetic 4D seismic response due to pressure change is based on the dry rock moduli models presented in Chapter 2.
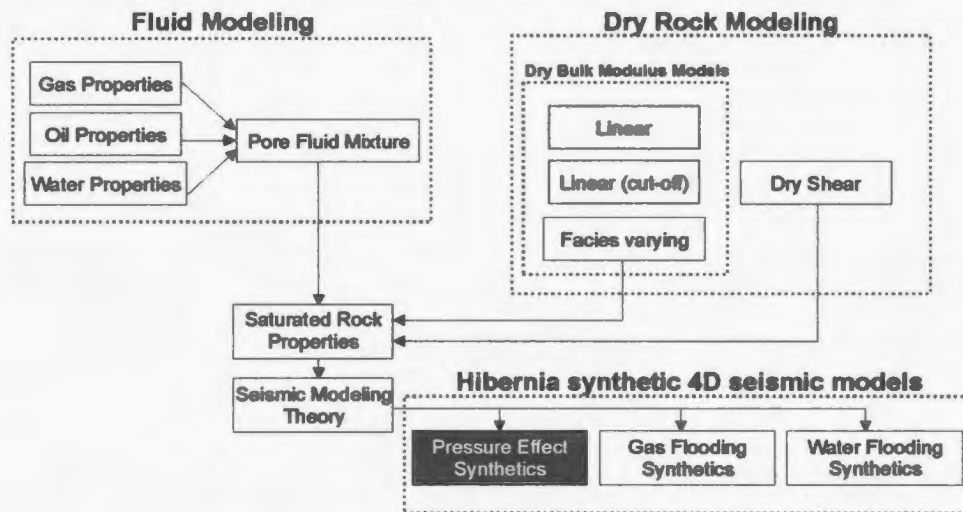
Figure 3.10. *Hibernia 4D seismic modeling workflow, with the calculation of synthetic seismic models for pressure change highlighted.*

The net effective pressure (P_{eff}) is simply the difference of overburden pressure (P_{over}) and pore pressure (P_{pore}):

$$P_{eff} = P_{over} - P_{pore} \qquad (3.8)$$

Because overburden pressure can be assumed a constant 90 MPa over the relatively short period of geologic time separating subsequent time-lapse seismic surveys, changes in pore pressure directly impact effective pressure. As pore pressure rises, as in the case of an injection well, effective pressure will decrease. Conversely, a decrease in pore pressure will result in an increase in effective pressure.

To isolate the effect that changes in pore pressure have on seismic properties, the pore pressure is varied while holding the saturation constant at initial conditions (0.95 oil saturation). For the pressure modeling, I neglect the effects of gas being exsolved from solution oil as the pore pressure drops below bubble point. Figure 3.11 displays the percentage change from initial conditions for bulk reservoir P-wave velocity (Vp), density (Rho), and acoustic impedance (Imp). Velocity drops substantially with increasing pore pressure because the net effective pressure decreases thus softening the rock frame, an effect also seen in Landro (2001). As bulk modulus varies with pressure logarithmically, the rate of decrease in velocity increases as pressure decreases along the curve shown in figure 2.14. Velocity rises with pore pressure decrease (provided it remains above bubble point), but the rate of velocity change is less than if the pore pressure were increased. This is due to the fact that a reduction in pore pressure from 40 to 30 MPa, increases the net effective pressure from 50 to 60 MPa, which by looking at

figure 2.14 is clearly on the more level portion of the logarithmic curve. Because this part of the modulus pressure curve is relatively flat, it results in less velocity change than a pore pressure increase of similar magnitude. The bulk rock density varies only slightly with pore pressure. The change can attributed to the decrease in oil density with increasing pore pressure. Therefore variations in reservoir impedance due to pore pressure are almost exclusively a velocity driven process.
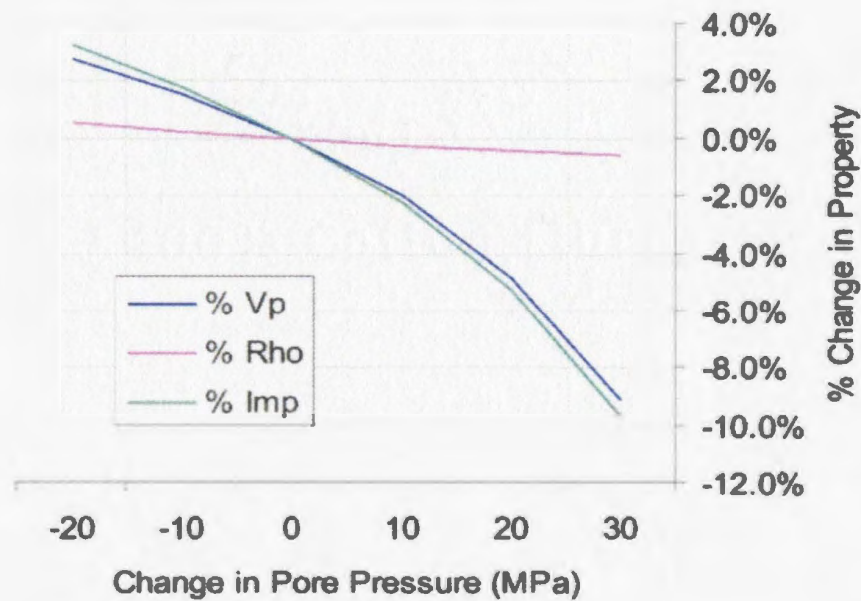
Figure 3.11. *Relative percentage changes in P-wave velocity, density, and acoustic impedance for changes in pore pressure from 40 MPa initial pore pressure.*

Using the seismic property changes due to modeled pore pressure change, I can forward model and produce synthetic seismic data for various pore pressure realizations. Seismic attributes are then extracted from the modeled data to calibrate physical change versus

attribute change relationships (Ecker et al., 1999). Figure 3.12 is a multi-panel display showing synthetic seismic data and extracted attributes for various reservoir pore pressures. For these synthetic seismic models, the saturation is held constant at 0.95 oil saturation (0.05 water saturation) so only the reservoir pressure varies. As the reservoir impedance decreases with increasing pore pressure, the impedance contrast with the underlying higher impedance shales increases. This results in a higher amplitude at the base reservoir reflection for increasing pore pressure, which is shown both visually in the seismic panels and by both the zero offset and stacked amplitude extraction plots. The change in instantaneous phase which is related to traveltime change by figure 3.9, decreases significantly with increasing pore pressure. This increasing time lag with pressure is due to the significant reservoir velocity decrease with increasing pore pressure shown in figure 3.11.

As simulated reservoir pore pressures can increase up to 20 MPa in the area of an injection well, it is possible that either the traveltime differences or amplitude variations may be significant enough to be imaged through attribute extraction in the real time-lapse seismic data. However, due to the difficulty in replicating micro fractures with pressure in a laboratory environment, it is important to keep in mind the possible limitations of using core rock physics analysis to represent in situ reservoir conditions (e.g. Lumley, 2004).
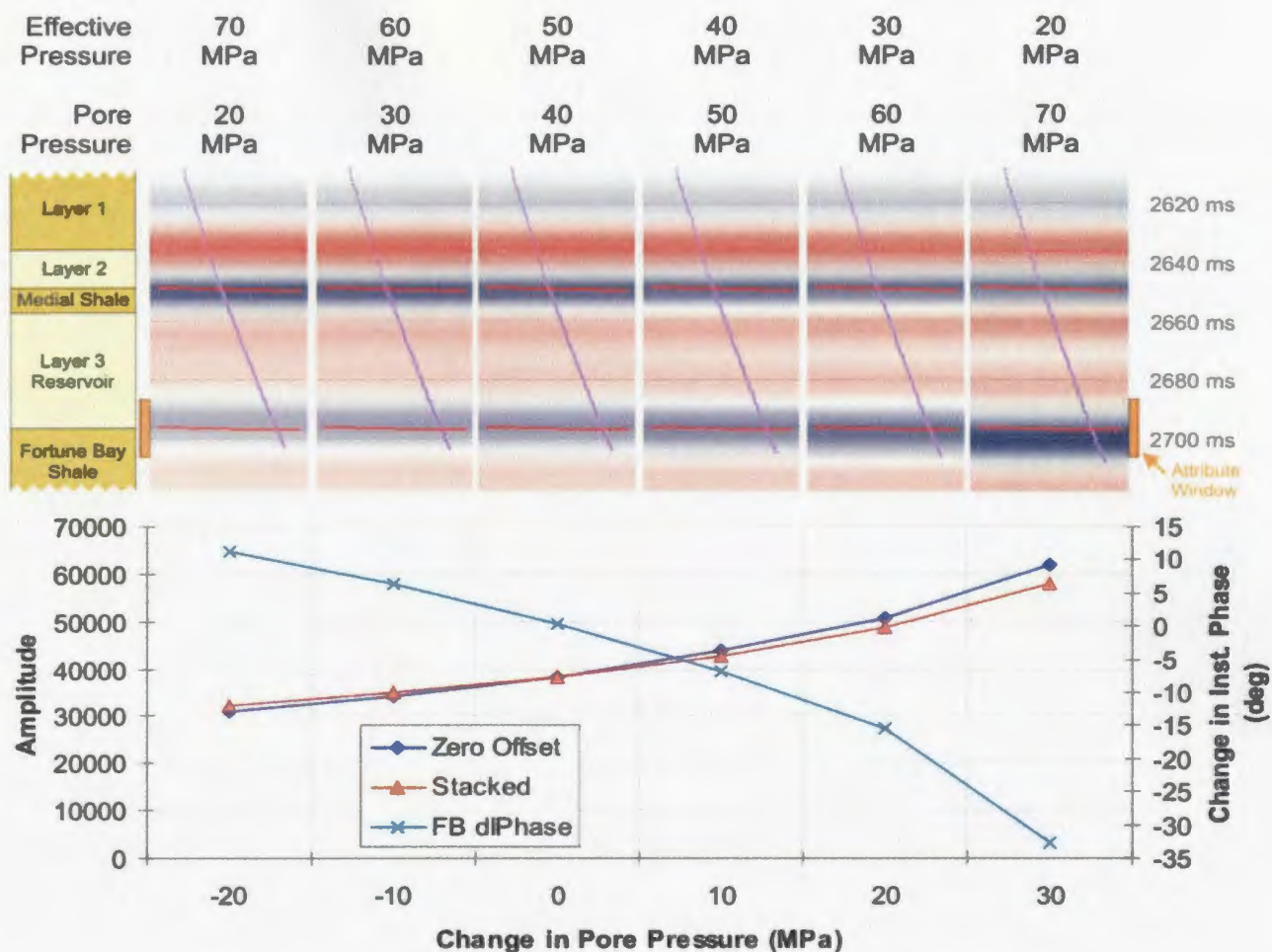
Figure 3.12. *Synthetic seismic models for a range of reservoir pressures. The graph displays amplitude (both zero-offset and stacked - left axis) and instantaneous phase attributes (right axis) calculated for a 20 ms window shown in orange. Both the amplitude (stacked and zero offset) and instantaneous phase attributes change more rapidly with increasing pore pressure. This model does not account for increasing gas saturation below bubble point pressure (bubble point pressure is approximately 30 MPa)*

3.7 Gas injection modeling

Having modeled the possible time-lapse seismic effect due to pressure change, I will now address the effect of pore fluid substitution, starting with gas replacing oil (workflow figure 3.13).

Figure 3.13. *Hibernia 4D seismic modeling workflow, with the calculation of synthetic seismic models for gas flooding highlighted.*

The properties of pore fluids established by Batzle and Wang (1992) and summarized in section 2.3 show the relative differences between pore fluid velocity and density between gas and oil (figure 2.11 and figure 2.12). By integrating these respective fluid property mixtures with the dry rock properties via Gassmann's relationship, one can simulate the replacement of oil with gas for the model section. Figure 3.14 displays the bulk seismic property changes in the model section as a result of the pore fluid substitution.

85

1.0%
0.5%
0.0%
-0.5%
-1.0%
-1.5%
-2.0%
-2.5%

% Change in Property

—— % Vp
—— % Rho
—— % Imp

1   0.8   0.6   0.4   0.2   0

Oil Saturation (1-Gas Sat)

Figure 3.14. *Relative percentage changes in P-wave velocity, density, and acoustic impedance for increasing gas saturation. The pore pressure is a constant 40 MPa.*

Starting with an initial oil saturation of 0.95, as more gas enters the system, the density of the rock decreases fairly linearly. This result is expected as the density of the fluid mixtures is simply a volume weighted average of the constituent fluid components, of which gas is less dense than oil. The somewhat unexpected result is the slight increase in velocity with increasing gas saturation. This counter intuitive result is due to the fact that with increasing gas saturation, the modeled density of the pore fluid mixture reduces the overall rock density (ρ_{sat}) at a greater rate than the modeled bulk modulus (K_{sat}). Because of the following relationship and the fact that the shear modulus (G_{dry}) doesn't change, the modeled bulk rock velocity (V_p) increases slightly.

$$V_p = \sqrt{(K_{sat} + \frac{4}{3} G_{dry})/\rho_{sat}} \quad (3.9)$$

86

This is largely due to the high dry bulk modulus (K_{dry}) (16-20 GPa) compared to the relatively small fluid modulus (K_f) component, so changes in the fluid bulk modulus have a small effect on the overall saturated bulk modulus (K_{sat}). This result is somewhat analogous to the reason that a small rise in shear velocity typically occurs during gas flooding (Jack, 1998). The density of the rock is reduced while the shear modulus remains constant, and because the two are related by the following expression, the shear wave velocity (V_s) rises slightly.

$$V_s = \sqrt{\frac{G_{sat}}{\rho_{sat}}} \quad (3.10)$$

Synthetic 4D seismic models for gas substitution can be generated using the computed velocity and density models. Figure 3.15 is a multi-panel display showing synthetic seismic data and extracted attributes for increasing gas saturation. This figure shows that with increasing gas saturation there is a very nominal increase in maximum peak amplitude at the base reservoir horizon (Fortune Bay). This is due to the decreased reservoir impedance (figure 3.14), which increases the impedance contrast with the underlying shales. The change in instantaneous phase with increasing gas saturation only varies from 0-5 degrees and is negligible compared to the traveltime effect seen from pressure variations. (figure 3.12). These relatively small changes in seismic attributes only account for the variation in pore fluid saturation. With the saturation only effects examined, I now examine the effect the combination of gas saturation increase and pressure change may have on Hibernia 4D seismic data.

Figure 3.15. *Synthetic seismic models for a range of gas saturations with a constant pore pressure of 40 MPa. The graph displays amplitude (both zero-offset and stacked - left axis) and instantaneous phase attributes (right axis) calculated for a 20 ms window shown in orange. Both the amplitude (stacked and zero offset) and instantaneous phase increase slightly with increasing gas saturation, although visual differences in the synthetic data are not obvious.*

The combination of pressure and saturation change can alter reservoir impedance in a cumulative manner with the pressure and the saturation change both increasing or decreasing impedance. The combined effects of pressure and saturation during gas injection are shown by arrows in figure 3.16. Conversely, a pore pressure drop below

bubble point where gas is exsolved from the oil solution has a conflicting impact on reservoir impedance. The increase in gas saturation decreases reservoir impedance while the decrease in pore pressure increases the reservoir impedance, but as shown in figure 3.16, the pore pressure effect generally dominates at Hibernia.

Figure 3.16. *Surface plot showing percent change in reservoir impedance with changes in pore pressure and increases in gas saturation. The yellow arrow shows the effect of a gas saturation rise only (no pressure change). Orange arrow shows the cumulative effect of a pore pressure rise of 10 MPa. The red dot indicates initial conditions.*

As shown in figure 3.16, a typical gas saturation increase (yellow arrow) decreases the impedance by only 1%. If there is a pore pressure increase of 10 MPa (orange arrow) with the gas saturation increase, the reservoir impedance drops 4%, a fairly significant increase compared to pore fluid substitution only. If gas saturation increases and a decrease in pore pressure occurs, there can in some cases be a net effect of no impedance change as the two effects offset one another.

As I am interested in measuring seismic attributes in the real data, it is important to calibrate amplitude and instantaneous phase changes with pore pressure and saturation variations. Figure 3.17 is a surface plot that illustrates the change in maximum peak amplitude at the base reservoir horizon of the Hibernia 4D seismic models as a function of changes in pore pressure and increasing gas saturation. As the impedance model in figure 3.16 demonstrates, the largest change in amplitude is in the area of the plot with both increased pore pressure and gas saturation. Alternatively, an increase in gas saturation with a slight decrease in pore pressure will have a negligible change in amplitude as shown by the light blue – green boundary in figure 3.17.

Figure 3.17. *Absolute amplitude change as a function of changes in pore pressure and increases in gas saturation. Red dot indicates initial conditions.*

The change in reservoir traveltime as a function of pore pressure change and increase in gas saturation is shown in figure 3.18. Traveltime is related to instantaneous phase in figure 3.9. Due to the slight velocity changes due to the fluid substitution (gas for oil), the traveltime and instantaneous phase changes are primarily pressure dependent.
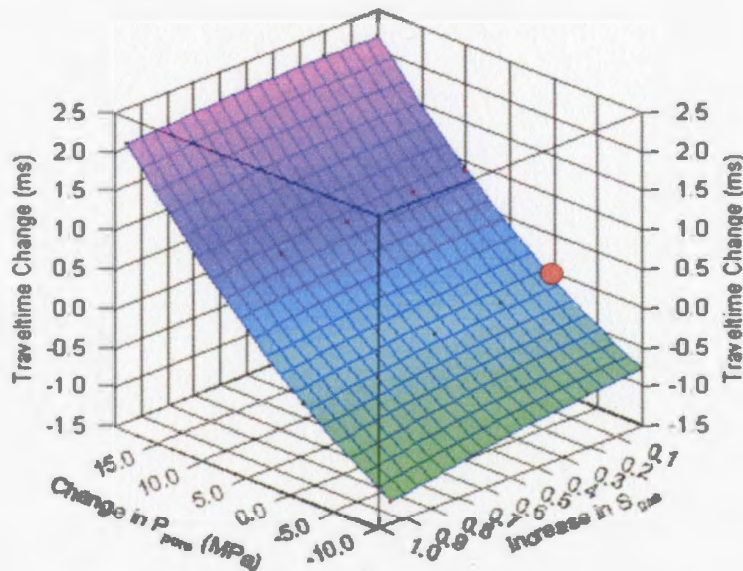
Figure 3.18. *Change in reservoir travel-time as a function of changes in pore pressure and increases in gas saturation. Initial conditions are represented by the red dot. The change in reservoir travel-time depends primarily on pressure change.*

This section has summarized some of the modeled effects that gas flooding has on 4D seismic data. Reservoir zones around a gas injector provide the best potential for detecting gas related time-lapse seismic effects, while areas where gas has come out of solution due to pore pressure dropping below bubble point are not optimal for observing 4D seismic amplitude anomalies, but depending on the magnitude of the pressure drop, may generate detectable changes in instantaneous phase or traveltime.

3.8 Water injection modeling

Along with gas injection, water injection is a key enhanced oil recovery process utilized on the Grand Banks. The water injection modeling is also the final step in the thesis modeling workflow, as shown in figure 3.19. From a purely conceptual standpoint, water injection involves the pumping of ocean water into the reservoir to both flush oil and balance the potential drop in reservoir pressure due to production. The section on pore fluid modeling (section 2.3) indicated that the compressibility contrast between the high GOR oil at Hibernia and water is higher than the contrast between gas and oil. Therefore, the modeling suggests that all other things being equal, water flooding may be more readily imaged using time-lapse seismic data than gas flooding. Based on the modeling in Chapters 2 and 3, figure 3.20 displays the modeled isobaric relative change in velocity, density and acoustic impedance due to increased water saturation.
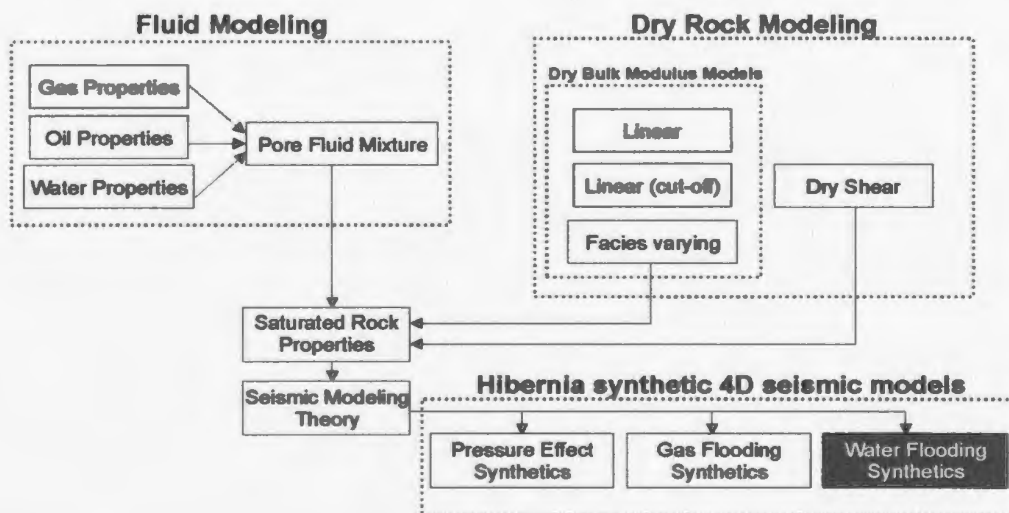
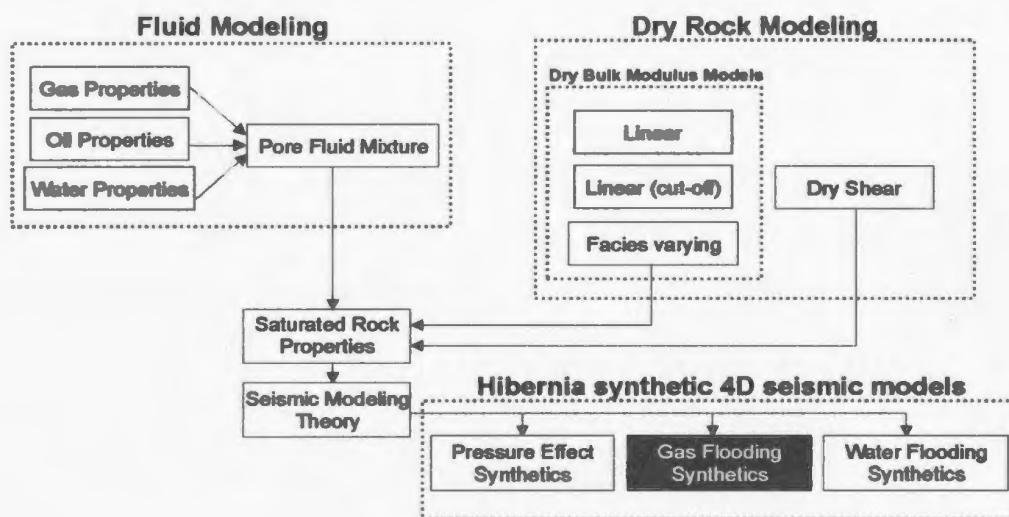**Figure 3.19.** *Hibernia 4D seismic modeling workflow, with the calculation of synthetic seismic models for water flooding highlighted.*
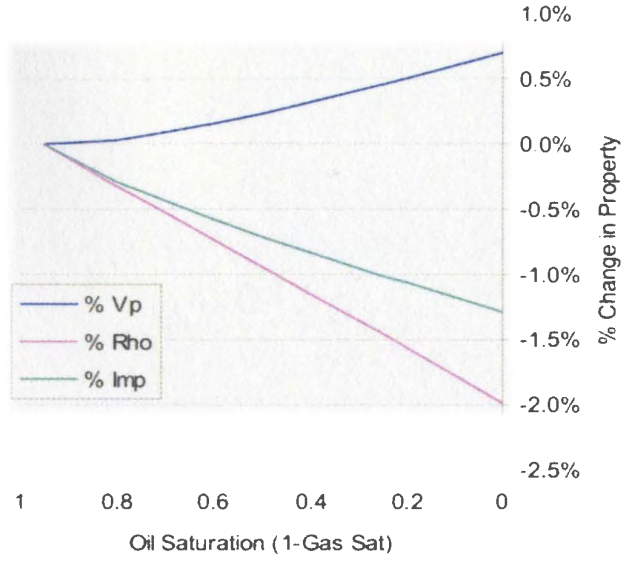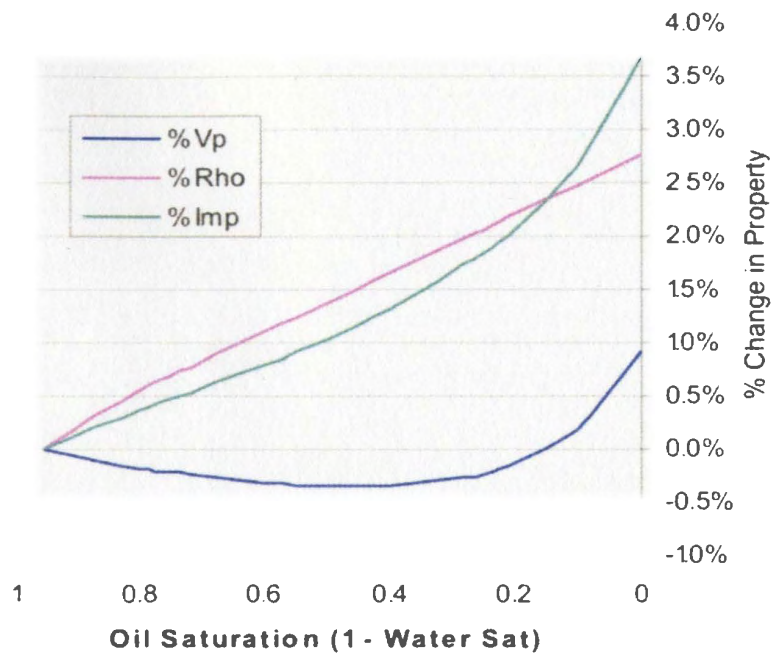
Figure 3.20. *Relative percentage changes in P-wave velocity, density, and acoustic impedance for increasing water saturation. The pore pressure is a constant 40 MPa.*

As water enters the system the velocity decreases for intermediate saturations due to density effects, but rises as oil is flushed from the pores. The relatively steep rise in velocity towards pure water saturation is due to the removal of high GOR oil from the reservoir, leaving the less compressible, higher velocity brine as the pore fluid. The density of the rock varies linearly with saturation change. The acoustic impedance line closely resembles the density track in magnitude, with some variations due to the slight velocity changes. From these plots, at Hibernia it is clear that the change in reservoir impedance due to water saturation change is largely a density driven process.

93

The synthetic seismic modeling for water substitution produces a visual change in the seismic data as a result of the fluid substitution as seen in figure 3.21. This figure shows that for increasing levels of water saturation, there is a decrease in seismic amplitude at the base reservoir reflector that dims more significantly the closer the system gets to 100% water saturation. This decrease in amplitude is attributed to the increase in reservoir impedance with increasing water saturation as seen in figure 3.20, and the consequent reduction of impedance contrast with the underlying Fortune Bay shales. The instantaneous phase attribute varies slightly over the range of saturations with a slight movement to 4 degrees as the oil is removed from the system. This can be correlated to the slight velocity rise in lower residual oil saturations seen in figure 3.20. Due to the subtle nature of the instantaneous phase change and the fact that the only change occurs at very low residual oil saturations that may be unattainable indicates that the modeling suggests in practicality it is not a good attribute for estimating changes in water saturation.

The second issue to consider is the effect that the changing pore pressure during water flooding may have on 4D seismic response. The reservoir impedance as a function of increasing water saturation and pore pressure change is shown in Figure 3.22. For a situation of water flooding with no pore pressure change, a general reservoir impedance rise is anticipated (figure 3.20). If however, there is an accompanying pore pressure rise which decreases impedance, the increase in impedance from increasing water saturation can be partially or completely offset by the pore pressure effect. Therefore, a rise in

reservoir impedance occurs in zones with an increase in water saturation and fairly constant to slightly decreasing pore pressure, although pore pressure must be maintained above bubble point, which is the expected condition over the Hibernia field.
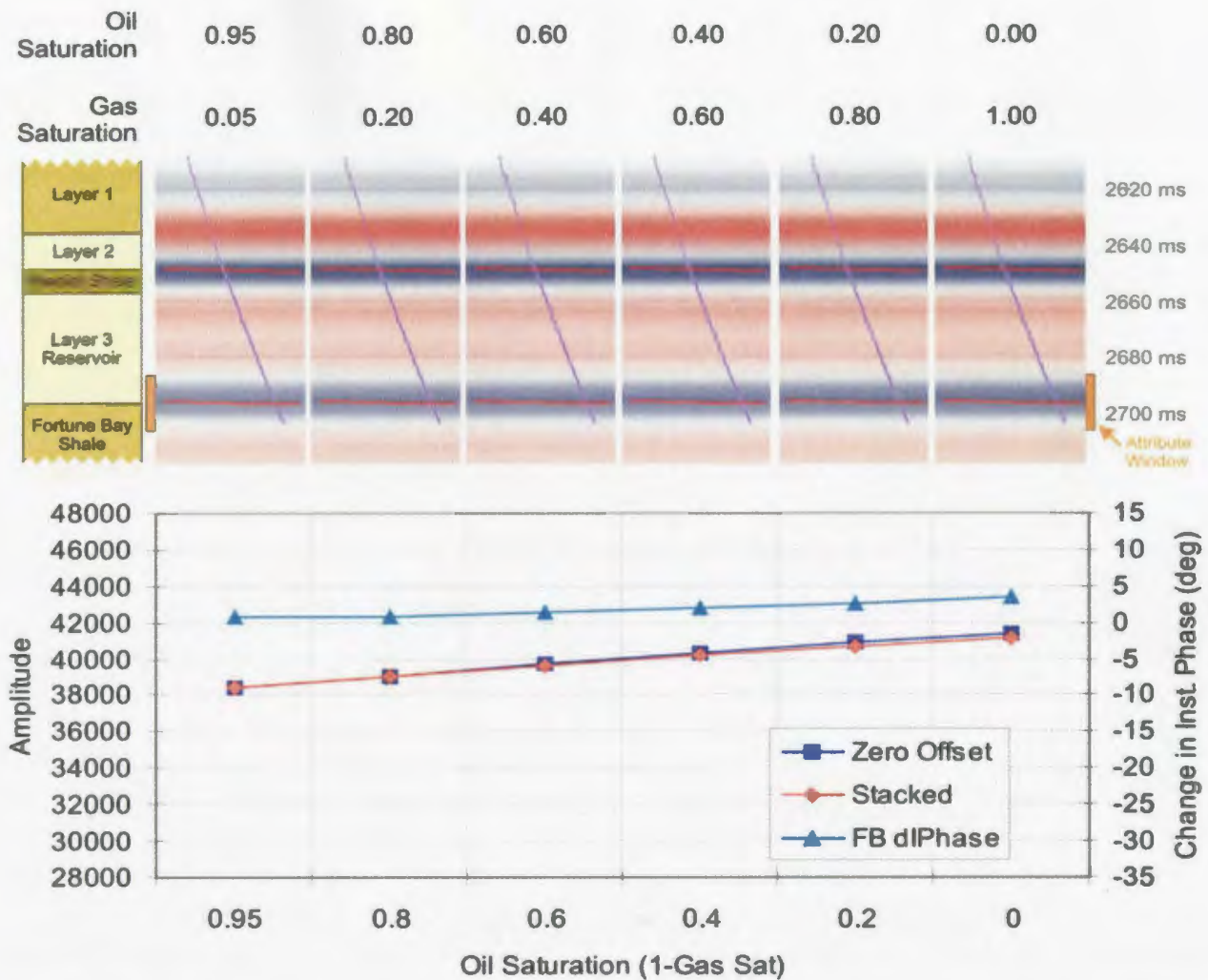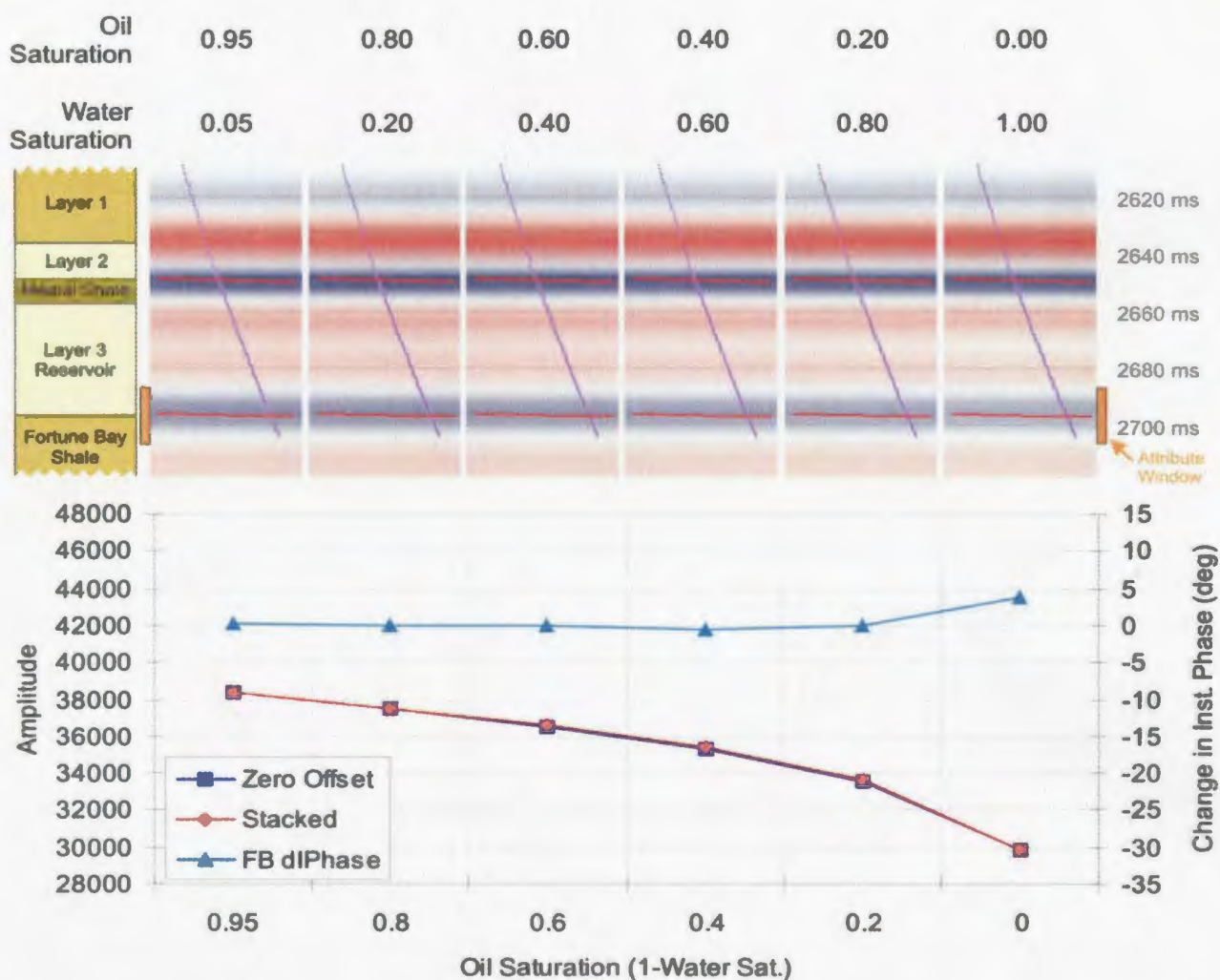

Figure 3.21. *Synthetic seismic models for a range of water saturations with a constant pore pressure of 40 MPa. The graph displays amplitude (both zero-offset and stacked - left axis) and instantaneous phase attributes (right axis) calculated for a 20 ms window shown in orange. While there is a slight variation in instantaneous phase, the amplitude (stacked and zero offset) decreases visually with increasing water saturation. The largest change in both amplitude and instantaneous phase occur as the oil is flushed from the system.*
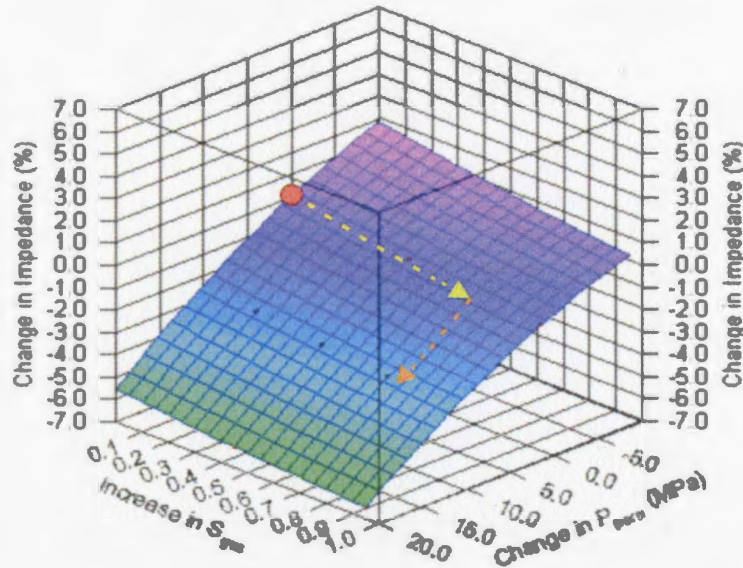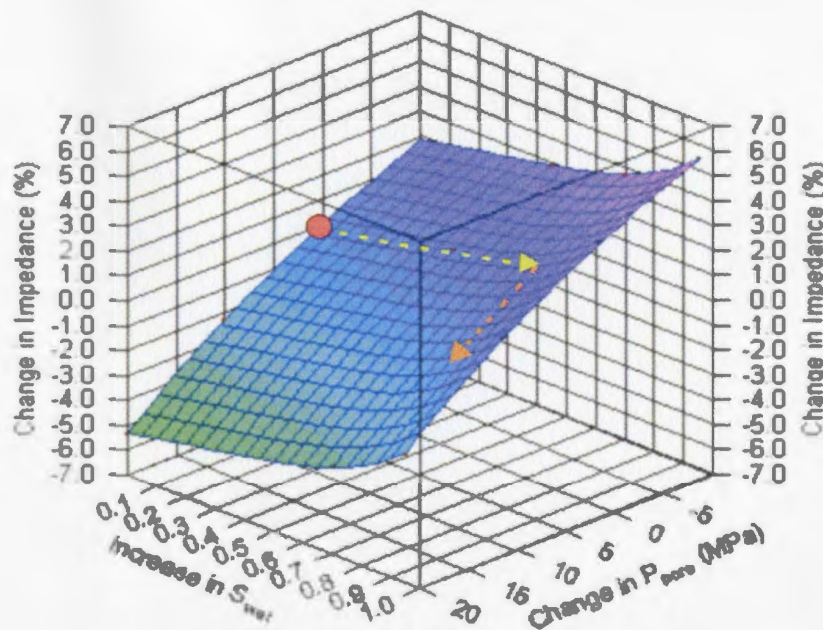
Figure 3.22. *Surface plot showing percent change in reservoir impedance with changes in pore pressure and increases in water saturation. The yellow arrow shows the effect of a water saturation rise only (no pressure change). Orange arrow shows the cumulative effect of a pore pressure rise of 10 MPa, which effectively offsets the impedance change. The red dot indicates initial conditions.*

Consistent with the changes in impedance due to pore pressure and water saturation, the maximum peak amplitude at the base reservoir shown in figure 3.23 decreases with saturation only if the pore pressure is held relatively constant or decreases slightly. If there is a significant pore pressure rise, the amplitude will remain constant or possibly increase with increasing water saturation. For example, if there is an increase in water saturation of 0.7 (0.25 residual oil) and a pore pressure rise of 10 MPa, the amplitude of the base reservoir reflector increases by approximately 150 amplitude units, while an isobaric increase in water saturation of 0.7 would result in an amplitude decrease of approximately -4000 amplitude units.

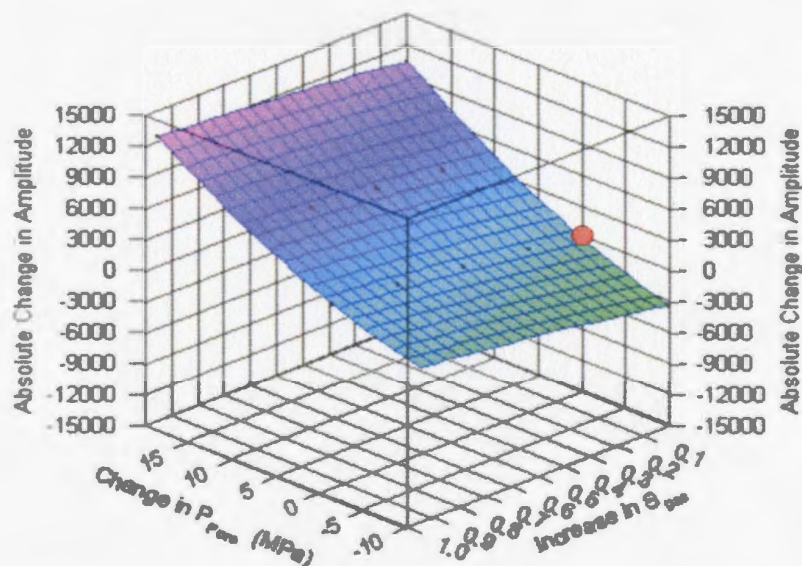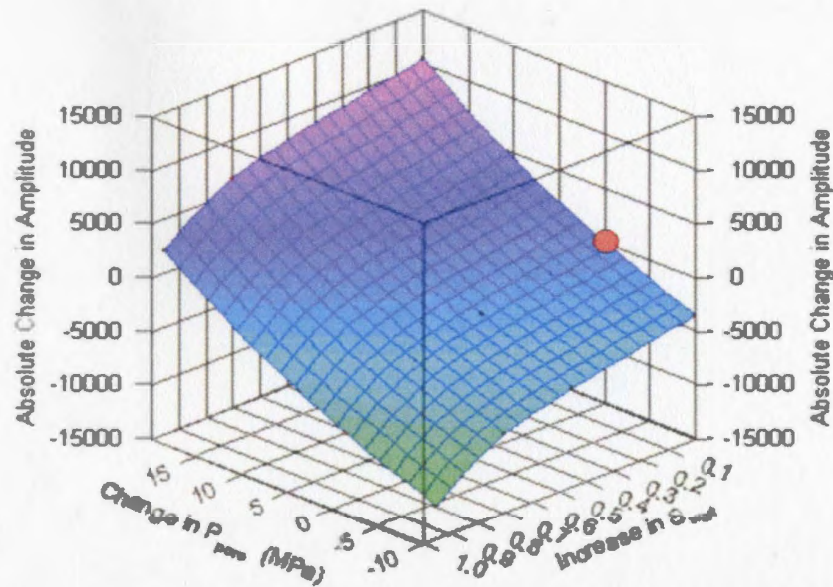**Figure 3.23** *Absolute amplitude change as a function of changes in pore pressure and increases in water saturation. Red dot indicates initial conditions.*

Figure 3.24 indicates that during water flooding, reservoir traveltime changes are dominated by pore pressure change, but in low residual oil saturations, there can be a slight decrease in traveltime due to the exsolving of high GOR oil from the system.

97
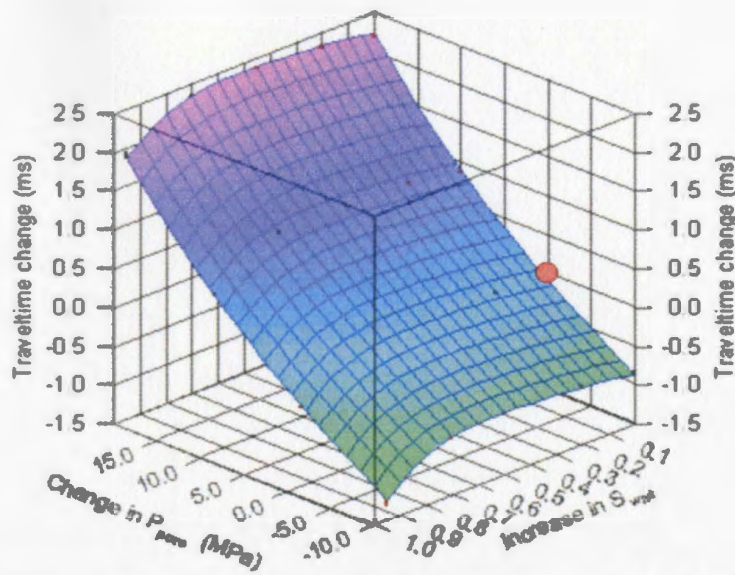
Figure 3.24. *Change in reservoir travel-time as a function of changes in pore pressure and increases in water saturation. Initial conditions are represented by the red dot. The change in reservoir travel-time depends primarily on pressure change, although some variation can be due to water saturation in areas of high water saturation.*

3.9 Inversion for pressure and saturation

The results of the forward modeling lead to a number of general observations concerning the variation of seismic properties and attributes with changes in physical reservoir properties. From these observations I quantify empirical relationships that invert the seismic attributes of amplitude and instantaneous phase for the underlying reservoir properties. This is an attempt to create relationships to solve for time-lapse pressure and saturation change in the reservoir, a normally difficult to impossible task with only stacked seismic data volumes. However, in the Hibernia case, modeling has demonstrated that the instantaneous phase attribute is almost exclusively related to pressure change. By first isolating the pressure variation, I will attempt to solve for

saturation by inverting the amplitude change which has been shown to be a function of both pressure and saturation change. This is a new and original approach, and may be suitable for other reservoirs as well.

The instantaneous phase attribute is shown for Hibernia data to vary primarily with pressure in both the water and gas floods. As a result, for inversion purposes I will attribute all of the instantaneous phase change to pressure, neglecting the slight effect due to saturation changes. Figure 3.25 displays a graph showing change in pore pressure versus change in instantaneous phase. Both gas and water flood values are plotted and the range in instantaneous phase at each pressure level is due to the slight variations attributed to saturation change. The second order polynomial is fit to the combination of gas and water flood results, and is a good approximation for change in pore pressure. By using this relationship to solve strictly for pressure change, one can now input the determined pore pressure into the amplitude-pressure-saturation relationship for both water and gas injection.

Given the pore pressure estimates, the forward models discussed in the previous sections can be inverted to estimate changes in both gas and water saturation. Inverting the axis in figure 3.17 and fitting a function to the data, I solve for the increase in gas saturation as a function of two known values: change in pore pressure which is derived from the instantaneous phase attribute, and change in seismic amplitude which is measured directly from the data. This relationship and the comparison of the model to the data are

displayed in figure 3.26, and the mathematical details of the fitting function are outlined in Appendix A.
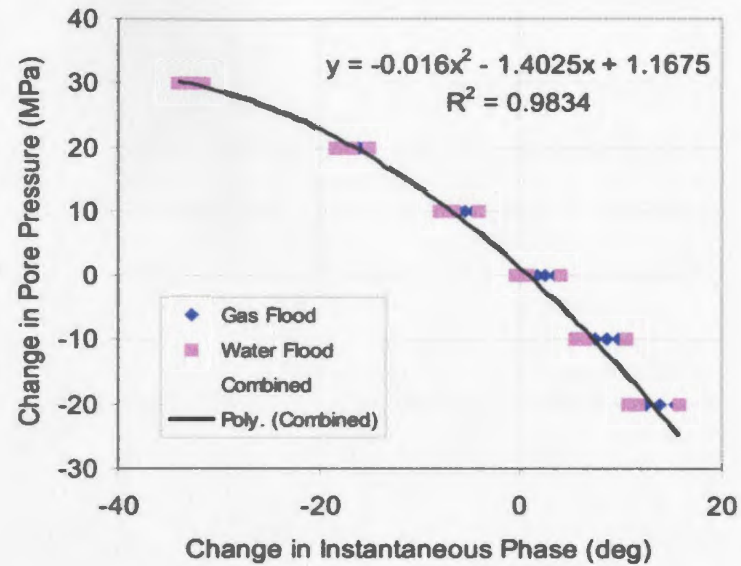
Figure 3.25. *Change in pore pressure as a function of change in the instantaneous phase attribute.*
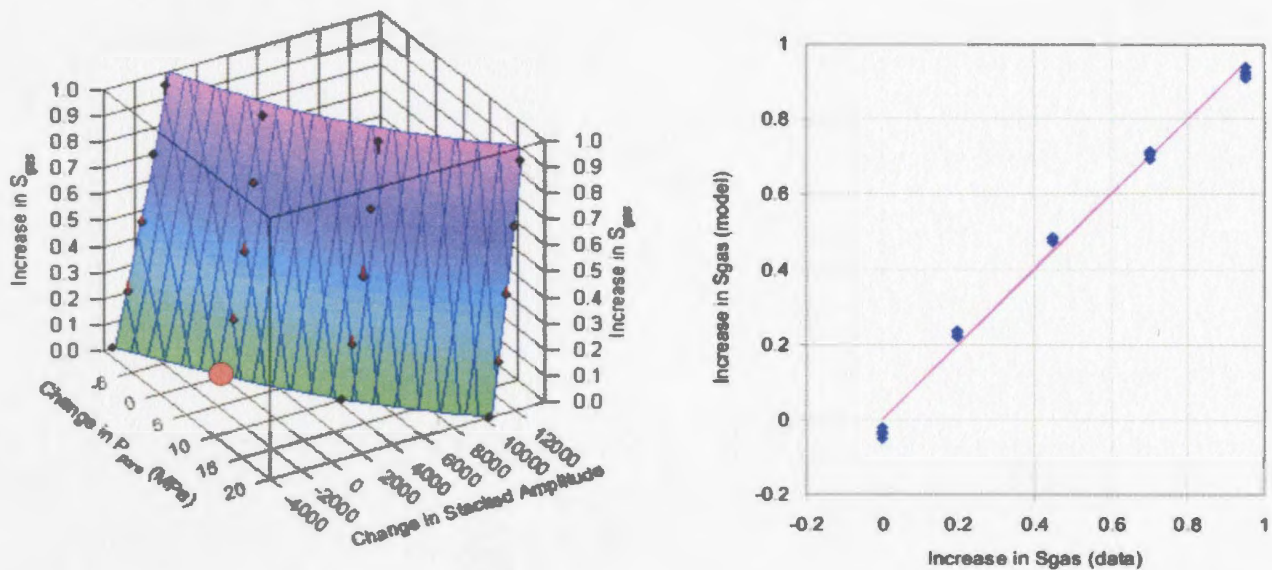
Figure 3.26. *Surface showing the increase in gas saturation as an inversion function of change in pore pressure and change in stacked amplitude. The figure on the right compares the model to the input data points. The details of this fit are available in Appendix A.*

Increases in water saturation in the reservoir can be approximated similarly by using the derived pore pressure and measured seismic amplitude change to solve for increase in water saturation as shown in figure 3.27. The mathematical details of this inversion function are available in Appendix B.
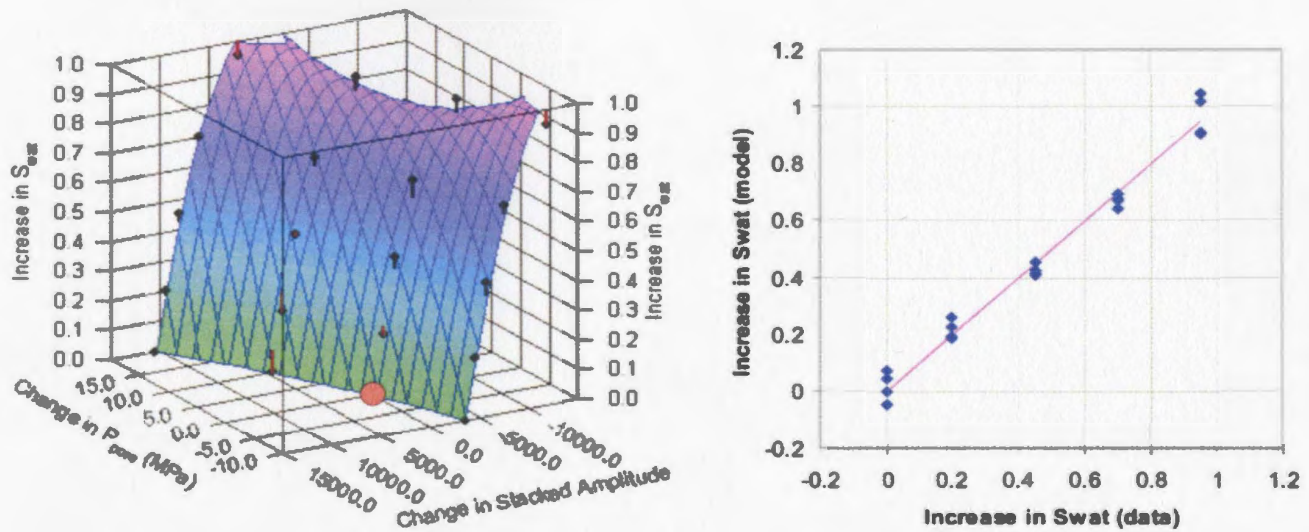
Figure 3.27. *Surface showing the increase in water saturation as an inversion function of change in pore pressure and change in stacked amplitude. The figure on the right compares the model to the input data points. The details of this fit are available in Appendix B.*

3.10 Conclusions

The modeling analysis presented in this chapter indicates that subtle production related variations in Hibernia seismic data are possible given the input reservoir parameters and expected production environment. The modeling predicts that the area around a gas injector with increased pore pressure and gas saturation cumulatively reducing the impedance of the reservoir is the best target for imaging potential Hibernia 4D seismic effects. In addition, a water flood with constant or slightly decreasing pore pressure may also be a good target. While Hibernia is not an ideal candidate for 4D seismology, the magnitude of 4D seismic response for some modeling scenarios suggests that it is possible that a detectable time-lapse signal may be obtained from some areas of the field. Due to the generally subtle nature of these modeled 4D seismic effects, the extraction of any potential time-lapse signal depends largely on a high degree of repeatability in the seismic data. In the following chapter, I present the elements and application of specialized 4D seismic processing with a goal of enhancing survey to survey repeatability in order to find the predicted subtle 4D seismic signals at Hibernia.

Chapter 4

Processing of 4D seismic data

4.1 Overview

The processing of 4D seismic data is an essential step to enhance survey repeatability leading to a more robust interpretation of the potential reservoir anomalies. This processing step is accomplished prior to interpretation and is displayed in the thesis flowchart in figure 4.1. Detection of seismic anomalies demonstrated by the modeling results in Chapter 3 requires a high degree of repeatability in the 4D surveys, and in this chapter, issues related to repeatability in the acquisition and processing of Hibernia 4D seismic data are addressed. The various methods that are employed to acquire 4D seismic data are presented. Different types of 4D seismic processing are then outlined, and the advantages and inherent limitations of these methods are discussed. A cross equalization processing flow, similar to one presented by Lumley et al. (2003) is then presented. This processing flow is then applied to the 1991 and 2001 Hibernia 3D seismic data sets, with the goal of enhancing repeatability to allow for a more robust 4D seismic interpretation. A section is allocated to each process in the cross equalization flow where the methods, application, and results are presented and discussed. In addition, qualitative and quantitative quality control is displayed for each processing step. Finally, based on the cross-equalization results, I assess the general suitability of these datasets for extracting coherent production related 4D seismic signals.
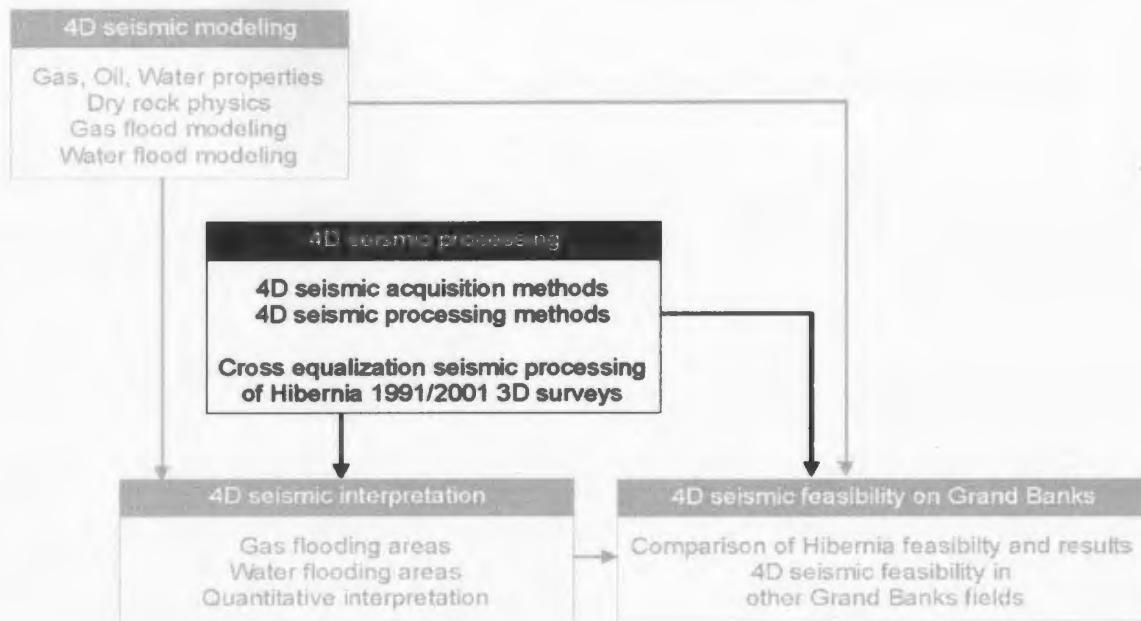
Figure 4.1. *Thesis outline flowchart. 4D seismic processing is required to enhance repeatability in the seismic datasets to allow for a more robust interpretation. By examining the general repeatability of the data in this study, the conclusions drawn can add to the discussion about the applicability of this method to other Grand Banks fields.*

4.2 Introduction

The general repeatability of the seismic data is fundamental to the success of any 4D seismic program (Jack, 1998). Multiple seismic datasets acquired over the same area at different times will inherently contain both repeatable and non repeatable signals. These repeatable and non-repeatable seismic signals are a function of differences in acquisition, changes in surface conditions, processing differences, random noise, and reservoir changes (Lumley, 2001). The goal in 4D seismic processing is to reduce the contribution of acquisition, processing, and noise, thereby enhancing seismic anomalies associated with dynamic reservoir properties.

4.3 Acquisition issues

As seismic survey design can play a key role in the imaging of subsurface geology, similar acquisition parameters can be important to the repeatability of multiple seismic surveys. According to Lumley et al. (2003), 4D seismic acquisitions can be subdivided into three categories: legacy, re-shoot, and 4D-design. A legacy 4D seismic program is where two or more 3D seismic surveys are acquired over the same general area with no consideration given to future 4D seismic application. A re-shoot 4D seismic program, is a program in which the original acquisition was not acquired with consideration of 4D seismic, but subsequent surveys were designed with some acquisition parameters optimized for 4D seismic purposes, such as shooting direction and grid alignment. The Hibernia data examined in this thesis is in this category. Finally, 4D seismic design surveys are the case where the original survey and all subsequent seismic surveys are acquired and processed with similar parameters optimized for reservoir monitoring purposes. In some circumstances, these 4D design surveys are being acquired with permanent receiver installations (Greaves and Fulp, 1987). These optimized acquisitions involve the use of ocean bottom cables for marine surveys, and buried/cemented geophones for land surveys (Pullin et al. 1987). These acquisition enhancements can increase repeatability, allow for shear wave acquisition in marine environments, and decrease the acquisition to interpretation time.

Even with the most repeatable acquisition parameters, Ebrom et al. (1997) suggest that the variability in reflection amplitude for multiple acquisition times is at least 3% for

streamer data. He contends that this inconsistency lies primarily in the seismic sources, and differences in recording equipment manifest only as a secondary effect. In addition noise from waves, wind, vessels, and drilling operations can also contribute to seismic noise in acquisition and can be difficult to fully attenuate in processing.

In this research, I use two 3D seismic surveys, acquired in 1991 and 2001, for 4D seismic analysis in the Hibernia oil field. As oil production in the field commenced in late 1997, the first survey was acquired prior to any production, while the second was acquired approximately four years into production. Table 4.1 summarizes acquisition parameters for the two surveys, which were acquired by marine seismic vessels equipped with airgun arrays and streamers. The similarities between the two surveys include that they were acquired along the same SSW-NNE shooting azimuth and matching parameters in source type, source depth, cable depth and sample rate which was 2 ms, but was re-sampled to 4 ms during processing. Although there are some azimuthal variations due to the increased number of streamers in the second survey as well as an undershot area surrounding the Hibernia platform, repeatability is enhanced by shooting the two surveys along a similar azimuth, allowing for more consistent seismic ray path trajectories. Differences in acquisition are numerous, including a larger airgun volume for the second survey, a longer streamer, increased fold, and higher recorded frequencies. The larger airgun volume and increased fold in the second survey yield a better signal to noise ratio at depth versus the original survey. In addition, two vessels were required to undershoot the platform as shown in figure 4.2, and as a consequence the azimuthal orientation of the

seismic ray paths are unlike the more in-line acquisition of the pre-production data. The processing discussed in the next section attempts to equalize the two seismic surveys to account for differences in some of these acquisition parameters.

Parameter		Hibernia 1991 3D	Hibernia 2001 3D
Source Data			
Source		Dual Airgun Arrays Separation = 50 m	Dual Airgun Arrays Separation = 37.5 m
Source Volume		2 x 1910 cu in	2 x 3090 cu in
Average Source Depth		6 m	6 m
Shotpoint Inverval		25 m	18.75 m
Instrument Data			
Sample Rate		2 ms	2 ms
Record Length		6 s	6.14 s
Filter	Low cut	Out	4.5 Hz / 12 dB/Oct
	High cut	128 Hz / 72 dB/Oct	206 Hz / 276 dB/Oct
Primary Navigation		DGPS	DGPS
Fold		30	60
Cable Data			
Cable Length		2 x 2975 m	8 x 4500 m
Cable Depth		7 m	7 m
Group Inverval		25 m	12.5 m
Number of Groups		240 (120 x 2)	2880 (360 x 8)
Near Group offset		230 m	300 m
Undershooting		No	Yes

Table 4.1. *Acquisition parameters for the 1991 and 2001 Hibernia 3D seismic surveys.*
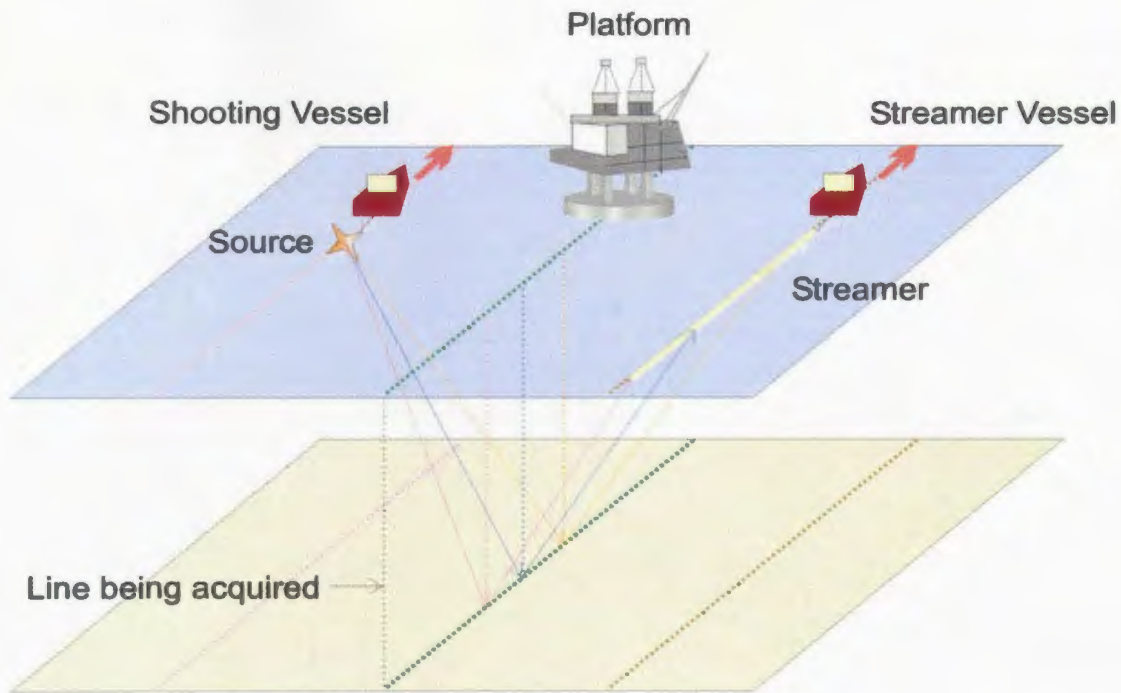
Figure 4.2 *Three dimensional schematic diagram showing principle of undershooting. One vessel tows only a source, while the other only a streamer. By sailing side by side, the vessels can acquire a line that runs underneath existing, unmovable facilities, in this case the Hibernia platform.*

4.4 Processing issues

Once seismic acquisition is complete, quality 4D seismic processing is vital to increase repeatability and recover a meaningful 4D seismic signal. Prior to any 4D seismic reservoir interpretation, the seismic differences outside of the reservoir must be minimized (Ross and Altan, 1996; Landro, 1999; Lumley et al., 2003) through processing, leaving a more accurate representation of production related effects in the reservoir. There are currently three primary methods that have been established to accomplish this data balancing: poststack cross equalization, prestack "parallel" processing, and 4D simultaneous processing (Lumley et al., 2003).

4.4.1 Prestack methods

If the seismic data available is prestack, the two surveys can either be parallel or simultaneously processed using the same processing flow. In parallel processing, the prestack datasets are processed independently but follow the same processing flow and have identical or very similar parameters. With simultaneous processing, the datasets are merged at various processing steps to create a single set of operators which is then simultaneously applied to both datasets (Lumley et al., 2003). Due to the nature of the merged design operators using both datasets at the same time, simultaneous processing requires a high degree of repeatability between surveys and is normally applied to 4D design projects.

These prestack methods enhance repeatability (Johnston et al., 2000), but eliminate from the newer dataset acquisition enhancements that may have been made since the original survey. These enhancements can include elements such as a longer streamer length which may be reduced (in processing) to the same length as the original to allow for a common offset range (Ross and Altan, 1997), and the frequency content, which must be reduced to match the lowest common frequency of the two surveys. A major benefit of parallel or simultaneous processing is the use of a common velocity model and migration algorithm which is critical to the consistent positioning of seismic energy (Johnston et al., 2000). In general, the application of parallel or simultaneous processing to 4D datasets enhances dataset to dataset repeatability as many seismic differences due to acquisition can be equalized during the prestack processing phase (Koster et al., 2000).

4.4.2 Poststack methods

The other type of processing method used for 4D seismic surveys is called poststack cross equalization (Ross et al., 1996; Lumley et al., 2003). This method is faster and less expensive than the prestack parallel method as the seismic data cubes are equalized only in the poststack domain. Because the data is only equalized poststack, some differences attributed to prestack processing can only be extraneously addressed in this type of equalization (Johnston et al., 2000). As a result, prestack equalization is generally considered more robust and suitable for quantitative reservoir property estimation from 4D seismic. Nevertheless, poststack cross-equalization has been shown to increase repeatability and interpretability of 4D seismic data (Johnston et al., 2000; Lumley et al., 2003).

There have been several methods presented for accomplishing this poststack seismic cross equalization. Ross et al. (1996) present a way to equalize the datasets utilizing a variety of match filters. In this method, the matching filter is optimized from a design window selected outside the reservoir and then applied to the entire dataset. While match filters can provide good dataset to dataset correlation, they can be unstable in noise (Lumley et al., 2003) and the matching rationale can lack physical justification. Lumley et al. (2003) present a step by step equalization approach that does not utilize match filters, but processes the poststack datasets by designing operators using non-reservoir data (ie. above the zone of interest) that attempt to minimize differences in a number of categories, such as static adjustments and migration corrections. This cross equalization

processing method is selected for this research because of the relatively noisy 1991 Hibernia seismic data cube, the sensitivity to noise in the Ross (1996) match filter method, and the ability to provide quality control at each processing step in the cross equalization method presented by Lumley et al. (2003). Promax 4D software is used for the cross equalization processing.

4.5   Cross equalization seismic processing flow

Sections 4.3 and 4.4 outline differences in seismic data acquisition and processing that can cause a time-constant, non-reservoir, lithologic unit to produce a dissimilar seismic reflection in the 4D seismic datasets.   The cross equalization seismic processing flow contains a number of individual processes designed to enhance overall seismic data repeatability by balancing and equalizing elements of each seismic dataset. By optimizing the equalization process on parameters extracted from the non-changing, non-reservoir overburden of the datasets, the overall repeatability of the seismic data can be enhanced and potential reservoir anomalies more confidently analyzed.   The cross equalization processing flow that is used in this study is outlined below and detailed in the sections to follow.

1. *Common positioning* - Placing the datasets on a common grid and reducing input seismic data to common live samples to both datasets

2. *Amplitude envelope balancing* – Smooth amplitude balancing of datasets

3. *Frequency balancing* – Balancing the frequency content to a range common to both datasets

4. *Global shifting* – A single parameter shift (e.g. adding 4 ms and 12.5 m in x to one entire seismic volume) that moves one dataset relative to the other

5. *Static shifting* – Trace by trace statics adjustment

6. *Phase shifting* – Trace by trace phase adjustment

7. *Volume warping* – 3D adjustment of datasets to account for differences in 3D event positioning

This flow is applied to the Hibernia 1991 and 2001 poststack 3D seismic datasets with the survey areal extent shown in figure 4.3. These datasets have been independently prestack processed including prestack time migrations with differing velocity models. The area chosen for poststack cross equalization is indicated by the white outline and includes most of the producing portion of the Hibernia reservoir. The arbitrary line running from northwest to southeast across a gas injection zone is the seismic line displayed for visual quality control purposes in each of the following sections. The quality of the cross equalization processing is also measured quantitatively by two measures which are displayed graphically in each processing section. The first measure compares the RMS amplitude extractions from a window above the reservoir (1000-2500 ms) of the 1991 and difference (2001-1991) seismic volumes.   The ratio of the RMS amplitude of the difference to the base survey (2001-1991)/(1991) decreases with increasing repeatability. The second measure is called the 4D signal to noise ratio (Lumley, 2004), which is extracted on the difference and is the ratio of the RMS amplitude of a 100 ms window centered on the reservoir to an equally sized window above the reservoir (1550-1650 ms) at a time window that has similar RMS amplitude as the reservoir. Prior to processing, the 4D signal to noise ratio is approximately 1, and as the reservoir anomaly is enhanced relative to the background, the ratio rises. For each processing step, optimal parameters were determined through a series of parameter tests

utilizing a combination of visual and quantitative measures (RMS difference amplitude,

4D signal/noise) for quality control.
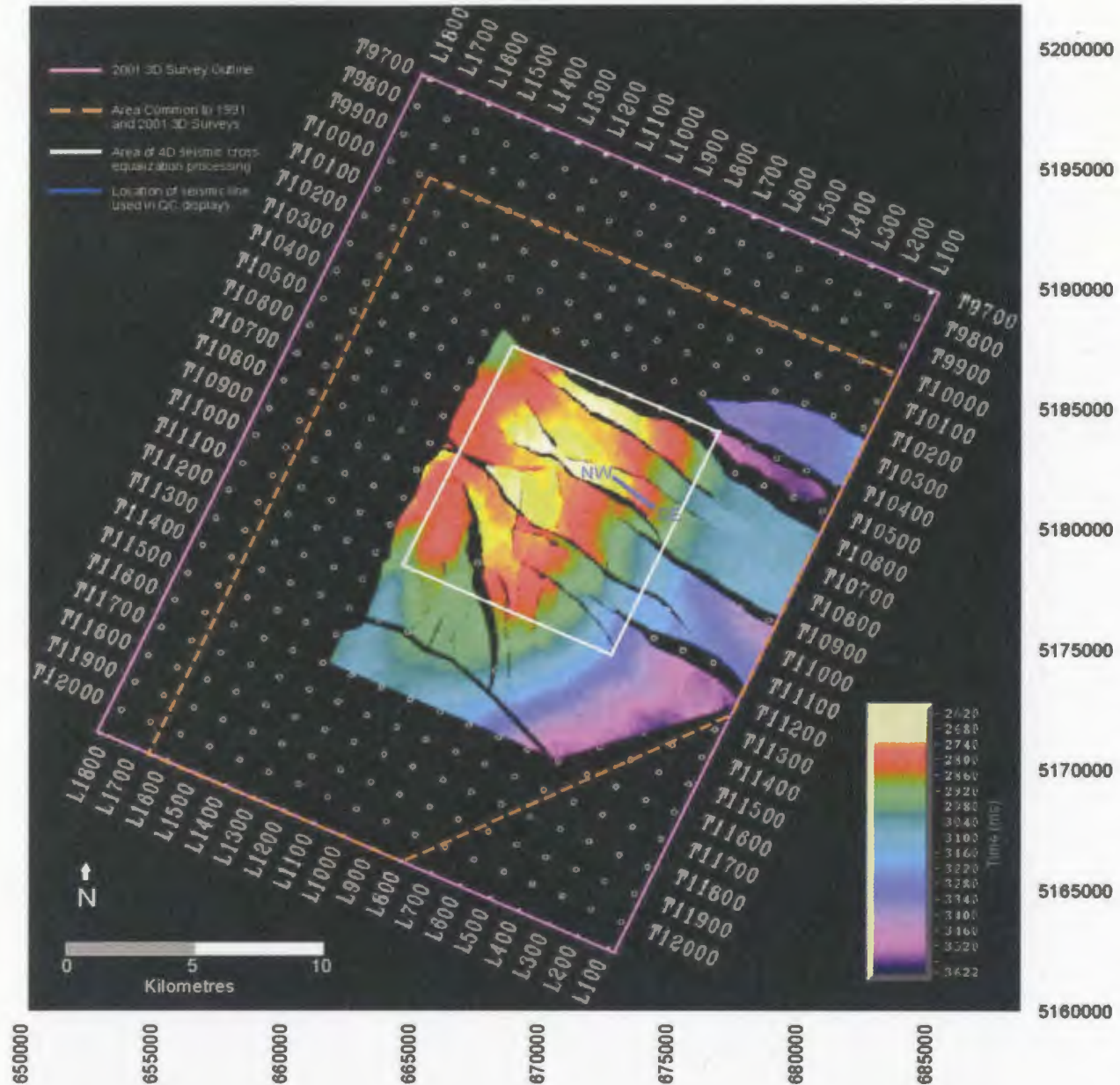
Figure 4.3. *Map of the Hibernia oil field's 3D seismic area with the Fortune Bay (base reservoir) time horizon displayed. The white outline indicates the area selected (line 500-1200 and crossline 10400-11200) for cross equalization processing. This area encompasses most of the producing Hibernia reservoir area and is approximately 87.5 km². The blue line running from NW to SE indicates the location of a seismic line through a gas injection area used for all quality control displays in this chapter.*

4.5.1 Common positioning

Consistent positioning of data from survey to survey is of primary importance to 4D seismic datasets as analysis of 4D data assumes data in one survey is spatially equivalent to the analagous trace in another survey.   To achieve this goal, a process of re-gridding the datasets to a common spatial grid is undertaken.   The 2001 Hibernia 3D seismic survey was acquired along the same azimuthal orientation as the original 1991 3D survey. The 2001 survey was then re-gridded by the processing contractors from a bin size of 6.25m x 18.75m to 12.5m x 12.5 m, which matched it by CDP location to the 1991 3D seismic survey.   The 1991 and 2001 poststack 3D seismic datasets were on a common grid when received at Memorial University for this research.   With the datasets sharing a common grid, it is important to check that live traces in the 1991 survey matched the live portion of traces in the 2001 survey.

To ensure common live samples, subset volumes of the 4D surveys that have no seismic data or data from only one survey are muted to ensure the processing flow is optimized and calculated based on live data samples common to both surveys (Cole, 2001; Lumley, 1995). This is accomplished by identifying in each volume the first sample in a trace that has amplitude exceeding a specified threshold value. Once a threshold value has been exceeded, the remainder of the trace is live and all subsequent samples are retained for further processing.   This amplitude threshold is selected to be greater than the noise in the water column so the trace isn't activated until a geologic boundary is encountered. Due to the acquisition orientation and the loss of near offsets in the undershot area (figure

4.2), the first live sample is much later in time when compared to the water bottom time of approximately 80 ms (20 samples). The 1991 and 2001 first live sample maps are compared in figure 4.4. The highest first live sample from each trace in the 1991 and 2001 surveys is selected as the first live sample for both surveys, above which all samples are muted. Once complete, the seismic datasets are on a common grid with equivalent live data samples. A section from the datasets and their differences is shown in figure 4.5. This seismic display shows the imbalance in amplitudes between the 1991 and 2001 datasets, and not surprisingly, the difference amplitude is nearly as large as the 1991 input seismic amplitude. Anomalies can be seen at the reservoir level, but anomalies of similar amplitude are identified in non-reservoir areas above the gas injection zone, the location of which is bounded by the dashed rectangle.
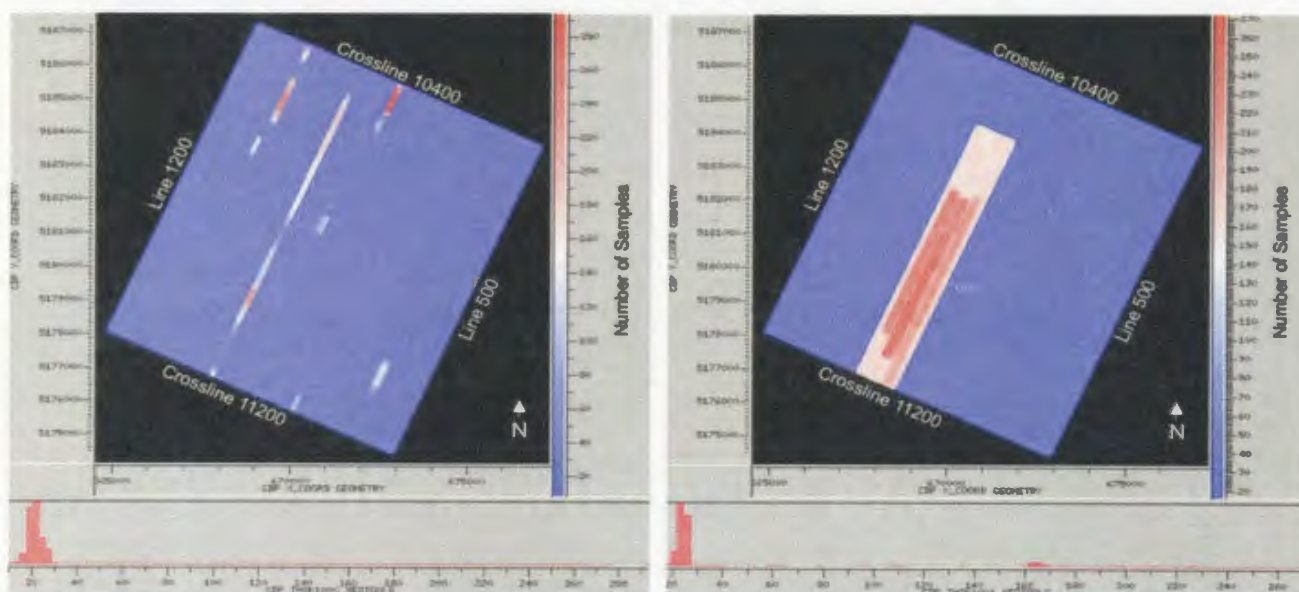
Figure 4.4. *First live sample maps from the Hibernia 1991 (left) and 2001 (right) 3D seismic surveys. The cluster of values around 20 represent the approximate water bottom time of 80 ms. On the 2001 survey, the undershot area is clearly visible by the increased time for the first live sample.*
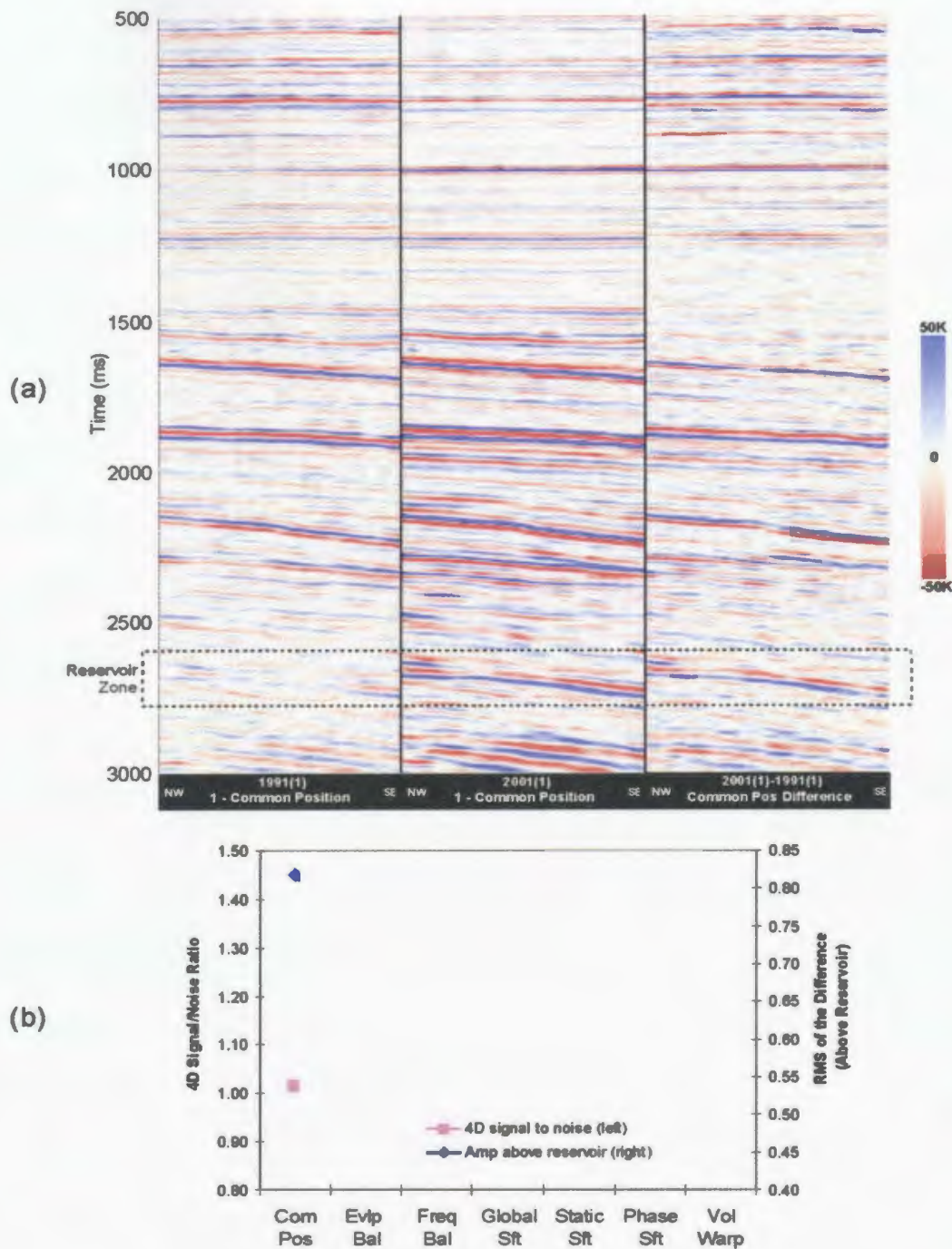
Figure 4.5. (a) *A three panel seismic display showing the same Hibernia seismic line. Left to right: 1991 common positioned seismic data, 2001 common positioned seismic data, and the 2001-1991 common position difference. The reservoir levels are indicated by two arrows* **(b)** *The RMS amplitude ratio of the difference data to the input 1991 data is approximately 0.83 (right axis), while the 4D signal to noise ratio is 1.02 (left axis) meaning that the RMS amplitude of the difference is similar inside and above the reservoir zone.*

116

4.5.2 Amplitude gain balancing

Amplitude variations between surveys can be the result of a number of factors including but not limited to source sizes and signatures, gain functions, recording equipment, migration algorithms, and signal to noise ratio (Johnston et al., 2000). To address these issues, a three dimensional, smoothly varying amplitude envelope of each dataset is computed and compared (Adams, 2001). By allowing one dataset to adapt the smoothed amplitude envelope of the other, approximate equalization in amplitude can be attained. The filter dimensions for amplitude envelope smoothing are chosen to be sufficiently large as to not remove nor adversely attenuate reservoir related changes in the seismic data, however, some amplitude smoothing of a potential reservoir anomaly is inevitable.

The two Hibernia poststack seismic datasets used in this study were unfiltered and gained independently by the processing companies prior to arrival at the university. By visual inspection in figure 4.5, the datasets have been gained differently, with the 1991 volume having relatively higher amplitudes nearer the surface, while the 2001 data has greater amplitudes at depth. For these datasets, a 3D filter smoothing 85 inline traces, 45 crossline traces, and 100 time samples is chosen for the amplitude envelope calculation. The preference to smooth along inline directions is two fold: the strike of the structure is approximately in the in-line direction, and secondly, the in-line oriented undershoot area requires different gain parameters from the rest of the data. Once a smoothly varying amplitude envelope is computed for each dataset as shown in figure 4.6, a ratio volume (2001/1991) of the two amplitude envelope cubes can be produced (figure 4.6). The

1991 dataset is then multiplied by this envelope ratio volume to adjust its gain so it has a smoothly varying amplitude envelope similar to the 2001 dataset. (Adams, 2001) While amplitude balancing is a statistical process that doesn't have a direct physical basis, the method does enhance the repeatability of the data as seen in figure 4.7(a) by correcting relative differences in amplitude gain between the two surveys. The reservoir zone is included in the envelope calculations and as a result 4D seismic anomalies will contribute slightly (with a large balancing window) to the amplitude corrections, thus relatively reducing the magnitude of the anomalies after balancing. After the amplitude gain balance, the RMS amplitude in the difference section was reduced while the 4D signal to noise ratio was enhanced from 1.02 to 1.08 as shown in figure 4.7(b).
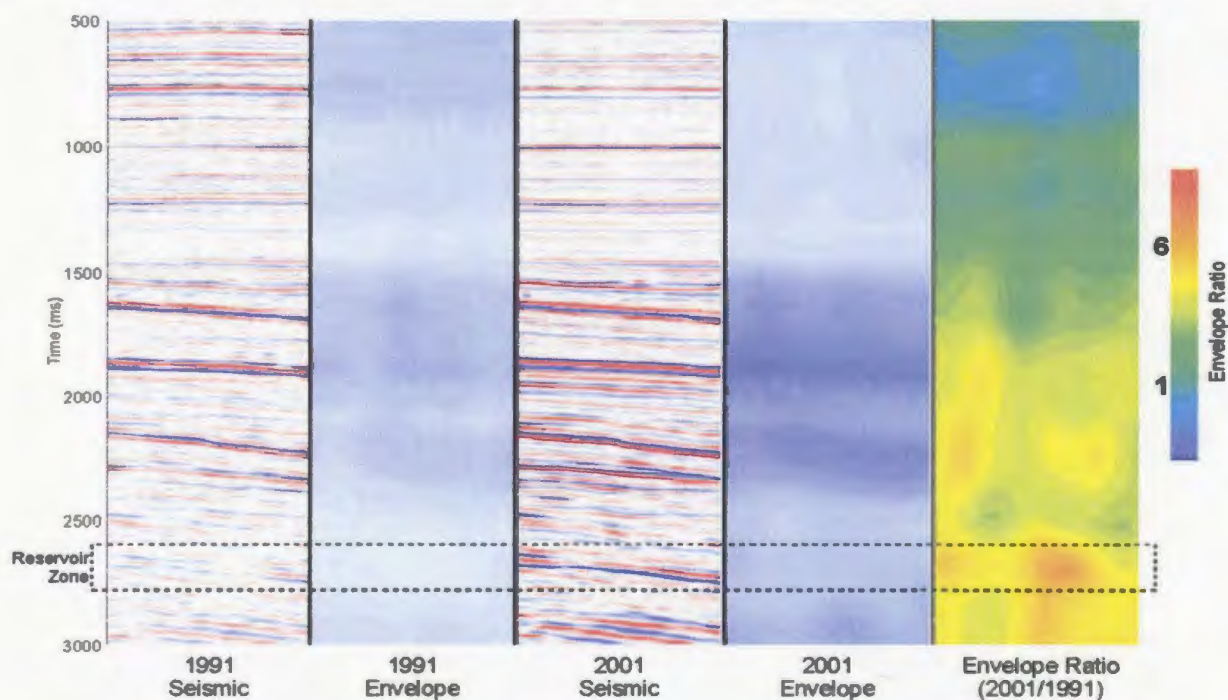
Figure 4.6. *Amplitude envelope balancing shown in a 5 panel display. Left to right: 1991 seismic data, smooth amplitude envelope for 1991, 2001 seismic data, smooth amplitude envelope for 2001, and 2001/1991 ratio of smooth amplitude envelopes. Notice the amplitudes of the 1991 dataset are stronger nearer the surface, while the 2001 has approximately 6 times the amplitude of 1991 deeper in the section.*

118
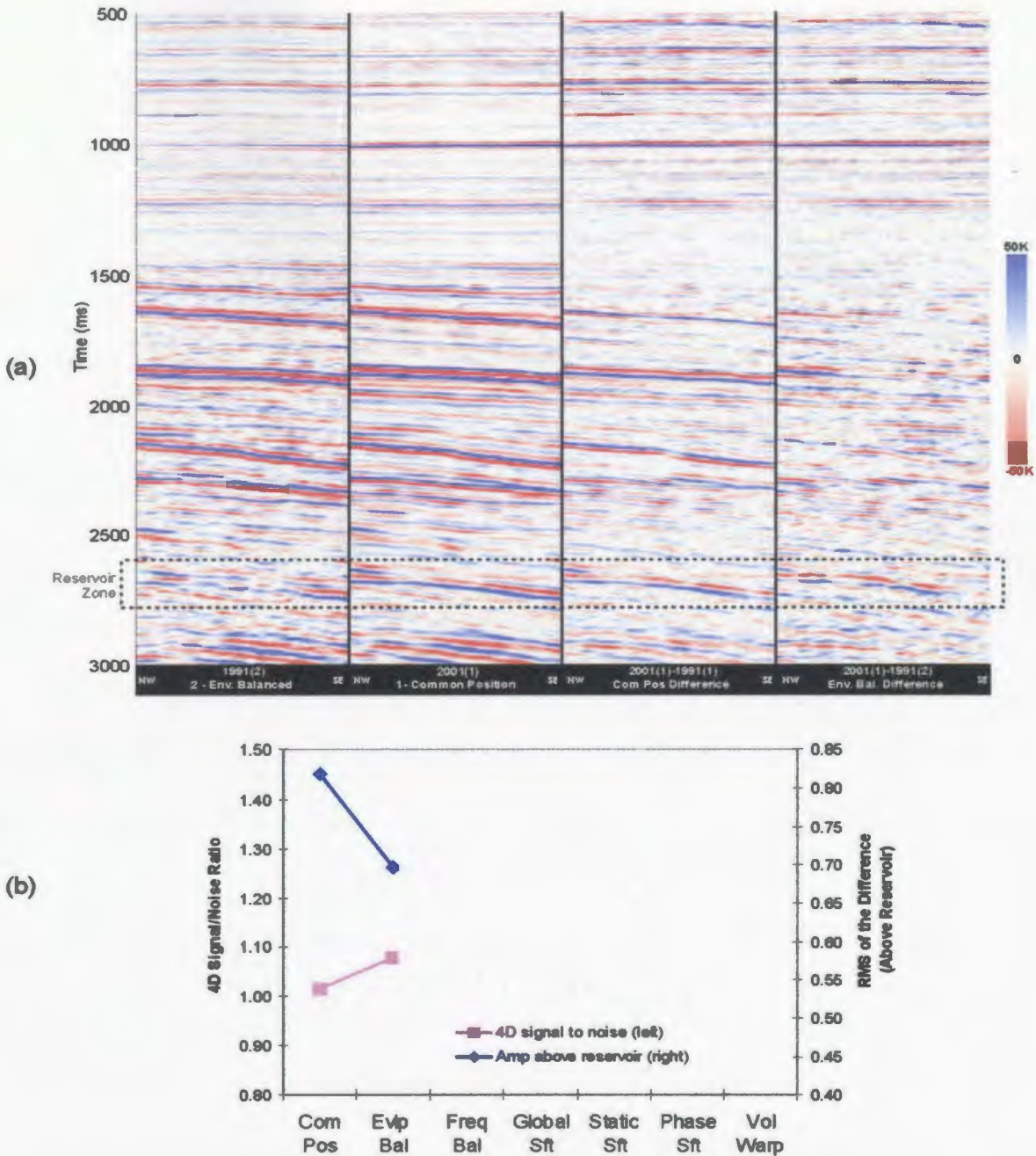
Figure 4.7. (a) *A four panel seismic display showing a Hibernia seismic line. Left to right: 1991 amplitude envelope balanced seismic data, 2001 common positioned seismic data, the 2001-1991 common position difference, and the 2001-1991 envelope balanced difference. The reservoir level is indicated by the dashed box. While residual difference is visually reduced, it is also indicated numerically* **(b)** *in the above graph that demonstrates that amplitude envelope balancing reduces the RMS difference amplitude above the reservoir and increases the 4D signal to noise ratio.*

119

4.5.3 Frequency balancing

When comparing seismic datasets for reservoir monitoring purposes, it is important that the resolution of the individual datasets be as comparable as possible. Often a more modern survey will have broader frequency spectrum content due to improved survey design and advancements in acquisition technology; however both prestack and poststack processing can alter frequencies of both datasets. Before any direct comparison can be made, it is crucial to balance the frequencies of the 4D seismic datasets to a common range (Lumley et al, 2003).

The Hibernia 1991 3D seismic survey recorded all frequencies to 128 Hz, while the 2001 survey had an acquired range from 4.5 to 208 Hz (table 4.1). In the individual prestack processing that was done to each dataset, these frequency ranges were narrowed from the acquisition values, but in general the 2001 seismic data has more data in the higher frequency range, while the 1991 data is weighted more heavily in the lower frequencies as seen in figure 4.8(a-b). Using a design window above the reservoir (1000-2500 ms), frequency balancing was performed on the datasets that reduced the higher frequencies in the 2001 dataset (figure 4.8(d)), and attenuated the contribution of lower frequencies in the 1991 dataset (figure 4.8(c)). The 1991 and 2001 frequency spectra are more similar after this frequency balance has been performed. The balancing of the frequency spectra improves the repeatability of the seismic data by reducing the residual RMS difference (2001-1991) by over 4% from the previous gain balancing processing step (figure 4.9(b)),

while the 4D signal to noise ratio is enhanced. Visually, a slight improvement can be noted in the difference section in figure 4.9(a), particularly in the lower amplitude events.

(a)

(b)

(c)

(d)
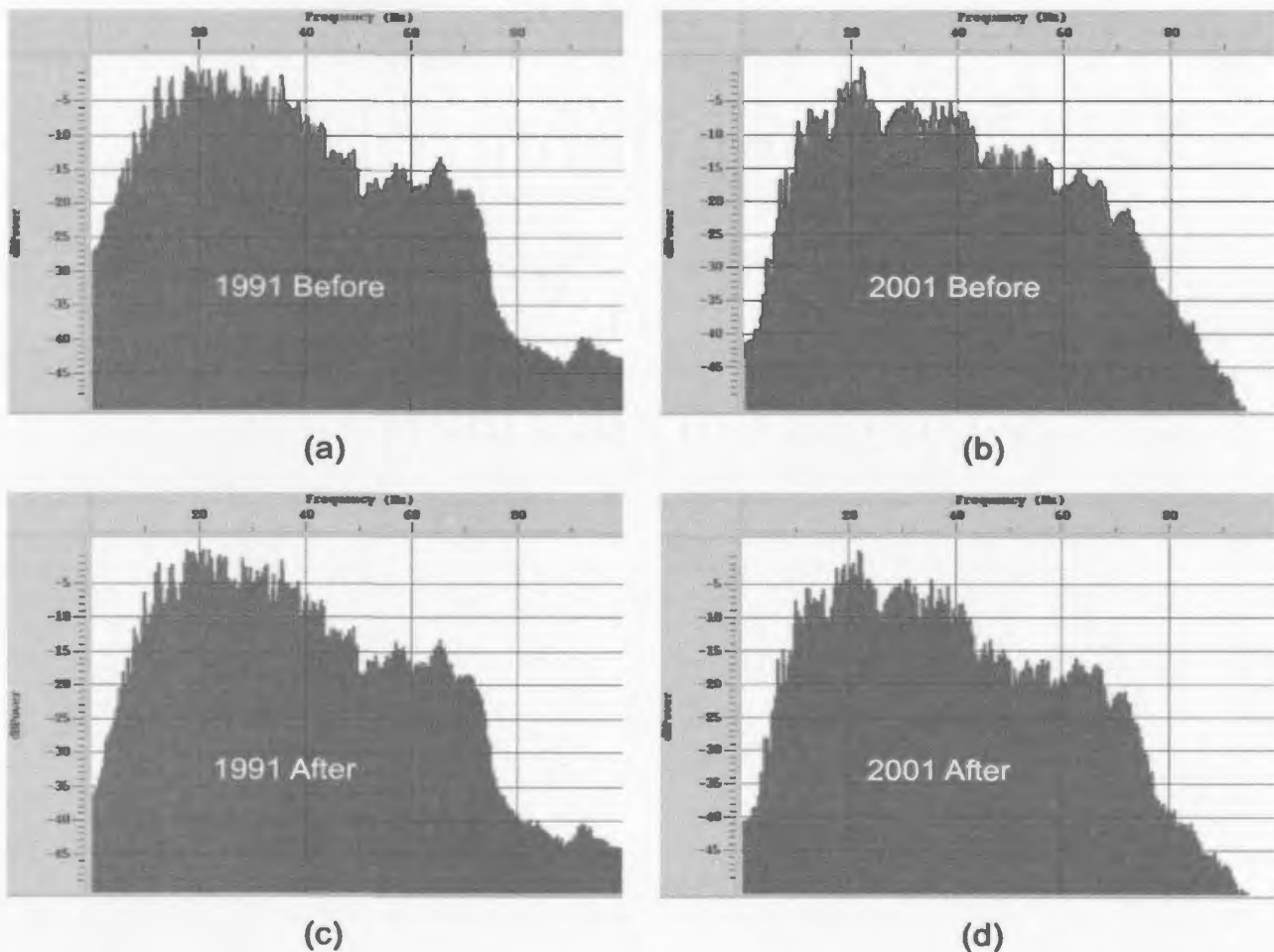
Figure 4.8(a-d) *Frequency spectra for* **(a)** *1991 data before frequency balancing,* **(b)** *2001 data before frequency balancing,* **(c)** *1991 data after frequency balancing, and* **(d)** *2001 data after frequency balancing. The lower frequencies in the 1991 data are reduced, while the higher frequencies in the 2001 are attenuated to bring the frequencies in both datasets to a common range.*

Figure 4.9(a) *A four panel seismic display showing a Hibernia seismic line. Left to right: 1991 frequency balanced seismic data, 2001 frequency balanced seismic data, 2001-1991 amplitude envelope difference, and the 2001-1991 frequency balanced difference. The reservoir level is indicated by the dashed box. While visual residual difference is marginally reduced, it is also indicated numerically **(b)** in the above graph that demonstrates that amplitude envelope balancing reduces the RMS difference amplitude above the reservoir and increases the 4D signal to noise ratio.*

4.5.4 Global shift balancing

Global differences in position can exist between 4D seismic datasets for a number of reasons. Residual differences in navigation can be caused by streamer position error and the type of positioning technology used. In addition, the time datum can vary for separate surveys as a result of varying tides, salinity, and temperatures (Jack, 1998). A global shift balance is designed to shift one dataset relative to the other with single bulk parameter in the following dimensions: inline, crossline, time, and phase.

The positioning data in the 2001 Hibernia survey is considered by the field operator to be more accurate than the 1991 survey, consequently, for this study I have chosen to use the 2001 survey as the reference volume to which the 1991 will be shifted. The optimized shifting parameters are first calculated and then applied to the data (Lumley et al., 2003). For the frequency and amplitude balanced poststack Hibernia volumes, a global shift of 0 inline, 0 crossline, 0 time samples, and a +40 degrees phase shift are the optimized parameters calculated by the global shifting algorithm. This phase shift is applied to the 1991 data as shown in figure 4.10(a). While difficult to detect visually in the difference section in figure 4.10(a), figure 4.10(b) demonstrates the RMS amplitude of the difference section was slightly reduced with the 4D signal to noise ratio being slightly enhanced. With the amplitude balance, frequency balance, and global shift applied to the data, the difference RMS amplitude above the reservoir has now been reduced by 22.4% over the initial difference prior to cross equalization processing, and the 4D signal to noise ratio has been enhanced from 1.02 to 1.23.
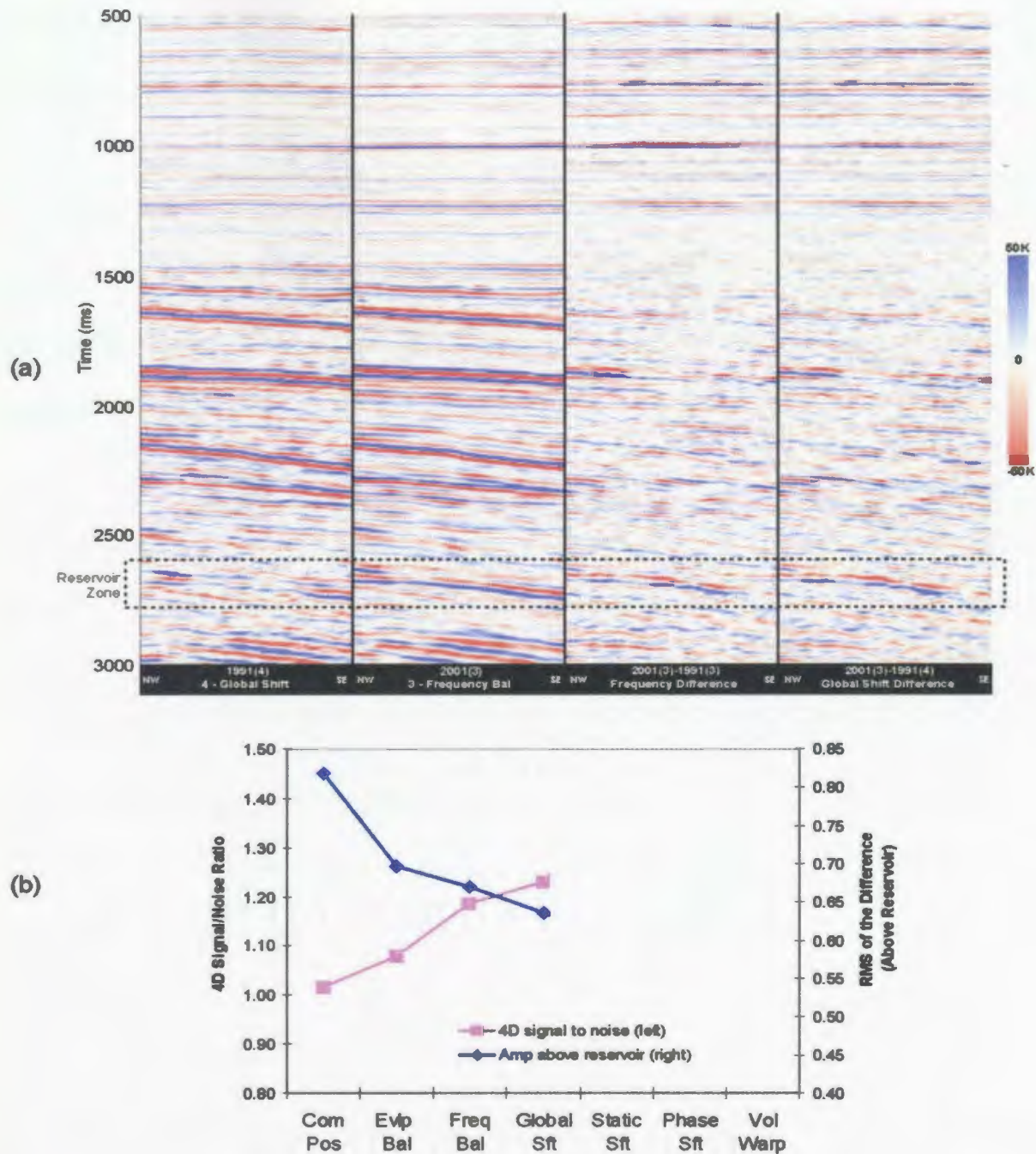
Figure 4.10(a) *A four panel seismic display showing a Hibernia seismic line. Left to right: 1991 global shift balanced seismic data, 2001 frequency balanced seismic data, 2001-1991 frequency balanced difference, and the 2001-1991 global shift balanced difference. The reservoir level is indicated by the dashed box. While visual residual difference is reduced slightly, it is also indicated numerically* **(b)** *in the above graph that demonstrates that amplitude envelope balancing reduces the RMS difference amplitude above the reservoir and increases the 4D signal to noise ratio.*

4.5.5 Static shift balancing

Differences in acquisition parameters and environmental conditions can lead to vertical misalignment of traces spatially throughout 4D seismic volumes. Specifically, acquisition parameters such as geometry, shooting direction, gun delay time, and different recording parameters can vary in 4D surveys for the same location causing subtle shifts in vertical alignment of the traces. For marine settings, environmental elements such as variations in tides can change the travel time in the water column, and changes in ocean temperature and salinity can have a subtle effect on water velocity shifting the seismic data up or down slightly as all reflected seismic waves propagate through the water column twice (Rickett and Lumley, 2001). It is not practical to approach this problem from a deterministic viewpoint by calculating the contributing effects of tides, sea state, acquisition direction etc., so a statistical method is employed. Correction for these alignment errors is accomplished with a trace by trace static shift which shifts traces in seismic volume A to match the vertical alignment of the corresponding traces in seismic volume B over a specific overburden design window (Cole, 2001).

The Hibernia 3D seismic datasets were acquired ten years apart and for a duration of a few months each. Between and during the surveys, environmental conditions such as tides and sea state vary with time. The design window for optimization is chosen to be 1000-2500 ms, focusing the optimization on areas above the reservoir, but below any near surface anomalies and undershooting effects. The 1991 data is shifted to the 2001

data in this case and the field wide shifts are shown in figure 4.11. The computed shifts are relatively small, varying approximately +/- 1 sample, but are generally aligned along the in-line shooting direction, a result consistent with physical justification and one that has been observed in other marine 4D projects (Lumley et al, 2003). These shifts while small, have a fairly substantial impact in improving repeatability of the seismic data shown in figure 4.12(a). In particular, there is a large event on the difference section at approximately 1800 ms that has been attenuated or removed as a result of the static shift balancing. Figure 4.12(b) indicates this process reduces the residual RMS difference amplitude above the reservoir and significantly enhances the 4D signal to noise ratio, improving it from 1.23 to 1.39.
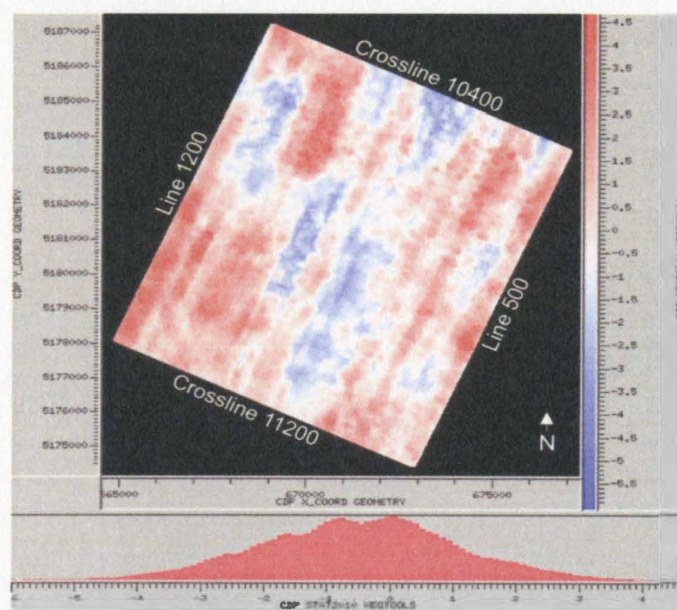
Figure 4.11 *Calculated static shift map of the Hibernia datasets. These trace by trace static shifts are applied to the 1991 data to balance it with the 2001 dataset. The shifts are relatively small (+4.5/-5.5 ms) and have an absolute maximum approximately equal to the sample rate of 4 ms. The orientation of these shifts is along the in-line sail direction. This indicates a relationship with time changing conditions that change the velocity of the water column such as tides, water temperature, and salinity as well as acquisition parameters associated with shooting in each direction.*

126

Figure 4.12(a) *A four panel seismic display showing a Hibernia seismic line. Left to right: 1991 static shift balanced seismic data, 2001 frequency balanced seismic data, 2001-1991 global shift balanced difference, and the 2001-1991 static shift balanced difference. The reservoir level is indicated by the dashed box. While visual residual difference is reduced slightly, it is also indicated numerically **(b)** in the above graph that demonstrates that amplitude envelope balancing reduces the RMS difference amplitude above the reservoir and increases the 4D signal to noise ratio.*

127

4.5.6   Phase shift balancing

Static and phase shifts are linked fundamentally, as they involve vertical shifting of the traces and are both performed in the frequency domain.   In this case, the trace by trace phase shift calculation is more sensitive to vertical mis-alignment of seismic data than the static shift, so it is employed following the static shift to correct for residual differences after the trace by trace static shift has been applied (Rickett and Lumley, 2001; Lumley et al, 2003).   The map in figure 4.13 displays the spatial distribution and subtle nature of the computed shifts (approximately +/- 20 degrees).   Similar to the static shifts, the phase shifts align spatially approximately along in-line shooting directions for reasons discussed in section 4.5.5.   Figure 4.14(a,b) demonstrates that the phase shift correction in the Hibernia data produces a negligible improvement in visual repeatability.
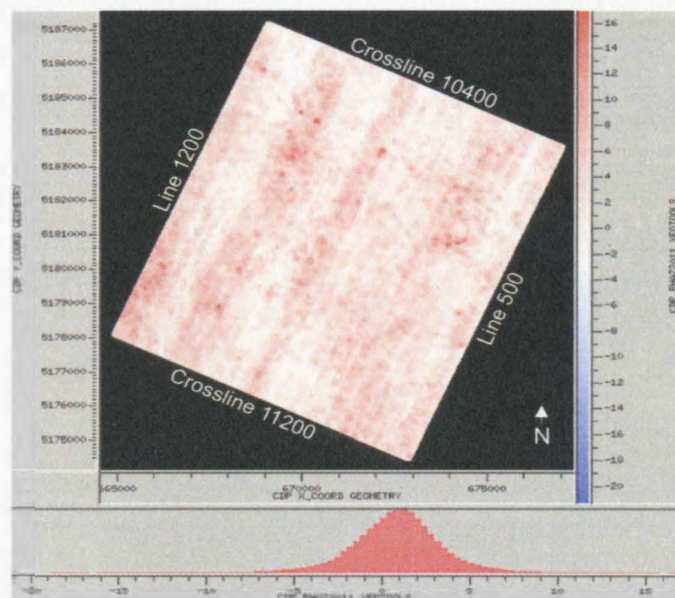
Figure 4.13 *Calculated phase shift map of the Hibernia datasets.   These trace by trace phase shifts are applied to the 1991 data to balance it with the 2001 dataset.   The shifts are fairly small (+/- 20 deg).   The orientation of these shifts is along the in-line sail direction.   This indicates both a relationship to physical causes as well as a residual "clean-up" of the static shifts which were also generally oriented in SW-NE trends.*
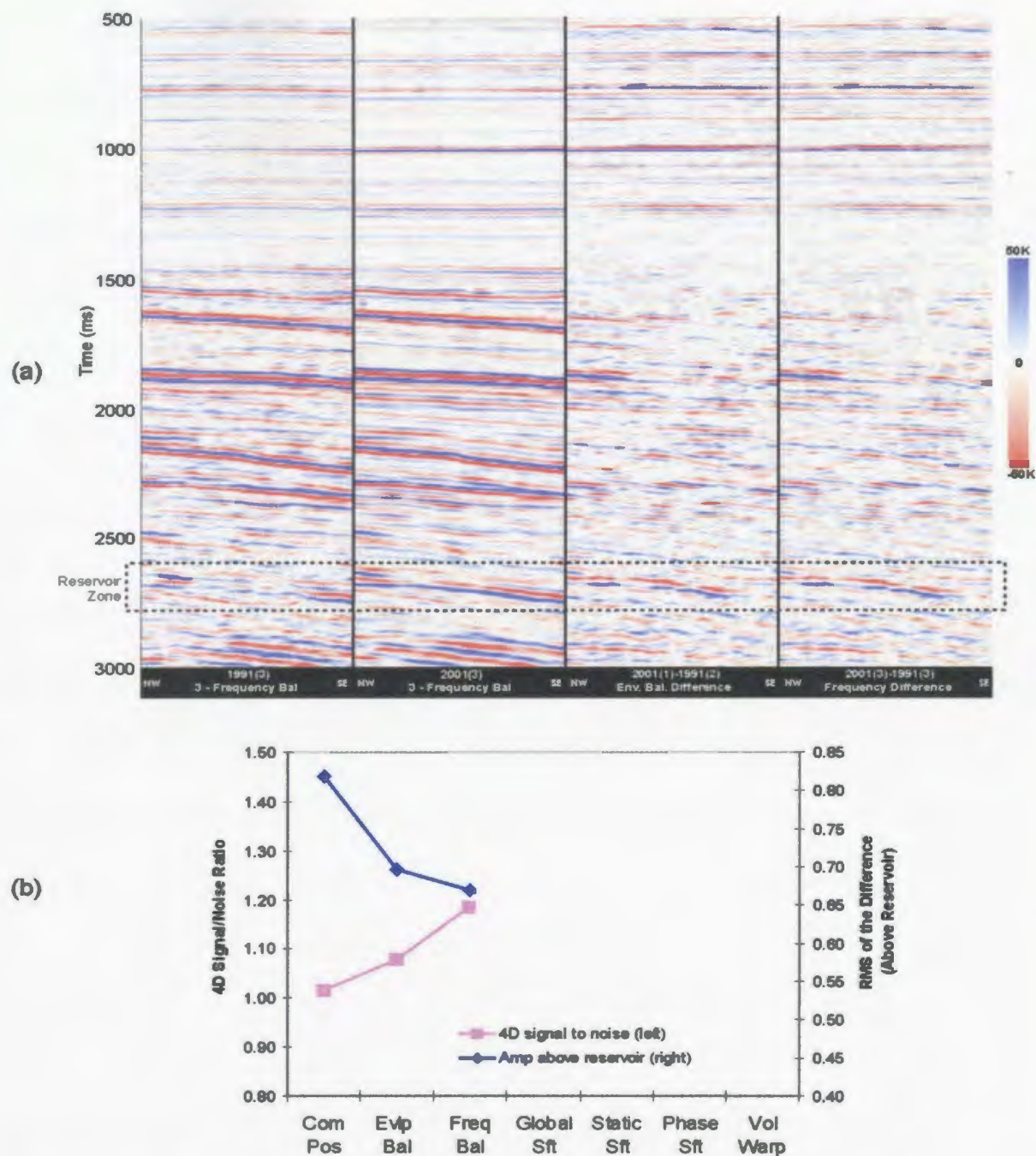
128
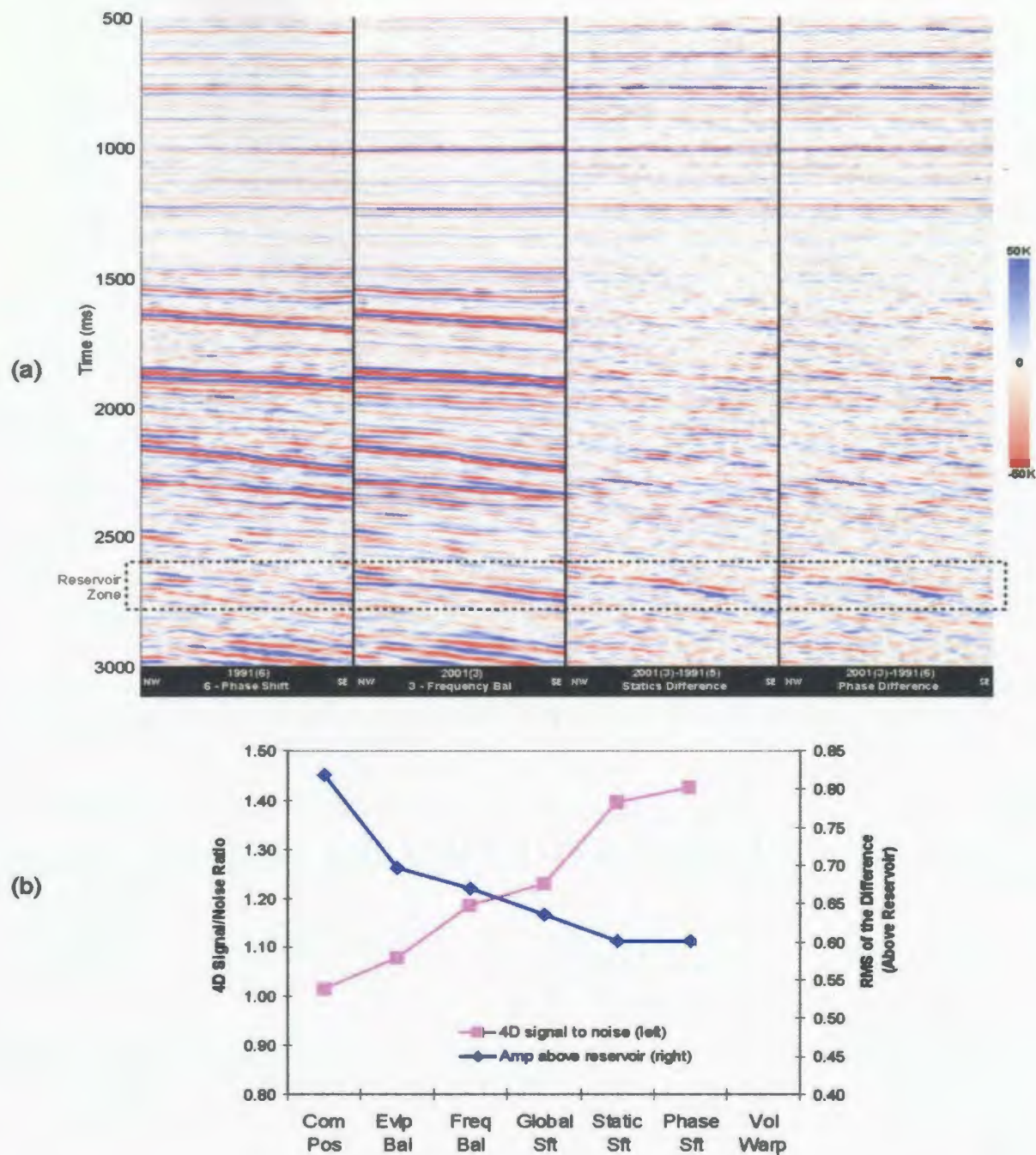
Figure 4.14(a) *A four panel seismic display showing a Hibernia seismic line. Left to right: 1991 phase shift balanced seismic data, 2001 frequency balanced seismic data, 2001-1991 static shift balanced difference, and the 2001-1991 phase shift balanced difference. The reservoir level is indicated by the dashed box. The visual residual difference is not improved for this step, but in (b) the 4D signal to noise ratio is increased slightly.*

4.5.7 Volume event warping

For optimal 4D seismic data positioning, a common migration method with a shared migration velocity model is applied to both datasets. By using a single offset range common to both surveys, these migrations place seismic events in both datasets in the same location spatially and in time thus enhancing repeatability. 4D seismic datasets that have been pre/poststack processed individually with poststack cross-equalization applied thereafter will have differences in seismic event positioning associated with the use of distinct migration methods and differing migration velocity models (Johnston et al., 2000). To correct for these potential differences due to migration, a poststack volume event "warping" process is applied to the data (Ricket and Lumley, 2001; Lumley et al., 2003). By using control points, the warping reshapes the seismic data in 3 dimensions (inline, crossline, and time) in a seismic volume to align more closely with the data in the other volume as shown in figure 4.15.
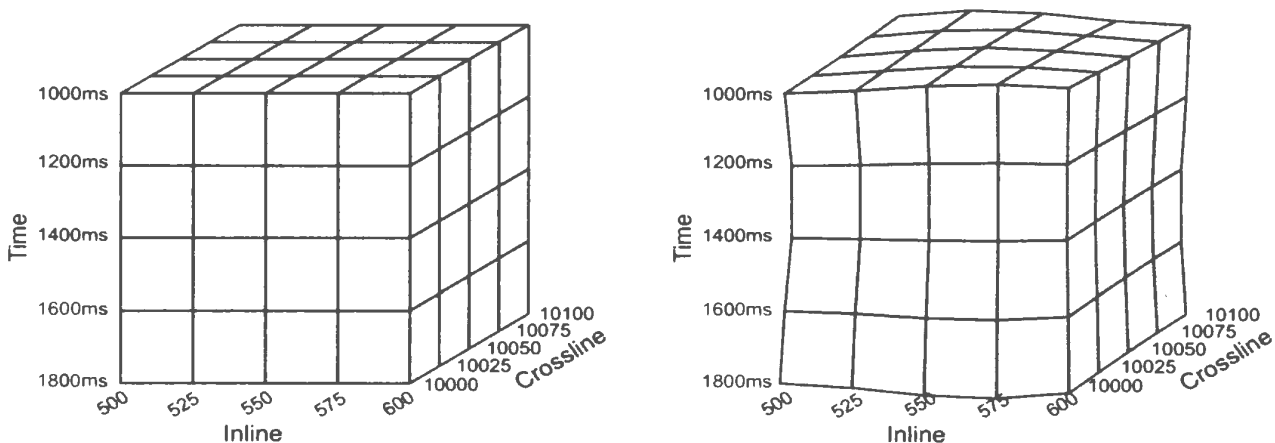
Figure 4.15. *Schematic 3D cubes showing the effect of the volume event warping cross equalization process. The diagram on the left shows a regularly spaced control mesh in the seismic volume prior to warping, while the right image shows the effect of moving these control point in the inline, crossline, and time dimensions with the original control mesh drawn in light gray. In the diagram, warp control points are output for every 25 traces (both inline and crossline) and every 200 ms in time.*

Filter size and maximum shift constraints are important parameters when warping seismic data. Sufficient filter size in each of the dimensions to smooth trace to trace variations caused by noise and other non-repeatable events is crucial for migration consistent warping of the data volume. In areas of the reservoir where production effects can induce seismic travel time changes, such as an area of gas injection, it should be noted that warping can attenuate or eliminate observable travel time change in the seismic data. It is therefore vital to view the seismic difference volumes before and after volume event warping in and below reservoir zones where production related travel time changes may occur.

The 1991 and 2001 Hibernia 3D seismic datasets were individually prestack time migrated using different migration velocity models. Consequently, the positioning of reflection events is not spatially uniform throughout the volumes, even after computation and application of the trace by trace static and phase shifts. To correct these positional errors, a volume event warping correction is performed on the 1991 dataset using the 2001 as the master dataset to which the 1991 will be matched. The warp calculation filter has the following dimensions: 40 traces inline (500 m), 25 traces crossline (312.5 m), and 100 time samples (400 ms). The inline preferred weighting in the filter is due to the fact the undershoot area is oriented along the inline direction and the strike of the structure is also oriented along the shooting azimuth. Figure 4.16 displays the calculated 1991 time warp deviations for three levels of control points (1000, 2000, and 3000 ms). These vertically exaggerated surfaces show the time dependent nature of the

deviation, and clarify why the time constant shift performed during the static shift process (section 4.5.5) was unable to correct such time varying deviations. Not shown are the inline and crossline shifts also calculated for all control points and constrained to shift a maximum of 2 traces in either dimension laterally. The lateral and time shifts are combined and applied to the 1991 data the result of which is shown in figure 4.17(a).
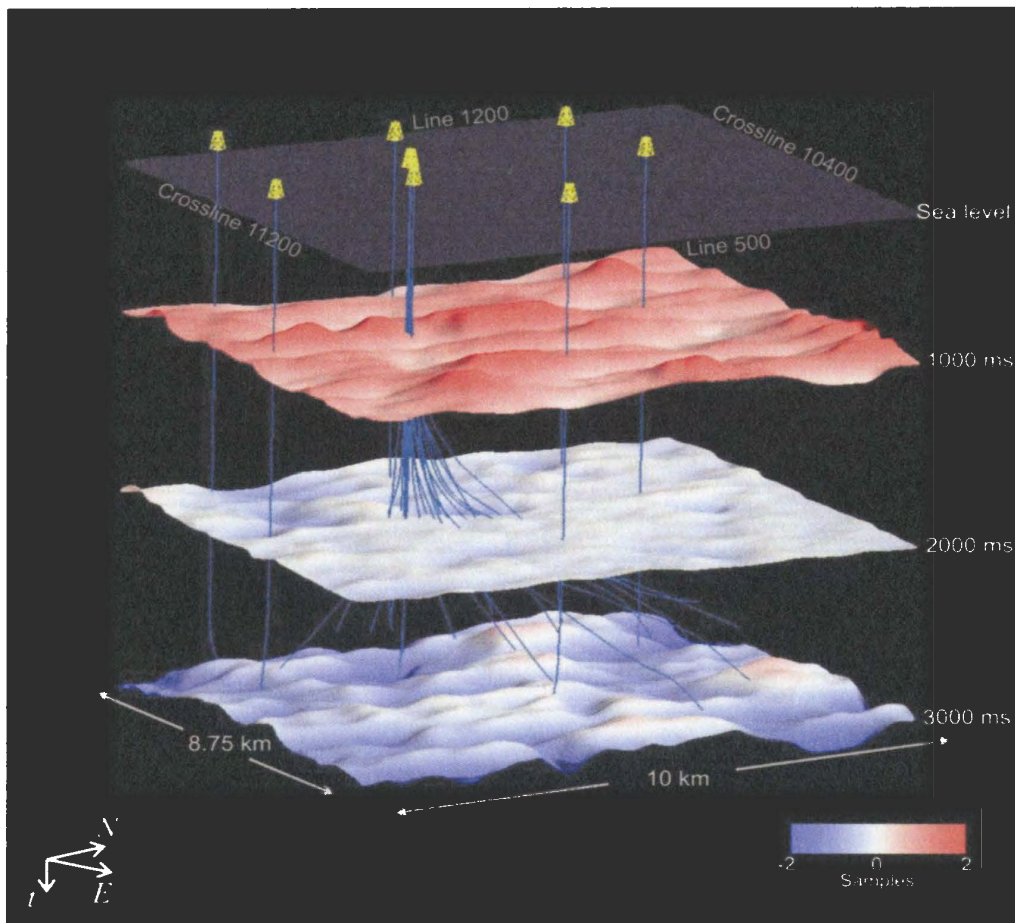
Figure 4.16. *Computed time warp deviations for the Hibernia 1991 dataset relative to the 2001 data at 1000, 2000, and 3000 ms. These vertically exaggerated surfaces show the relative time placement of seismic events in the 1991 data compared to the 2001 data. For example, at 1000 ms, the bulk of the surface is positive indicating that the 1991 data is 1-2 samples shallower than the 2001 data at these positions, and a correction will require shifting the 1991 data deeper by the same values. The 2000 ms surface demonstrates a near constant warp function while the deeper 3000 ms surface indicates that a shift upwards is needed for large portions of the data to equalize it with 2001 data.*

Illustrated in figure 4.17(b), the volume event warping reduces the residual difference (2001-1991) RMS amplitude extraction by approximately 8% over the phase balanced difference, however, the 4D signal to noise ratio is also reduced slightly. In figure 4.17(a), the 2001-1991 warped difference section has noticeably less amplitude above the reservoir compared to the difference section before volume event warping.
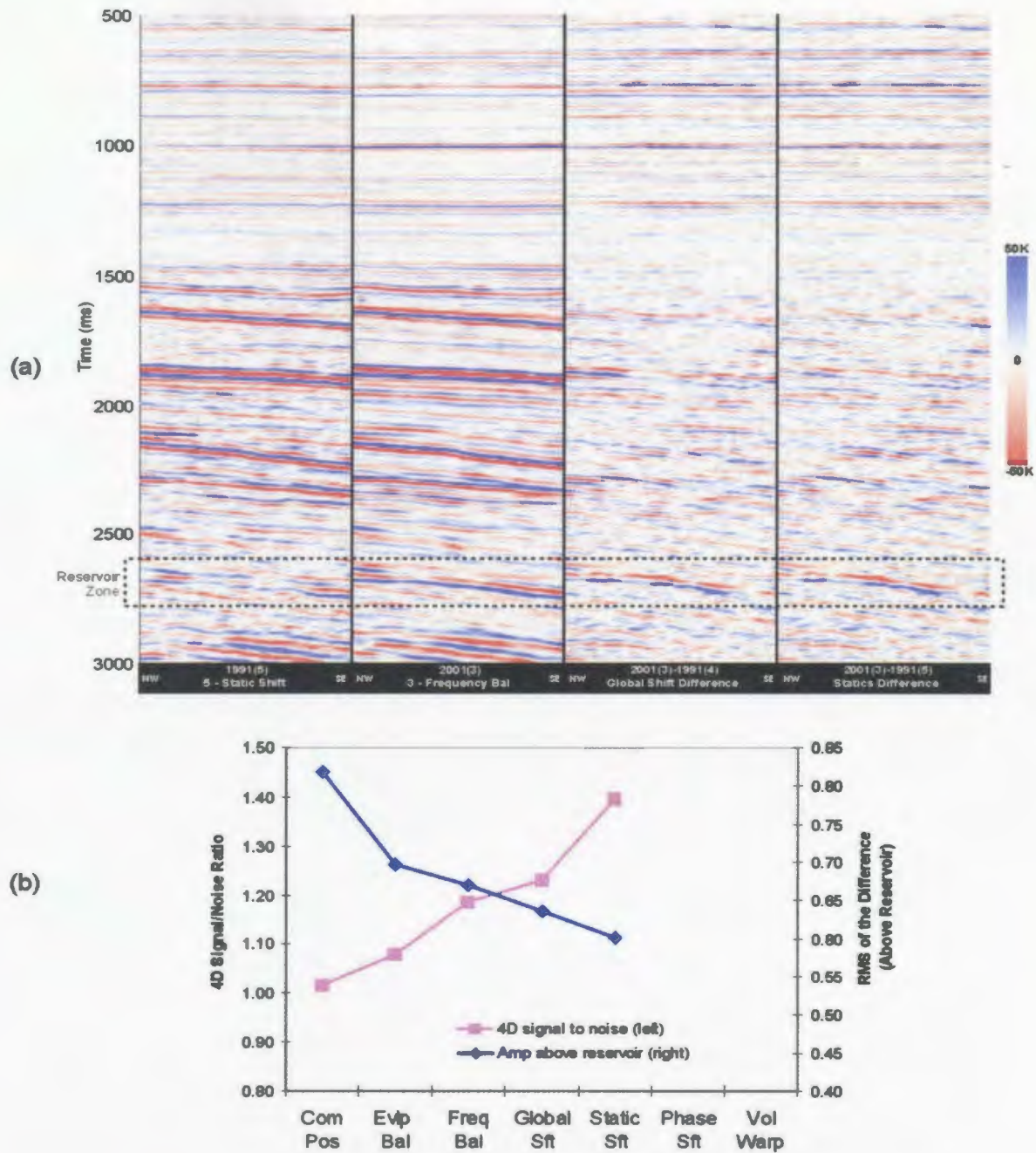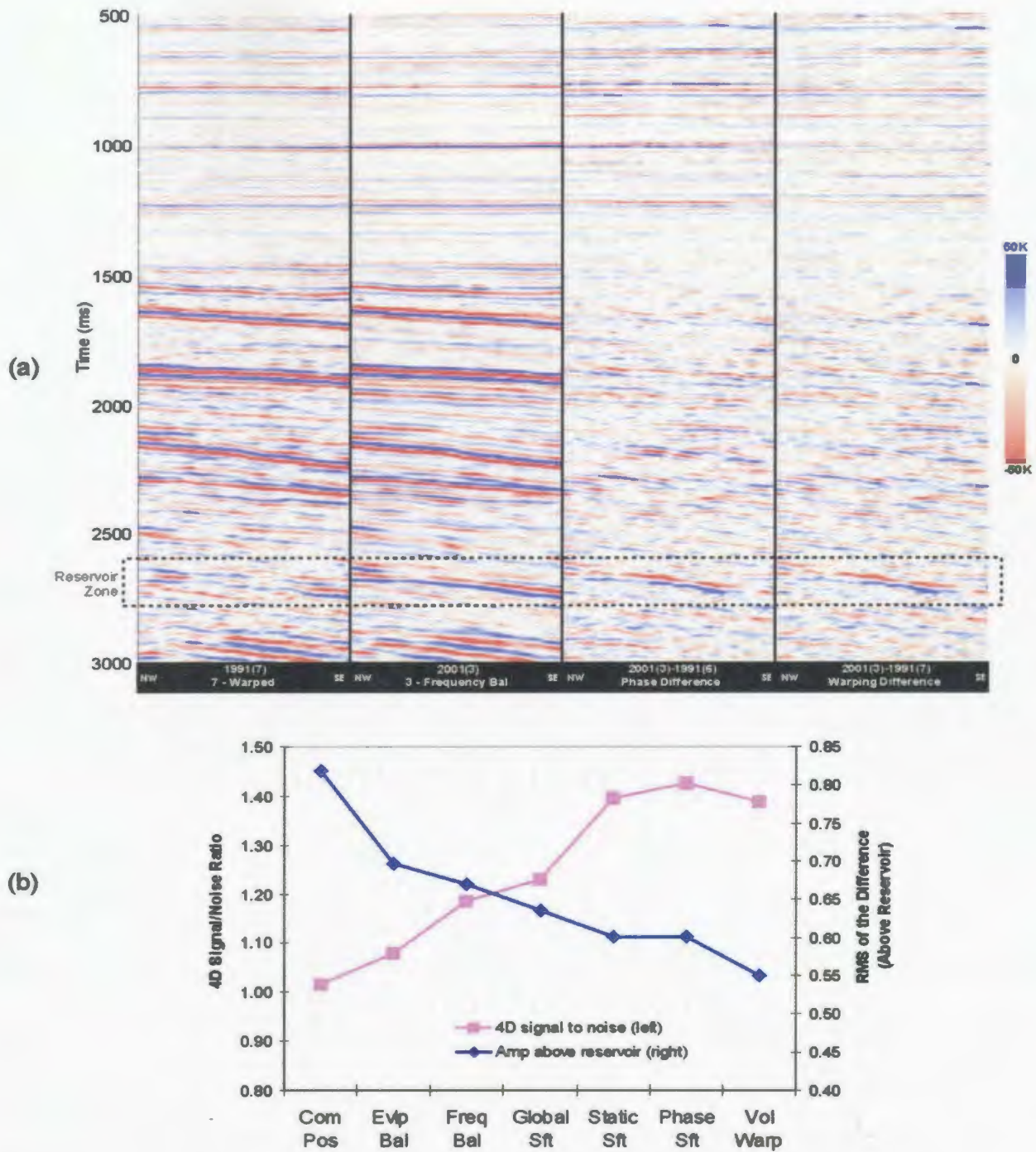
Figure 4.17(a-b) *A four panel seismic display showing a Hibernia seismic line. Left to right: 1991 migration warped seismic data, 2001 frequency balanced seismic data, 2001-1991 phase shift balanced difference, and the 2001-1991 migration warped difference The reservoir level is indicated by the dashed box. The visual residual difference is improved for this step, and in* **(b)** *the residual RMS difference amplitude above the reservoir is reduced, but the 4D signal to noise ratio is also reduced slightly.*

4.6 Conclusions

The effectiveness of 4D seismic processing relies on a number of factors ranging from acquisition quality to the data balancing method selected. The cross equalization processing flow, similar to Lumley et.al. (2003), was chosen for this project for a number of reasons: the Hibernia 4D seismic data was poststack migrated, the option to perform quality control after each step, and the relative algorithm stability in noisy data. The computed amplitude gain, static shifts, and phase shifts, are consistent conceptually with physical acquisition rationale, thus adding a quasi-deterministic contribution to the processing output. Qualitatively, the complete cross equalization flow reduces coherent seismic energy difference in the overburden while relatively enhancing reservoir anomalies as shown in figure 4.18. Visually it is quite clear that the cross equalization process eliminates many false anomalies both at and above the reservoir level (figure 4.18) – a very important result that lends increased confidence to the reservoir anomalies that remain after cross-equalization processing. Quantitatively, this processing flow reduces the ratio RMS amplitude extraction for the difference (2001-1991) over the same extraction for the 1991 volume from a pre-processed value of 0.82 to 0.55, a significant improvement in repeatability of approximately 33%. In addition, the 4D signal to noise ratio increases from 1.02 before application of cross equalization processing to 1.39 after processing (figure 4.17(b)). This means that it is possible in at least some areas to distinguish the reservoir anomalies from the background noise after cross equalization processing, but the 4D anomalies are very close to the noise level. As a consequence of the 4D anomalies being just above the 4D seismic noise level, quantitative inversion

135

methods may not be successful for these cross equalized datasets, so interpretation may be limited to more general qualitative conclusions.
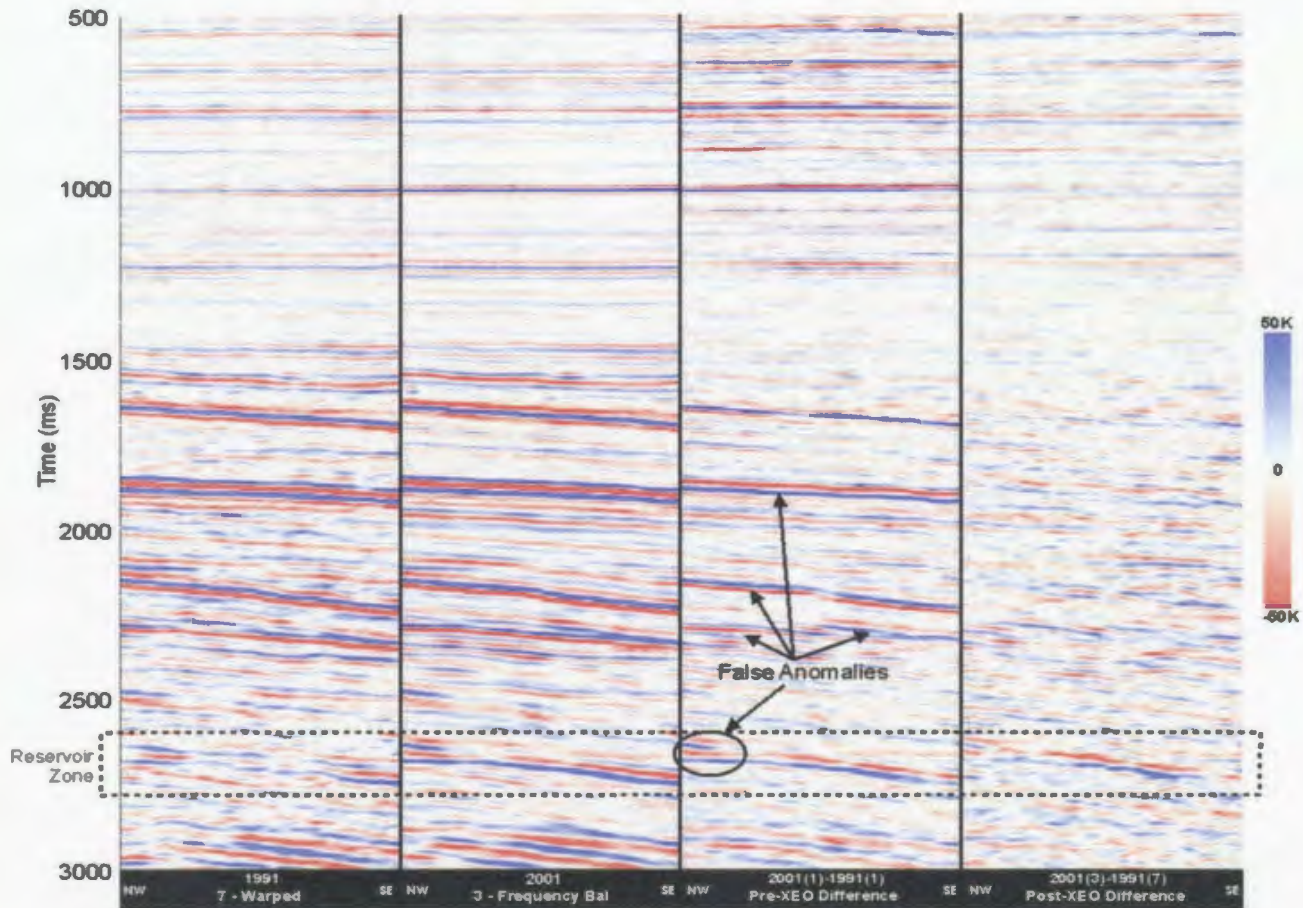
Figure 4.18. *Left to right: 1991 migration warped seismic data, 2001 frequency balanced seismic data, 2001-1991 difference before cross equalization (Pre-XEQ), and the 2001-1991 difference after cross equalization (Post-XEQ). These sections show the significant repeatability enhancement as a result of applying cross equalization processing to the data. In the Pre-XEQ difference, there are a number of anomalies at the same approximate amplitude as the reservoir anomalies. Through cross equalization processing, the amplitude differences have been reduced throughout the volume with differences outside of the reservoir attenuated more than those in the reservoir, thus eliminating many false anomalies and relatively enhancing reservoir anomalies.*

136

Chapter 5

Interpretation of 4D seismic data

5.1   Overview

In this chapter, the interpretation of the cross equalized 4D seismic data is undertaken. As outlined in figure 5.1, for the interpretation I use the cross equalized seismic data and the modeling relationships to examine 4D seismic anomalies in both gas and water injection areas.   Prior to interpretation of the time-lapse seismic anomalies, I balance the two datasets for AVO effects at the reservoir interval that were not corrected during cross equalization.   In addition, I apply *f-xy* deconvolution to the seismic datasets and then median filter the amplitude maps to reduce the short wavelength spatial noise at the anticipated cost of degrading the spatial resolution.   The full cross equalized area is examined firstly to determine the relative spatial noise in the data from non-producing areas.   Then 4D seismic anomalies in areas of gas and water injection are identified for in-depth analysis.   I then examine the correlation of these anomalies to the expected responses determined by 4D seismic modeling.   The pressure/saturation inversion methods presented in Chapter 3 are applied to the 4D seismic data. Finally, relationships between reservoir structure and 4D seismic amplitude anomalies are explored for the possible effect that pore pressure change has on reservoir travel time. The results of these interpretations will help to delineate the applicability of the 4D seismic method in challenging fields such as those found on the Canadian Grand Banks.
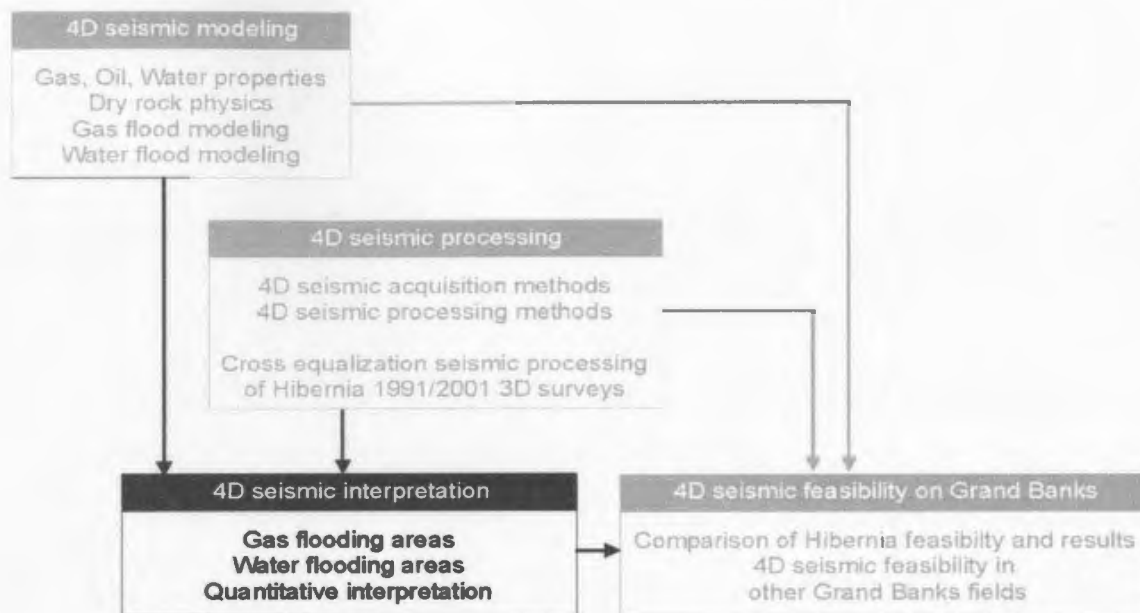
Figure 5.1. *Thesis outline flowchart. 4D seismic interpretation uses the cross equalized seismic data and the modeling relationships to examine time-lapse seismic anomalies in both gas and water injection areas.*

5.2 Introduction

In this thesis, I have modeled the impact production effects could have on Hibernia 4D seismic data and have processed the seismic datasets to optimize repeatability and improve the 4D signal to noise ratio. In this chapter, the primary objective is to find 4D seismic anomalies that are above the noise level and use the modeling results from Chapter 3 to cross-validate them from a first order perspective. To do this, a combination of visual inspection, quantitative amplitude and instantaneous phase measurements, and inversion methods are used. Prior to interpreting the seismic data, I employ some statistical approaches to spatially filter and balance the data accounting for different streamer lengths used in the two surveys.

5.3 Data filtering and calibration

The interpretation of 4D seismic data requires comparable seismic datasets. The processing sequence outlined in Chapter 4 balanced aspects of the seismic datasets related to acquisition and processing differences. While the cross equalization processing improved repeatability, there remain residual differences in the amplitudes of the respective time-lapse data volumes. In this section, I attempt to address residual differences attributed to amplitude variation with offset, and also the spatial resolution of the seismic data.

5.3.1 AVO-Stack calibration

For the past few decades, geophysicists have made use of the fact that amplitudes of seismic data vary with the incident angle and thus source-receiver offset (Aki and Richards, 1980; Graul, 2003). The amplitudes vary with offset as a function of the physical properties of the two media that make up the seismic boundary as shown by Aki and Richards (1980) generalized linear approximation of the Zoeppritz equations (equation 3.3). For this study, the Aki and Richards (1980) approximation is used to calculate the potential effect that the different offset ranges for the respective surveys may have on base reservoir amplitude.

The 4D seismic datasets used in this study have two different offset ranges. The 1991 survey has an offset range of approximately 230-3205 m while the 2001 survey has a range of 300-4800 m. The approximately 1600 m extra offset range in the 2001 survey

biases the stacked amplitude response of the 2001 survey more toward the far offset response compared to the 1991. Figure 5.2 displays a plot showing the reflection coefficients of the base reservoir (Fortune Bay) reflection and a normal reflection as a function of offset. A normal reflection is the reflection across a boundary where the P-velocity, S-velocity, and density all increase or decrease by the same percentage. Additionally, figure 5.2 displays the respective offset ranges for the two surveys. For the base reservoir Fortune Bay reflector - the reflection upon which this project's attribute work is based – there is an increase in reflection coefficient with offset. Consequently, the calculated "stacked" amplitude of the 2001 Fortune Bay horizon is 2.3% higher than the equivalent reflection in the 1991 stack.
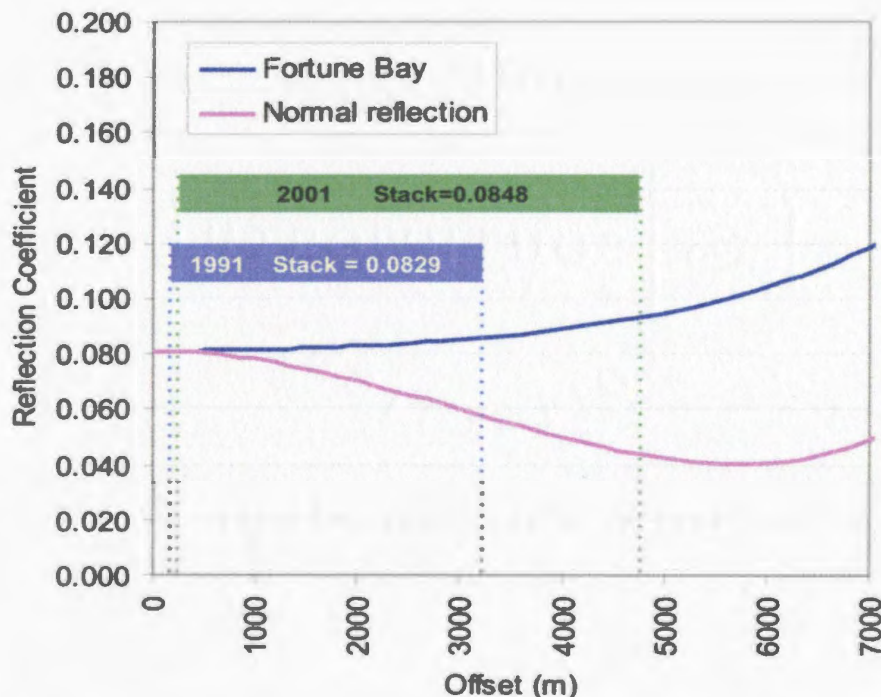
Figure 5.2. *Graph showing reflection coefficient as a function of offset for both a normal reflection and the base reservoir Fortune Bay reflection. The offset ranges of the two surveys are shown as well as the calculated mean stacked Fortune Bay amplitude for each survey.*

While this amplitude calculation is probably fairly accurate, the large unknown is the effect that amplitude balancing in the cross equalization process has had on the real data. If amplitude for all reflections outside of the reservoir was invariant with amplitude, it would be expected that balancing the 1991 and 2001 Fortune Bay amplitude horizons would require a simple scaling factor of 2.3% (the 2001/1991 stack from figure 5.2: 0.0848/0.0829) applied to the 1991 dataset. In reality, almost all reflections vary with offset, and as shown in figure 5.2, a simple normal reflection can vary significantly with offset. As a result of the inherent difficulty in deterministically calculating AVO corrections, the approach taken in this thesis to AVO-Stack balancing is statistical in nature.

To approach this statistically, I attempt to balance the reflection amplitudes from both surveys by equalizing the amplitude histograms of the non-producing areas of the Fortune Bay reflector in both surveys. Firstly, maximum peak amplitude extractions are taken from the Fortune Bay reflection. These amplitude data are then windowed to exclude production areas and histograms are made of the amplitude values for non-production areas of both surveys. These histograms are displayed in figure 5.3. The 1991 map has a median Fortune Bay amplitude of 33845 while the 2001 map is 7.8% higher at 36489. This is clearly demonstrated in figure 5.4 where the difference (2001-1991) in amplitude is largely positive or reddish in color. The seismic modeling in Chapter 3 used an initial condition (0.95 S_{oil}, 40 MPa) stacked amplitude of approximately 38000, so I simply scale the 1991 amplitudes to the 2001 by multiplying the 1991 by the 7.8% scale factor and then increase both amplitudes by 4.1% to bring their non-production

mean amplitude to 38000. This scaling factor is larger than the simple 2.3% scaling factor estimated from simple AVO modeling, but none the less is consistent with the estimate that the amplitude of the Fortune Bay reflector increases with offset.

1991   2001
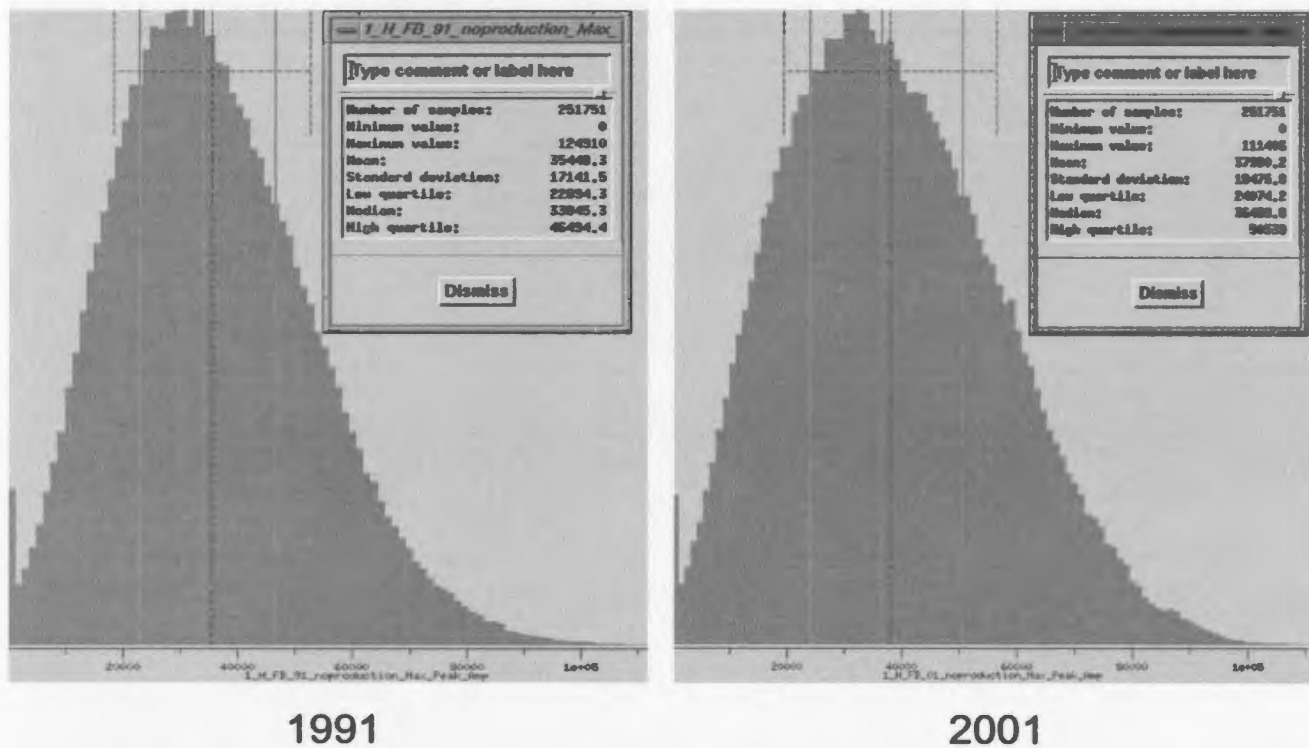
Figure 5.3 *Histograms of maximum peak amplitude extracted from the Fortune Bay horizon for the 1991 (left) and 2001 (right) cross equalized seismic datasets.*

After scaling, the two amplitude surfaces are more comparable as shown in figure 5.5. The distinctly reddish (positive) hue observed in the un-scaled difference is removed and a more even distribution of positive and negative differences can be observed in the scaled difference map.
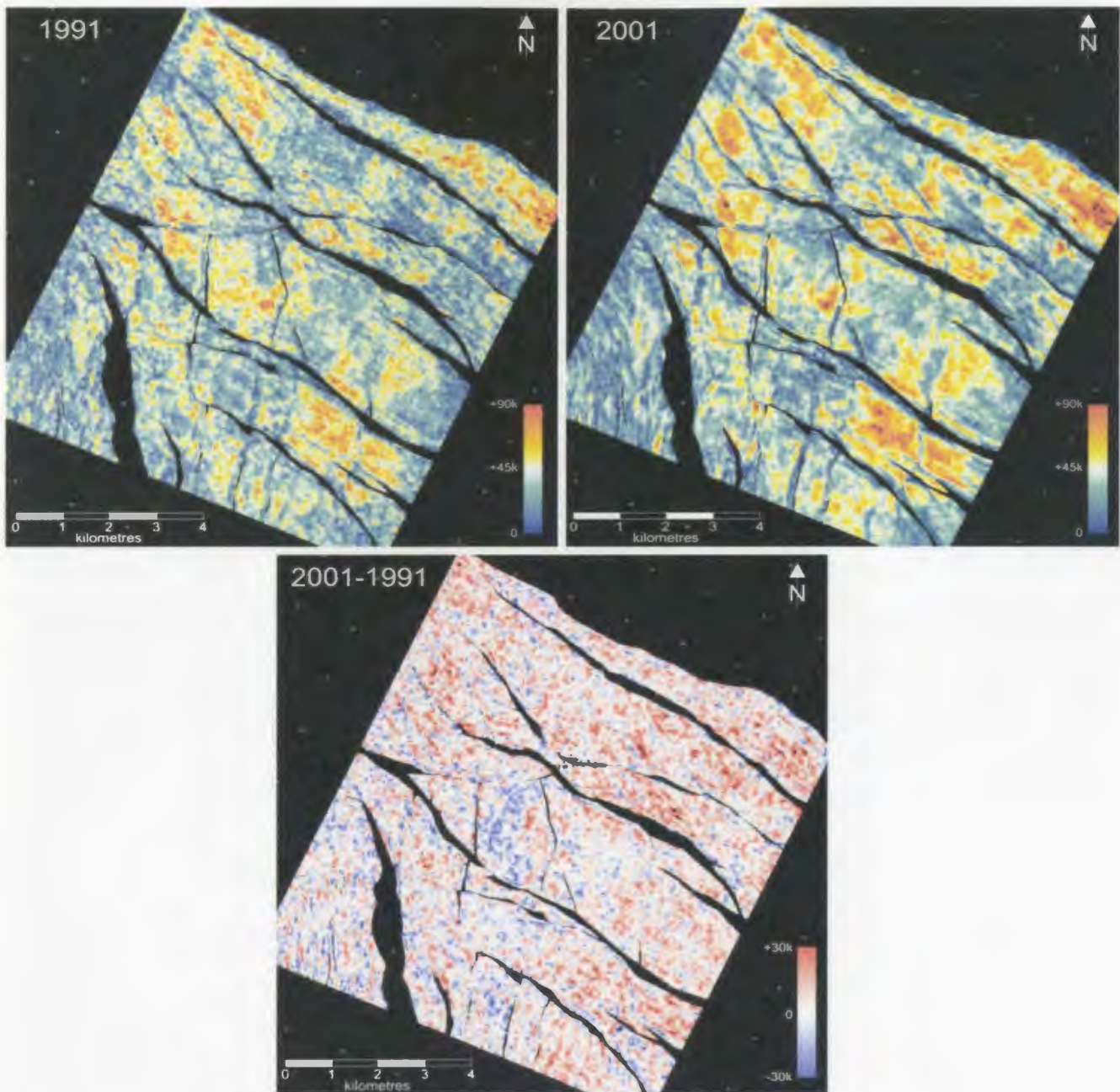
Figure 5.4 *Fortune Bay amplitude maps showing the 1991, 2001 and 2001-1991 difference prior to any AVO-Stack balancing. Positive values dominate the difference map, indicating that the 2001 reflection likely has greater inherent amplitude at the base reservoir than does the 1991.*
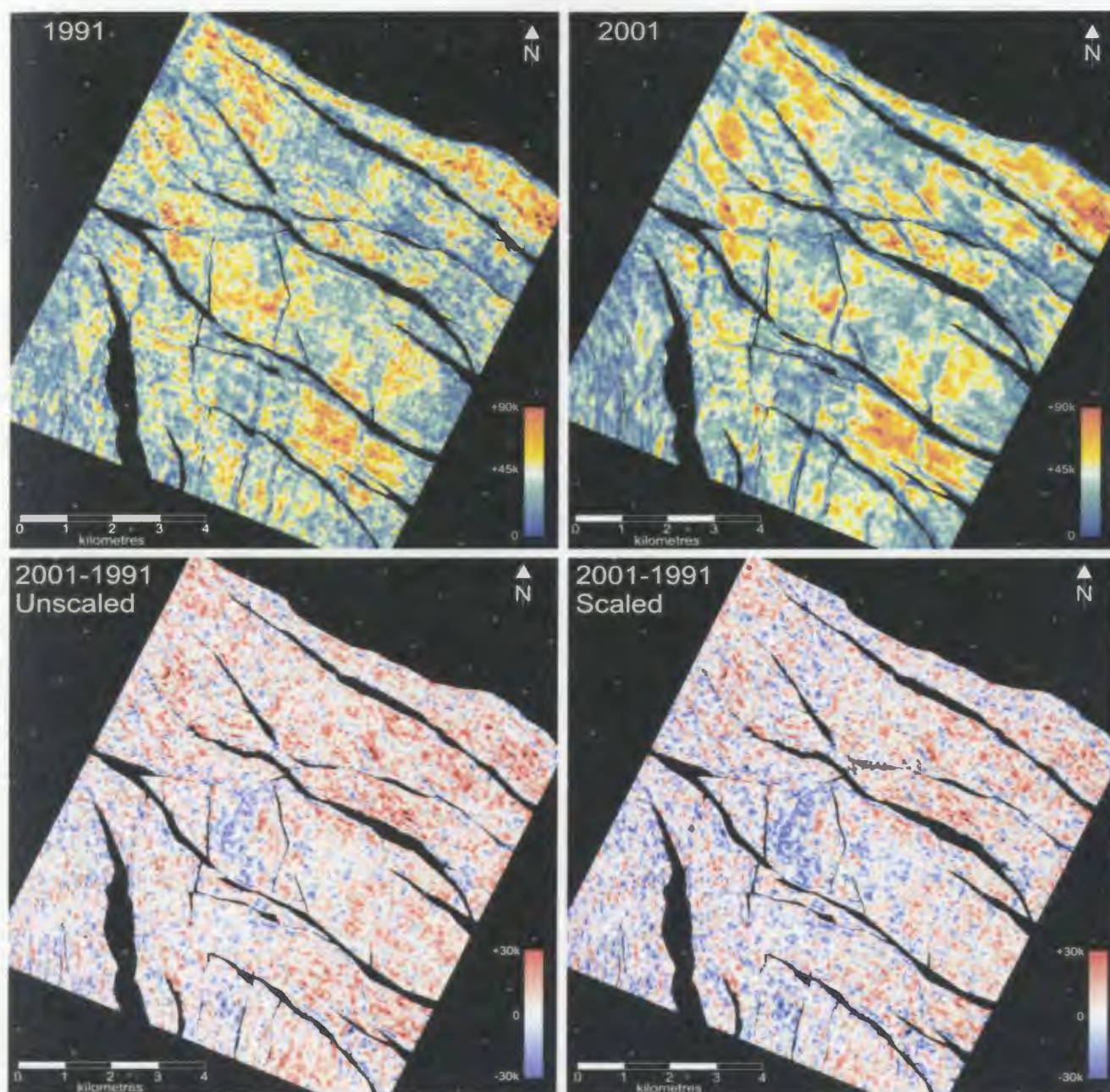
Figure 5.5 *Fortune Bay amplitude maps showing the 1991 scaled, 2001 scaled, and 2001-1991 unscaled and scaled difference. The effect of AVO-Stack balancing is clearly evident as the scaled difference has more even distribution of positive and negative amplitudes.*

5.3.1 Spatial filtering

In the previous section, a single scalar was applied to balance the amplitudes of the two time-lapse seismic datasets. In this section, I examine the spatial resolution of the datasets and attempt to filter the map data to attenuate noise thus relatively enhancing potential 4D seismic anomalies.

The spatial resolution of features in a migrated seismic dataset is approximately equal to ¼ of a seismic wavelength (λ) (Claerbout, 1985; Lumley, 1995). Wavelength is defined:

$$\lambda = \frac{v}{f} \quad ,(5.1)$$

where v is the rms velocity of the reflector and f the dominant frequency of the reflection event. For the Hibernia reservoir with an RMS velocity of approximately 2700 m/s and a dominant frequency of approximately 25 Hz, this translates into a ¼ λ resolution of 108 m. While the bin sizes for both surveys are 12.5 m square, the smallest resolvable signal is almost an order of magnitude greater, spanning 8-10 bins. As a result, reasonable spatial filtering is justified to attenuate sub-resolution spatial noise.

Prior to spatial filtering, the spatial frequency spectra are extracted from a base reservoir amplitude map as shown in figure 5.6. This graph demonstrates that the radially averaged power spectrum contains little signal below a radius of 8 spatial samples (bins) and a maximum signal contribution above 25 samples resolution. These results are very similar to the results obtained from forward calculation.

RADIALLY AVERAGED POWER SPECTRUM
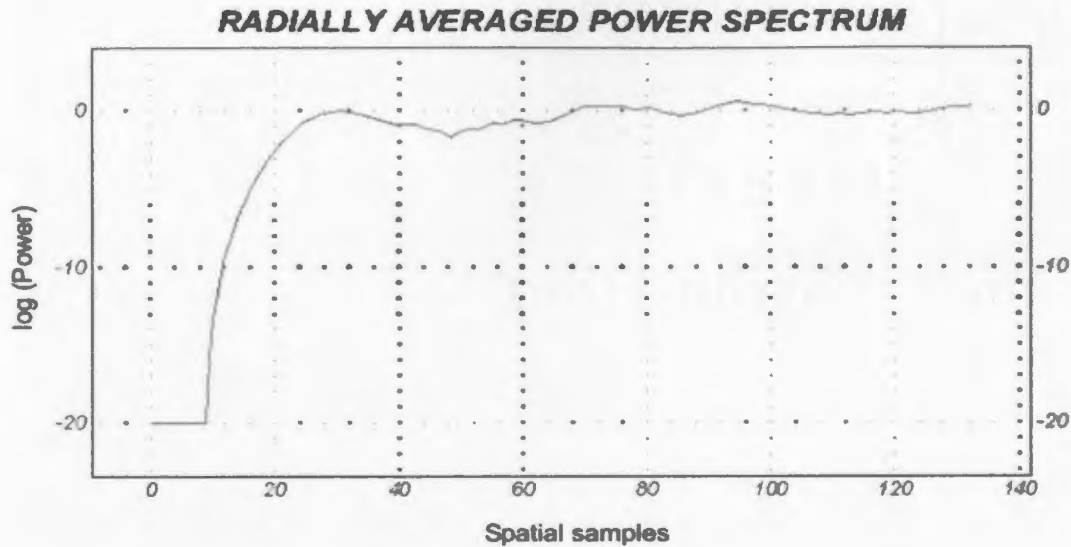
Figure 5.6. *Radially averaged power spectrum for Fortune Bay amplitude horizon*

To accomplish the initial spatial data filtering, *f-xy* deconvolution is employed. *f-xy* deconvolution is a spatial signal prediction tool that reduces spatial random noise. By defining spatial operator size in *x* and *y*, *f-xy* deconvolution is used to filter out noise by predicting what a continuous signal may look like spatially, and the use of larger operator window sizes results in greater data filtering. *f-xy* deconvolution is applied to each cross equalized 4D seismic dataset individually.

From the radically averaged power spectrum (figure 5.6), it is obvious that the prediction window size for *f-xy* deconvolution should likely be between 10 and 30 spatial samples. As *f-xy* deconvolution is a computationally intense process, I choose a subset area of the field to generate filter panels showing the results of a number of different *f-xy* deconvolution operator sizes. These filter panels, the resulting seismic difference, and

146

residual filtered energy are shown in figure 5.7. The filtered out (residual) energy for the *f-xy* size=20 panel shows an incoherent pattern that is replicated in the *f-xy* size=25, only with higher amplitudes being removed. The residuals in the *f-xy* size=30 case seem to indicate that coherent signal is being removed from the data, which is an undesirable effect.
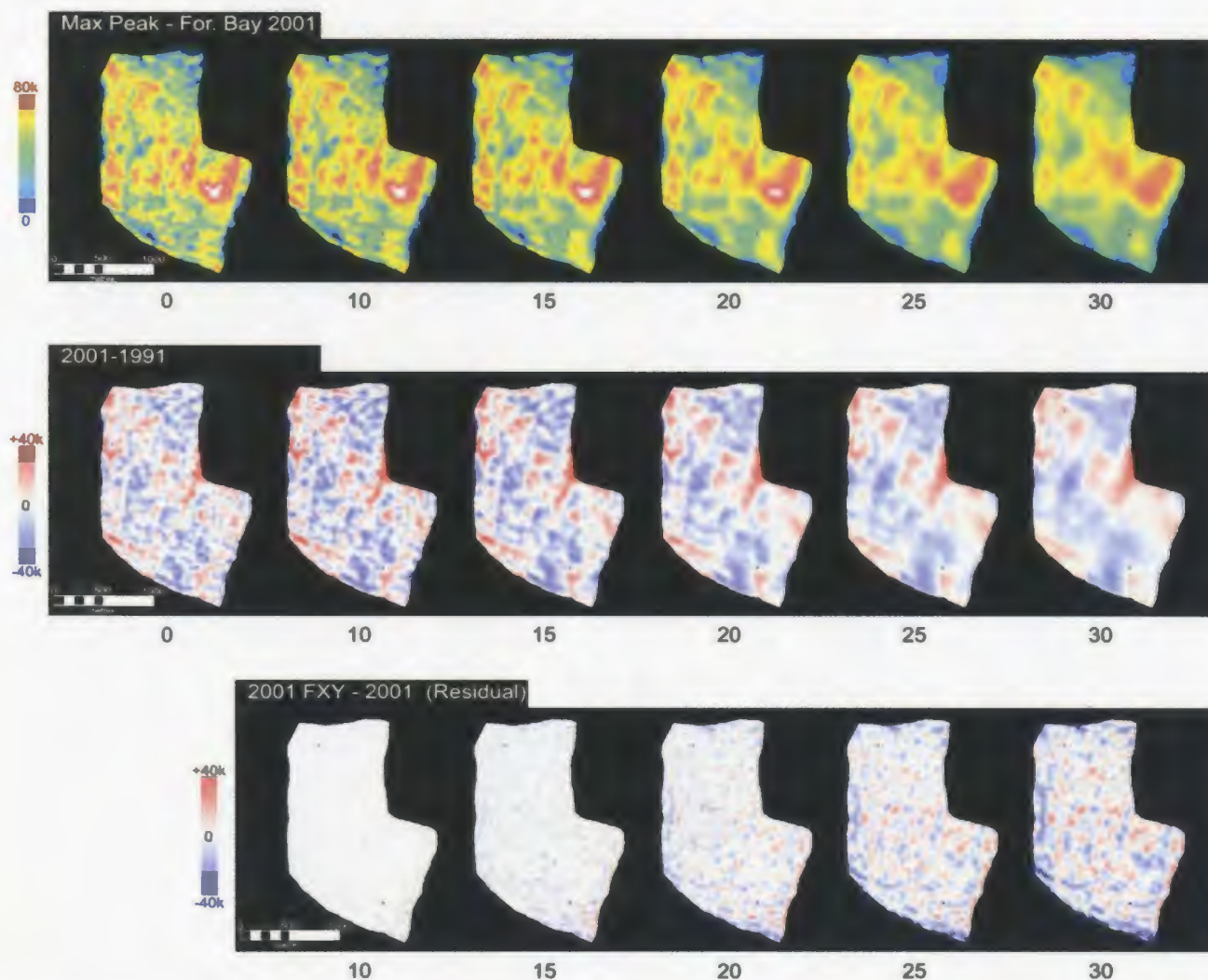
Figure 5.7 *f-xy deconvolution filter panels. The top row shows the 2001 maximum peak amplitude extraction for the base reservoir, the middle row the 2001-1991 difference, and the bottom the residual energy that was removed from the original map to make the corresponding top row map. The number below the images indicates the f-xy design operator size (in samples) for the particular column of displays.*

Therefore an *f-xy* operator value of 25 is chosen as the optimum operator window. The *f-xy* operator of 25 samples is consistent with the onset of maximum signal in the radially averaged frequency spectrum (figure 5.6). The residual energy anomalies that are filtered out of the data (lower panels) for the *f-xy* size=25 operator window are on the order of 100 m width or less, meaning they are below the calculated resolvable spatial limit calculated in equation 5.1 of 108 m. Using this fact, and the incoherent visual appearance of the residual map, it is likely that the bulk of the energy removed by the *f-xy* filtering is noise in the seismic data. Figure 5.8 displays the effect that *f-xy* deconvolution has on the base reservoir Fortune Bay amplitude. The 2001-1991 *f-xy* difference map contains marginally less spatial noise. Even with the application of *f-xy* deconvolution, there appears to be some spatial frequency content difference between the 1991 and 2001 Fortune Bay amplitude maps. The 1991 appears to be higher frequency and a slightly noisier than the 2001. Through experimentation I apply to the 1991 map a statistically determined 4 inline by 4 crossline median filter and rescale the 1991 amplitude map with a single scalar to match the amplitude content before filtering. The result of this additional median filtering is displayed in figure 5.9. The spatial resolution of the two amplitude horizons is now more comparable than before median filtering of the 1991 amplitude map. While the median filtering makes the amplitude maps more comparable visually, the subtraction of the amplitude surfaces in figure 5.9 creates a map that is very blotchy, a product of only one surface being median filtered. It is decided to use the 2001-1991 amplitude difference map shown in figure 5.8 for further work.
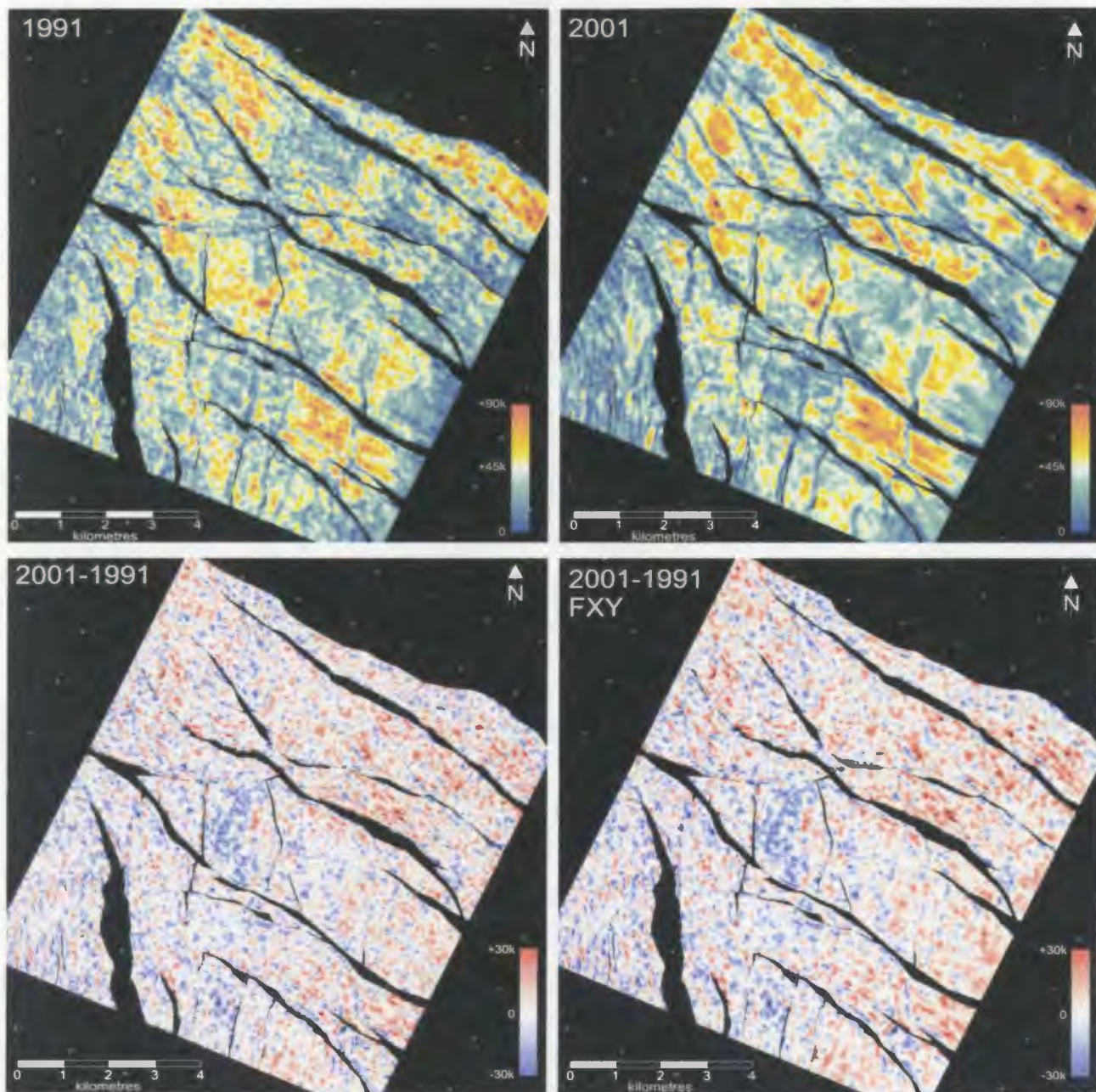
Figure 5.8 *Fortune Bay maximum peak amplitude extractions (top) for the 1991 f-xy 25 and 2001 f-xy 25. Below is the 2001-1991 difference before (left) and after (right) f-xy deconvolution.*
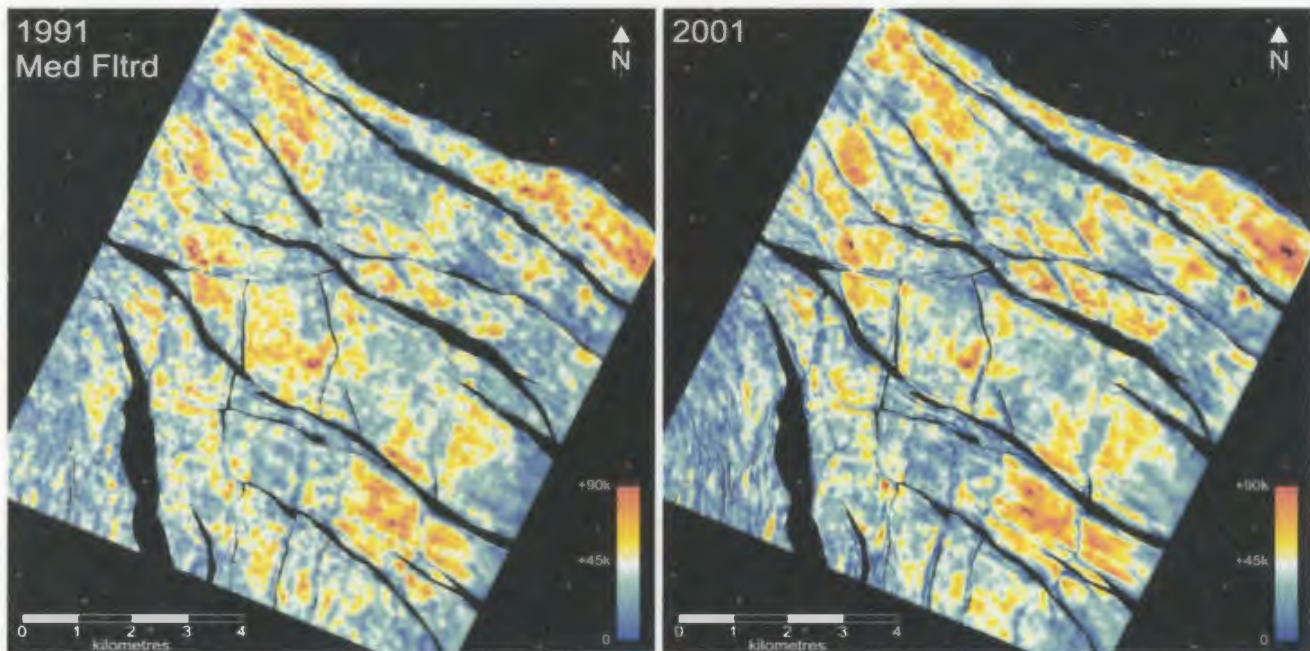
Figure 5.9 *Base reservoir amplitude maps. Left is the median filtered map from the 1991 f-xy decon, while the right image displays the amplitude from the 2001 f-xy decon.*

The final step in the amplitude data preparation is to filter the 2001-1991 difference map to improve interpretability. It is determined by experimentation that the application of a 9 inline by 9 crossline (112.5m x 112.5m) median filter to the 2001-1991 difference amplitude map reduces spatial noise in non-production areas while retaining broader anomalies as shown in figure 5.10. The residual map shown in this figure indicates that the energy removed by median filtering is largely incoherent and of similar amplitudes and resolution throughout the study area. The amplitude balancing and filtering produces more interpretable amplitude horizons and difference horizons by reducing the spatial noise while retaining broader anomalies.
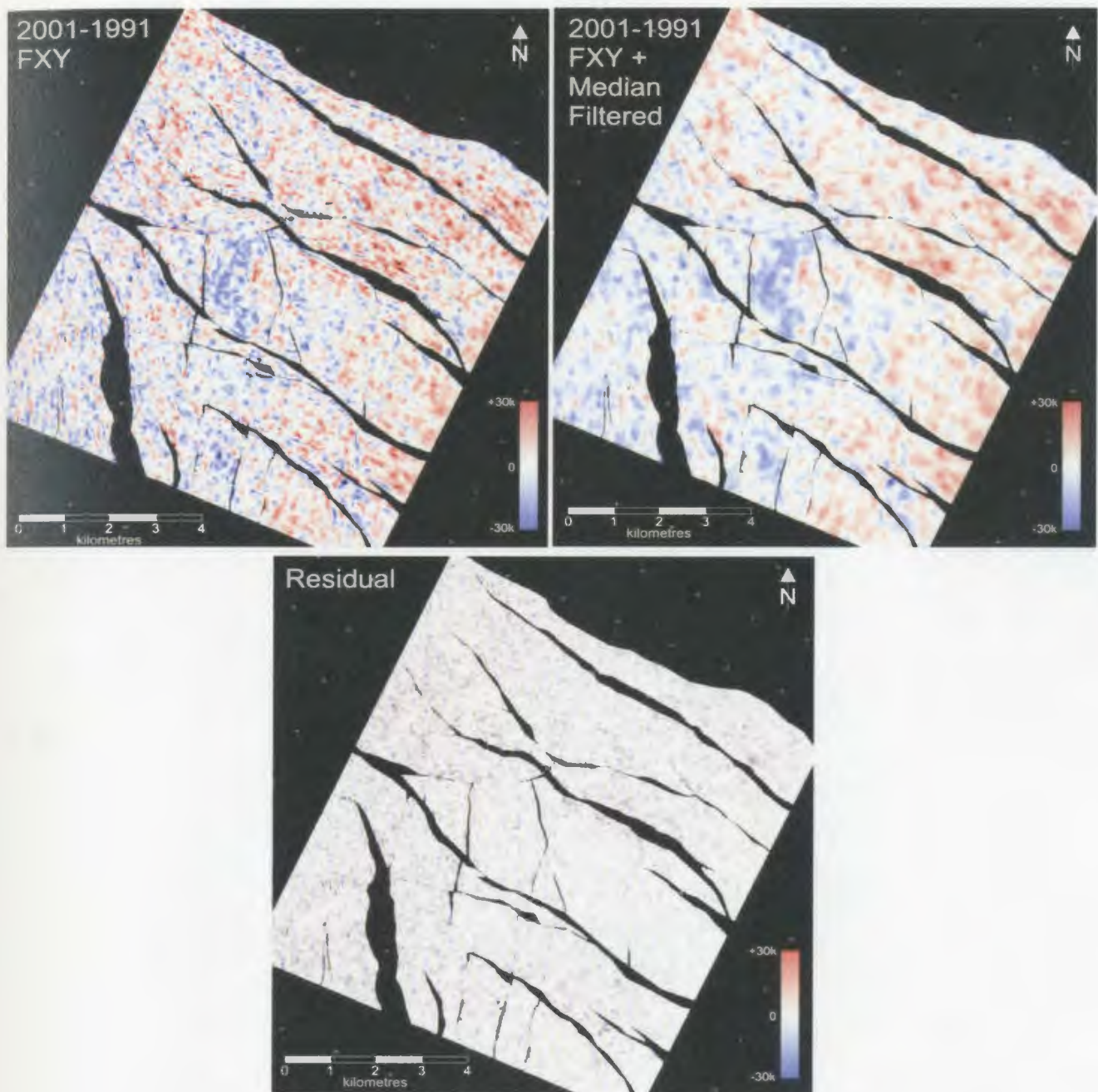
Figure 5.10 *Fortune Bay 2001-1991 amplitude difference maps. Top left is the 2001-1991 difference from the f-xy deconvolution data. Top right is the same map with a 9x9 sample median filter applied. Below is the median filter residual difference map which is the subtraction of the top amplitude difference maps.*

5.4   Data interpretation

With data properly scaled and spatial noise attenuated, analysis and interpretation of the 4D seismic data is possible.   The interpretation in this section will focus firstly on an overview of the large area 4D seismic attributes.   From the analysis of the larger area, zones of gas injection and water injection with potential time-lapse seismic anomalies are identified for closer examination.   In a couple of the subset areas, I will closely inspect the time-lapse seismic anomaly and the structural position of the anomaly.

5.4.1   Field wide analysis

To investigate the potential time-lapse seismic response to production effects, I examine the scaled and filtered amplitude and instantaneous phase reservoir horizons.   The use of reservoir reflection amplitude change for time-lapse seismic analysis is well established and has been utilized in numerous studies such as Johnson et al.(1997) and Watts et al. (1996).   The full cross equalized area is examined in an attempt to gauge the reservoir attribute changes within and outside of known production areas.   Figure 5.11 displays the scaled and filtered Fortune Bay maximum peak amplitude maps and a time structure map for reference.   Figure 5.12 displays the same difference information, but with color scales that illuminate separately positive and negative time-lapse amplitude anomalies.   Many broad scale amplitude anomalies both inside and outside production areas can be correlated in the two seismic vintages.   In non-production areas, there is a significant amount of difference amplitude, the distribution of which can be seen in the histogram in
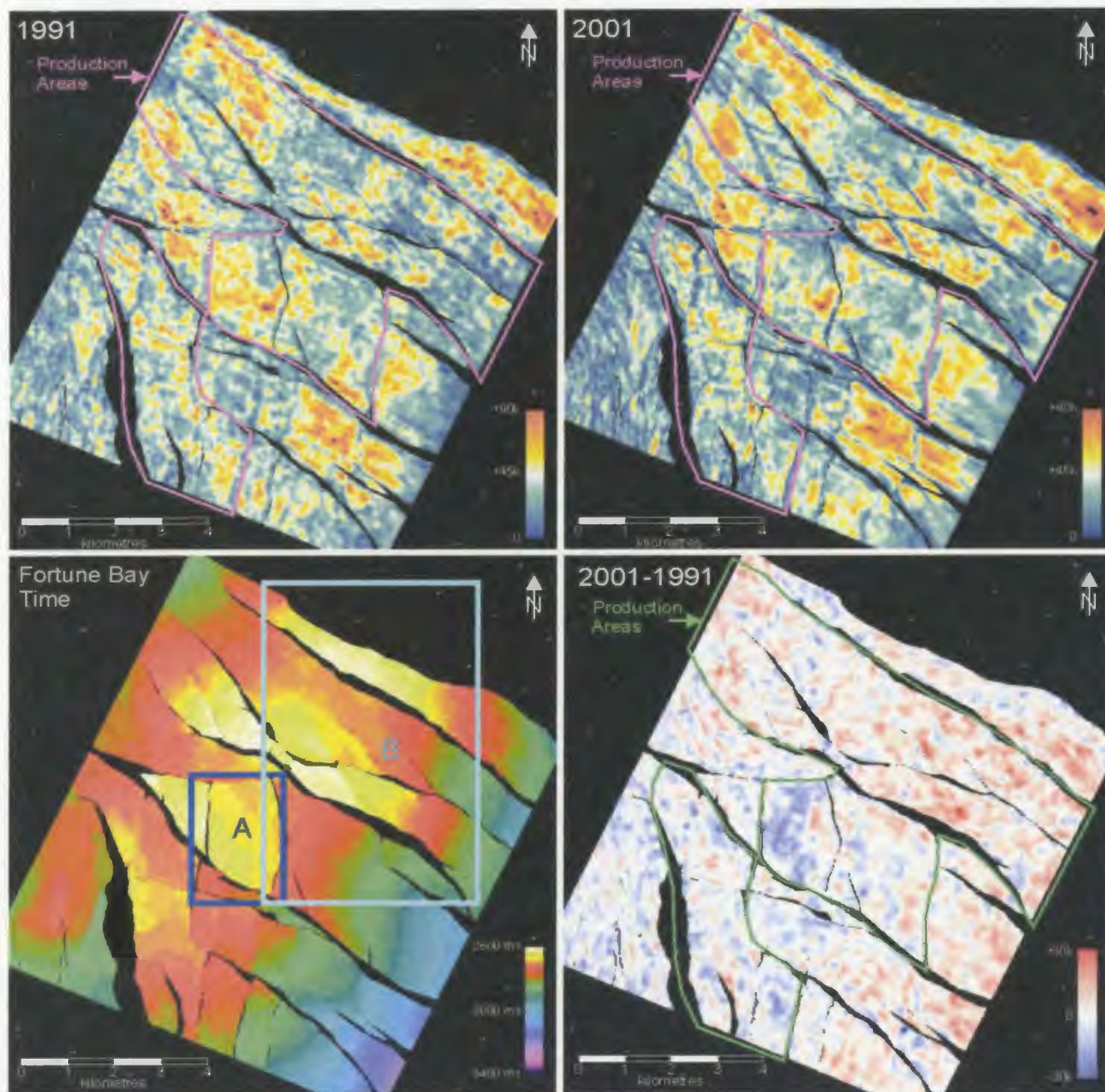
Figure 5.11. *Full area base reservoir amplitude maps. The upper maps display the 1991 and 2001 Fortune Bay maximum peak amplitude extractions (top left and top right respectively). The lower maps display a time structure map (lower left) and 2001-1991 amplitude difference map (lower right). The production area is outlined in purple in the top maps and green in the lower. The blocks "A" and "B" indicate the approximate location of the water and gas injections areas respectively selected for additional study.*

153
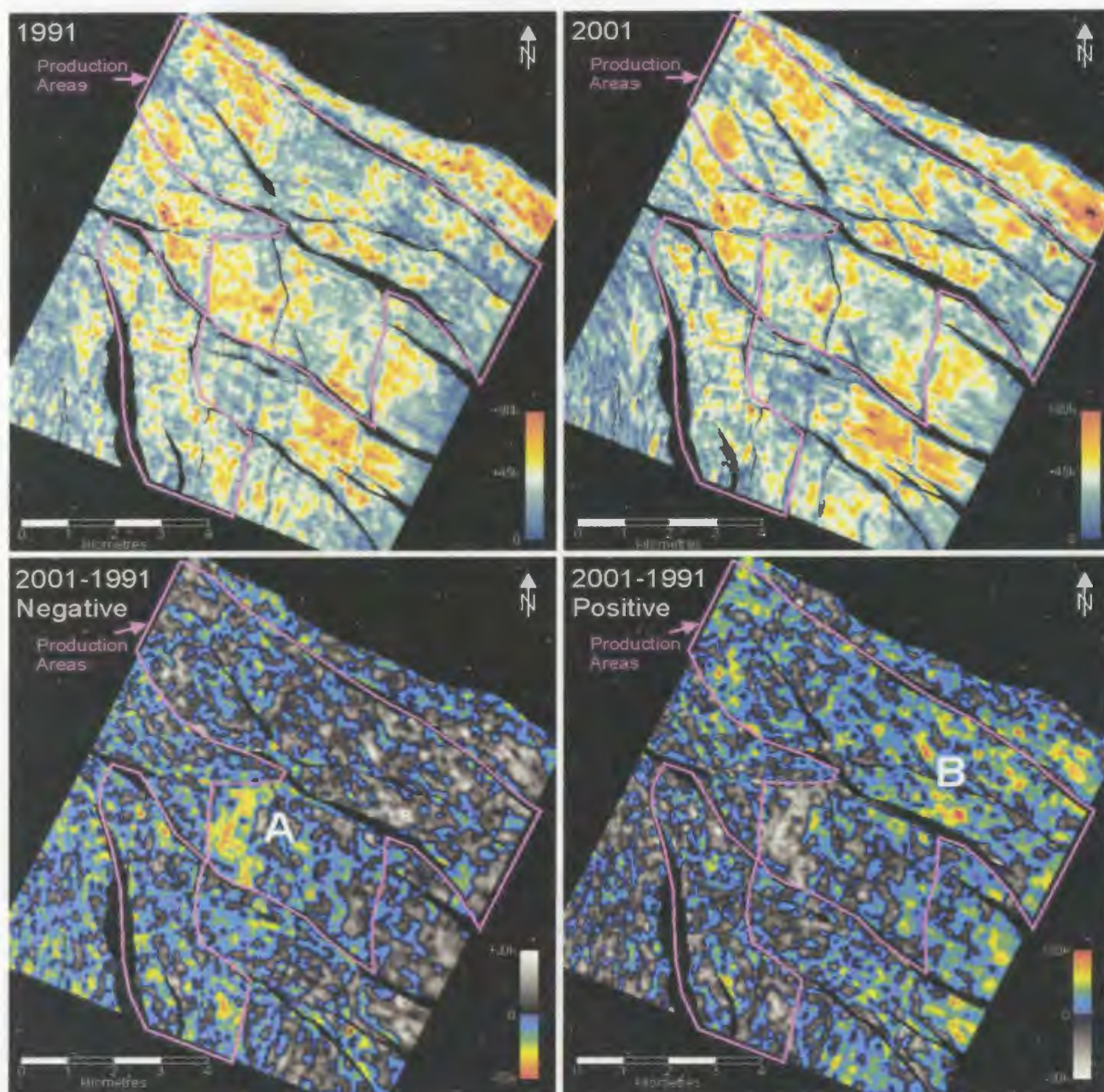
Figure 5.12. *Full area base reservoir amplitude threshold maps. The upper maps display the 1991 and 2001 Fortune Bay maximum peak amplitude extractions (top left and top right respectively). The lower maps display the same 2001-1991 amplitude difference map with a color bar that emphasizes decreases in amplitude (left) and increases (right). Areas with production area amplitude anomalies are included in the "A" and "B" subset areas selected for in depth investigation.*

154

figure 5.13. The standard deviation of the difference amplitude in non- production areas is approximately 7800 amplitude units from the mean. Referencing the magnitudes of seismic amplitude change expected from the water and gas flood modeling conducted in Chapter 3 (figure 3.17 and figure 3.23), it is likely that due to the noise in the seismic data, it may be possible to only image end member production scenarios such as full saturation change (to residual oil saturations) or high pressure change. Based on the model response and the measured noise in the seismic dataset, it is unlikely that small changes in pressure and saturation can be imaged in this cross equalized 4D seismic dataset.
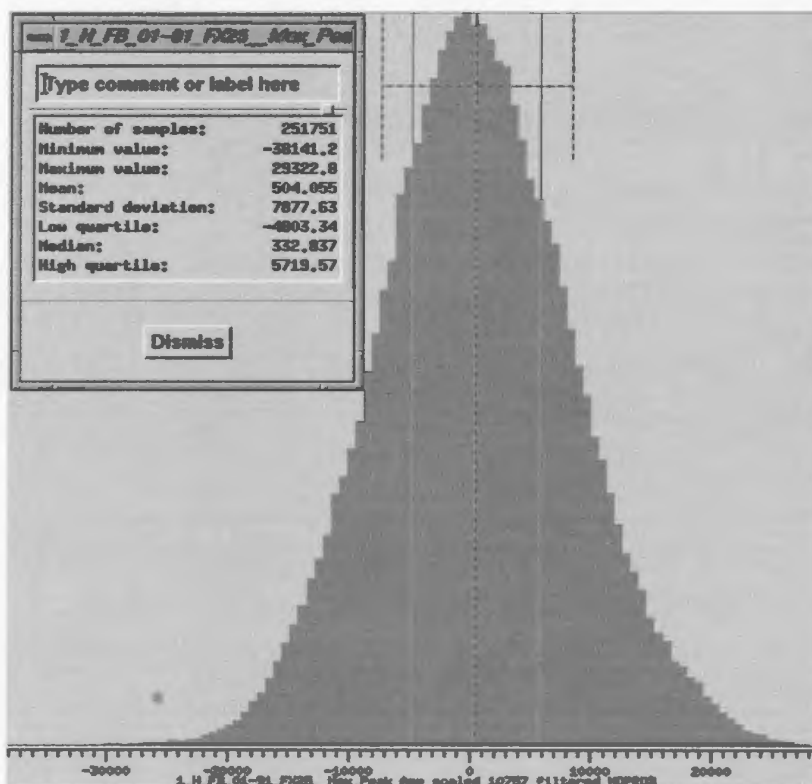
Figure 5.13. *Histogram showing 2001-1991 amplitude distribution for non-production areas.*

Some general observations can be made about the differences in seismic amplitude in non-production areas. In the southeast portion of the data extent, there is a broad trend of positive amplitude difference, meaning that the amplitudes in the 2001 survey are greater than those in the 1991. Most of the reddish anomalies in this area correspond with lower amplitudes in the base reservoir horizon, reducing somewhat the confidence in the amplitude difference. In addition, this zone has a greater depth and structural dip than other non-production areas, and greater dip has been shown to contribute to non-repeatability without careful event alignment in Eastwood et al. (1998). The greater depth can contribute to time-lapse seismic anomalies because many of the cross equalization processes were calculated based on a fixed time window. For example, this means that the entire field would have to have had global shift, statics, phase, and frequency calculations extracted from a fixed window the bottom of which would be above the highest part of the reservoir or about 2500 ms. In these deeper portions, this leaves almost 700 ms of time immediately above the reservoir with no operator design contribution. As a result, these events can be somewhat dissimilar in the cross equalized result, creating false time-lapse anomalies. In addition, areas with greater structural dip can have higher time-lapse seismic noise as a result of the effect of different prestack migration algorithms and velocities.

While the presence of significant seismic noise in the time-lapse data complicates interpretation, in the area of the survey where known production is taking place there are some notable amplitude anomalies (figure 5.11 and figure 5.12). There is a noticeable

decrease in amplitude (blue) in a central water injection fault block (figure 5.11 and figure 5.12 – "A"). To the northeast, there is an area of amplitude increase that occurs in a gas injection zone (figure 5.11 and figure 5.12 – "B"). These amplitudes stand out visually due to their magnitude and relative spatial coherency. These anomalies will be more closely examined in later sections.

The instantaneous phase attribute was demonstrated in modeling to correlate with time-lapse time change primarily related to reservoir pore pressure changes. Figure 5.14 displays the extracted instantaneous phase for both surveys and the calculated difference. The maps contain a fair degree of noise and spatial variability in non-production areas. Contributing to this variability is the fact that the instantaneous phase attribute is extracted on a horizon that has not been carefully re-picked specifically for time-lapse traveltime difference analysis. The trace by trace re-picking of the entire horizon is beyond the scope of this study. The large degree of noise in the data precludes the data wide use of pressure inversion algorithms discussed in section 3.9.

While quantitative phase analysis for the field wide area is beyond the scope of this study, in two areas, indicated by "A" and "B" in figure 5.11 and figure 5.12, the Fortune Bay horizon is meticulously re-picked to align with the mathematical seismic peak. Figure 5.14 indicates that area "A" has an increase in instantaneous phase, and in depth examination should help determine the correlation between this increase in instantaneous phase and modeled effects that would be consistent with production history. The

157

instantaneous phase in "B" is less conclusive from the field wide map, and is used to help

delineate a single anomaly in the gas injection zone.
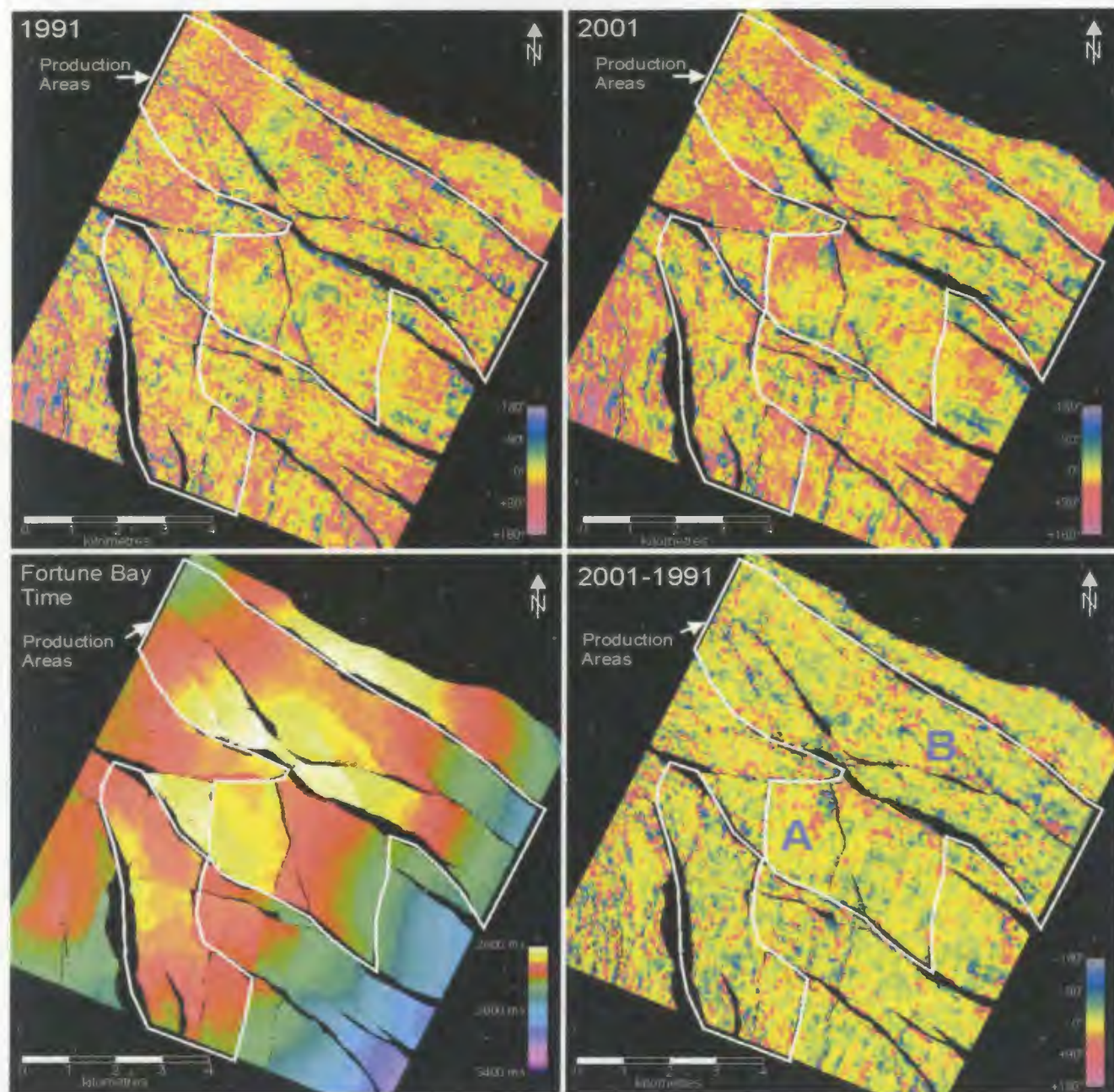
Figure 5.14. *Full area base reservoir instantaneous phase maps. The upper maps display the 1991 and 2001 Fortune Bay instantaneous phase extractions (top left and top right respectively). The lower maps display a time structure map (lower left) and 2001-1991 instantaneous phase difference map (lower right). Production areas are outlined in white.*

In this section, a couple of 4D seismic anomalies in areas that have undergone production have been identified. The amplitude in zones outside of the production areas are generally noisy, but the "A" and "B" anomalies in the reservoir zones appear to be above the noise threshold, both in magnitude and visual coherence. The instantaneous phase map is very noisy, which may be the result of an inexact horizon pick, but there appears to be an increase in instantaneous phase in the zone indicated by "A". With an overview of the 4D seismic dataset response complete, areas of gas and water injection can be examined for individual attribute characteristics that may be consistent with expected production effects.

5.4.2 Gas injection zone

In Chapter 3, the potential impact of production related physical changes in the reservoir on 4D seismic response were discussed. In this section, I examine an area of the field denoted by "B" in figure 5.11. This area has three gas injection wells and two oil producing wells and is comprised of a number of individual fault blocks. The objective is to determine if any 4D seismic anomalies appear to be above the noise level and are consistent with modeled responses to gas flooding. It should be noted that no reservoir simulation history matching was done for this study, so the data-model comparisons are drawn from the oil-gas-pressure relationships outlined in Chapter 3, and not the potential migration paths of hydrocarbons or pressure fronts determined by reservoir engineering. As this thesis is the first 4D seismic research project on the Grand Banks, I am primarily interested in determining firstly if an observable 4D signal can be imaged seismically,

and secondly, if that response occurs in an area that is probable to have the type of signal observed.

Figure 5.15 displays a series of maps that illustrate a close up view of the area of gas injection. The location of 3 injection wells and 2 producing wells are indicated in addition to the orientation of 2 cross sections (A-B, C-D) used for seismic data comparisons. While the maps are contaminated with noise, there are anomalies that occur near injection and production wells that appear to be laterally coherent and have 2001-1991 difference amplitude exceeding the standard noise levels seen in figure 5.13.

The first amplitude anomaly that I discuss is the brightening or increase in base reservoir amplitude along the A-B line occurring in the area of the I3 injection well. From the difference maps, the brightest portion of the amplitude anomaly includes areas immediately around the injector extending down dip about half way towards the off-map (producer). Figure 5.16 displays a three panel seismic cross section (A-B) showing the 1991, 2001, and the 2001-1991 difference seismic data. This cross section extends from an area southwest of the injector down dip towards the production well. The 1991 and 2001 seismic data is fairly comparable, with major events having similar location and amplitudes. The amplitude at the base reservoir increases from 1991 to 2001 for the up dip part of the fault block, but is nearly constant survey to survey for the down dip (southeast) portion. In addition, the reservoir reflection (red event above Fortune Bay)
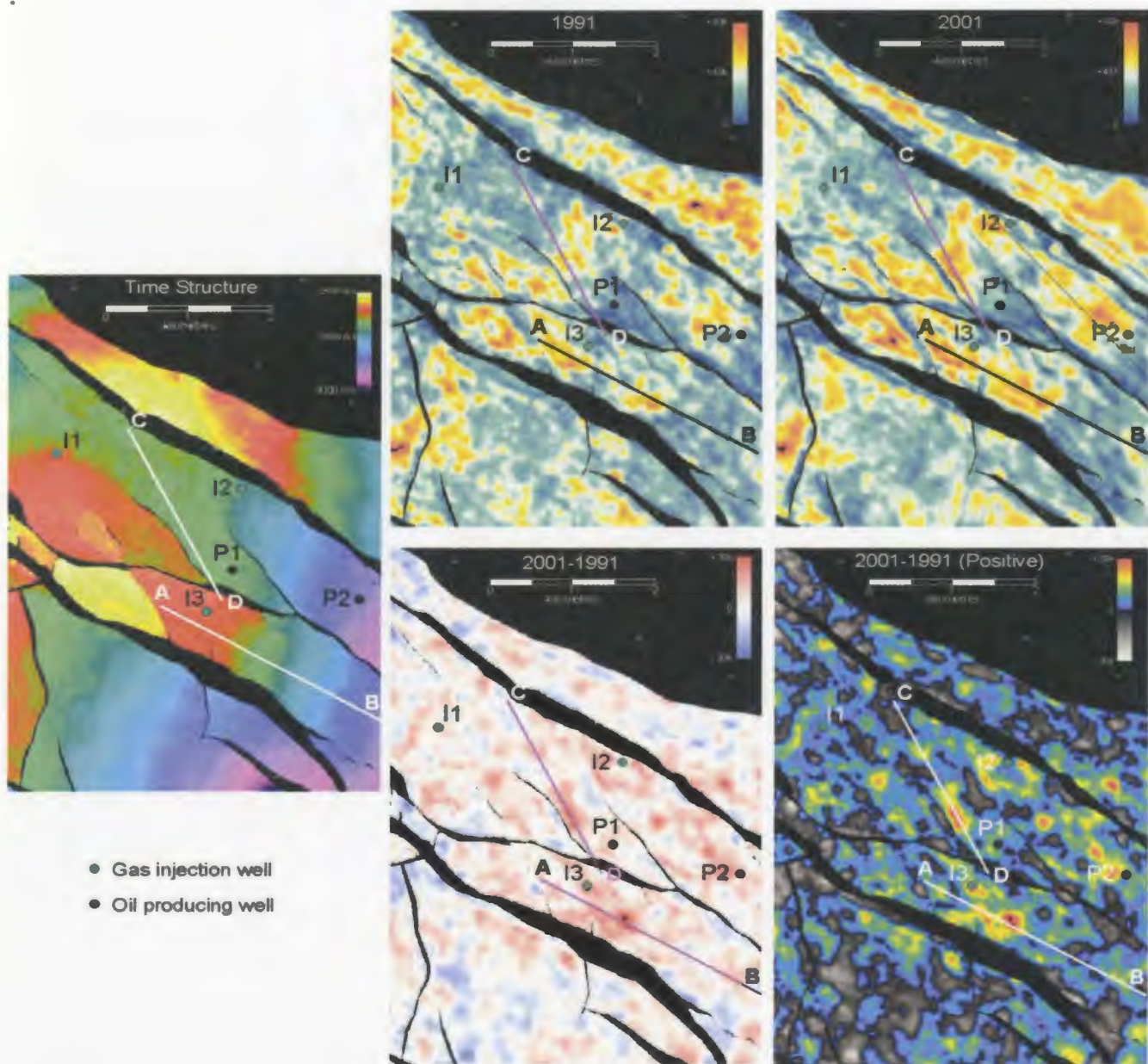
Figure 5.15. *Maps of an area containing gas injection wells. On the left is a time structure map for reference. The top row of images displays the extracted base reservoir (Fortune Bay) amplitudes for 1991 and 2001. The lower row shows the 2001-1991 amplitude difference data in two color schemes. The lines A-B and C-D indicate the spatial location of seismic lines illustrated in this section. Wells are referenced by letter and number, so for example "I2" would be gas injection well 2.*
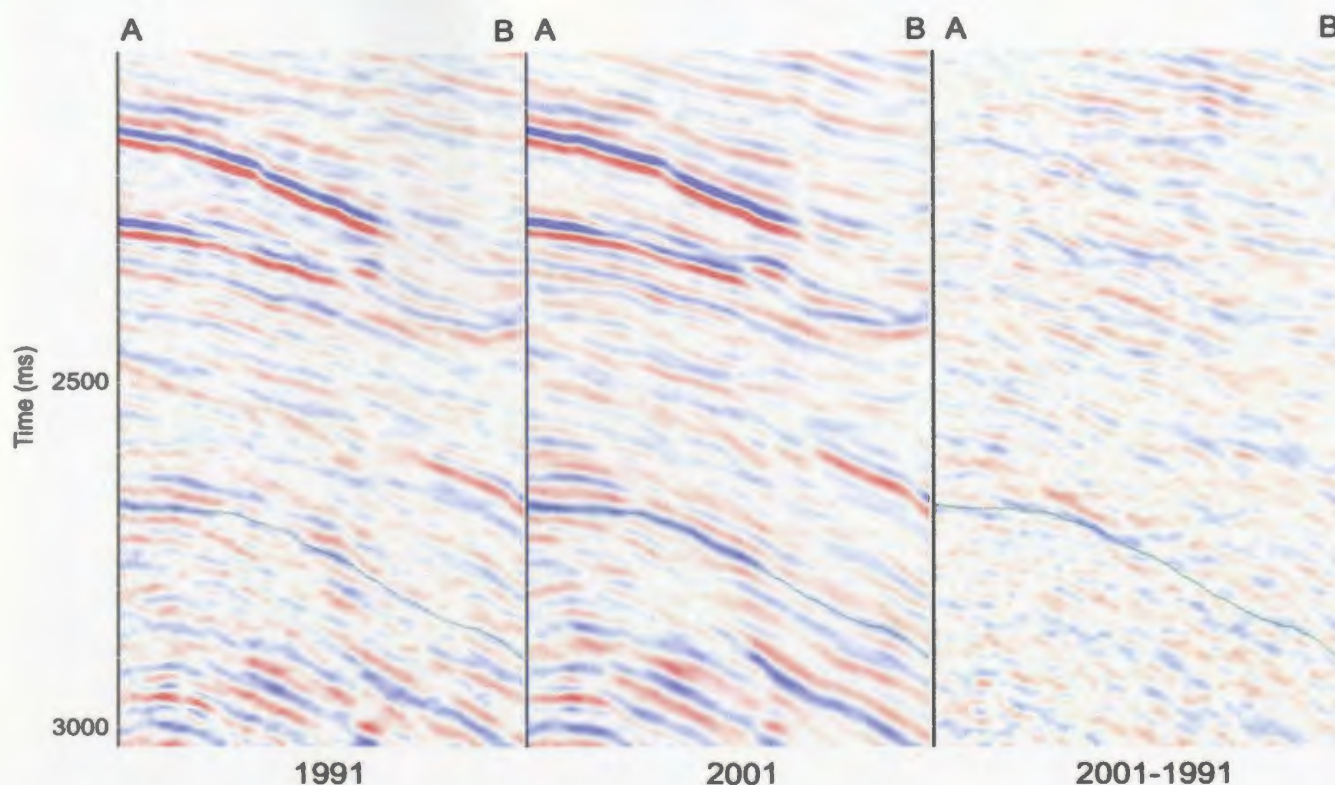
Figure 5.16. *Seismic panels from the line A-B showing the 1991 (left), 2001 (centre), and the seismic difference (right). The base reservoir (Fortune Bay) horizon is depicted in green. Blue is positive amplitude, red negative.*

also brightens in the up dip part of the section. In the 2001-1991 difference section, it can be noted that the up dip portion of the Fortune Bay horizon has the highest 2001-1991 difference amplitudes in the section - including the prominent reflections at 2150 and 2300 ms which have little difference amplitude. As a result, from examining both the maps and section, the amplitude of this anomaly appears to be above the noise level in the seismic data indicating that it can likely be attributed to physical changes in the reservoir. Based on the modeling done in Chapter 3, the result of brightening (increasing positive) amplitude at the base reservoir reflection is consistent with decreases in

162

reservoir impedance (figure 3.16) which increases the contrast with the higher impedance underlying Fortune Bay shales. Decreases in reservoir impedance and as a result increases in Fortune Bay amplitude are consistent with increases in reservoir pore pressure and/or increases in gas saturation (figure 3.17). The increase in reservoir amplitude up dip and the relatively unchanged amplitude down dip is consistent conceptually with a possible gas flood that has only extended part way down the structure at the time of the second survey. Full reservoir simulation is required to delineate possible flow paths and the lateral extent of flood fronts. While reservoir simulation is outside the scope of this study, the time-lapse seismic response in this area is consistent with modeled amplitude responses to increasing gas saturation and/or pore pressure increases.

The second amplitude anomaly that I explore is an area of brightening or increase in base reservoir amplitude along the C-D line (figure 5.15) occurring about 500 m northwest of the P1 production well. This amplitude anomaly occurs against a fault near a production well, but is not in the immediate vicinity of an injection well. To more closely examine this anomaly, the Fortune Bay horizon was carefully re-interpreted to match the mathematical peak in the immediate area. The time structure map along with the seismic amplitude extractions and difference map are displayed in figure 5.17. The maps in this figure indicate that the amplitude brightening anomaly occurs at a local structural high. Figure 5.18 displays a three panel seismic cross section (C-D) showing the 1991, 2001, and the 2001-1991 difference seismic data along the profile indicated in figure 5.15 and

163

figure 5.17. The brightening of both reservoir and base reservoir amplitude can be clearly seen by comparing the 1991 and 2001 sections. Other non-reservoir reflection events in the section are fairly repeatable from survey to survey. As a result, the reservoir reflection difference has the largest amplitude and spatial continuity in the difference section and appears to be above the difference noise level and as a result is likely the result of physical changes in the reservoir.
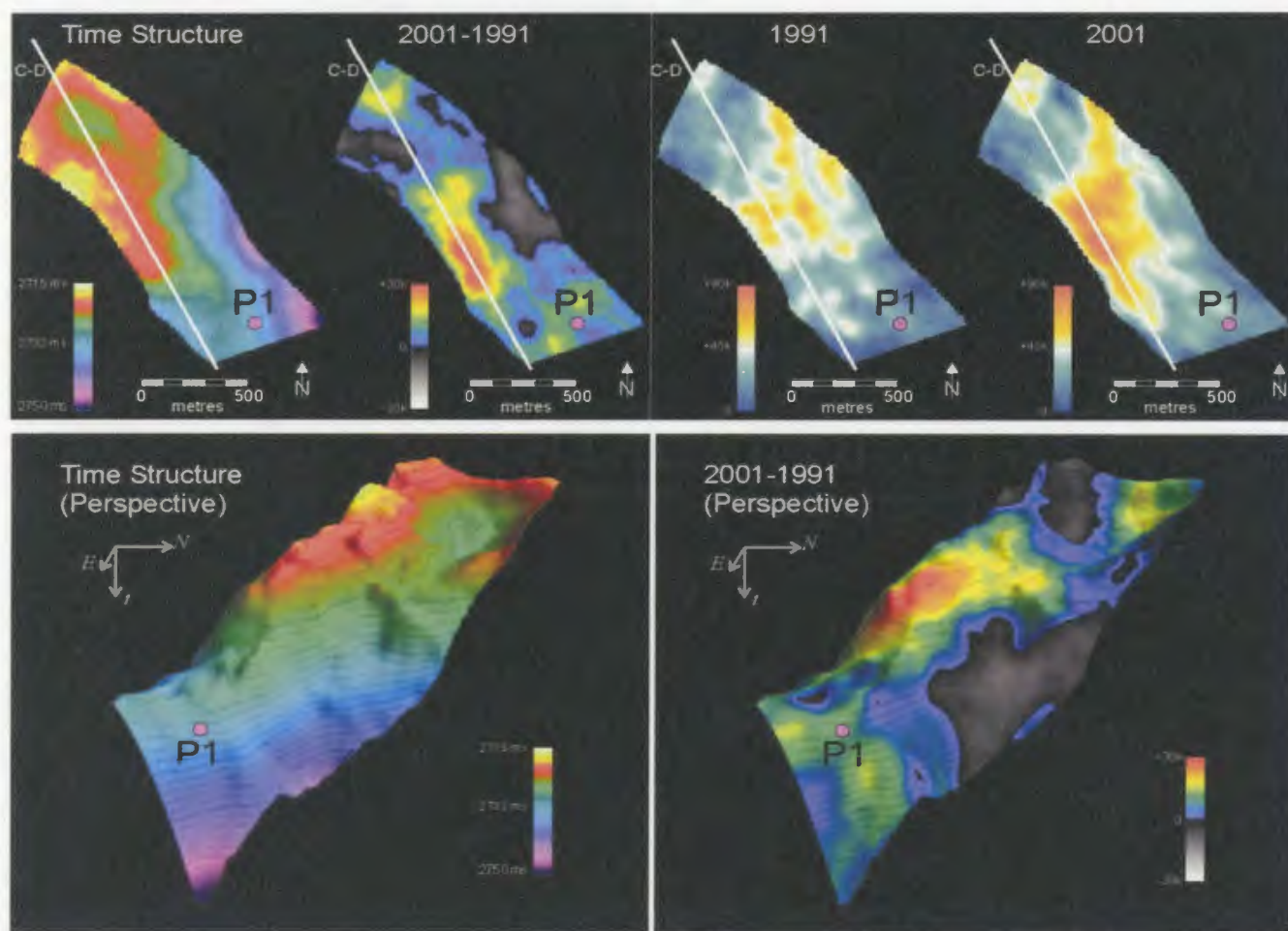
Figure 5.17. *Close up maps of base reservoir seismic amplitude anomaly. From left to right, detailed time structure map, 2001-1991 amplitude difference, 1991 amplitude, and 2001 amplitude. The line indicates the section profile C-D. A 3D perspective view displays the location of the anomaly at a local structural high. Contour lines are 1 ms.*
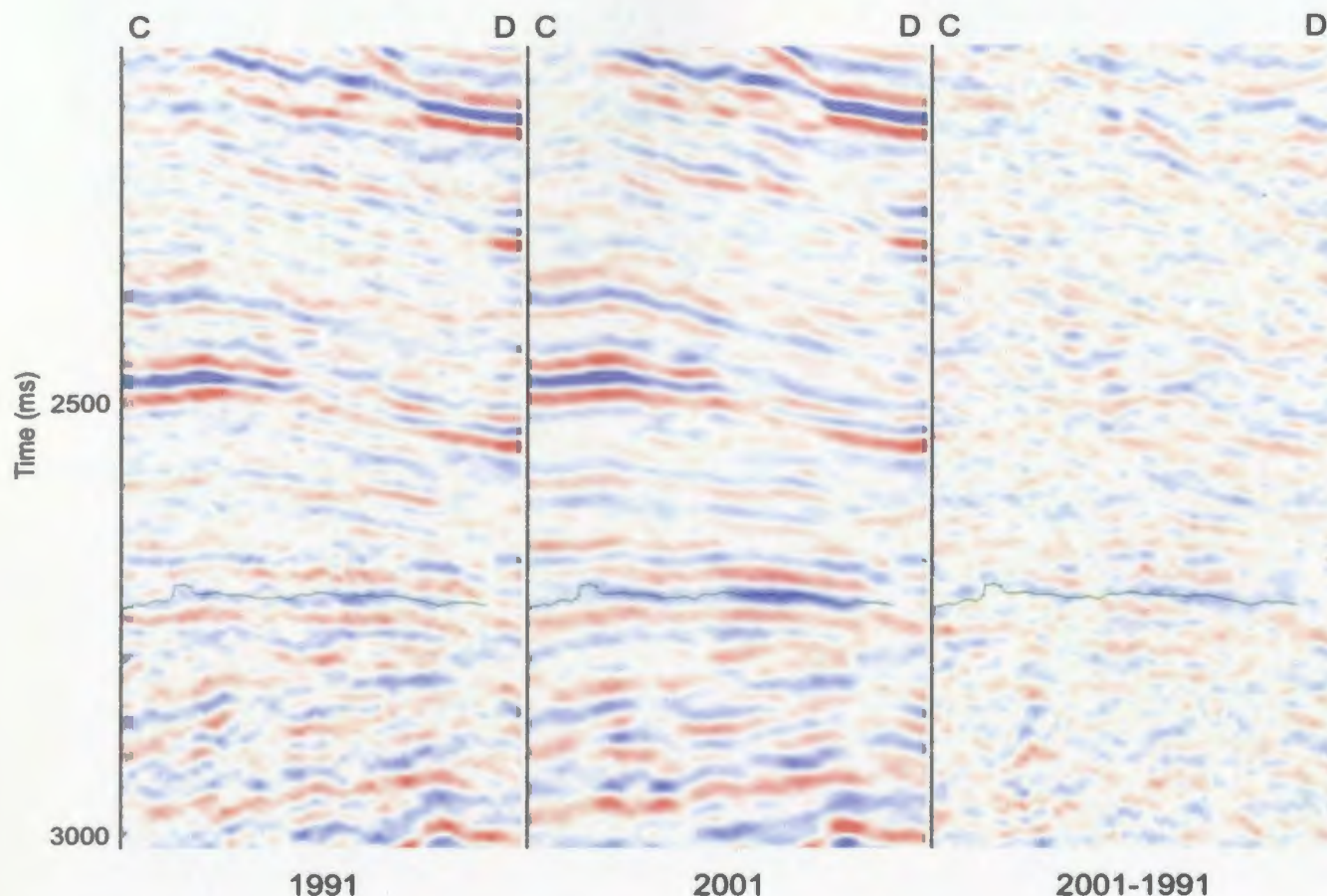
Figure 5.18. *Seismic panels from the line C-D showing the 1991 (left), 2001 (centre), and the seismic difference (right). The base reservoir (Fortune Bay) horizon is depicted in green. Blue is positive amplitude, red negative.*

Based on the 4D seismic modeling work done in Chapter 3, the result of brightening (increasing positive) amplitude at the base reservoir reflection is consistent with decreases in reservoir impedance (figure 3.16) which increases the contrast with the higher impedance Fortune Bay shales. Decreases in reservoir impedance and as a result increases in Fortune Bay amplitude are consistent with increases in reservoir pore pressure and/or increases in gas saturation (figure 3.17). The location of this anomaly at a local structural high near a production well, it is conceivable that there may be gas accumulation near the local high and against the fault. From the modeling work in

Chapter 3, brightening amplitude is consistent with increasing gas saturation, but the magnitude of the brightening in the data of about 25,000 amplitude units far exceeds the model response to full gas saturation change of about 4,000 amplitude units (figure 3.14). The instantaneous phase maps for this anomaly as shown in figure 5.19 are inconclusive, due to the high degree of noise in the 1991 instantaneous phase data.
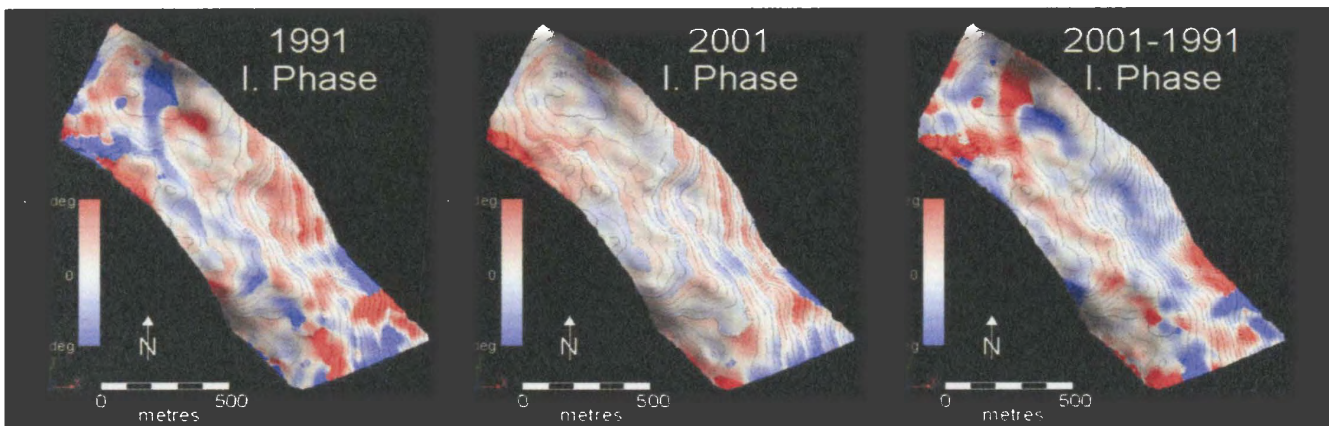
Figure 5.19. *Instantaneous phase data for the anomaly along the C-D transect.*

There are a few possibilities to be considered to account for the magnitude of this anomaly. It is possible that this area also has undergone a pore pressure increase in addition to a possible gas saturation increase, which would substantially increase the amplitude of the time-lapse seismic response. However, a large pore pressure increase seems unlikely due to the fact that the time lag measuring instantaneous phase data doesn't contain any obvious anomalies above the noise threshold (figure 3.12), and the fairly long distance to an injection well. Another possibility is that the 4D seismic modeling work in Chapter 3 underestimates the seismic response to gas saturation. In

addition it should be considered that this anomaly could be a combination of noise and signal cumulatively increasing the difference between 1991 and 2001 amplitudes, or the result of noise outright, but the latter seems highly unlikely given the structural location and relative signal to noise in the seismic section.

In addition to the two anomalies that have been closely examined, there is a ring of amplitude increase (brightening) surrounding the I2 injection well (see figure 5.15). In addition, the ring terminates to the west along the inferred extension of the NW-SE fault. This pattern is very interesting and the amplitude brightening would be consistent with an increase in pore pressure and/or an increase in gas saturation.

In this section, I have examined a few 4D seismic anomalies in a zone of gas injection. By examining the seismic sections and amplitude maps, one can reasonably conclude that these amplitude anomalies are above the noise level and consistent with physical production related changes in the reservoir. Determining the magnitude of the physical changes and the separation of 4D seismic response into pressure and saturation components is not possible in this area using these datasets given the relative noise in the seismic dataset and the inconclusive nature of the instantaneous phase results. With full prestack time-lapse re-processing, it may be possible that meaningful physical properties may be determined from these and other time-lapse seismic anomalies, assuming they are in fact the result of physical reservoir changes, which the evidence in this thesis strongly suggests.

5.4.3 Water injection zone

The next area of study is a fault block that has undergone water injection denoted by the bounding box "A" in figure 5.11. This fault block has a water injection well in the south and an oil producing well in the north, with a well to well distance of approximately 1.9 km. The objective in this area is to determine if the large negative amplitude anomaly "A" imaged in figure 5.12 is consistent with modeled responses to water injection. As with the study of the area of gas injection in the previous section, no history matched 4D seismic modeling was conducted in this zone, so the data-model comparisons made in this section are from oil-water-pressure relationships outlined in Chapter 3, and not potential water or pressure fronts determined by careful reservoir simulation.

The area of study for this section is enlarged in maps shown in figure 5.20. The location of the injection (south) and production well (north) are displayed. The amplitude maps in this figure indicate that there has been significant base reservoir amplitude decrease from the 1991 to the 2001 seismic survey. The magnitude and spatial coherency of the amplitude change is greater than the level of background noise as clearly shown in figure 5.12. To better characterize this 4D seismic anomaly, the base reservoir Fortune Bay horizon was re-interpreted on a trace by trace basis to carefully match the structure.

168
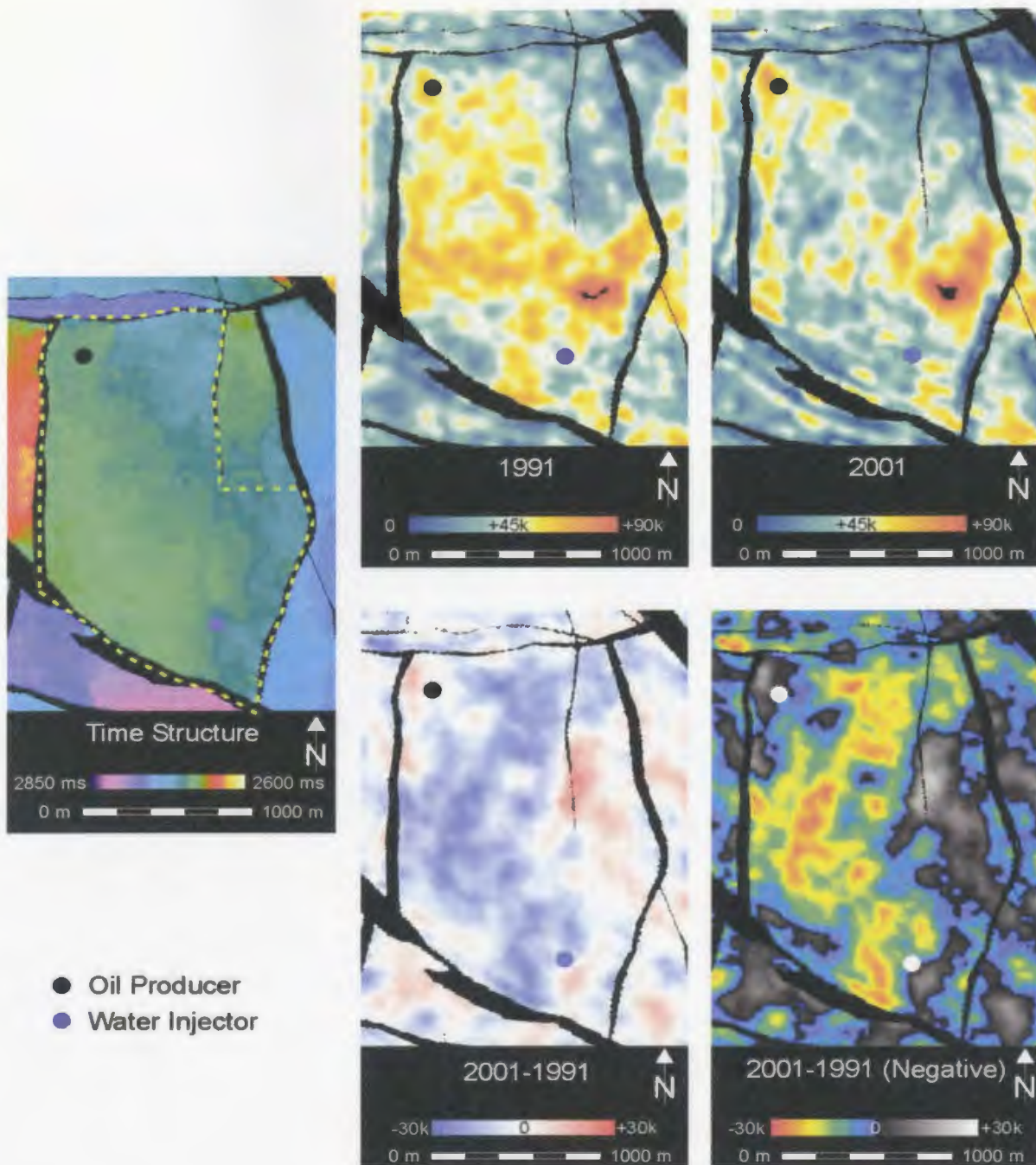
Figure 5.20. *Maps of a fault block containing a water injector/producer pair. On the left is a time structure map for reference with a yellow dashed line to indicate the areal extent of the detailed interpretation area to follow. The top row of images displays the extracted base reservoir (Fortune Bay) amplitudes for 1991 and 2001. The lower row shows the 2001-1991 amplitude difference data in two color schemes.*

The base reservoir horizon was re-interpreted to be centered on the 1991 amplitude peak. This careful re-picking was undertaken to have a more detailed look at small scale structure variation, and to enable the extraction of meaningful instantaneous phase data for the two vintages of seismic data. The new re-interpreted horizon was then depth converted using well log time-depth relationships. This water injection fault block lies partially in an area that was undershot using two vessels during the 2001 seismic survey. By extracting RMS amplitudes in the cross equalized seismic datasets immediately above the reservoir in a non-reservoir interval, it is determined that a scalar multiplier should be applied to the 2001 data to further "equalize" it with the 1991 amplitude data. The depth structure map and undershoot multiplier are displayed in figure 5.21.
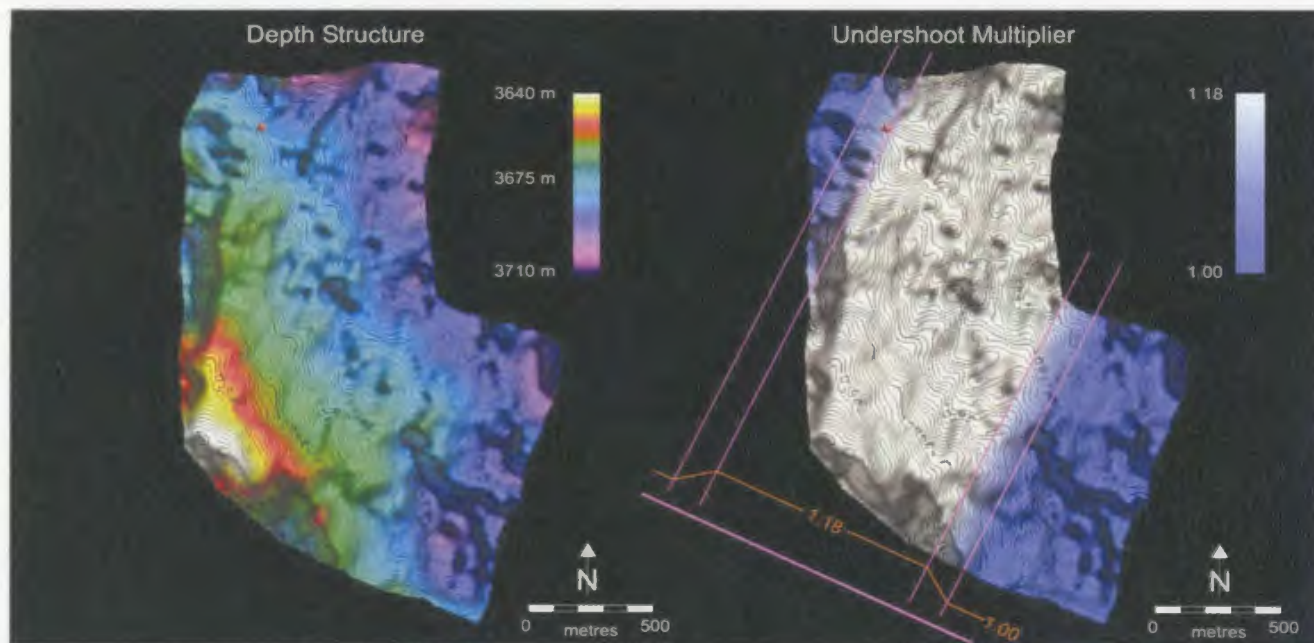
Figure 5.21. *Detailed interpretation zone showing structure (left) and undershoot area (right). The undershoot multiplier was a multiplier applied to traces in the 2001 data to equalize it to the 1991.*

Amplitude variations in the undershoot area were found to be fairly local, and as a result, the XEQ amplitude balancing with it's large smoothing window didn't adequately address the more subtle amplitude variations due to the undershooting. Figure 5.21 displays the undershoot multiplier function as a scalar multiplier of 1.18 with a 10 trace taper on either side that is applied to the 2001 amplitudes. The effect of this undershoot multiplier is that the large negative amplitude 2001-1991 differences clearly seen in figure 5.20 will be reduced as the amplitude of the 2001 survey is increased. Figure 5.22 displays the 1991 Fortune Bay amplitude, 2001 undershoot scaled Fortune Bay amplitude, and the scaled 2001-1991 difference amplitude painted on a depth structured base reservoir surface. From these maps, a few amplitude patterns can be noted. The broad area of relatively high amplitude in the extreme eastern part of the map is relatively constant from survey to survey. Along the well to well EFGH line indicated in the maps, there is a general pattern of base reservoir amplitude decrease or dimming from the 1991 to the 2001 seismic survey. Figure 5.23 displays 1991 and 2001 seismic panels along the EFGH transect from injector to producer. Lower Fortune Bay amplitude in 2001 can be seen visually in the sections. In addition, it can be noted that in the 1991 data, the reservoir reflection (red, above Fortune Bay) is vertically smooth or in some instances a doublet (F-G). In the 2001 data, the character of this reflection has changed especially in the dashed line area (F-H) and now has the bulk of the negative reflection energy at the top of the reservoir while near the base of the reservoir it is a fairly subtle reflection compared to the equivalent reflection in the 1991 data (incidated by two arrows).
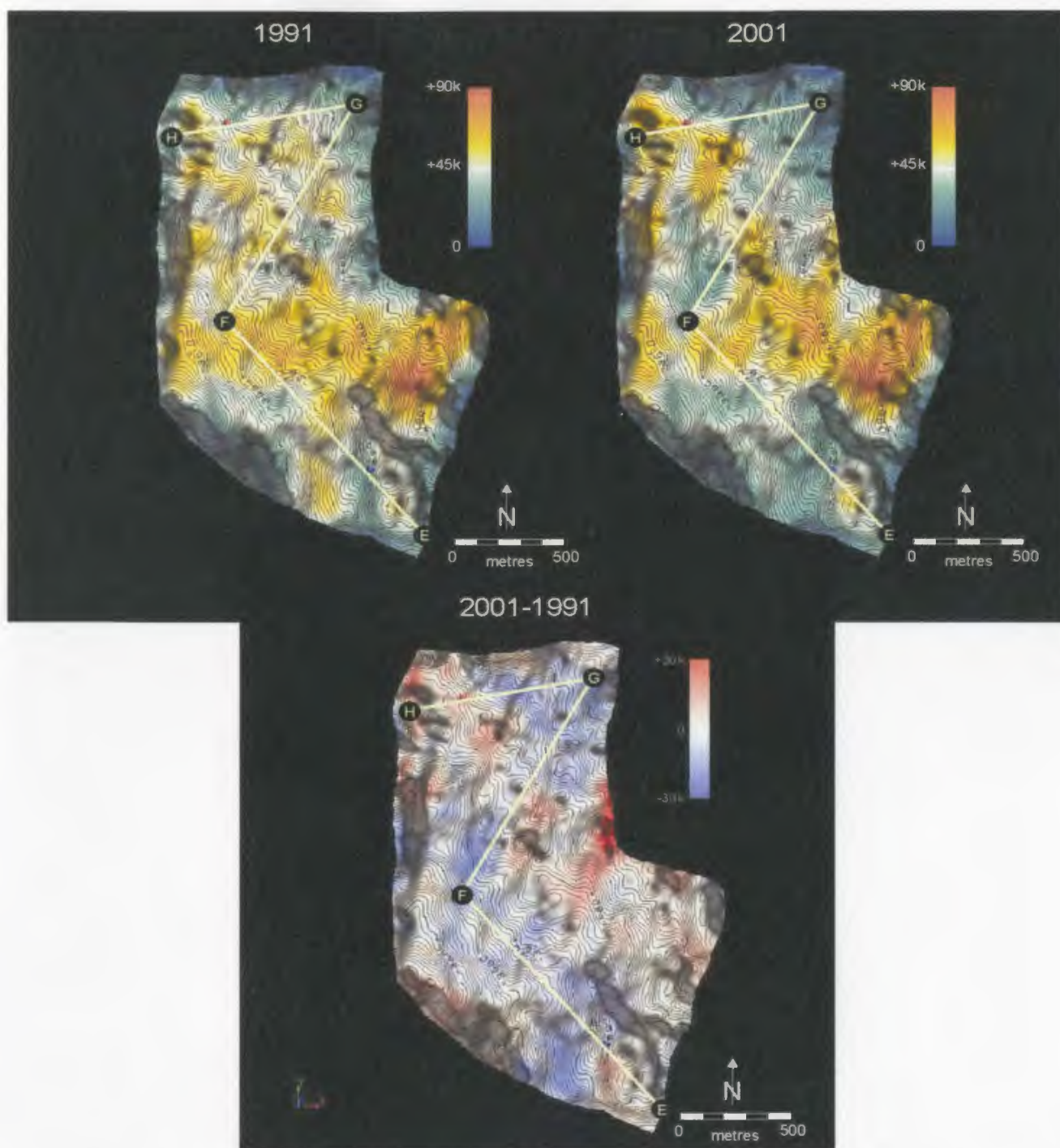
Figure 5.22. *Fortune Bay maximum peak amplitude extractions for the 1991 (left), 2001 (right), and 2001-1991 difference bottom). The line EFGH denotes the orientation of seismic sections used for viewing the time-lapse seismic effect in section. The blue dot in the south denotes the location of the water injection well, and the red dot in the north indicates the oil producing well.*
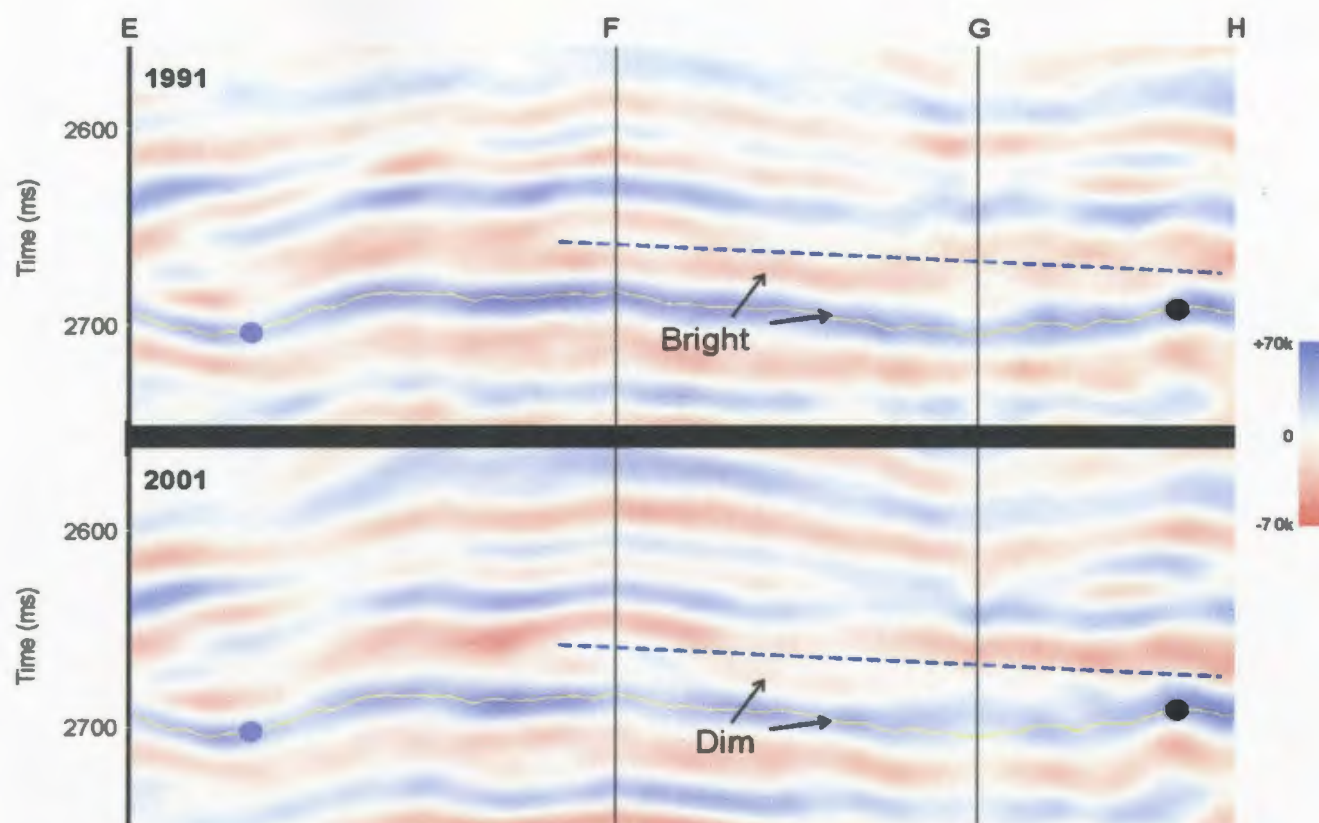
Figure 5.23. *1991 (top) and 2001 (bottom) seismic lines through the water injection fault block. The blue dot indicates the location of the water injection well and the black dot the oil producer. The yellow line is the base reservoir Fortune Bay horizon. The dashed green line is used for illustrative purposes separating where the reservoir changes from survey to survey.*

The dimming of the base reservoir horizon (Fortune Bay) and the dimming of the lower portion of the reservoir reflection are both consistent with the modeled 4D seismic response to water saturation increase seen in figure 3.21. In figure 5.24, the amplitude difference maps are displayed with the structure map and some interpretation is displayed. White lines indicate the extent of the negative amplitude anomaly. While reservoir simulation is required to fully delineate possible fluid flow paths, this amplitude pattern would be consistent with an increase in water saturation originating near the water

injection well and moving initially northwest. It can be noted from the maps that the NW-SE structural deviation approximately 150 m north of the water injection well seems to separate areas of amplitude change to the south from area of little change to the north.
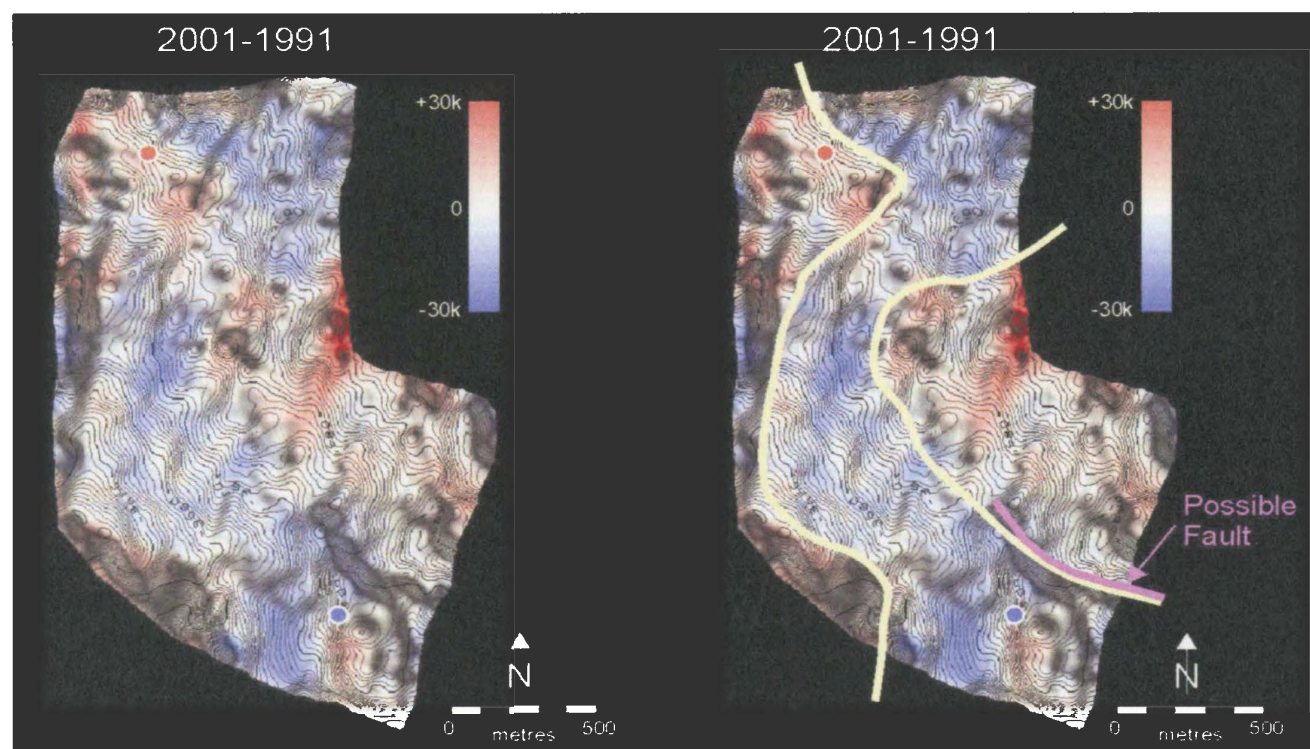
Figure 5.24. *Maps showing the relationship between structure and time-lapse seismic amplitude change. Blue dot is the water injector, red dot the oil producer. The interpreted map (right) displays lines around the amplitude dimming (decreasing base reservoir amplitude) extent as well as the location of a possible small scale sealing fault.*

As a result, it is possible that this small structural perturbation could be a sealing fault. From the base reservoir depth map, there is a structural low to the east of the production well that has negative 2001-1991 amplitude consistent with increased water saturation and/or decreased pore pressure. It is possible that this local structural low could be a

174

collection point for injected water. The 2001 section in figure 5.23 displays decreased reservoir amplitude and decreased reservoir traveltime at point "G" in the central part of this local structural low. This is a result consistent with the modeled time-lapse seismic effect from increases in water saturation and/or decreases in pore pressure. Another area of interest is in the immediate area of the water injection well. It is interesting that there is a base reservoir amplitude decrease to the northwest while an amplitude increase can be imaged to the southeast. The increase in amplitude may be consistent with an increase in pore pressure that contributes a greater decrease on reservoir impedance than the possible increase due to increased water saturation. This effect is modeled in figure 3.22.

To more closely examine the change in reservoir traveltime, the instantaneous phase attribute is extracted on a 15 ms window centered 8 ms below the re-interpreted Fortune Bay horizon for both the 1991 and 2001 datasets. It is extracted from a window centered below the Fortune Bay horizon so that change in reservoir reflection character will have less impact on the calculation. As a result, the 1991 and 2001 instantaneous phase extractions have a median phase of approximately 80 degrees and are not in the range to be affected by phase wrapping. Figure 5.25 displays the 1991, 2001, and 2001-1991 instantaneous phase maps. What is of particular note in these maps is the pattern formed by the 2001-1991 difference in instantaneous phase. In the area immediately around the injection well, there is a decrease in instantaneous phase or an increase in reservoir travel
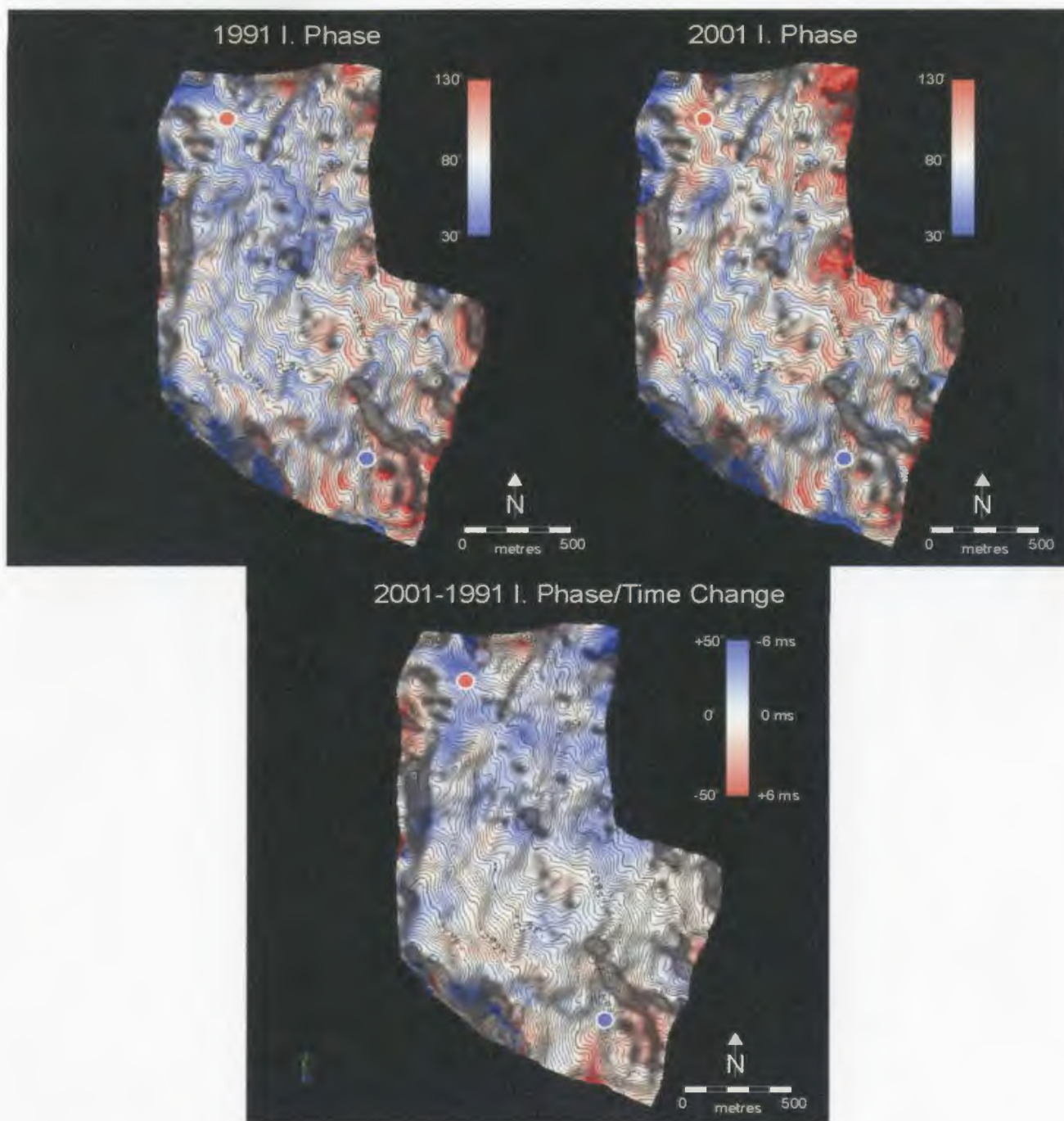
Figure 5.25. *Fortune Bay instantaneous phase extractions for the 1991 (left), 2001 (right), and 2001-1991 difference (bottom). Note that in the difference map, there is an increase in travel time around the injector in the south, and a decrease in travel time in the north towards the producer.*

time. This is a result that is consistent with increased pore pressure around the injection well, and it is corresponds to the slight increase in base reservoir amplitude imaged in this area. In the northern part of the fault block near the production well, there is a decrease in instantaneous phase between the 1991 and 2001 survey which translates into a reservoir traveltime decrease. A decrease in reservoir traveltime is clearly seen in figure 5.23 "G" and based on the modeling in figure 3.24 is a result consistent with increasing water saturation and/or decreases in pore pressure. In the central portion of the fault block between the injection and production wells, there is an area of relatively no traveltime change possibly suggesting that there is little pore pressure change in this area. In addition, it is interesting to note that the change in instantaneous phase is sectioned by the possible fault outlined in figure 5.24, with areas to the south having increased reservoir traveltime and areas to the north experiencing little to no change which further provides evidence that this structural event may potentially be a barrier to reservoir fluid flow. Figure 5.26 gives a vertically exaggerated 3D perspective view of this water injection fault block with the change in amplitude and instantaneous phase painted on the structure. These images further suggest the possibility that the amplitude change pattern is related to structural control and that there is a reservoir traveltime increase immediately around the injector and a decrease towards the production well. This could suggest a possible pressure rise around the injector, and a combination of water saturation increase and/or pore pressure drop around the production well.
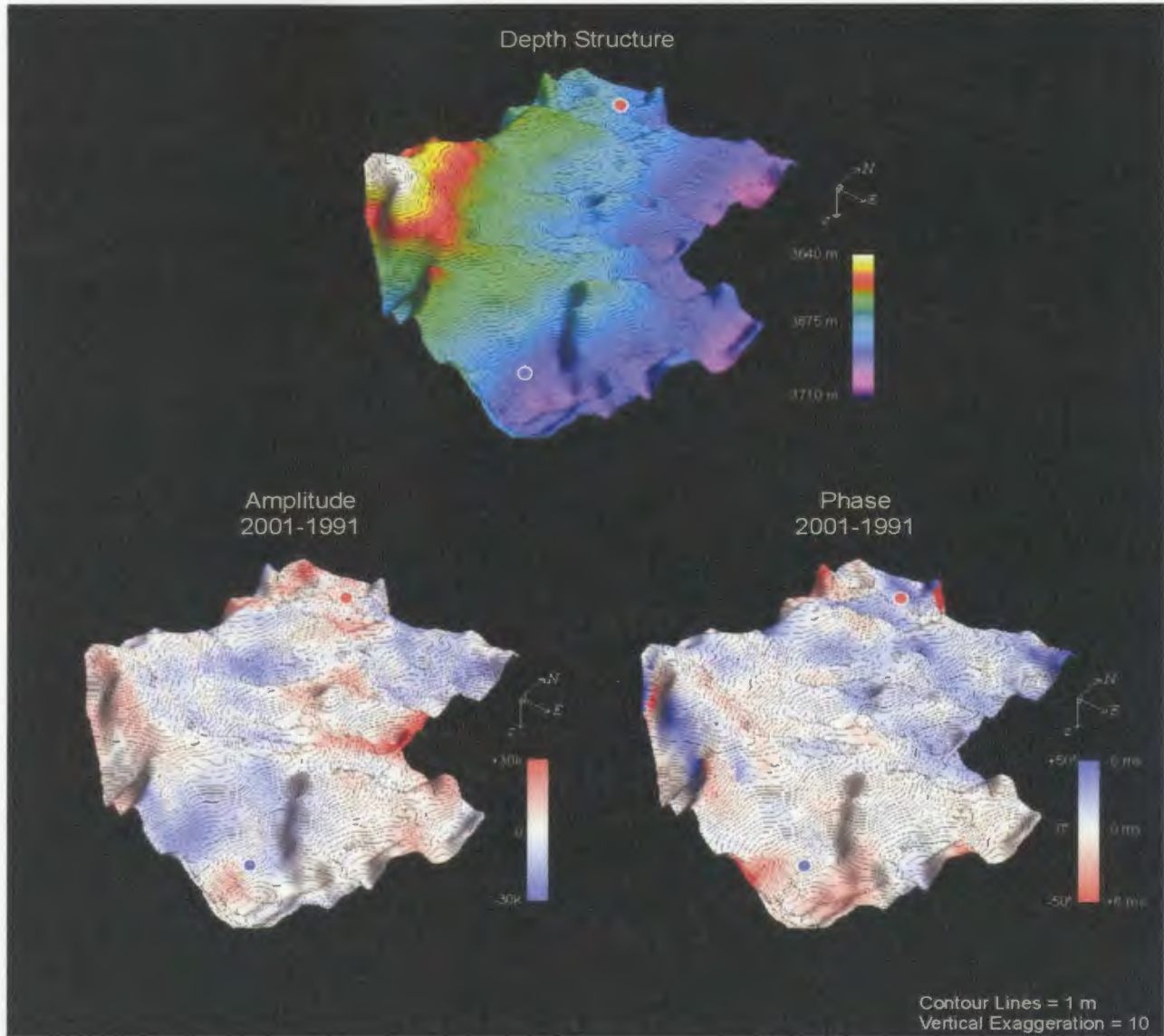
Figure 5.26. *3D perspective maps of the water injection fault block showing changes in base reservoir amplitude (left) and phase (right). The blue dot denotes the location of the water injector, the red the oil producer.*

5.4.4 Pressure and saturation inversion attempt

In this thesis, I have presented qualitatively a number of 4D seismic anomalies that can be imaged in the Hibernia 4D seismic data. I now make an attempt to quantitatively

invert the poststack 4D seismic data for pressure and saturation, using the new and original methods outlined in section 3.9. This is a high risk venture, because the modeled anomalies are subtle, the data is relatively noisy, and the inversion is based solely on poststack methods with no cross-validation of seismic data results with reservoir flow simulation response. However, in the water flooded block, the pressure/saturation inversion did produce some interesting patterns as shown in figure 5.27. Considering the inversion for changes in pore pressure, which is directly related to changes in traveltime (or instantaneous phase), the patterns make some conceptual sense. From the inversion, the greatest pressure rise is around the injector and the largest pressure drop is in the northern part of the fault block where the producing well is located. However, the values for pore pressure change are very unreasonable (up to +/-30 MPa), considering according to well pressure tests, the pressures in this fault block didn't change considerably between the surveys. Attempts to scale this data to values in a reasonable range were not successful, so I have displayed the results without any scaling.
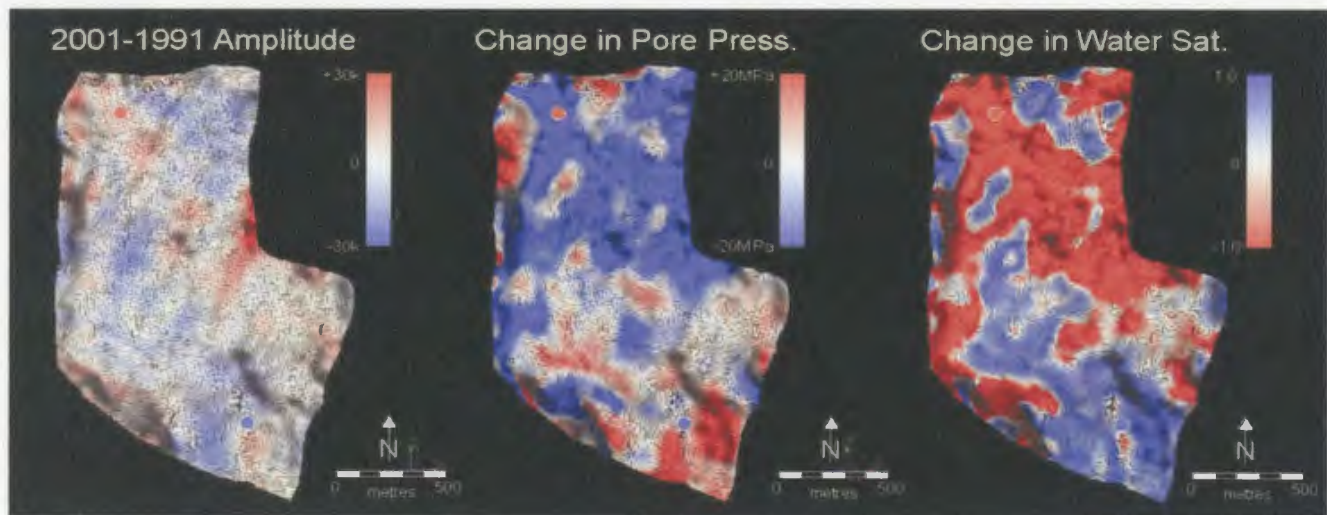
Figure 5.27. *4D seismic pressure and saturation inversion results for the Hibernia water flooded block.*

179

The errors in the inverted results (figure 5.27) attributable to seismic data errors are large compared to potential errors in the choice of modeling methodology (i.e. Voigt vs. Reuss fluid mixing assumptions). The inversion for water saturation yields interesting patterns, but again the data quality (e.g. large negative changes in water saturation) limits any interpretation of the inverted data to qualitative analysis. However, the qualitative patterns for increases in water saturation around the injection well seem to provide a more reasonable interpretation of possible fluid substitution than amplitude differences alone. The patterns appear more reasonable because the entire southeast zone (to the faults) is shown as flooded in the inversion model, while the amplitude difference is negligible and/or inconclusive to south and east of the injection well. In this area, with the pore pressure inversion predicting a pore pressure increase, and the seismic amplitude difference slight, it is likely that the 4D seismic effect of pore pressure rise and increased water saturation are offsetting each other (as in figure 3.22), keeping impedance change, and as a result, amplitude low. These patterns are intriguing, and these original poststack inversion methods require future examination as they may with proper calibration and a low noise dataset prove useful at quickly estimating physical changes in a reservoir with similar properties.

For the Hibernia 4D seismic data, Chapter 4 determined that the 4D signal to noise ratio is approximately 1.4, meaning the magnitude of the 4D seismic anomalies are just above the noise level. As a result of the fairly high noise level, quantitative reservoir property determination is not possible on this dataset using the pressure and saturation inversion

algorithms introduced in this thesis. Full prestack 4D processing of the Hibernia data may possibly allow for the quantitative interpretation of pressure and saturation changes from the 4D seismic data. If undertaken, this process would likely use prestack attributes, flow simulations, detailed production data, and well rates to cross-validate seismic interpretations.

5.5 Conclusions

In this chapter, I have highlighted 4D seismic anomalies located in various areas of the Hibernia field. As the 4D seismic method relies on the imaging of subtle changes in seismic data, the importance of scaling and filtering the data is clearly demonstrated in this chapter. The removal of lateral noise and the AVO-Stack calibration render the 4D seismic data more comparable and therefore more suitable for interpretation, although it contains lower spatial resolution. The calibration and filtering allowed for a number of 4D seismic anomalies in production areas to be identified. While there has not been history matched modeling of the 4D seismic data response, the data response in gas and water injection areas is consistent with modeling increases in gas and water saturation respectively. In addition, using instantaneous phase to monitor traveltime change produces results in the water injection area consistent with a pressure rise around the injection well and a decrease in the area of the producer. The 4D seismic amplitude pattern imaged in the water injection block suggests the possibility that reservoir fluid flow may be partially influenced by structural controls. A pressure and saturation inversion is attempted, and it yields some interesting qualitative results around a water

injector, but the numerical values are too unstable for direct pressure and saturation measurement.

While full prestack 4D seismic processing of these seismic datasets will yield more accurate 4D seismic results with a potential to invert for quantitative reservoir measurements, this research has produced very strong evidence that physical reservoir changes in both gas and water injection zones can be imaged seismically, a very important result. With the ability to detect reservoir related 4D signals demonstrated, future work is needed to delineate the potential that the 4D seismic method can be used in challenging Grand Banks fields such as Hibernia for integrated quantitative reservoir monitoring purposes.

Chapter 6

Feasibility of 4D seismic on Canada's Grand Banks

6.1 Overview

Having studied the modeling, processing, and interpretation of 4D seismic data for the Hibernia field, in this chapter I broaden our study to examine the first order 4D seismic potential that the other major Grand Banks fields hold. The position of this study in the thesis flowchart is displayed in figure 6.1. After a brief review of the locations and backgrounds of the respective fields on the Grand Banks; White Rose, Terra Nova, and Hebron, a risk analysis will be undertaken.   To determine the potential applicability of the 4D seismic method to other fields on Canada's Grand Banks, an established time-lapse seismic feasibility risk analysis spreadsheet as per Lumley et al. (1997) is utilized. The risk analysis is comprised of two principal components. The first is the assembly of relevant time-lapse seismic reservoir parameters for the fields of interest.   The second is the ranking and scoring of each field in "seismic" and "reservoir" categories.   The higher the score for a particular field, the lower the risk of 4D seismic project failure. The fields on the Grand Banks are shown to be higher risk time-lapse seismic projects, comparable in parameters and score to existing time-lapse projects in the North Sea.   Some general comments are then made regarding the possible future implementation of 4D seismic technology on the Grand Banks.
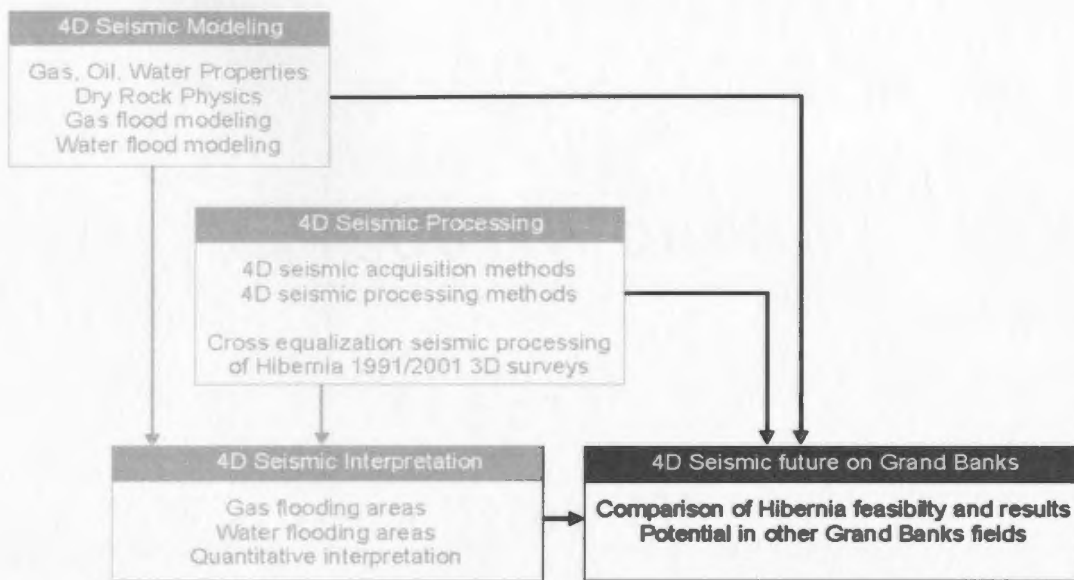
Figure 6.1 *Thesis outline flowchart. This chapter which discusses the future of 4D seismic on the Grand Banks draws on theory, modeling, processing, and interpretations to yield insight as to the more general applicability of this reservoir seismic method in the hard-rock harsh-environment of the Canadian Grand Banks.*

6.2 Introduction to other Grand Banks fields

Having discussed in detail the potential of the time-lapse seismic method for the Hibernia field, I now expand the analysis to other oil fields on the Canadian Grand Banks, particularly in the Jeanne d'Arc basin. In this chapter, I examine the 4D seismic feasibility of the principal reservoirs in the Terra Nova field, the White Rose field, and the Hebron field. The location of these oil fields is displayed in figure 6.2. By examining the fields parameters using a time-lapse seismic feasibility risk assessment as per Lumley et al. (1997) and comparing the results to existing 4D projects worldwide, some insight can be gained into the potential future implementation of this seismic technology on the Canadian Grand Banks.
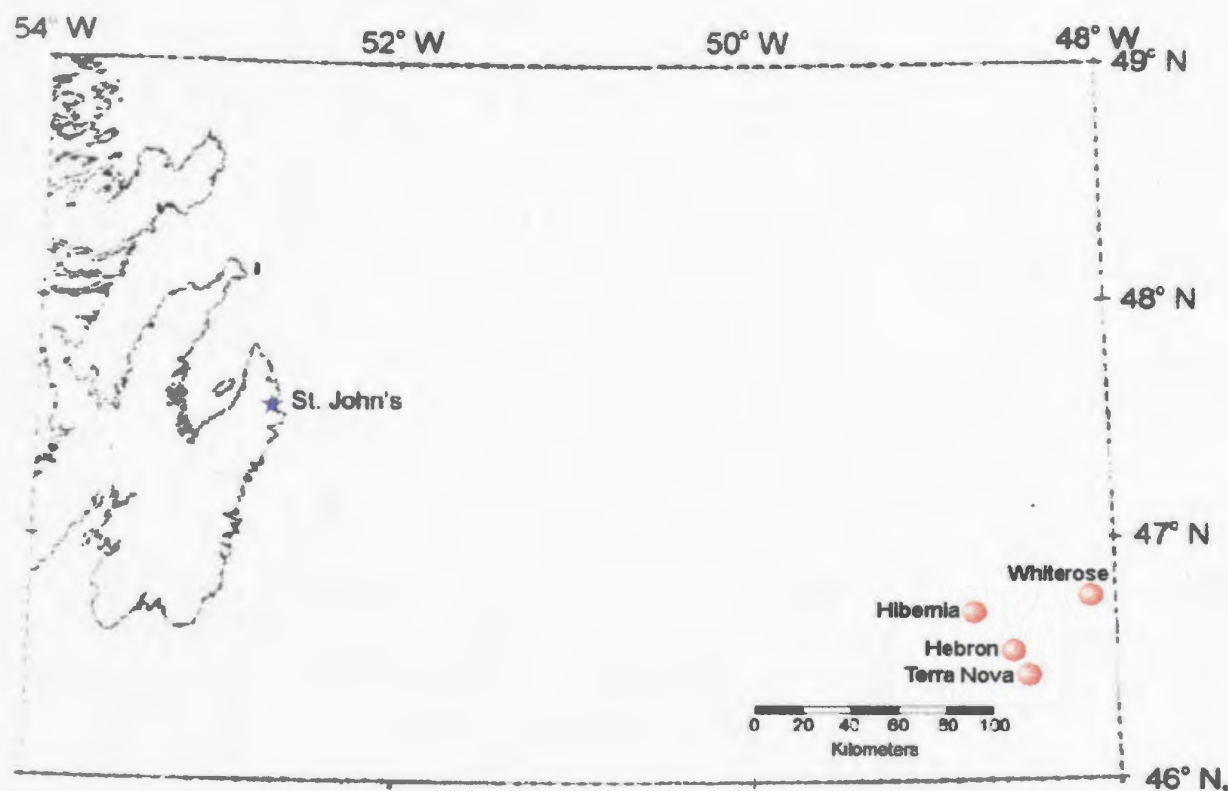
Figure 6.2. *Location map of the Grand Banks oil fields included in this feasibility study.*

6.2.1 Review of the Hibernia field

The first major discovery on the Grand Banks, the 865 million barrel (CNOPB, 2003) Hibernia oil field was discovered in 1979. The reservoir is at an average depth of approximately 3700 m and the reservoir rocks are Upper Jurassic (Tithonian) to Lower Cretaceous in age (GSC, 1992). A 3D seismic survey was acquired in 1991 with a subsequent survey acquired in 2001 or 4 years into production. Hibernia uses both gas and water injection as a secondary recovery process.

6.2.2 Terra Nova field

Discovered in 1984, the Terra Nova oil field is a 405 million barrel (CNOPB, 2003) oil field located 39 km southeast of Hibernia. Production commenced in early 2000 and is expected to last approximately 15 years. The principal reservoir is Late Jurassic in age and has an average depth of approximately 3300 m. A modern 3D seismic survey was acquired in 1997, prior to the onset of production. Terra Nova utilizes both gas and water injection to enhance recovery.

6.2.3 White Rose field

The third field scheduled for production on the Grand Banks is the White Rose field, located approximately 52 km east of Hibernia. Discovered in 1984, this field is estimated to contain 283 million barrels of oil and 2.5 Tcf of gas (CNOPB, 2003). The principal reservoir in the field, the Avalon/Ben Nevis, lies at an average depth of 3000 m and is

Aptian to Albian in age (GSC, 1992). A 3D seismic survey was acquired in 1997 and production is currently scheduled to commence in late 2005/early 2006 (Husky, 2004). It is currently planned to use water injection to enhance reservoir recovery.

6.2.4 Hebron field

The Hebron oil field was discovered in 1981 and is located approximately 28 km southeast of Hibernia. The field is estimated to contain 325 million barrels of oil (CNOPB, 2003). The principal reservoir, the Avalon/Ben Nevis reservoir, lies at an average depth of approximately 1900 m. As the Hebron consortium is currently evaluating the economic feasibility of this oil project, if approved, production is still a number of years away. A 3D seismic survey was acquired over the field in 1997. Preliminary planning suggests that if the project is approved, the intent is to utilize water injection as a means of enhanced oil recovery (Evans, 2004).

6.3   4D seismic feasibility comparison

Prior to the decision being made to initiate a time-lapse seismic program, there is typically some effort directed at determining whether the use of time-lapse seismic will be successful for a given project (Lumley et al., 1997). As different oil fields have unique reservoir and seismic characteristics, the feasibility of a time-lapse seismic program varies greatly from project to project. Lumley et al. (1997) present a straightforward 4D seismic technical risk assessment. Using first order seismic and reservoir parameters, this risk assessment returns a quantitative score that helps assign a

risk value for the proposed 4D seismic project. In the sections to follow, I calculate the 4D seismic feasibility ratings for the major Grand Banks oil fields and compare them to the feasibility scores of existing time-lapse projects worldwide. In addition, I examine the Hibernia feasibility score in light of the 4D seismic data results from Hibernia which have been illustrated in this thesis. This comparison will yield insight into the type of time-lapse seismic response that is possible in a given feasibility score range.

6.3.1   4D seismic parameter summary

As the success of a time-lapse seismic project depends on both reservoir and seismic parameters, I firstly assemble data in key time-lapse seismic categories. These 4D seismic elements were thoroughly reviewed in the earlier chapters on modeling (Chapter 2 and Chapter 3). Figure 6.3 displays a summary table of pertinent seismic and reservoir parameters for Hibernia and a number of existing time-lapse seismic projects in various parts of the world. The details of the individual variables are given in depth in Lumley et al. (1997), and will only be briefly discussed here, but it should be noted that units are in both metric and imperial and I have converted Grand Banks field parameters to imperial for comparison purposes where applicable. The "ideal" category (from Lumley et al., 1997) is a qualitative descriptor indicating what the respective parameter should be for the greatest contribution to time-lapse seismic success. Parameters that are positive for potential 4D seismic detection at Hibernia include: a high GOR oil (1000+ scf/bbl) which gives greater contrast with the injected water, large saturation

	IDEAL	INDONESIA	GULF OF MEXICO	WEST AFRICA	NORTH SEA	HIBERNIA
RESERVOIR						
Depth(ft)	shallow	650	7000-8000	4000-6000	9200-10400	12500
Overburden Pressure (PSI)	low	530	7000-8000	4000-6000	6500-7500	13000
Pore Pressure (PSI)	high	100-350	3100-3300	2200	5250-6500	5800
Net Pressure (PSI)	low	430-180	3900-4700	1800-3800	0-2250	7200
Bubble Point (PSI)	---	110	3100	4500	1250	4800 - 5400
Temperature (F)	high	100-430	176-180	175	215	215
Unit Thickness (ft)	high	100	100-150	50-150	15-40	150-250 ft
ROCKS						
Dry Bulk Modulus (Gpa)	low	2.0-3.0	3.0-5.8	5.0-8.0	10.0-30.0	13-17
Dry Density (g/cc)	low	1.54-1.67	1.7-2.1	1.76	2.07-2.23	2.07-2.23
Porosity (%)	high	30-38	21-34	26-30	16-23	15-25
OIL						
Solution GOR (scf/bbl)	high	0	250-350	350-400	>300	850 - 1500
Gravity (API)	high	22	25	22-28	36	35
Density (g/cc)	low	0.9	0.85	0.77	0.75	0.64
Bulk Modulus (Gpa)	low	1.5	1.2-1.5	1	0.92	0.5
WATER						
Salinity (ppm)	high	40000	190000	40000	200000	50000
Density (g/cc)	high	1	1.1	1	1.08	1.04
Bulk Modulus (Gpa)	high	2.25	3.35	2.25	3	3
GAS						
Density (g/cc)	low	0.100	0.100	0.100	0.120	0.250
Bulk Modulus (Gpa)	low	0.100	0.100	0.100	0.230	0.110
4D FLUIDS						
Fluid saturation change (%)	high	90 -> 10	90 -> 10	75 -> 25	75 -> 40	90 -> 30
Fluid compress. Change (%)	high	>1000	150-200	125	200	Water/Oil = 300 Gas/Oil = 50
SEISMIC						
Dominant Frequency (Hz)	high	125	50	30	25	25
Average Resolution (ft)	low	15	50	85	100	100
Image Quality (1-5)	5	4	5	4	3	4
Repeatability (1-5)	5	6	4	4	3	2
Fluid Contact Visibility (1-5)	5	4	4	4	2	0
Predicted traveltime change (samples)	>4	20	0	0-4	0	0
Predicted impedance change (%)	>4	55	8.0-10.0	4.0-6.0	3.0-7.0	2.0-3.0

Figure 6.3 *Time-lapse seismic feasibility spreadsheet with examples from Lumley et al. (1997) compared to Hibernia parameters.*

change, and a high reservoir thickness of about 60 m. Parameters that make detection of time-lapse seismic signals more difficult include: a depth of approximately 10000-13000 ft, high dry rock bulk modulus (13-17 GPa), high pore and effective pressures (40 and 50 MPa respectively), low seismic frequencies (20-25 Hz), a challenging acquisition environment, and no visible seismic fluid contacts in the legacy data. Of the examples shown in figure 6.3, the parameters for Hibernia are most comparable to the Jurassic-reservoir North Sea time-lapse seismic project example in Lumley et al. (1997).

In figure 6.4, the Hibernia 4D seismic risk assessment data is compared to parameters from the White Rose, Terra Nova, and Hebron oil fields. The data for these fields was supplied by personnel at the respective operator companies and through the

	IDEAL	HIBERNIA	WHITE ROSE	TERRA NOVA	HEBRON
RESERVOIR					
Depth(ft)	shallow	12500	10000	11000	6000
Overburden Pressure (PSI)	low	13000	9100	11000	6520
Pore Pressure (PSI)	high	5800	4350	5100	2750
Net Pressure (PSI)	low	7200	4750	5900	3770
Bubble Point (PSI)	—	4600 - 5400			
Temperature (F)	high	215	230	203	120.2
Unit Thickness (ft)	high	150-250 ft	75-280	120	120
ROCKS					
Dry Bulk Modulus (Gpa)	low	13-17	13-17	13-17	10-14
Dry Density (g/cc)	low	2.07-2.23	2.2-2.3	2.1-2.3	2.0-2.2
Porosity (%)	high	15-25	15	17	23
OIL					
Solution GOR (scf/bbl)	high	850 - 1500	600	700	280
Gravity (API)	high	35	31	34	30
Density (g/cc)	low	0.64	0.7	0.68	0.76
Bulk Modulus (Gpa)	low	0.5	0.6	0.55	0.9
WATER					
Salinity (ppm)	high	50000	50000	50000	50000
Density (g/cc)	high	1.04	1.04	1.04	1.04
Bulk Modulus (Gpa)	high	3	3	3	3
GAS					
Density (g/cc)	low	0.250	N/A	0.230	N/A
Bulk Modulus (Gpa)	low	0.110	N/A	0.090	N/A
4D FLUIDS					
Fluid saturation change (%)	high	90 -> 30	85 -> 30	88 -> 30	80 -> 30
Fluid compress. Change (%)	high	Water/Oil = 300 Gas/Oil = 50	Water/Oil = 220	Water/Oil = 250 Gas/Oil = 80	Water/Oil = 100
SEISMIC					
Dominant Frequency (Hz)	high	25	25	20	30
Average Resolution (ft)	low	100	100	120	80
Image Quality (1-5)	5	4	1	3	4
Repeatability (1-5)	5	2	2	2	2
Fluid Contact Visibility (1-5)	5	0	0	0	2
Predicted traveltime change (samples)	>4	0	0	0	0
Predicted impedance change (%)	>4	2.0-3.0	2.0	2.0	2.0

Figure 6.4 *Time-lapse seismic parameter spreadsheet comparing Hibernia values to parameters from White Rose, Terra Nova, and Hebron. Values have been obtained from the Canada-Newfoundland Offshore Petroleum Board (CNOPB) and the respective operator companies. Where data was not available, parameters were estimated and/or calculated based on reasonable assumptions; such estimated data are indicated in red.*

Canada-Newfoundland Offshore Petroleum Board.   For parameters that were not readily available or easily calculated, an estimate was made and these numbers are highlighted in

red.   The overburden pressure was estimated using typical basin densities and the reservoir depth.   The net pressure relies on the overburden pressure and as a result is also uncertain.   The dry bulk modulus was calculated using V_P, V_S, and ρ parameters from each field (equations 3.9 and 3.10), and assuming the fluid modulus makes up a relatively small portion of the overall rock bulk modulus, for the purposes of this risking spreadsheet I assume $K_{dry} \approx K_{sat}$.   The water parameters for Hibernia are used for all fields.   A water salinity of 50,000 ppm is chosen for reasons outlined in section 2.3.3. For the fluid saturation change parameter, the values for the Hebron field are estimated, while the other fields the initial oil saturation is accurate and a reasonable residual oil saturation of 0.30 is used.   For the repeatability score (out of 5), I have used Hibernia's value of 2 for each field.   A value of 2 indicates that a repeat survey uses the same acquisition method (marine streamer), and the lines are oriented in the same direction as the baseline survey.   As full time-lapse seismic modeling, as completed for the Hibernia field in Chapter 3, would be required to delineate the traveltime and impedance changes for the other fields and is outside the scope of this project, these values have been estimated at 0 samples and 2% impedance change respectively.   The 2% impedance change is somewhat arbitrarily chosen as the seismic values in the risk assessment indicate that from fluid substitution alone their time-lapse impedance change will possibly be similar to slightly less than that obserserved at Hibernia.   This is due to the relatively high fluid compressibility contrast, thick reservoir, high porosities, and good sweep efficiency in the Hibernia reservoir.   In the following paragraphs, I outline the key

191

4D seismic elements of the White Rose, Terra Nova, and Hebron fields from the 4D seismic fact sheet in figure 6.4.

The White Rose field's Avalon/Ben Nevis sandstone reservoir has time-lapse seismic parameters comparable to the Hibernia reservoir. The reservoir is at a shallower depth resulting in a lower effective pressure (net pressure). The oil has a lower GOR than the Hibernia oil (but still high), thus the fluid compressibility contrast between oil and water is slightly less at 220% versus 300% at Hibernia.

The Terra Nova sandstone reservoir has net effective pressures that are slightly lower than Hibernia but greater than those estimated at White Rose. The Terra Nova oil has a lower GOR than Hibernia oil. Terra Nova utilizes both water and gas injection as an enhanced oil recovery method. Compared to Hibernia, the consequence of the lower GOR oil is an increased impedance contrast compared to Hibernia for cases where gas is replacing oil (gas injection), and a decreased impedance contrast where there is active water flooding.

Compared to Hibernia, White Rose, and Terra Nova, the Hebron field's Ben Nevis reservoir is significantly shallower at an average depth of approximately 6000 ft (1900 m). Consequently, there is significantly less overburden pressure and the pore pressure of 2750 PSI (19 MPa) is roughly half of the pore pressure at Hibernia. Due to the low GOR oil found in this reservoir, the compressibility contrast with water is lower

compared to the other fields that contain relatively live oil. While the fact sheet in figure 6.4 makes it possible to make general inferences about the potential success of a time-lapse seismic survey, a quantitative estimate is desirable.

6.3.2   Grand Banks 4D seismic risk assessment

To properly compare the results discussed in the previous section, it is advantageous to pursue a numerical comparison. Lumley et al. (1997) present a scoring scheme for the data collected in the 4D seismic parameter sheet displayed in figure 6.4 with a view to ranking the possible risk of potential 4D seismic prospects. As has been previously mentioned throughout this thesis, a meaningful time-lapse seismic signal is a function of both adequate physical reservoir change and the ability of seismic imaging to detect such changes. Lumley et al. (1997) break their scoring method into two subsets; one for reservoir, the other for seismic parameters. The scoring is wholly derived from information in the 4D seismic parameter sheet (figure 6.4) and ranks each parameter on a scale of 0 to 5, with 5 being ideal for 4D seismic success. The method for assigning individual scores for various parameter ranges is discussed extensively in the referenced paper (Lumley et al. 1997).

Figure 6.5 displays a table with the completed scores for the ideal case (45/45 points), the four reservoir examples given by Lumley et al. (1997), and the four fields on the Grand Banks that have been discussed in this thesis. The Grand Banks fields score high in terms of fluid compressibility contrast and saturation change, and have relatively good

seismic image quality.   The lower scores are under categories such as dry bulk modulus (which is high), absence of seismic fluid contacts, and an estimated relatively low impedance change.   The overall seismic and reservoir scores for all fields discussed are plotted in a graph shown in figure 6.6.   This plot has contours showing increasing levels

	IDEAL	INDONESIA	GULF OF MEXICO	WEST AFRICA	NORTH SEA	HIBERNIA	WHITE ROSE	TERRA NOVA	HEBRON
RESERVOIR									
Dry Rock bulk modulus	5	5	4	3	2	2	2	2	2
Fluid Compress. Contrast	5	5	4	3	4	5	4	4	3
Fluid Saturation Change	5	5	5	4	3	5	5	5	4
Porosity	5	5	4	4	3	3	3	3	3
Impedance Change	5	5	4	3	3	2	1	1	1
Subtotal	25	25	21	17	15	17	15	15	13
	100%	100%	84%	68%	60%	68%	60%	60%	52%
SEISMIC									
Seismic Image Quality	5	4	5	4	3	4	1	3	4
Seismic resolution	5	5	4	3	1	3	3	2	2
Seismic fluid contacts	5	4	4	4	2	0	0	0	2
Seismic repeatability	5	5	4	4	2	2	2	2	2
Subtotal	20	18	17	15	8	9	6	7	10
	100%	90%	85%	75%	40%	45%	30%	35%	50%
TOTAL SCORE	45	43	38	32	23	26	21	22	23
	100%	96%	84%	71%	51%	58%	47%	49%	51%

Figure 6.5   *Time-lapse seismic risk assessment scores for existing time-lapse seismic projects (Lumley et al., 1997) and Grand Banks fields.*

of risk as the seismic and reservoir scores decrease.   The Grand Banks fields including Hibernia are in the high risk time-lapse seismic category, but have similar feasibility scores to an existing Jurassic-reservoir 4D seismic project in the North Sea.   With an understanding of the high degree of risks involved, I can proceed to discussing the types of production anomalies that 4D seismic may be most likely to detect in these Grand Banks fields.   While the Hibernia 4D seismic modeling results in this thesis can be used as reference for other fields, for an accurate estimate of 4D seismic response for a particular field, it is imperative that careful time-lapse seismic modeling be conducted over a representative reservoir section using a typical wavelet.
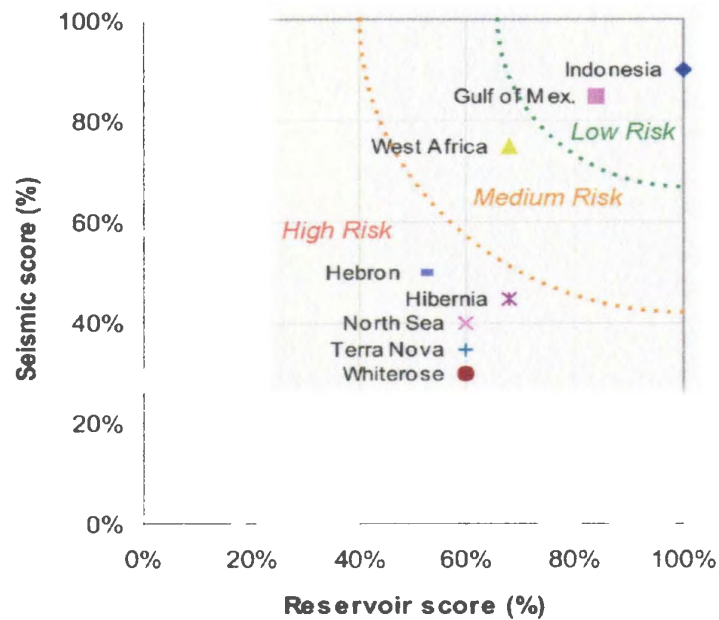
Figure 6.6 *Graph of reservoir and seismic scores from figure 6.5. Concept from Lumley et al., 2000.*

White Rose

The White Rose field has a time-lapse seismic feasibility risk score of 30% for the seismic portion, and 60% for the reservoir component. While these scores place White Rose in the highest level of risk of those fields studied, there are some elements that may prove positive for 4D seismic detection at White Rose. Firstly, the reservoir score with elements such as dry bulk modulus, porosity, and fluid compressibility change are constant throughout production history cannot be improved upon through newer technologies. In this category, White Rose scored 60%, a marginal return, but significantly higher than the low seismic score of 30%. Seismic image quality and survey to survey repeatability can be improved upon through improved acquisition and processing parameters including but not limited to the acquisition of converted wave

195

data. As with Hibernia, if 4D seismic effects can be detected, the optimal place to image these effects in the White Rose field will likely be areas of water replacing oil that have relatively constant to decreasing pore pressures. In addition, another good candidate area to generate time-lapse seismic anomalies in the White Rose field could be an area near an injection well that has a significant pore pressure rise. To make a clear anomaly, the impedance decrease due to rising pore pressure would have to exceed (perhaps significantly) the impedance increase due to water saturation increase.

Terra Nova

The reservoir score for Terra Nova at 60% is identical to the reservoir score for White Rose, while the seismic score is slightly better at 35%. Much of the same commentary given for White Rose applies to Terra Nova in terms of acquisition and processing enhancements that may be able to marginally improve time-lapse seismic detection. As Terra Nova utilizes both water and gas injection, there are a couple of potential reservoir areas that may have the best chance at producing a measurable time-lapse seismic anomaly. The gas-oil fluid compressibility contrast is greater at Terra Nova compared to Hibernia due to the lower GOR oil. As a result, an area of gas injection with a pore pressure rise could be the reservoir zone most likely to produce a time-lapse seismic signal, and due to the lower GOR oil and lower effective pressures, it is possible that the time-lapse seismic response could be greater at Terra Nova than that seen in gas injection zones in the Hibernia reservoir. Compared to gas injection, a water flood is likely a less anomalous target for time-lapse seismic at Terra Nova due to the lower GOR oil

compared to Hibernia, but the oil is still considered live oil and has a fair degree of dissolved gas which gives it a good compressibility contrast with injected water.

Hebron

The lower depth, pressure and bulk modulus in the Ben Nevis reservoir of the Hebron field signifies that the pore fluid modulus contribution to the bulk modulus of the rock is higher on a percentage basis compared to the Hibernia field. As a result, it is possible that even though there is less compressibility contrast between the oil and water due to the low GOR of the oil, there could be a fluid substitution based time-lapse seismic effect on the order of magnitude similar or even greater compared to that seen in the Hibernia time-lapse seismic models where the oil has significant levels of dissolved gas (Chapter 3). The fact that there are fluid contacts that can be imaged in the seismic data is a positive for the possible use of time-lapse seismic to monitor fluid flow. Thorough time-lapse seismic modeling is required to properly delineate the magnitude of any potential oil-water time-lapse seismic effect at Hebron. For the Hebron field, areas around water injectors or oil producers with appreciable changes in reservoir pore pressure will possibly provide the best opportunity to examine time-lapse seismic anomalies. The net and pore pressures for Hebron are roughly half the magnitude of the pressures for the Hibernia field, and there is some evidence of time-lapse seismic anomalies related to pore pressure change for the less susceptible Hibernia reservoir given in Chapter 5. From the preliminary feasibility analysis and comparisons with time-lapse seismic modeling in Chapter 3 it is possible that in the Hebron field, pore pressure change could have a more

significant contribution to potential time-lapse seismic anomalies than pore fluid substitution.

6.4 Conclusions

Results from this time-lapse seismic feasibility analysis indicate that the White Rose, Terra Nova, and Hebron fields on the Grand Banks are all high risk time-lapse seismic candidates. However, it should be noted that an existing Jurassic-reservoir 4D seismic project in the North Sea, and Hibernia, which shows good evidence of production related time-lapse seismic anomalies in the cross equalized data (Chapter 4), have similar time-lapse seismic risk profiles to the other fields on the Grand Banks. In addition, the baseline 3D seismic survey for the Hibernia field was shot in 1991, while all three of the other major fields on the Grand Banks have more modern pre-production surveys acquired around 1997. In the time-lapse seismic feasibility study, the seismic scores were the lowest component of the total score for each of the Grand Banks fields. As elements of the seismic acquisition and processing can be improved for time-lapse seismic purposes, a few general conclusions can be reached. It is possible that at least the first future seismic surveys (into production) over Terra Nova, White Rose, and Hebron will be similar to the Hibernia 2001 3D re-shoot in that it was acquired primarily for advanced structural imaging purposes and secondarily for 4D seismic purposes. While the 2001 Hibernia survey was designed for structural imaging purposes, many acquisition elements were kept the same as the baseline 1991 3D survey. The decision to align the 2001 Hibernia 3D shooting direction and grid orientation to the same azimuth of the

original 1991 acquisition was a key element in the somewhat surprising repeatability of the Hibernia time-lapse cross equalized datasets. Therefore, for other fields in the structurally complex Jeanne d'Arc basin it should be noted that when a new seismic survey is undertaken (into production), as many acquisition parameters as operationally possible should be kept the same as the original survey. The priority elements that should be kept constant are the acquisition direction, bin spacing, navigation positioning, streamer length, and airgun volume. If there is indication that meaningful 4D seismic response can be gathered from the time-lapse seismic datasets, consideration should be given to full 4D prestack co- or parallel- processing of the datasets.

The Grand Banks fields are a very challenging, high risk environment for the implementation of time-lapse seismic. Based in part on the Hibernia time-lapse seismic model response (Chapter 3) and the feasibility spreadsheet comparison with the cross equalized seismic data, it appears as though there is a possibility that meaningful time-lapse seismic data can be obtained from the Hibernia field as well as the potential to detect time-lapse signals in future projects over White Rose, Terra Nova, and Hebron. The feasibility spreadsheet is a first order evaluation of a 4D seismic prospect. Full time-lapse modeling and seismic data signal to noise analysis is required to more accurately assess the suitability of a given reservoir for 4D seismic monitoring.

Chapter 7

Conclusions

7.1 4D seismic analysis of the Hibernia field, Grand Banks, Canada

In this thesis, I have methodically conducted a 4D seismic analysis of the Hibernia oil field, Grand Banks, Canada; a challenging environment for the implementation of the 4D seismic method. This thesis has shown through modeling, processing and interpretation that 4D seismic anomalies in areas of water flooding and gas flooding are above the noise level and have responses consistent with quantitatively modeled responses for each respective scenario. With the possibility of detecting 4D seismic signals in this environment demonstrated by this research, future pre-stack co-processing of 4D seismic data (currently underway at Hibernia) and future dedicated 4D seismic acquisitions will allow for more robust time-lapse seismic analysis and help delineate the potential of using 4D seismic data as a reservoir management tool in this challenging environment.

7.2 Principal contributions and findings of this thesis

I conduct this analysis by modeling the 4D seismic response to various production scenarios, specially processing the seismic datasets to improve repeatability, interpreting various 4D seismic anomalies and verifying them with the modeled response. I then use the results from Hibernia, to assess the feasibility of the 4D seismic method for other fields on the Grand Banks.

In Chapter 2, I present detailed analysis of the Hibernia rock and fluid properties related to modeling 4D seismic response. Firstly, Hibernia pore fluid properties are calculated producing the interesting result that due to the high GOR oil at Hibernia, the gas and oil are more similar in terms of physical properties than are the oil and water. Once pore fluid physics models are determined, original methods for calculating the dry bulk modulus and grain modulus as a simultaneous function of effective pressure and porosity are presented. These three new and original models increase the robustness and determination of the rock physics relationships, and allow for the accommodation of porosity change with pressure within a single core sample. The final model, a facies-varying dry rock modulus model, is demonstrated to be applicable for the lithologies encountered at Hibernia, and significantly improves the accuracy of the modeled reservoir velocities. For the modeling research in this thesis, the Hibernia pore fluid physics and the pressure dependent dry rock changes are independently calculated, and prior to synthetic seismic modeling are merged into a saturated rock model.

In Chapter 3, I present the Hibernia 4D synthetic seismic data. Using the Hibernia rock physics detailed in Chapter 2, synthetic seismic models are generated that show qualitatively and quantitatively the potential 4D seismic response to gas flooding, water flooding, and pressure changes. The modeled 4D seismic response demonstrates that the best areas to image 4D seismic effects at Hibernia are zones around a gas injector (increase in gas saturation, increase in pore pressure) and water flooded areas with a small decrease in pore pressure. In addition, it is shown through modeling that the time-

lapse traveltime change at Hibernia is almost entirely due to pore pressure change, while the modeled amplitude changes at Hibernia are a combination of pore pressure and fluid saturation change. While it isn't possible given the data quality of the cross-equalized datasets to make a quantitative interpretation, the fact that the modeling indicates that traveltime change is pressure driven and relatively independent of saturation change at Hibernia is a significant result that could be utilized in future pressure/saturation inversion algorithms.

In Chapter 4, I use specialized processing techniques to enhance Hibernia 4D seismic anomalies. The goal of such processing is to improve repeatability so a data based interpretation is more robust. Despite the inherent limitations of poststack cross equalization, the processing applied significantly improved data repeatability, enhanced the interpretability, and increased the 4D seismic signal to noise ratio by approximately 40%. In addition to equalizing prestack co-processed or parallel-processed time-lapse seismic datasets, poststack cross equalization is demonstrated to have an important role as a tool for relatively fast evaluation of 4D seismic potential. Poststack cross equalization could be utilized on newly acquired 4D seismic datasets to determine if there is sufficient 4D seismic signal to proceed with the more costly and time consuming dedicated 4D seismic full prestack co-processing or parallel-processing.

In Chapter 5, I present an interpretation of Hibernia 4D seismic anomalies. Using the results of the field-wide cross equalization processing, several 4D seismic anomalies are

202

identified and determined to be above the level of noise in the data. The anomalies in a gas injection area (increasing gas saturation, increasing pressure), display characteristics consistent with the modeled 4D seismic response to gas injection, but the magnitude of the 4D seismic anomalies exceed the response predicted through modeling in Chapter 3. These discrepancies are likely attributed to greater physical changes in the reservoir (higher pressure/saturation change, greater reservoir thickness, etc.) than were modeled.

Another 4D seismic anomaly that I presented was located in a water flooded fault block. This 4D seismic anomaly has characteristics that are consistent with the modeled seismic response to water flooding. The coherent nature of the "pathway" of the 4D seismic anomaly may indicate the presence of a channel or the existence of structural controls on fluid migration. In addition, the spatial extent of this anomaly is bounded by a possible small scale fault that may influence fluid flow direction. Full pre-stack processing of the 4D seismic data is required to fully evaluate such details with an acceptable degree of certainly.

Using the 4D seismic pressure/saturation inversion methods established in Chapter 3, I attempt to invert the time-lapse anomalies for pressure and saturation information. However, due to the relatively low 4D seismic signal to noise ratio, the inversion method fails to produce reasonable physical property values from the 4D seismic data. However, interesting qualitative pressure change/saturation change anomalies are generated around a water injection well for which the amplitude difference alone was negligible. While the

Hibernia 4D dataset did not have sufficient signal to noise for these new and original methods to work, such quantitative pressure/saturation inversion methods may be successful with a more repeatable seismic acquisition, full pre-stack co-processing, and more favorable acquisition/reservoir conditions.

In Chapter 6, I present a 4D seismic feasibility study for the major oil fields on the Grand Banks. Similar to Hibernia, the White Rose, Terra Nova, and Hebron fields are all predicted to be high risk, but not impossible, 4D seismic candidates. Each field does have characteristics that hold potential for the detection of 4D seismic signals. Detailed 4D seismic modeling is required to more accurately assess the 4D seismic potential in each reservoir. I would strongly recommend that when future seismic surveys are acquired (even if acquired solely for structural imaging purposes) over these producing fields, as many acquisition parameters as operationally possible should be kept the same as the baseline survey. These parameters would particularly include acquisition shooting direction, so that the acquired data is optimized for potential 4D seismic purposes. If there is indication that meaningful time-lapse response can be gathered from the 4D seismic datasets – possibly through fast poststack cross equalization, consideration should be given to full 4D prestack co- or parallel-processing of the datasets.

As the Grand Banks oil fields are in the early stages of development, it is difficult to predict exactly how future development will proceed. The seismic feasibility analysis in Chapter 6 demonstrated that a fair degree of the risk associated with potential time-lapse

seismic projects is due to the seismic parameters, while the reservoir score is comparable to North Sea fields that have ongoing dedicated 4D efforts. As the acquisition and processing of 4D seismic data is continually evolving, it is probable in my opinion that the technological improvements over time will allow for 4D seismic technology to be utilized in the future as a reservoir monitoring tool on the challenging fields of the Canadian Grand Banks.

8. References

Adams, D. 2001. Personal Communication

Aki, K. and Richards, P.G. 1980, Quantitative seismology. W.H. Freeman & Co.

Batzle, M. and Wang, Z. 1992. Seismic Properties of Pore Fluids. *Geophysics*. Vol. 57. No. 11 P. 1396-1408.

Berryman, J. G., 1999, Origin of Gassmann's equations: *Geophysics*, Soc. of Expl. Geophys., 64, 1627-1629.

Berryman, J. G. and Milton, G. W., 1991, Exact results for generalized Gassmann's equations in composite porous media with two constituents: *Geophysics*, Soc. of Expl. Geophys., Vol. 56, P. 1950-1960.

Biot, M. A., 1956. "Theory of propagation of elastic waves in a fluid-saturated porous solid, part I: low frequency range," *J. Acoust. Soc. Am.*, 28, pp. 168-178, 1956.

Brie, A., Pampuri, F., Marsala, A. F., and Meazza,O., 1995, Shear sonic interpretation in gas-bearing sands: SPE paper 30595, 701–710.

CNOPB. 2003. Discovered reserves and resources – May 2nd, 2003. Canada Newfoundland Offshore Petroleum Board. http://www.cnopb.nfnet.com/

CNOPB. 1997. Properties of oil bearing reservoirs. Canada Newfoundland Offshore Petroleum Board. http://www.cnopb.nfnet.com/

Christie, M., MacBeth, C. and Subbey, S., 2002, Multiple history-matched models for Teal South: *The Leading Edge*, Vol. 21, no. 03, P. 286-289.

Claerbout, J. F., 1985, Imaging the Earth's interior: Blackwell Scientific Publications

Clark, V. A., 1992, The effect of oil under in-situ conditions on the seismic properties of rocks: *Geophysics*, Soc. of Expl. Geophys., Vol. 57, P. 894-901.

Cole, S., Lumley, D., Meadows, M. and Tura, A., 2002, Pressure and saturation inversion of 4D seismic data by rock physics forward modeling, 72nd Ann. Internat. Mtg: Soc. of Expl. Geophys., 2475-2478

Cole, S. 2001. Personal Communication

Domenico, S. N., 1976, Effect of brine-gas mixture on velocity in an unconsolidated gas reservoir: *Geophysics*, Vol. 41, P. 882–894.

Dvorkin, J., Moos, D., Packwood, J. L., and Nur, Amos. M. 1999. Identifying patchy saturation from well logs. *Geophysics*. Vol. 64, No. 6 ; P. 1756–1759.

Eastwood, J. E., Johnston, D., Huang, X., Craft, K. and Workman, R., 1998, Processing for robust time-lapse seismic analysis: Gulf of Mexico example, Lena Field, 68th Ann. Internat. Mtg: Soc. of Expl. Geophys., 20-23.

Ebrom, D., 1999, Permanently instrumented offshore oilfields: opportunities and challenges, 69th Ann. Internat. Mtg: Soc. of Expl. Geophys., P. 1986-1987.

Ebrom, D. A., Purnell, G. and Krail, P., 1997, Repeatability of marine seismic streamer data for prestack analysis at the Orca basin, 67th Ann. Internat. Mtg: Soc. of Expl. Geophys., 59-62.

Ecker, C., Lumley, D., Tura, A. C., Kempner, W. and Klonsky, L., 1999, Estimating Separate Steam Thickness and Temperature Maps from 4D Seismic Data: An Example from San Joaquin Valley, California, 69th Ann. Internat. Mtg: Soc. of Expl. Geophys., 2032-2034.

Evans, J. 2004. Personal communication

Gassmann, F. 1951. Elastic waves through a packing of spheres: *Geophysics*, Vol. 16: P673-685.

Graul, M. 2003. AVO-Seismic Lithology. SEG Short Course. Dallas, Texas, October 2003.

Greaves, R., and Fulp, T. 1987, Three-dimensional seismic monitoring of an enhanced oil recovery process, *Geophysics*, Vol 52, No 9, P 1175-1187

GSC. 1992. Petroleum Resources of the Jeanne d'Arc Basin and Environs, Grand Banks, Newfoundland. Geological Survey of Canada. Paper 92-8.

Han, D. H., Nur, A. and Morgan, D., 1986, Effects of porosity and clay content on wave velocities in sandstones. *Geophysics* Vol. **51,** 2093-2107.

Helgeson, H.C. and Kirkham, D. H. 1974. Theoretical prediction of thermodynamic behavior of aqueous electrolytes: *American Journal of Science.* 274, P. 1089-1198.

Hibernia rock physics report. 2000. Prepared by the Stanford Rock Physics Laboratory.

Hilterman, F.J.. 2001. *Seismic Amplitude Analysis.* Society of Exploration Geophysicists, pub. Tulsa, Ok.

Husky. 2004. Husky Energy Whiterose information website. http://www.huskyenergy.ca/whiterose/

Jack, I. 1998. *Time-Lapse Seismic in Reservoir Management.* Society of Exploration Geophysicists. Tulsa, Ok.

Johnston, D. H., Eastwood, J. E., Shyeh, J. J., Vauthrin, R., Khan, M. and Stanley, L. R., 2000, Using legacy seismic data in an integrated time-lapse study: Lena Field, Gulf of Mexico: *The Leading Edge,* Vol 19, no. 03, P. 294-302.

Johnston, D. H., McKenny, R. S. and Burkhart, T. D., 1997, Time-lapse seismic analysis of the North Sea Fulmar field, 67th Ann. Internat. Mtg: Soc. of Expl. Geophys., 890-893.

Koster, K., Gabriels, P., Hartung, M., Verbeek, J., Deinum, G. and Staples, R., 2000, Time-lapse seismic surveys in the North Sea and their business impact: *The Leading Edge*, Vol. 19, no. 03, P. 286-293.

Landmark Graphics Corporation. 1999. *Poststack Family Reference Manual.*

Landro, M. 1999. Repeatability issues of 3-D VSP data. *Geophysics*, Vol 64, No 6, P. 1673-1679

Landro, M. 2001. Discrimination between pressure and fluid saturation changes from time-lapse seismic data. *Geophysics*, Vol 66, No. 3. P. 836-844

Lumley, D. 2004. Personal Communication.

Lumley, D., Adams, D., Meadows, M., Cole, S. and Wright, R., 2003, 4D seismic data processing issues and examples, 73rd Ann. Internat. Mtg.: Soc. of Expl. Geophys., 1394-1397.

Lumley, D., Meadows, M., Cole, S. and Adams, D., 2003b, Estimation of reservoir pressure and saturations by crossplot inversion of 4D seismic attributes, 73rd Ann. Internat. Mtg.: Soc. of Expl. Geophys., 1513-1516.

Lumley, D. 2001. Time-lapse seismic reservoir monitoring. *Geophysics*, Vol. 66, No. 1, P. 50-53.

Lumley, D., 2001b, The next wave in reservoir monitoring: The instrumented oil field: *The Leading Edge*, Vol. 20, no. 6, 640-648.

Lumley, D., Cole, S., Meadows, M., Tura, A., Hottman, W., Cornish, B., Curtis, M. and Maerefat, N., 2000, A risk analysis spreadsheet for both time-lapse VSP and 4-D seismic reservoir monitoring, 70th Ann. Internat. Mtg: Soc. of Expl. Geophys., 1647-1650.

Lumley, D., Behrens, R. A., and Wang, Z., 1997. Assessing the technical risk of a 4-D seismic project: *The Leading Edge*, 16, no. 09, P. 1287-1291.

Lumley, D. 1995. Phd Thesis, Stanford University, Stanford, California.

Mavko, G., Mukerji, T., and Dvorkin, J. 1998, *"The rock physics handbook – Tools for seismic analysis in porous media"*: Cambridge University Press.

Mavko, G. and Mukerji, T., 1998, Bounds on low-frequency seismic velocities in partially saturated rocks: *Geophysics*, Soc. of Expl. Geophys., 63, 918-924.

Meadows, M., Adams, D., Wright, R., Lumley, D., Tura, A. and Cole, S., 2002, Rock physics analysis for time-lapse seismic at Schiehallion Field, North Sea, 72nd Ann. Internat. Mtg: Soc. of Expl. Geophys., 1743-1746.

Meadows, M. 2002b. Personal communication

Nolen-Hoeksema, R.C., 2000, Modulus - porosity relations, Gassmann's equations, and the low-frequency elastic-wave response to fluids: *Geophysics*, Soc. of Expl. Geophys., 65, 1355-1363.

Nur, A., 1989, Four-dimensional seismology and (true) direct detection of hydrocarbons: The petrophysical basis: *The Leading Edge*, Vol. 08, no. 09, P. 30-36.

Ocean Resources, 2003. "Projects: Hibernia" Anon author, Ed. Elliott, J. Vol. 21, No. 8, P. 6

Pullin, N., Matthews, L., Hirsche, K. 1987, Techniques applied to obtain very high resolution 3D seismic imaging at an Athabasca tar sands thermal pilot, *The Leading Edge*, Vol. 6, No. 12, P 10-15.

Rickett, J. and Lumley, D. E., 2001, Cross-equalization data processing for time-lapse seismic reservoir monitoring: A case study from the Gulf of Mexico: *Geophysics*, Vol. 66, P. 1015-1025.

Ross, C. P., and Altan, S., 1997, Time-lapse seismic monitoring: Some shortcomings in nonuniform processing: *The Leading Edge*, Vol 16, P. 931-937

Ross, C.P. Cunningham, G.B., and Weber, D.P., 1996. Inside the cross equalization black box. *The Leading Edge*, 15: No. 11: P. 1233-1240

Sheriff R. and L. Geldart, 1982. *Exploration Seismology.* 1st ed, Cambridge University Press,

Sonneland, L., Veire, H. H., Raymond, B., Signer, C., Pedersen, L., Ryan, S. and Sayers, C., 1997, Seismic reservoir monitoring on Gullfaks: *The Leading Edge*, Vol. 16, no. 09, P. 1247-1252.

Standing, M.B. 1962. Oil systems correlations, in Frick, T.C. editor, *Petroleum production handbook, volume II*: McGraw-Hill Book Co., part 19.

Thomas, L. K., Hankinson, R. W., and Phillips, K. A., 1970. Determination of acoustic velocities for natural gas. *Journal of Petroleum Technology.* Vol. 22, P. 889-892.

Tura A. and Lumley D. 1998. Subsurface fluid-flow properties from time-lapse elastic-wave reflection data. 43rd Ann. Mtg. International Society for Optical Engineering (SPIE), Proceedings, 125-138.

USGS, 2003. Ocean Salinity. United States Geological Survey website. http://wwwga.usgs.gov/edu/whyoceansalty.html

Wang, Z. 2001. "Fundamentals of seismic rock physics": *Geophysics*, 66: P398-412

Wang, Z., Hirsche, W. K. and Sedgwick, G., 1991, Seismic monitoring of water floods? A petrophysical study: *Geophysics*, Soc. of Expl. Geophys., Vol. 56, P. 1614-1623.

Wang, Z. and Nur, A. and Levin, F.K., Ed., 1989, *Seismic and Acoustic Velocities in Reservoir Rocks*, Vol. 2, Society of Exploration Geophysicists

Wardlaw, N.C. 2002   How rock and reservoir properties determine oil and gas recovery; a course for production geologists and reservoir engineers.   Memorial University, St. John's, Canada

Watts, G., Jizba, D., Gawith, D., and Gutteridge, P., 1996.   Reservoir Monitoring of the Magnus field through time-lapse seismic analysis. *Petroleum Geoscience*. Nov. 1996.

Wright, R. 1999.   B.Sc. (Hons) Thesis, Memorial University, St. John's, Canada.

Wyllie, M. R. J., Gregory, A. R. and Gardner, G. H. F., 1958, An experimental investigation of factors affecting elastic wave velocities in porous media: *Geophysics*, Soc. of Expl. Geophys., Vol. 23, P. 459-493.

Appendix A

Inversion equations.

Gas Flooding

X1	Change in Pore Pressure (MPa)
X2	Change in Stacked Amplitude (absolute)
Y	Increase in Gas Saturation

DataFit version 7.0.36
Results from project "c:\rich\gradwork\phd thesis\chapter3\datafit\3d images\gas_inversion.dft"
Equation ID: a+b*x1+c*x1^2+d*x1^3+e*x2+f*x2^2+g*x2^3+h*x2^4+i*x2^5
Model Definition:
Y = a+b*x1+c*x1^2+d*x1^3+e*x2+f*x2^2+g*x2^3+h*x2^4+i*x2^5

Number of observations = 20
Number of missing observations = 0
Solver type: Nonlinear
Nonlinear iteration limit = 250
Diverging nonlinear iteration limit =10
Number of nonlinear iterations performed = 6
Residual tolerance = 0.0000000001
Sum of Residuals = -1.40859546249317E-15
Average Residual = -7.04297731246584E-17
Residual Sum of Squares (Absolute) = 1.60196404376032E-02
Residual Sum of Squares (Relative) = 1.60196404376032E-02
Standard Error of the Estimate = 3.81619044188444E-02
Coefficient of Multiple Determination (R^2) = 0.9930590813
Proportion of Variance Explained = 99.30590813%
Adjusted coefficient of multiple determination (Ra^2) = 0.9880111404
Durbin-Watson statistic = 1.49826723245287

Regression Variable Results

Variable	Value	Standard E	t-ratio	Prob(t)
a	-0.04907	0.028992	-1.692547	0.11864
b	-0.121906	0.007892	-15.44627	0
c	-0.002952	0.000417	-7.081408	0.00002
d	-4.85E-05	4.81E-05	-1.008872	0.33471
e	0.000319	1.92E-05	16.61375	0
f	1.24E-08	4.81E-09	2.565579	0.02626
g	-3.56E-13	1.24E-12	-0.286953	0.77948
h	-7.13E-17	2.82E-16	-0.253277	0.80473
i	5.09E-21	1.39E-20	0.365855	0.72141

Appendix B

Inversion equations.

Water Flooding

X1   Change in Pore Pressure (MPa)
X2   Change in Stacked Amplitude (absolute)
Y   Increase in Water Saturation

DataFit version 7.0.36
Results from project "c:\rich\gradwork\phd thesis\chapter3\datafit\3d images\water_inversion.dft"
Equation ID: $a+b*x1+c*x2+d*x1\hat{}2+e*x2\hat{}2+f*x1*x2$
Model Definition:
$Y = a+b*x1+c*x2+d*x1\hat{}2+e*x2\hat{}2+f*x1*x2$

Number of observations = 20
Number of missing observations = 0
Solver type: Nonlinear
Nonlinear iteration limit = 250
Diverging nonlinear iteration limit =10
Number of nonlinear iterations performed = 3
Residual tolerance = 0.0000000001
Sum of Residuals = -4.04579147961215E-13
Average Residual = -2.02289573980607E-14
Residual Sum of Squares (Absolute) = 3.94521881120476E-02
Residual Sum of Squares (Relative) = 3.94521881120476E-02
Standard Error of the Estimate = 5.30849643173548E-02
Coefficient of Multiple Determination (R^2) = 0.982906331
Proportion of Variance Explained = 98.2906331%
Adjusted coefficient of multiple determination (Ra^2) = 0.9768014492
Durbin-Watson statistic = 1.06595631576423

Regression Variable Results

Variable	Value	Standard E	t-ratio	Prob(t)
a	0.042679	0.023692	1.801432	0.09321
b	0.078371	0.005685	13.78546	0
c	-0.000187	1.19E-05	-15.7234	0
d	-0.001386	0.000357	-3.888186	0.00164
e	-9.98E-09	1.43E-09	-6.986802	0.00001
f	9.37E-06	1.38E-06	6.798859	0.00001

Appendix B

Inversion equations.

Water Flooding

X1	Change in Pore Pressure (MPa)
X2	Change in Stacked Amplitude (absolute)
Y	Increase in Water Saturation

DataFit version 7.0.36
Results from project: "c:/Hob/gradschool/phd thesis/chapter3/datafit/3d images/water_inversion.dft"
Equation ID: a+b*x1+c*x2+d*x1^2+e*x2^2+f*x1*x2
Model Definition:
Y = a+b*x1+c*x2+d*x1^2+e*x2^2+f*x1*x2

Number of observations = 20
Number of missing observations = 0
Solver type: Nonlinear
Nonlinear iteration limit = 250
Diverging nonlinear iteration limit = 10
Number of nonlinear iterations performed = 3
Residual tolerance = 0.0000000001
Sum of Residuals = -4.04579147961218E-13
Average Residual = -2.02289573950807E-14
Residual Sum of Squares (Absolute) = 3.9452188112047E-02
Residual Sum of Squares (Relative) = 3.9452188112047E-02
Standard Error of the Estimate = 5.30849643173549E-02
Coefficient of Multiple Determination (R^2) = 0.9829063531
Proportion of Variance Explained = 98.29063531%
Adjusted coefficient of multiple determination (Ra^2) = 0.9768014462
Durbin-Watson statistic = 1.06699631519422

Regression Variable Results

Variable	Value	Standard Error	t-ratio	Prob(t)
a	0.042879	0.023692	1.801432	0.09321
b	0.017837	0.000885	13.78246	0
c	-0.000187	1.19E-05	-15.7234	0
d	-0.007365	0.000357	-3.88618	0.00184
e	-9.86E-08	1.43E-08	-6.89602	0.00001
f	9.37E-06	1.36E-06	6.79088	0.00001